Mechanical and electrical properties of carbon nanofiber–ceramic nanoparticle–polymer composites

Vom Fachbereich für Maschinenbau und Verfahrenstechnik

der Technischen Universität Kaiserslautern

zur Erlangung des akademischen Grades

Doktor-Ingenieur (Dr.-Ing.)

genehmigte Dissertation

von

Dipl.-Phys. Pablo Carballeira Pol

aus Oviedo, Spanien

Tag der mündlichen Prüfung:	18. Januar 2010
Prüfungsvorsitzender:	Prof. Dr.-Ing. E. Kerscher
1. Berichterstatter:	Prof. Dr.-Ing. Dr. h.c. mult. K. Friedrich
2. Berichterstatter:	Prof. Dr. R. Pelster
3. Berichterstatter:	Prof. Dr.-Ing. M. Maier

Acknowledgements

The present work was completed between October 2005 and October 2009 at the department of materials science from the Institut für Verbundwerkstoffe GmbH (IVW), at the Technical University of Kaiserslautern. This work was carried out with the financial support of the Federal Ministry of Education and Research (BMBF) as a part of the research project “Nanopartikelverstärkte polymere Hochleistungskunststoffe - Technische Leistungsfähigkeit und wirtschaftliche Herstellverfahren“ (Project number: 03X5500). Industrial partners in this endeavour were the companies Sachtleben Chemie GmbH and Evonik Industries AG.

First and foremost, I would like to convey my gratitude to my PhD supervisor Prof. Dr.-Ing. Dr. h.c. mult. K. Friedrich for his scientific support and concern about the progress of my research. I would also like to thank Prof. Dr. h.c. J. Karger-Kocsis and Dr.-Ing. B. Wetzel for the fruitful scientific discussions on polymer reinforcement. Many thanks to Prof. Dr.-Ing. E. Kerscher for accepting the presidency of the examination committee and to Prof. Dr. Pelster and Prof. Dr.-Ing Maier for being co-referees of this PhD thesis.

I am also grateful to Prof. A. K. Schlarb and Dr. F. Haupert for providing me the opportunity of working in an outstanding environment from the scientific and technical point of view. Many thanks to the whole IVW-Staff, especially the colleagues of Department II and the “Nanoforschergruppe”, Markus Englert, Birgit Bittmann, Nicole Knör and Rolf Walter. Thanks to Heidrun Plocharzik for her help and assistance in the laboratory and to Hermann Giertzsch for the outstanding SEM pictures that illustrate this research. I would also like to express my gratefulness to my HiWis and practicum students, Javier Calvo, Maria González, Gaoping Wang, Ignacio Buezas, Jordi Mateu, Pablo Bernal, Antonio Ruesca and Julia Arca without whose help this work could not have been accomplished.

I am especially grateful to my dear good friends, Christina Baltá and Núria Castellà, among many others for their constant encouragement and for the all the good times spent together. I wish to thank my entire family, especially my sister, my aunts, uncles and cousins, and my grandmother for their love and encouragement.

Very special thanks to my girlfriend Jenny for the love and support that she has given me over the past years, especially during the long, dark and cold German winters.

Last but not least I would like to express my special gratitude to my parents, Carmen Pol Méndez and Jesús Carballeira Cueto (Carba). They bore me, raised me, educated and ”travelled” me while giving me all their love and support. Con mi mayor y más profundo agradecimiento, este trabajo está dedicado a ellos.

“Felix, qui potuit rerum conoscere causas. ”

Georgicon (Book II, v. 490), Publius Vergilius Maro (70 BCE-19 BCE)

“None but those who have experienced them can conceive of the enticements of science.”

Frankenstein; or, The Modern Prometheus (Chapter IV),

Mary Shelley (née Mary Wollstonecraft Godwin; 1797-1851)

“There are things known and things unknown and in between are the doors.”

Jim Morrison (1943-1971)

Table of contents

Abstract

The present research is focused on the manufacturing and analysis of composites consisting of a thermosetting polymer reinforced with fillers of nanometric dimensions. The materials were chosen to be an epoxy resin matrix and two different kinds of fillers: electrically conductive carbon nanofibers (CNFs) and ceramic titanium dioxide (TiO_2) and aluminium dioxide (Al_2O_3) nanoparticles. In an initial step of the work, in order to understand the effect that each kind of filler had when added separately to the polymer matrix, CNF–EP and ceramic nanoparticle–EP composites were manufactured and tested. Each type of filler was dispersed in the polymer matrix using two different dispersion technologies. CNFs were dispersed in the resin with the aid of a three roll calender (TRC) whereas a torus bead mill (TML) was used in the ceramic nanoparticle case.

Calendering proved to be an efficient method to disperse the untreated CNFs in the polymer matrix. The study of the physical properties of undispersed CNF composites showed that the tensile strength and the maximum sustained strain, were more sensitive to the state of dispersion of the nanofibers than the elastic modulus, fracture toughness, impact energy and electrical conductivity (for filler loadings above the percolation threshold of the system). Rheological investigation of the uncured CNF–epoxy mixture at different stages of dispersion indicated the formation of an interconnected nanofiber network within the matrix after the initial steps of calendering. CNF–EP composites showed better mechanical performance than the unmodified polymer matrix. However, the tensile modulus and strength of the CNF composites accused the presence of remaining nanofiber clusters and did not reach theoretically predicted values. Fracture toughness and resistance against impact did not seem to be so sensitive to the state of nanofiber dispersion and improved consistently with the incorporation of the CNFs. The electrical conductivity of the CNF composites saw an eight orders of magnitude percolative enhancement with increasing nanofiber content. The percolation threshold for the achieved level of CNF dispersion was found to be 0.14 vol. %. It was also determined that, for these composites, the main mechanism of electrical transmission was the electron tunnelling mechanism.

Ceramic nanoparticle–EP composites were manufactured using TiO_2 and Al_2O_3 particles as fillers in the epoxy matrix. Mechanical dispersion of the nanoparticles in the liquid polymer by means of a torus bead mill dissolver led to homogeneous distributions of particles in the matrix. Remaining particle agglomerates had a mean value of 80 nm. However, micrometer sized agglomerates could clearly be observed in the microscopical analysis of the composites, especially in the TiO_2 case. The inclusion of the nanoparticles in the epoxy resin resulted in a general improvement of the modulus, strength, maximum sustained strain, fracture toughness and impact energy of the polymer matrix. Nanoparticles were able to overcome the stiffness/toughness problem. On the other hand, nanoparticle–EP composites showed lower electrical conductivity than the neat epoxy. In general, there were no significant differences between the incorporation of TiO_2 or Al_2O_3 particles.

Based on the previous results, CNFs and nanoparticles were combined as fillers to create a nanocomposite that could benefit from the electrical properties provided by the conductive CNFs and, at the same time, have improved mechanical performance thanks to the presence of the well dispersed ceramic nanoparticles. Nanoparticles and CNFs were dispersed separately to create two batches which were blended together in a dissolver mixer. This method proved effective to create well dispersed CNF–nanoparticle–epoxy composites which showed improved electrical and mechanical properties compared with the neat polymer matrix. The well dispersed ceramic nanofillers were able to introduce additional energy dissipating mechanisms in the CNF–EP composites that resulted in an improvement of their mechanical performance. With high volume loadings of nanoparticles most of the reinforcement came from the presence of the nanoparticles in the polymer matrix. Therefore, the observed trends were, in essence, similar to the ones observed in the ceramic nanoparticle–EP composites. The enhancement in the mechanical performance of the CNF composites with the inclusion of ceramic nanoparticles came at the price of an increase in the percolation threshold and a reduction of the electrical conductivity of the CNF–nanoparticle–EP composites compared with the CNF–EP materials. A modified Weber and Kamal's fiber contact model (FCM) was used to explain the electrical behaviour of the CNF–nanoparticle–EP composites once percolation was achieved. This model was able to fit rather accurately the experimentally measured conductivity of these composites.

Kurzfassung

Die vorliegende Forschungsarbeit konzentrierte sich auf die Herstellung und Analyse von Verbundwerkstoffen, die aus einem duroplastischen Polymer bestehen, das mit nanoskaligen Füllstoffen verstärkt wurde. Als Materialien wurden eine Epoxidharz-(EP) Matrix und zwei verschiedene Arten von Verstärkungsstoffen gewählt: elektrisch leitende Kohlenstoffnanofasern (CNFs) und keramische Titandioxid- (TiO_2) und Aluminiumdioxid- (Al_2O_3) Nanopartikel. In einem ersten Schritt der Arbeit wurden CNF-EP- und TiO_2-EP- bzw. Al_2O_3-EP-Verbundwerkstoffe gefertigt und geprüft, um die Wirkung jedes Füllstoffes alleine auf die Polymermatrix zu verstehen. Zur Dispergierung der Verstärkungsstoffe im polymeren Grundmaterial wurden zwei verschiedene Dispergiermethoden verwendet. Die Kohlenstoffnanofasern wurden mithilfe eines Dreiwalzwerks im Harz dispergiert, wohingegen für die keramischen Nanopartikel eine Tauchmühle verwendet wurde.

Es stellte sich heraus, dass der Einsatz des Dreiwalz-Kalanderwerks eine effiziente Methode zur Dispergierung der unbehandelten CNFs in der Polymermatrix ist. Die Studie der physikalischen Eigenschaften von undispergierten CNF- Verbundwerkstoffen zeigte, dass die Zugfestigkeit und die maximale Dehnung deutlich stärker vom Dispergierzustand der Nanofasern abhängen als der elastische Modul, die Bruchzähigkeit, die Schlagzähigkeit und die elektrische Leitfähigkeit (für Füllstoffgehalte oberhalb der Perkolationsschwelle des Systems). Rheologische Untersuchungen von unvernetzten Kohlenstoffnanofaser-Epoxidharz-Mischungen in verschiedenen Dispergierzuständen zeigten die Bildung eines ineinandergreifenden Nanofaser-Netzes innerhalb der Matrix nach den ersten Kalanderschritten. CNF-EP-Verbundwerkstoffe zeigten bessere mechanische Eigenschaften als die unmodifizierte Polymermatrix. Der Zugelastizitätsmodul und die Zugfestigkeit dieser Werkstoffe erreichten jedoch die theoretisch vorausgesagten Werte aufgrund der im Material verbliebenen Nanofaser-Cluster nicht. Die Bruchzähigkeit und Schlagzähigkeit hingegen schienen stark durch den Dispergierzustand beeinflusst zu werden und stiegen durchweg mit steigendem Kohlenstoffnanofaser-Gehalt an. Das elektrische Leitvermögen der Nanofaser-Verbundwerkstoffe erfuhr eine perkolative Erhöhung um acht Größenordnungen mit steigendem Nanofaser-Gehalt. Die Perkolationsschwelle für das erreichte Dispergierniveau der CNFs lag bei

0,14 Vol.-%. Es wurde außerdem festgestellt, dass für diese Verbundwerkstoffe der Hauptmechanismus der elektrischen Leitfähigkeit der Tunneleffekt war.

Zur Herstellung von Keramik-Nanopartikel-EP-Verbundwerkstoffen wurden TiO_2- und Al_2O_3-Nanopartikel als Füllstoffe für eine Epoxidharzmatrix verwendet. Die mechanische Dispergierung der Nanopartikel im flüssigen Polymer mittels einer Tauchmühle führte zu einer homogenen Verteilung der Partikel in der Matrix. Die verbleibenden Partikelagglomerate hatten einen Mittelwert von 80 nm. Jedoch konnten bei der mikroskopischen Analyse der Verbundwerkstoffe besonders im Fall des TiO_2 Agglomerate im Mikrometerbereich beobachtet werden. Die Verstärkung des Epoxidharzes durch die keramischen Nanopartikel führte zu einer allgemeinen Verbesserung des Moduls, der Festigkeit, der maximalen Dehnung, der Bruchzähigkeit und der Schlagzähigkeit der Polymermatrix. Die Nanopartikel konnten das Steifigkeits-/Zähigkeits-Problem überwinden. Auf der anderen Seite zeigten die Nanopartikel-EP-Werkstoffe eine geringere elektrische Leitfähigkeit als das reine Epoxidharz. Im Allgemeinen führte die Einarbeitung von TiO_2 oder Al_2O_3 zu keinen größeren Unterschieden zwischen den beiden Werkstoffen.

Beruhend auf den vorherigen Ergebnissen wurden Kohlenstoffnanofasern und Nanopartikel als Füllstoffe kombiniert, um einen Nanoverbundwerkstoff zu schaffen, der sowohl bessere elektrische Eigenschaften, die durch die leitenden Nanofasern hervorgerufen wurden, zeigt als auch eine gute mechanische Leistungsfähigkeit dank der Verstärkung durch die gut dispergierten Nanopartikel. Die keramischen Nanopartikel und die Nanofasern wurden getrennt dispergiert und so zwei Mischungen hergestellt, die dann in einem Dissolver zusammengemischt wurden. Diese Methode erwies sich als wirksam, um gut dispergierte CNF-Nanopartikel-Epoxy-Verbundwerkstoffe zu fertigen, die verbesserte elektrische und mechanische Eigenschaften im Vergleich zur ungefüllten Polymermatrix zeigten. Die gut dispergierten nanoskaligen Füllstoffe waren im Stande zusätzliche Energiedissipations-Mechanismen im CNF-EP-Verbundwerkstoff zu induzieren, die eine allgemeine Verbesserung der mechanischen Eigenschaften zur Folge hatten. Bei den Werkstoffen mit einem hohen Nanopartikelvolumengehalt wurde die Verstärkungswirkung vor allem durch die Nanopartikel hervorgerufen, und die hier beobachteten Tendenzen sind ähnlich wie die der reinen

Keramik-Nanopartikel-EP-Materialien. Die Erhöhung der mechanischen Eigenschaften der CNF-Verbundwerkstoffe durch die keramischen Nanopartikeln ging auf Kosten der elektrischen Eigenschaften. Ein Anstieg der Perkolationsschwelle und eine Reduktion der elektrischen Leitfähigkeit gegenüber dem reinen CNF-EP-Material waren die Folge. Ein modifiziertes Faser-Kontakt-Modell (FKM) von Weber und Kamal wurde verwendet, um das elektrische Verhalten der CNF-Nanopartikel-EP-Verbundwerkstoffe nach Erreichen der Perkolation zu erklären. Dieses Modell war im Stande die experimentell gemessene Leitfähigkeit der Verbundwerkstoffe relativ genau zu beschreiben.

List of abbreviations and symbols

Abbreviations

AFM	Atomic force microscopy
CB	Carbon black
CF	Carbon fiber
CNF	Carbon nanofiber
CNT	Carbon nanotube
CT	Compact tension
DGEBA	Di-glycidyl ether of bisphenol A
DLS	Dynamic light scattering
DMTA	Dynamical mechanical thermal analysis
DNA	Deoxyribonucleic acid
DSC	Dilute solution of clusters
DWCNT	Double wall carbon nanotube
EMI	Electromagnetic interference
EP	Epoxy resin
ESC	Electrostatic charge
ESD	Electrostatic discharge
FCM	Fiber contact model
GF	Glass fiber
IPD	Interparticle distance
LCF	Long carbon fiber
MCF	Medium carbon fiber
MCP	Metal coated polymer

MWCNT	Multi wall carbon nanotube
PA	Polyamide
PANI	Polyaniline
PP	Polypropylene
PVDF	Polyvinylidene Fluoride
RFI	Radio frequency interference
SCF	Short carbon fiber
SEM	Scanning electron microscopy
SWCNT	Single wall carbon nanotube
TEM	Transmission electron microscopy
TML	Torus mill
TRC	Three roll calender
VGCNF	Vapour grown carbon nanofiber

Symbols

a_0	[mm]	Distance from the applied load to the crack tip (CT sample)
B	[mm]	Thickness of compact tension samples
D	[m^2/s]	Translational diffusion coefficient
D_{50}	[nm]	Mean nanoparticle diameter
d_c	[nm]	Diameter of the circle contact between two nanofibers
d_h	[m]	Hydrodynamic diameter
E	[MPa]	Young's modulus
$\left\|E^*\right\|$	[MPa]	Complex Young's modulus
e	[C]	Electrical charge

$F_{\max}$	[N]	Maximum sustained force (tensile tests)
$F_{Q,\max}$	[N]	Maximum sustained force (compact tension tests)
G'	[Pa]	Storage modulus
G''	[Pa]	Loss modulus
$\vec{J}$	[A/mm^2]	Current density
k	[MPa]	Bulk modulus
K_{IC}	[MPa$\cdot\sqrt{\mathrm{m}}$]	Critical stress intensity factor (mode I)
K_B	[J/K]	Boltzmann's constant
$K_{Q,\max}$	[MPa$\cdot\sqrt{\mathrm{m}}$]	Maximum stress intensity (compact tension tests)
m	[1]	Number of contacts between nanofibers
p_c	[wt. %]	Critical weight content
q_0	[C]	Initial charge concentration
$R_{CNF-CNF}$	[Ω]	Resistance of a CNF segment between two contacts
$R_{contact}$	[Ω]	Resistance of CNF contact
R_{EPfilm}	[Ω]	Resistance of an epoxy film between CNF
$\vec{r}_i$	[1]	Position of the contact point i
R_S	[Ω]	Surface resistance
$S_{contact}$	[nm^2]	Surface area of the contact between nanofibers
$\tan\delta$	[1]	Mechanical loss factor
T_g	[°C]	Glass transition temperature
T_s	[°K]	Temperature of the particle suspension
t	[1]	Critical exponent

ΔU	[V]	Potential difference
W	[mm]	Distance from applied load line to the end of CT sample
X	[1]	Function of the number of contacts between fibers
α	[1]	Normalized crack length (a_0/W)
β	[1]	Parameter of fiber contact model
γ_0	[%]	Strain amplitude
δ	[nm]	Thickness of polymer shell around conductive filler
ε	[1]	Localized volume content of CNFs in an agglomerate
ε_0	[F·m^{-1}]	Electrical permittivity of free space
ε_r	[1]	Dielectric constant or relative permittivity
η	[Pa·s]	Viscosity
$\lvert\eta^*\rvert$	[Pa·s]	Complex viscosity
θ	[°]	In plane orientation angle
μ	[MPa]	Shear modulus
ν	[1]	Poisson's ratio
ξ	[1]	Volume fraction of agglomerated CNFs in the composite.
ρ_{tunnel}	[Ω·cm^2]	Tunnelling resistivity of the epoxy film
ρ_v	[Ω·cm]	Volume resistivity
$\sigma(t)$	[MPa]	Linear shear stress
σ_c	[S/cm]	Volume conductivity of the composite
σ_f, σ_{CNF}	[S/cm]	Fillers volume conductivity, CNF volume conductivity
σ_m	[S/cm]	Volume conductivity of the polymer matrix
σ_v	[S/cm]	Volume conductivity

τ	[s]	Relaxation time for decay of free charge
ϕ_c	[vol. %]	Critical volume content, percolation threshold
ϕ_p	[vol. %]	Volume fraction of nanofibers in a conductive network
ϕ_t	[vol. %]	Saturated volume fraction of fillers
ω	[s^{-1}]	Frequency
ω_1	r.p.m.	Rotation speed of 1st calender roll (feed roll)
ω_2	r.p.m.	Rotation speed of 2nd calender roll (center roll)
ω_3	r.p.m.	Rotation speed of 3rd calender roll (apron roll)

1 Introduction

The use of high performance composite materials for engineering applications under high demanding working conditions has been growing increasingly in the past years. In order to ensure safety and economic efficiency, these composites must provide excellent mechanical and tribological properties as well as low specific weight and high resistance to degradation. Due to their good mechanical performance and low density, these composites are also considered for applications where a certain degree of electrical conductivity is required.

Composite materials used for industrial applications often consist of a polymer matrix (thermosetting or thermoplastic), which, on its own, might cover some of the demanded properties. However, because the polymer must withstand high mechanical and tribological loads, it is usually reinforced with fillers. Traditionally, mechanically reinforcing fillers have been chosen as fibers (glass, carbon and aramid) or particles such as ceramic powders. Particles usually have dimensions in the range of 1 - 10 or even more micrometers. These fillers favourably stiffen the material and may also increase the strength under certain load conditions but, on the other hand, it has to be considered that they often yield a detrimental effect on important properties such as the material's toughness and resistance against impact.

To overcome these drawbacks, nanoparticles have been increasingly used in recent years as reinforcement elements in polymers to improve mechanical and/or electrical properties of composites. The particle size, morphology, surface treatment, amount and the dispersion homogeneity within the matrix strongly influence the nanocomposite performance. Nanoparticles provide a very high specific surface area. This area can generate a new material behaviour, which is widely determined by interfacial interactions, offering unique properties and a completely new class of materials. Additionally nanoparticles constrain the matrix deformation less than microparticles, because they integrate better into the polymer microstructure as they approach nearly molecular dimensions. Depending on more or less strong interactions with the matrix, it can be expected that they influence deformation mechanisms in the polymer on the micro- or even the nanoscale. However, the improvement of the fracture mechanics properties by the addition of particles can

only be achieved when a sufficiently good interaction between the nanoparticles and the matrix polymer takes place which can only be effective if the nanoparticles are well dispersed in the surrounding polymer matrix.

There are a number of ways in which an insulating polymer material can increase its conductivity. A traditional method is to cover its surface with a conductive layer. This structure presents some drawbacks such as limited service live due to peeling or wear, the need of post-processing (with an increase in cost) and the difficulty of developing parts with complicated geometry. Such disadvantages are not found in polymers containing specific conductive fillers such as metallic powders or fibers, carbon black (CB) and carbon fibers (CF). However, polymers filled with these micro-sized materials show some other shortcomings (the need of high loadings to achieve good electrical conductivities, reduction of mechanical properties, sloughing, impossibility to develop thin films…).

More recently carbon nanotubes, carbon nanofibers and metallic nanowires have been used to provide electrical conductivity to polymers. A wide range of electrical conductivity can be achieved in this way. As in the case of non conductive nanoparticles a good dispersion of the nanofibers in the polymer matrix results in a more uniform stress distribution and minimizes the presence of agglomerates that can act as stress concentration centers which decrease the general strength and modulus of the composite. Furthermore, the final conductivity of the polymer composites depends not only on the concentration and specific conductivity of the fillers used but also on their state of dispersion in the matrix. The critical amount of filler needed to initiate a continuous conductive network within the polymer matrix is known as the percolation threshold.

The aim of this research was to develop epoxy resin polymer composites with superior mechanical and electrical properties. In order to do that, two kinds of nanofillers were mixed in an epoxy matrix: electrically conductive carbon nanofibers (CNFs) and ceramic nanoparticles. In an initial stage of the work, in order to identify which effect each kind of filler had when added separately to the polymer matrix, CNF–EP and ceramic nanoparticle–EP composites were manufactured and tested. Each type of filler was dispersed in the polymer matrix using two different dispersion

technologies. CNFs were dispersed in the resin with the aid of a three roll calender (TRC) whereas a torus bead mill (TML) was used in the ceramic nanoparticle case.

In a second stage of the research, CNFs and ceramic nanoparticles were combined as fillers to create a nanocomposite that could benefit from the electrical properties provided by the conductive CNFs and, at the same time, have improved mechanical performance thanks to the presence of the well dispersed ceramic nanoparticles. Finally, existing theoretical models were applied to predict the electrical conductivity of the manufactured composites.

2 Fundamentals and state of the art

2.1 Polymer nanocomposites

Polymer nanocomposites are two-phase systems consisting of a polymer matrix loaded with high-surface-area reinforcing fillers which have, at least, one of their dimensions in the nanometric scale (1 nm=10^{-9} m) [1]. Such systems have attracted a great deal of attention from the materials science community in recent years because they theoretically promise substantial improvements of mechanical and electrical properties at very low filler loadings. In addition, nanocomposites are compatible with conventional polymer processing, thus avoiding costly layup required for the fabrication of conventional fiber-reinforced composites.

Much research has been performed on the incorporation of low and high aspect ratio organic and inorganic nanofillers into thermosetting and thermoplastic polymer matrices, these fillers have already demonstrated their capability to improve the toughness of polymers and other important properties such as wear resistance and electrical conductivity [2-6]. Unfortunately, despite the reported improvements, with the exception of reinforced elastomers, nanocomposites have not lived up to theoretical expectations in modulus reinforcement. The gap between theoretical and real mechanical performances of nanocomposites has been attributed to a number of factors including poor dispersion, poor interfacial load transfer, process-related deficiencies, poor alignment, poor load transfer to the interior of filler bundles, and the fractal nature of filler agglomerates [7]. Nevertheless, despite worst than expected mechanical performances, the reported electrical behaviour of polymers filled with conducting nanofillers has been quite remarkable, specially in the carbon nanotube case, with electrical conductivities achieved in single-walled carbon nanotube–epoxy composites with filler loadings as extremely low as 0.0025 wt. % [8].

In order to illustrate the effect that composite morphology has on the physical properties of reinforced polymers schematic illustrations of the nanosized reinforcing particles have been extensively used. On Figure 2.1, for example, idealized one-, two-, and three-dimensional colloidal particles can be seen. Examples include one-dimensional carbon nanotubes and nanofibers, two dimensional layered silicates and nanoclays, and three-dimensional ceramic or metallic nanospheres. Such simple

representations are helpful when analyzing nanocomposite properties. In general low-dimensional fillers tend to be more difficult to disperse than their three-dimensional counterparts. Ideally, three-dimensional, quasi-spherical particles touch at a point, whereas one-dimensional rods or tubes can contact along a line, thus leading to enhanced surface interactions. Two-dimensional sheets offer even larger contact area. As a result of these enhanced interactions, layered silicates exist naturally as stacks and carbon nanotubes form ropelike networks with side-by-side packing. Stacking and side-by-side packing lead to enhanced electrostatic van der Waals attraction forces which are responsible for the propensity of low-dimensional fillers to form agglomerates. Therefore, spherical particles are expected to be easier to disperse than either rods or sheets. This prediction is borne out.

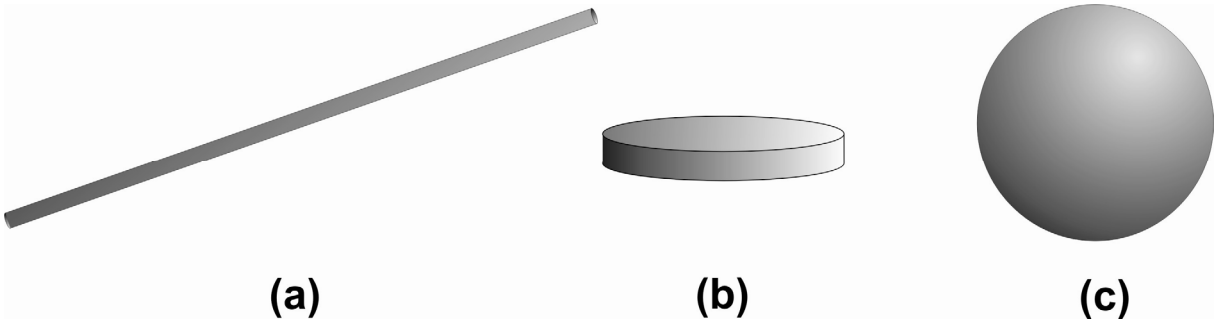

Figure 2.1: Schematic illustrations of (a) 1-dimensional, (b) 2-dimensional, and (c) 3-dimensional fillers.

Still so far, high material costs, complex processes and limitations in production technology limit the production and the application of nanocomposites on a large industrial scale. Specifically, there are still difficulties to distribute individual nanoparticles homogeneously in the matrix.

2.2 Electrically conductive composites

The rising amount and sophistication of electronics in everyday life, from mobile electronic devices to desktop personal computers or large supercomputers, makes it crucial to insure that electrostatic charges do not build up in these devices and that, if they do, they are controllably dissipated i.e. protection against electrostatic discharge (ESD). Furthermore, in certain applications, it is also necessary to protect the instruments against electromagnetic or radio interference (EMI/RFI) which could

negatively affect their performance e.g. corruption of data in large-scale computers or malfunction of medical devices such as pacemakers [9,10]. The continuing trend for smaller and faster electronic devices will cause ESD and EMI/RFI to remain a major concern.

Depending on their degree of conductivity materials are generally divided into three categories: insulators, semiconductors and conductors (Figure 2.2). Optimal ranges of conductivity for different applications (antistatic protection, ESD protection and EMI/RFI shielding) are also displayed together with the electrical conductivity of some common materials for comparison.

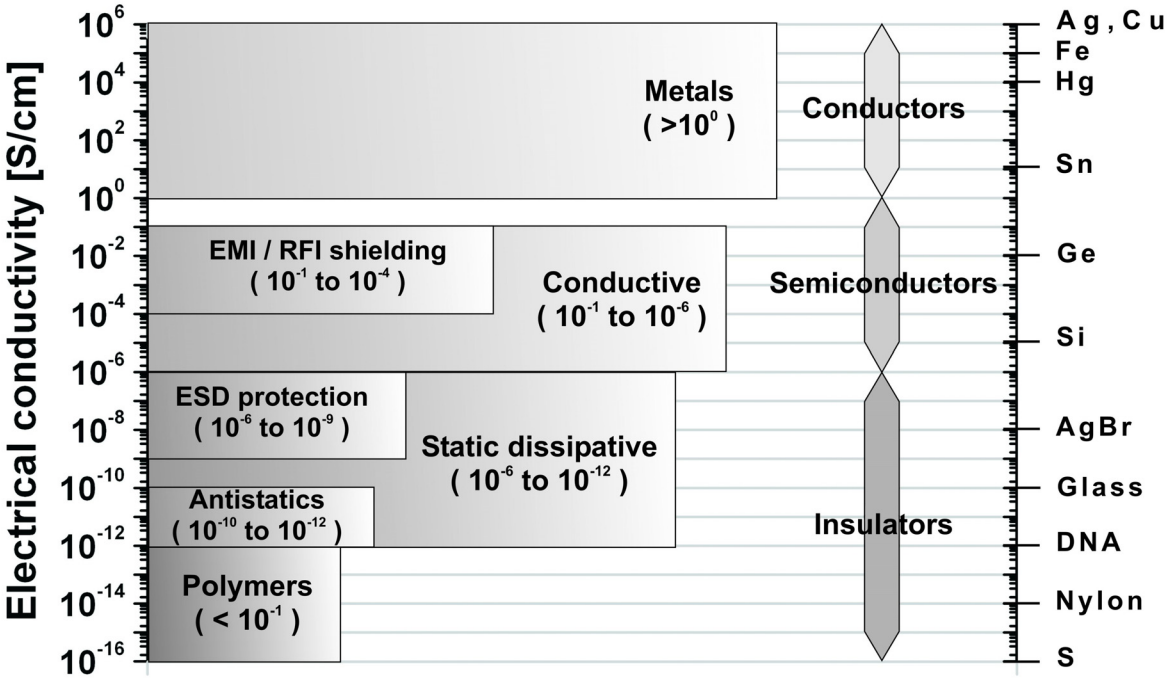

Figure 2.2: Classification of materials by degree of electrical conductivity [11,12].

As it can be seen, polymers are classified as electrically insulating materials having electrical conductivities lower than 10^{-12} S/cm. However, adding electrically conductive fillers to a polymer matrix can increase its conductivity by several orders of magnitude, making the resulting composites suitable for applications such as antistatic dissipation, ESD protection or EMI/RFI shielding.

2.2.1 Electrostatic discharge (ESD) protection

Electrostatic discharge ESD is an issue that has been a focus of attention to those in the electronics industry for a long time [13]. ESD is the rapid, spontaneous transfer of electrostatic charge by a high electrostatic field. Common observable ESD events include lightning and the occasional zap felt when reaching for a door knob. ESD, in these forms is easily seen and quite noticeable. However it is ESD that is not readily apparent that is more of a hazard to the electronics industry. For instance the typical human threshold of ESD awareness begins around 4000 Volts but it only takes a discharge of less than 250 Volts to harm to an electronic device. ESD causes both catastrophic and latent failures in sensitive electronic devices. This leads to higher manufacturing costs, lower yields, decreased reliability and reduced profits. It is essential therefore that ESD be effectively controlled. Contributing to the problems of ESD control is that polymers and polymer composites have become the materials of choice in the manufacturing and packaging of electronic devices. This is a result of economic benefits and greater design freedom over metals. As it has been pointed out earlier, the typical polymers of choice in these applications are insulators, which raise the likelihood of an ESD event. Therefore, in order to provide ESD protection a certain degree of static dissipation needs to be imparted to the polymer part.

Electrostatic charge (ESC) occurs due to sliding, rubbing or separating a material. The electric charge is caused by polarization (i.e., the concentration of electrons in the same object, or through conductive charging from one object to another). Permanent electrostatic charges arise on the surface of one material when separated from another. These processes are a prime generator of electrostatic voltages in materials such as plastics, rubbers and textiles. Electrostatic discharge (ESD) of these accumulated voltages will eventually occur via an arc or a spark when the charged material comes close or in contact with a counterpart of a sufficient potential difference. ESD through an electrical component can have consequences that range from incorrect measurements to permanent damage resulting in a costly repair or the total replacement of the device in which the component is housed [9].

Providing ESD protection to a device enables it to reduce a high applied voltage (up to 20000 V) to a level where damage is not caused (generally under 1 V).

A locally high concentration of electric charge inside any material will decay exponentially with time, current flowing away under the influence of the self-field created by the charge (initial concentration q_0)

$$q = q_0 \exp\left(-t/\tau\right) \qquad \text{Eq. 2.1}$$

where the time constant τ, which receives the name of relaxation time for decay of free charge, depends on the product of the material's inherent charge-storage capacity as expressed by the following relation:

$$\tau = \varepsilon_0 \varepsilon_r \rho_v \qquad \text{Eq. 2.2}$$

As it can be seen, the relaxation time is directly proportional to ε_0 which is the electrical permittivity of free space ($8.854 \cdot 10^{-12}$ $F \cdot m^{-1}$ (or $C^2 \cdot N^{-1} \cdot m^{-2}$)), ε_r, the relative permittivity of the material and ρ_v, its volume resistivity. For metals, where the resistivity is extremely low, τ is so short that is hardly measurable (e.g. for copper $\tau \sim 10^{-18}$ s). Common polymers, on the other hand, have very high resistivities which lead to long relaxation times. In other words, polymer matrices can retain electrical charges for very long periods of time, sometimes up to several years; this fact illustrates an important aspect of their insulating character. Although charges may in certain circumstances become trapped within the bulk of the polymer specimen, it is the surface of the polymer which is the most vulnerable towards charging effects. The charging process can be either electronic or ionic in origin. There are many different ways in which charges can be imparted to the polymer, the commonest and most basic being simple contact charging, whenever any two different materials come into contact there is always a redistribution of electrons or ions across the interface. The understanding of this elementary process is not complete, partly as a consequence of being a surface effect suffering from the usual complications of high concentrations of impurities and structural defects which tend to be more common at surfaces [10].

As we have seen, if a material is not as electrically insulating as plastics, the accumulated electrostatic charge will naturally dissipate in a short period of time which will make that material capable of protection against ESD. Moreover, the

material should be able to control the discharge and thus the high conductivities of metals are also undesirable. An optimal range of electrical conductivity for such kind of applications is estimated between 10^{-9} to 10^{-6} S/cm [11].

There are a number of techniques to provide adequate ESD protection to a polymer component. Two conventional methods are the use of conductive paints or coatings and filling the polymer with electrically conductive materials. The application of paints and coatings presents its own problems; it requires a post-processing step and potential solvent recovery and volatile organic compound emission concerns. On the other hand filled thermoplastics can be moulded or extruded without these drawbacks and have been used successfully in a number of ESD applications. In fact, EMI shielding and electrostatic discharge (ESD) protection are the major applications for conductive polymer composites [14].

Filled static dissipative polymers have traditionally been prepared by the compounding of additives such as hygroscopic agents or conductive fillers such as carbon black, carbon fibers or metallic particles into the polymer matrix. Filled polymers have a long history and a wide use in electronic devices. This is attributed to the aforementioned ease of processing as well as a wide range of electrical properties available with the fillers. This is not to say that conventionally filled polymers for ESD control do not have disadvantages. Their inherent weakness is that they are inhomogeneous multi-phase systems. This usually leads to reduced properties such as strength and toughness. There are also shortcomings with each type of additive. For example hygroscopic agents are by nature dependent on moisture for proper functioning, and therefore, fail in low humidity environments. Additionally, hygroscopic agents are migratory which leads to permanence and contamination issues. The agents are easily washed or wiped off and performance degrades over time. Finally these additives can only achieve the antistatic portion of the dissipative range (see figure 2.1). In this range, a part will resist triboelectric static charge generation but may not be able to safely drain charges to ground fast enough.

Most commonly metal coated polymers (MCP) and carbon black (CB)-filled polymers are used for EMI shielding and ESD protection, respectively [15,16]. These materials have some disadvantages and limitations. For example, MCP can delaminate and

are difficult to recycle. In some cases, there are hidden costs in coating applications which increase the production cost [15]. Likewise, for CB-filled polymers, the high concentration of the CB required to achieve good electrical properties reduces certain composite mechanical properties and ease of processing, while increasing the cost [17]. In addition, for CB powders, sloughing could damage the packaged electronics and is also an environmental concern [18].

In the last few years, conductive nanofiller–polymer composites have been widely investigated in academia and industry because of their outstanding multifunctional properties compared to conventional conductive polymer composites [19-21]. Those composites have been mainly formulated using high aspect ratio 1D conductive nanofillers including carbon nanotubes (CNTs) [22-25], vapour grown carbon nanofibers (VGCNFs) [26-30] and to a less extent metal nanowires [31,32].

2.2.2 Carbon nanotube and carbon nanofiber composites

Since the reported discovery of carbon nanotubes (CNTs) in 1991 by Iijima [33] and the realization of their unique mechanical, thermal, and electrical properties [34], many investigators have attempted to produce innovative CNT composite materials that exhibit one or more of these properties. CNTs can be thought of as the ultimate carbon fiber with break strengths reported as high as 200 GPa, and elastic moduli in the terapascal range [35]; electrical conductivities of up to 10^4 S/cm (for metallic single-walled carbon nanotubes) [36], approximately 500 times more surface area per gram (based on equivalent volume fraction of typical carbon fibers) and aspect ratios of around 10^3. These outstanding properties have spurred a great deal of interest in using carbon nanotubes as a reinforcing phase for polymer matrices. For example, as conductive filler in polymers, CNTs are quite effective compared to traditional carbon black microparticles, primarily due to their high aspect ratios. The electrical percolation threshold was recently reported at 0.0025 wt. % of CNTs and conductivity of $2 \cdot 10^{-2}$ S/cm at 1.0 wt. % CNT in an epoxy matrix [8]. The scientific literature devoted to carbon nanotubes and their composites is both immense and growing. Interested readers in CNT–polymer composites can refer to a general review by Thostenson et al. [37], CNT–polymer composites reviews by Breuer and Sundararaj [19] and by Moniruzzaman and Winey [38], reviews of mechanical

reinforcement of CNTs by Coleman et al. [39,40] and by Miyagawa et al. [41] and a review of dispersion and alignment of CNTs in polymer by Xie and co-workers [42]. However, as it was mentioned in the introduction, despite all the research effort, CNT-polymer composites have not reached the theoretical levels of mechanical reinforcement expected of fillers with such exceptional properties.

Vapour-grown carbon nanofibers (VGCNFs) are sub-micrometic filaments of highly graphitic structure. Their diameter lies in the range of hundreds of nanometers and they have lengths of a few tens of microns which gives them high aspect ratios (l/d >100).Their size places them between carbon nanotubes and commercially available carbon fibers (see Figure 2.3) although the distinction between carbon nanofibers and multi-walled carbon nanotubes (MWCNTs) is not clearly defined [36].

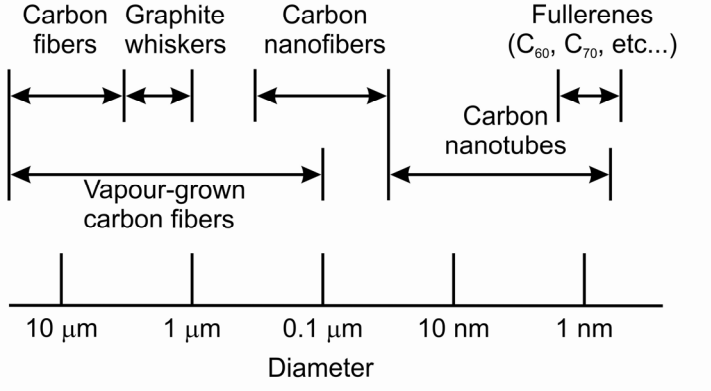

Figure 2.3: Comparative diameters of some fibrous carbon-based materials, adapted from [36].

VGCNFs are generally manufactured by catalytic chemical vapour deposition of a hydrocarbon (such as natural gas, propane, acetylene, benzene, ethylene, etc.) or carbon monoxide over a surface of a metal (Fe, Ni, Au, Co) or metal alloy catalyst (such as Ni-Cu, Fe-Ni) [26,50,110]. The catalyst can be placed on a substrate or directly fed with the gas phase [43]. The reaction is usually carried out in reactor operated at a temperature of 500 - 1500 °C [43]. The hydrocarbon decomposes on the metal catalyst; this decomposition both nucleates and grows the nanofibers [47]. The residence time of carbon in the reactor is only few milliseconds. Nanofibers produced by this method have a volume conductivity of about $4 \cdot 10^3$ S/cm. However, this conductivity can be further increased by graphitization [28]. Depending on the

feedstock, catalyst and operating conditions different morphologies and characteristics of VGCNFs can be obtained.

The use of VGCNFs as polymer fillers has received less research attention than CNTs because, due to microstructural defects [44], VGCNFs have worse mechanical and electrical properties than CNTs (see Table 2.1). VGCNFs also have larger diameters, higher density and lower aspect ratios compared with CNTs. However, because of their availability and relatively low price, VGCNFs are an excellent alternative for CNTs; in addition, VGCNFs could be used for research purposes to build knowledge that might be transferable to the more expensive CNTs. MWCNTs are 2 - 3 times more expensive than VGCNFs and single wall carbon nanotubes (SWCNTs) are even more expensive. In 2009, the prices of VGCNFs, MWCNTs, and 90 % pure SWCNTs were 200 $/kg, 450 $/kg and 50000 $/kg, respectively [45,46]. It has been predicted that due to increase in production capacities, VGCNF price might drop significantly [47]. For electrical applications, VGCNFs are also competitive fillers with carbon fibers (CFs) and high structure carbon black (CB), owing to the lower loading of VGCNFs compared to CFs and CB required to achieve certain electrical conductivities.

Property	**Units**	**Material**		**Ref.**
		MWCNTs	VGCNFs	
Elastic modulus	[GPa]	270 - 950	230	[36,48]
Tensile Strength	[GPa]	11 - 63	2.7	[35,48]
Electrical conductivity	[S/cm]	Up to 10^4	~10^3	[36,48]
Outer mean diameter (TEM)	[nm]	~1 - 50	~50 - 200	[36]
Length (SEM)	[μm]	1 - 50	50 - 100	[36]
Specific surface area BET (N_2)	[m^2/g]	1000 - 1350	150 - 200	[49 50]

Table 2.1: Comparison of physical properties of MWCNTs and VGCNFs.

VGCNF–polymer conductive composites are materials that exhibit superior electrical, electromagnetic interference (EMI) shielding effectiveness and thermal properties compared to conventional conductive polymer composites. Apart from their possible ESD applications, conductive VGCNF–polymer composites can also be used as sensors for organic vapours [51]. The mechanism is based on changing the composite conductivity when it is exposed to an organic vapour because of swelling

of the polymer matrix. Organic vapours can be distinguished based on the composite conductivity after certain time of exposure. A good sensor is the one that can give different electrical conductivity for different vapours [51].

VGCNFs also have potential applications in automotive industry that could lead to better quality, lower cost, less fuel consumption and lower environmental emissions. Those applications include: electrostatic painting of exterior panels, shielding of automotive electronics and addition of VGCNFs to tires to improve stiffness [52]. VGCNFs are promising materials for batteries, where multifunctional carbon materials are used as electrodes or as support materials [53]. For this application, carbon materials have many advantages over other materials such as metal oxides and sulfides in terms of cost, thermal and chemical stability, ease of formulation in various shapes and environmental impact [54].

In addition to the conductivity related applications, polymers filled with VGCNFs have potential biological applications. VGCNFs are more attractive than SWCNTs and MWCNTs for applications which require the incorporation of biological components such as proteins and DNA in the hollow core of the fiber, because they have much larger hollow core diameter [55]. Additionally, VGCNFs could be used in many applications that previously required CB or conventional CFs.

2.2.3 Modelling aspects of conductive polymer composites

Whether the conductive fillers included in an insulating polymer matrix have nano or micrometric dimensions, both systems consist of a mixture of a conductive and an insulating phase. With respect to the mechanisms of conductivity in such mixtures usually two circumstances can be considered. One deals with the formation of a conductive three dimensional network within the polymer and the other with the movement of electrical charge carriers along this network. Both mechanisms are closely related with the concentration of the conductive fillers in the matrix.

The improvement in conductivity in fiber filled polymers is commonly attributed to the percolation phenomenon, which is based on the notion that the conductive fillers are able to come in contact with each other once the filler content reaches a critical concentration known as the percolation threshold. When this critical value is reached,

the conductivity of the composite shows a sharp increase. After that, further increase in filler loading increase the electrical conductivity more modestly. In percolative systems, the plots of the electrical conductivity as a function of filler content often resemble the sigmoid function (see Figure 2.4). It has been proved experimentally that this percolation threshold strongly depends on the structure, specific conductivity, geometry and distribution of the fillers in the matrix. Other factors which might affect this critical filler content include the rheology and thermal behaviour of the polymer and the thermodynamic interaction between filler and polymer.

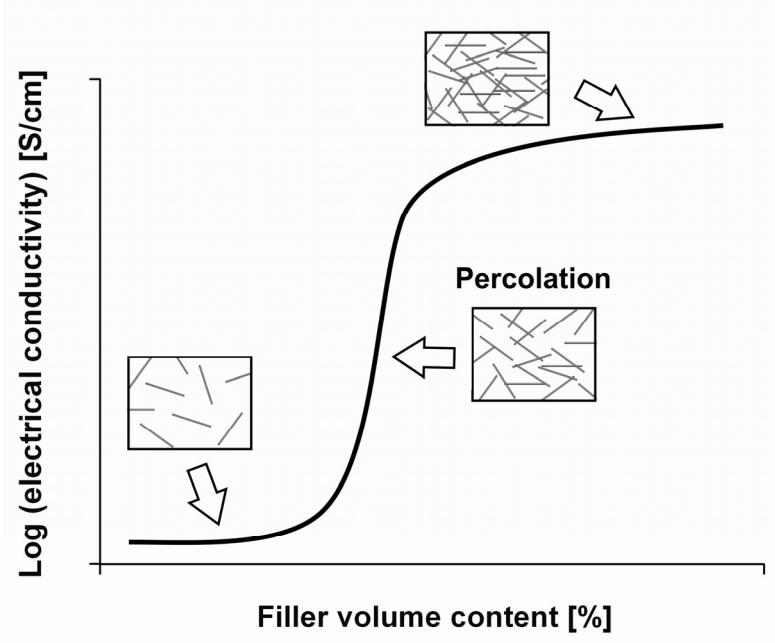

Figure 2.4: Electrical conductivity dependence on filler volume content.

Building a conductive network within an insulative matrix at lower concentration does not necessarily require well distributed fillers. However, it does need well dispersed fillers [12,56]. Figure 2.5 shows the ability of 1D fibers in percolating a 2D plane based on different dispersion and distribution scenarios. The number of fibers shown is not enough to perfectly percolate the 2D structure. Diagrams (a) and (b) show that poor dispersion of the fibers prevents network formation, while diagram (d) shows that a perfect distribution of well dispersed fibers increases the gap between the fibers. Only the preferential distribution of well dispersed fibers, case (c), forms a conductive 2D network. It should be noted that the formation a conductive network by preferential distribution of the conductive filler might not be suitable for applications

such as ESD, because the poor homogeneity of the surface, depending on the degree of distribution and the filler dimensions, might allow for static charge build up.

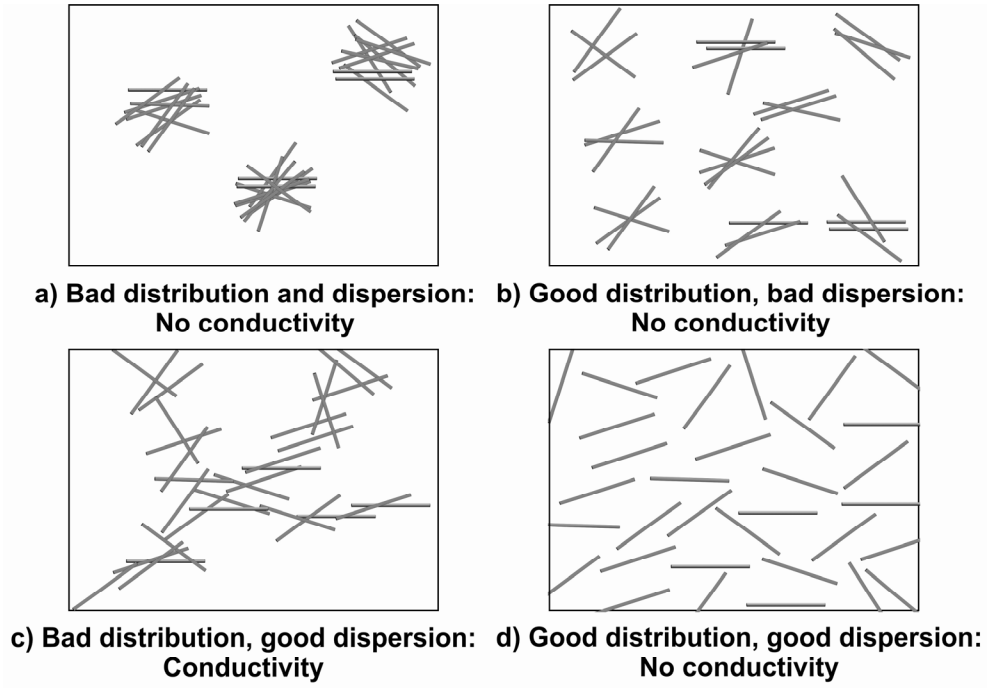

Figure 2.5: Diagrams showing the effect of the distribution and dispersion of one dimensional conductive fillers on the conductivity of a polymer composite.

Many researchers have tried to predict the critical filler concentration and the electrical conductivity of the polymer composites based on these aspects. The models found in the literature can be divided into four main categories: statistical, thermodynamical, geometrical and structure-oriented. Some examples are briefly discussed in this section. For more information about the percolation theory and other models developed to predict the electrical conductivity and percolation threshold in composites of conductive fillers in insulative matrices one can refer to the work of Lux [57], Clingerman [58] and Weber [59].

Statistical percolation models

Kirkpatrick [60] and Zallen [61] developed a theoretical explanation for the percolation behaviour of an insulating polymer filled with randomly distributed conductive fillers. According to this theory, a composite is regarded as a lattice of

conductive phases joined by resistive bonds. The composite conductivity above the percolation threshold follows a power law dependence of the following form:

$$\sigma_v \propto (\phi - \phi_c)^t \quad (for\ \phi > \phi_c) \qquad \text{Eq. 2.3}$$

Where σ_v is the volume electrical conductivity of the composite; ϕ, the filler volume fraction; ϕ_c, the critical volume fraction, and t a critical exponent related to the dimensionality of the lattice. For example, in an ideal statistical distribution of spherical mono-dispersed particles which do not interact with the polymer matrix ϕ_c and t (the critical parameters) take the value of 0.16 and 1.6 respectively. Attempts to generally apply this model to real composites often see a strong disagreement between the theoretical predicted values of the critical parameters and the experimentally measured ones. This divergence arises from the fact that in the composites the conductivity depends strongly on the geometric parameters of the fillers, the quality of their contacts and the filler-matrix interactions. These parameters are not taken into account into the purely statistical percolation theory. Particulate filled composites such as those reinforced with silver particles or carbon black have critical exponents in the range of 1.5 to 2. In samples reinforced with conductive fibers, t has been reported to reach values as high as 3.1 for carbon fibers [59] and 3 for carbon nanofibers [62], a fact ascribed to the higher aspect ratio of the fibers compared with the particle fillers.

Thermodynamical models

Surface properties of the polymer and the fillers are parameters which affect the conductivity of the composite by influencing filler-polymer interactions. How well the polymer wets the surface of the filler can be quantified by the difference between the surface energies of the two materials. Small differences between filler and polymer surface energies lead to a better wetting of the fillers by the polymer matrix. Better wetting results in larger amounts of polymer covering the filler surface and a better distribution of the fillers in the matrix. This might result in an increase in the percolation threshold and the resistivity of the composite as larger loadings of filler are needed before the particles will come in contact with each other. Therefore a slightly large difference between filler and matrix surface energies is desirable.

Sumita et al. [63] and Wessling et al. [64] proposed thermodynamic percolation models for composites where carbon black and intrinsically conductive polymers were used as the conductive phase in polymer matrices, because of the serious disagreements between the predictions of the statistical percolation models and the experimentally found percolation concentrations. Both models emphasize the importance of the interfacial interactions at the boundary between the individual filler particles and the polymeric host for the network formation. As a consequence, these models interpret the percolation phenomenon as a phase separation process. The experimental results of these researches were in agreement with the predictions from their proposed models.

Mamunya et al. [65] studied the composite conductivity versus the filler volume fraction for different polymers in a way that allowed them to evaluate the influence of other factors on the conductivity. These factors included filler and polymer surface energies and polymer melt viscosity, among others. The resulting model showed that the percolation behavior was dependent on the polymer-filler interaction, in addition to the size and amount of the filler material. This model produced good agreement between the calculated values and the experimental data for a number of different polymers filled with carbon black; however, it was not extended to include other types of fillers.

Geometrical percolation models

This class of percolation models was originally intended to predict the conductivity of sintered mixtures of conducting and insulating powders. The major assumption is that during the sintering process the insulating material forms regular cubic particles, while the conductive particles arrange in a regular manner on the surface of the insulating particles. The main parameters used in determining the conductivity are the diameters of the non-sintered particles or the edge length of the sintered particles. A well-known model in this class is the one proposed by Malliaris and Turner [66]. Two equations are used to predict two volume fractions; one to calculate the percolation threshold, and the other, for the volume fraction at the end of the conductivity increase. These equations use the diameter of the particles, the probability for the occurrence of long bands of conductive particles, and the

arrangement of the conductive particles on the surface of the insulating particles. Bhattacharya and Chaklader [67] optimized the model proposed by Malliaris et al. [66] and, although their predictions for the percolation concentrations gave better estimates than the original model, disagreement with respect to the experimental values was still around ±15 - 20 %.

Structure-oriented models

Structure-oriented models are based on the physical construction of the final composite. The electrical conductivity of composite materials is often affected by structural properties such as the filler aspect ratio and filler orientation. These properties are typically a result of the processing techniques employed to make the composite. For example, injection molding a composite will cause an alignment of fillers within a polymer due the flow through the nozzle and the mold. Alignment of the fillers can result in different conductivity results depending on the direction of measurement. Extrusion and injection-molding processes can also degrade fillers, shortening the lengths. Weber and Kamal [59] proposed two models accounting for the filler concentration, dimensions, aspect ratio, and orientation. The system studied was nickel-coated graphite fibers in polypropylene. The “end-to-end” model assumed that the sample consisted of conductive “strings” of fibers and that they are connected end-to-end. Another model was proposed which took into account the fiber-fiber contacts in addition to the other parameters. More details of this fiber contact model (FCM) can be found in section 5.3.4 and in section 0 of the appendix.

2.3 Improvement of the mechanical properties

As it has been discussed in the previous sections the inclusion of nanofillers in a polymer matrix has been known to have a beneficial effect on the properties of the polymer. Several research groups have experimentally proved that nanoparticles of metallic or inorganic type can effectively reinforce polymer matrices [68].This reinforcement included the improvement in modulus without loosing strength and the simultaneous increase in fracture toughness and impact energy of the studied composites, the latter however, depended strongly on the filler volume content [69].

Nanoparticles provide a very high specific surface area which leads to interfacial interactions between the particles and the polymer matrix that mainly control the new properties of the materials [70]. This high specific surface, however, causes the nanoparticles to attract each other due to electrostatic van der Waals' forces and to form agglomerates with dimensions of several micrometers (Figure 4.5, Figure 4.6). To extract the maximum benefit from their high specific surface, nanoparticles have to be homogenously dispersed in the polymer matrix in order to increase the effective interfacial surface between the fillers and the matrix. This interfacial surface allows a good transfer of the applied load from the matrix to the nanoparticles. Good dispersion also results in a more uniform stress distribution and minimizes stress concentration centers which decrease the general strength and modulus of the composites [71].

2.3.1 Deformation and fracture mechanisms in epoxy nanocomposites

Nanoparticles constrain the matrix deformation less than microparticles, because they integrate better into the polymer microstructure as they approach nearly molecular dimensions. It has been already experimentally established that the toughness and strength of structural ceramics rises strongly, if nanoparticles instead of microparticles are used as building blocks [72]. Depending on more or less strong interactions with the matrix, it can be expected that they influence deformation mechanisms in the polymer on the micro- or even the nanoscale. It is conceivable that nanoparticles could promote, for example, the formation of a large number of subcritical micro-cracks or micro-voids and retard the collapse into critical cracks by coalescence.

Many properties, however, are still scale independent and the absolute number of particles per unit volume is then irrelevant. Some of the known energy dissipating mechanisms observed and reported in the fracture analysis of thermosetting polymers and their filler reinforced versions (either with 1D (fibers) or 3D (particle) fillers) will be briefly discussed in the following sections. In real life composites these reinforcing mechanisms often appear combined or/and superimposed and it is often difficult to estimate which one prevails. Such toughening mechanisms include: matrix

plastic deformation, crack deflection, crack pinning, particle debonding, micro-cracking and crack bridging.

Plastic deformation of the polymer matrix (shear yielding), blunting effect

Inelastic plastic deformation of the polymer matrix (shear yielding) is an important mechanism in the toughness improvement of filler reinforced epoxy resins [73,74]. In this process whole polymer chains or chain segments slide against each other. The shear generated by these movements and the rupture of some of the chains absorb part of the deformating energy applied to the composite. The process starts as soon as the applied strain reaches the flow strain of the matrix. At the tip of a crack, particles and interparticle matrix ligaments are able to locally restrict co-operative chain movements. This often comes associated with a change of the polymer macrostructure. Chain movements depend on the cross-linking density, that is to say, the ductility, of the polymer matrix.

Shear bands are created by the locally restricted deformation of the matrix. These bands are break signs which are easily recognizable features in the fracture surfaces of the composites, especially after compression tests. As a result of the shear, intersecting shear bands can be the origin of micro-cracks and cavitation [75,76]. It is believed that the reason for the increase in yield stress originates in an influence of nanoparticles on the physico-chemical response of the polymer matrix. Interactions between nanoparticles and the matrix can alter properties of the polymer. Any changes in structure and mobility of the polymer molecules would not only affect yield stress, but also modulus, glass transition temperature, and toughness [77].

Crack deflection and crack branching

Crack deflection processes at particle obstacles in a matrix have been proposed to play an important role in the toughening. The theory was described by Faber and Evans [78,79]. It is assumed that a crack can be deflected at an obstacle and that it is forced to move out of the initial propagation plane by tilting and twisting. Such deflection causes a change in the stress state from mode I (opening) to mixed-mode, e.g. mode I/II (tensile/in-plane shear) in the case that the crack tilts, and mode I/III (tensile/out of plane-shear) if the crack twists.

The extension of a crack under mixed mode conditions requires a higher driving force than in pure mode I [78,79], which results in a higher fracture toughness of the material. Tilting and twisting subsequently continues at further particles if the crack follows a three-dimensional pathway. Therefore, an increase in total fracture toughness of a composite can be expected if this mechanism holds. Compared to the fracture surface area generated by an undeflected crack, the deflection processes increase the total fracture surface area.

Crack pinning

The crack pining theory was first proposed by Lange [80] and further extended by Evans [81] and Green [82,83]. They describe the interaction of a propagating crack front with impenetrable obstacles in brittle composites, which are believed to result in higher toughness. A crack propagating through a particle filled matrix will encounter the particles as obstacles and may be pinned by them. The crack front moves on amid the obstacles and extends by bowing between them, this effect results in an increase in the total crack length which is suggested to enhance the crack resistance [84]. Besides, secondary cracks and new fracture surface may be generated. These secondary cracks unify after passing an obstacle and a fracture step may then be formed due to the fact that the crack fronts moving around each side of the particle never end in the same plane. This fracture step will be visible in the resulting fracture surface as a characteristic ‘tail’ after the obstacle [85,201].

Debonding, particle pull-out, particle fracture

Debonding is an energy absorbing mechanism that consists on the separation of the fillers (particles or fibers) from the matrix in which they are embedded. Debonding depends on the adhesion forces between the fillers and the polymer matrix [81]. The separation of both phases requires a change from mechanical energy into surface energy which requires a higher energy absorption which results in an increase in the composite toughness. The strength and toughness of a composite material can be directly affected by the strength of the adhesive force or the chemical bonding energy between fillers and matrix which can be easily modified (for example by chemical functionalization of the filler surface). Such modifications, however, might introduce

structural defects on the nanofillers and also alters the propensity of the filler to disperse in the matrix, both of which influence mechanical properties in ways similar to the influence of interfacial bonding. Thus, it is difficult to isolate the effect of functionalization on load transfer.

The quality of the interphase and the strength of the filler-matrix bonding also influence the interaction of the particles with a crack propagating in the material and the propagation of the crack in the vicinity of the filling particles. A crack will tend to follow the less energy consuming path, that is to say the path which offers less resistance. If the bonding between filler and matrix is weak the crack will find its way through the surface of separation between the two phases. This will result in concave features in the fracture surface of the composites. If the matrix is filled with well bonded particles with high modulus (for example ceramic (TiO_2, Al_2O_3, SiO_2…) particles) the matrix will cohesively fail near the particle and the crack will propagate through that area. Strongly bonded particles with lesser toughness than the surrounding polymer medium (for example silica plates or glass spheres), will fracture as the crack front goes through them. This is often the case of filler agglomerates, bonded by relatively weak electrostatic forces, which display an effective elastic modulus much lower than the individual particles or fibers which conform the cluster [86]. Particle pull-out is caused by the debonding of the particles so is often not considered as an independent strengthening mechanism.

Micro-crack formation

In the stress field in front a propagating crack micro-cracks can be created. These cracks can grow up to a critical size and then coalesce. Micro-cracks can also be created around particles and particle agglomerates due to local stress concentrations [87]. With increasing crack opening size, voids and cavities will be created in the polymer matrix. In order to create a micro-crack energy is needed therefore the toughness of the material will be increased. However, the creations of micro-cracks will effectively reduce the modulus of the material around the crack tip. The main crack will deflect towards the micro-cracks created around the particles. Linkage of the main propagating crack with the micro-cracks increases the total crack length and therefore, the energy absorbed thus reducing the stress intensity in that area.

Crack bridging

This mechanism of reinforcement is occasionally found in fiber reinforced epoxy systems, although some times, large particles can have a similar effect. Shortly after the transit of the crack front, a fiber can form a bridge between both crack surfaces, holding them together. This bridging hinders any further crack opening so additional energy is needed for the crack to extend. As most of the reinforcement mechanisms described previously, bridging depends on the interfacial adhesion between fiber and matrix and the mechanical properties of the fibers. In case of a weak interfacial bonding simple pull-out of the fiber from the matrix occurs. In contrast, a very strong bonding between fiber and matrix might lead to a complete rupture of the fiber or to fracture of the outer layer and a telescopic pull-out of the inner tube(s) in the case ofcarbon nanotube and carbon nanofiber reinforced epoxies. A good bonding between the fiber ends and the polymer matrix (often as a result of some type of chemical functionalization), enables a partial debonding of the lateral interface, allowing crack bridging [88].

2.4 Dispersion techniques

As it was pointed out earlier, a good dispersion of the nanofillers in the polymer matrix is very important to increase the effective interfacial surface between the fillers and the matrix and obtain the maximum benefit provided by the nanofillers' high specific surface. This increment in interfacial surface allows a good transfer of the applied load from the matrix to the fillers. A good dispersion also results in a more uniform stress distribution that minimizes the presence of stress concentration centers which decrease the general strength and modulus of the composites. Processing methods and processing conditions strongly influence the filler distribution, dispersion, and in the case of one dimensional fillers the orientation and aspect ratio.

Nanoparticle agglomerates can be broken up and dispersed in polymer matrices using different technologies such as the application of high shear forces during mechanical stirring (in the case of thermoplastic matrices this is normally carried out by twin screw extrusion) [89,90], pulsed ultrasound vibrations [91] or chemical

methods which are able to generate individual and non-agglomerated nanoparticles ‘‘in situ’’ within a thermosetting polymer [92,93]. Chemical treatment of the nanoparticles surfaces can also improve the filler-matrix bonding and further enhance the composite’s properties [94,95].

In order to achieve a low percolation threshold and enhance composite conductivity and mechanical properties, VGCNF should disperse well without degrading the aspect ratio. One of the direct consequences of reducing the aspect ratio of conductive filler is to increase the electrical percolation threshold and conductive filler loading required to achieve certain EMI shielding effectiveness. As in the case of nanoparticles nanofiber agglomerates can be broken up and dispersed in polymer matrices using different technologies such as mechanical stirring and pulsed ultrasounds [6,23]. These methods sometimes are not strong enough to effectively separate the nanofiber clusters and can only be applied to small batches, sonication has also been reported to have another disadvantage and that is the rupture and shortening of the nanotubes due to the local energy input [96]. As in the case of nanoparticles, chemical functionalization of the nanotubes and nanofibers surfaces can also improve the filler-matrix bonding and further enhance the composite’s properties [97,146]. Such chemical modification, however, might introduce structural defects on the fillers and also alters the propensity of the filler to disperse in the matrix, both of which influence mechanical properties in ways similar to the influence of interfacial bonding. Thus, it is difficult to isolate the effect of functionalization on load transfer. On the other hand, the use of a three roll calender for the dispersion of carbon nanotubes was first reported by Gojny et al. [98]. This technology achieved excellent dispersion results without reducing the aspect ratio of the nanotubes which, as mentioned before, is important to enable a good load transfer from the polymer matrix and to achieve good electrical properties. One further advantage of the calendering method is the possibility of up-scaling the manufacturing process to meet technical demands.

Mechanical dispersion of the nanofillers in the epoxy matrix was the technology chosen to manufacture the composites studied in this work. The ceramic nanoparticles were dispersed with the aid of a torus ball mill while the carbon

nanofibers were dispersed with a three roll calender. A brief description of both devices can be seen in the following sections.

2.4.1 Torus mill (TML)

The TML (Figure 2.6) is a grinding system which combines the working principles of ball milling (a traditional method used for grinding (or mixing) materials like ores, chemicals, ceramic raw materials and paints) with those of a conventional dissolver. This technique has already been used successfully to achieve homogeneous dispersions of ceramic nanoparticles in a polymer matrix [107].

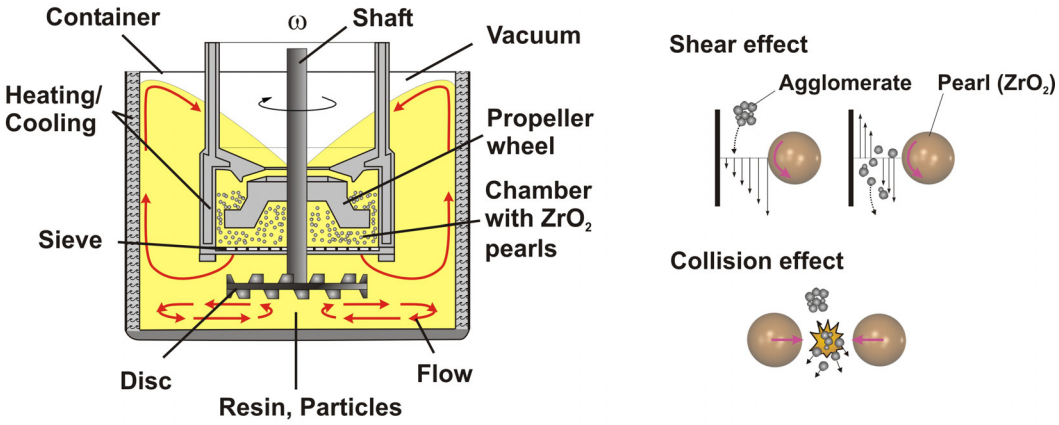

Figure 2.6: Torus mill, schematic diagram and working principle; adapted from [107].

The TML consists of a grinding chamber filled with small zirconium oxide (ZrO_2) beads which is lowered into the mixture to disperse it. During the dispersion process the grinding chamber stands still while the milling shaft, to which the milling tool, dissolver disc and propeller wheel are attached, rotates. The rotating milling tool agitates the ZrO_2 beads inside the chamber which introduce both a shear and a collision effect in order to disperse the mixture.

The temperature of the walls of the grinding chamber can be controlled to avoid the mixture overheat due to the high energy input provided by the machine. Vacuum can also be applied to remove entrapped air and to avoid further inclusion of air in the mixture. The dissolver disc at the tip of the shaft and the propeller wheel generate effective circulation of the mixture helping to achieve the dispersion of the fillers within the epoxy matrix. Additionally, the rotation of the metal dissolver disc is able to

apply high shear forces which further contribute to the break up of nanoparticle agglomerates, the separation of the particles and finally the homogeneous distribution of those particles within the matrix.

2.4.2 Three roll calender (TRC)

Two roll mills and calenders belong to the earliest group of equipment used for processing natural rubber. They were introduced in the 1830s by Edwin Chaffe and Charles Goodyear in the United States [99]. Nowadays the calendering process is commonly used for shaping high melt viscosity thermoplastic sheets and is particularly suitable for polymers susceptible of thermal degradation or which contain substantial amount of solid additives. This is because the calender can convey large rates of melt with a small mechanical energy input (compared to other techniques such as extrusion).

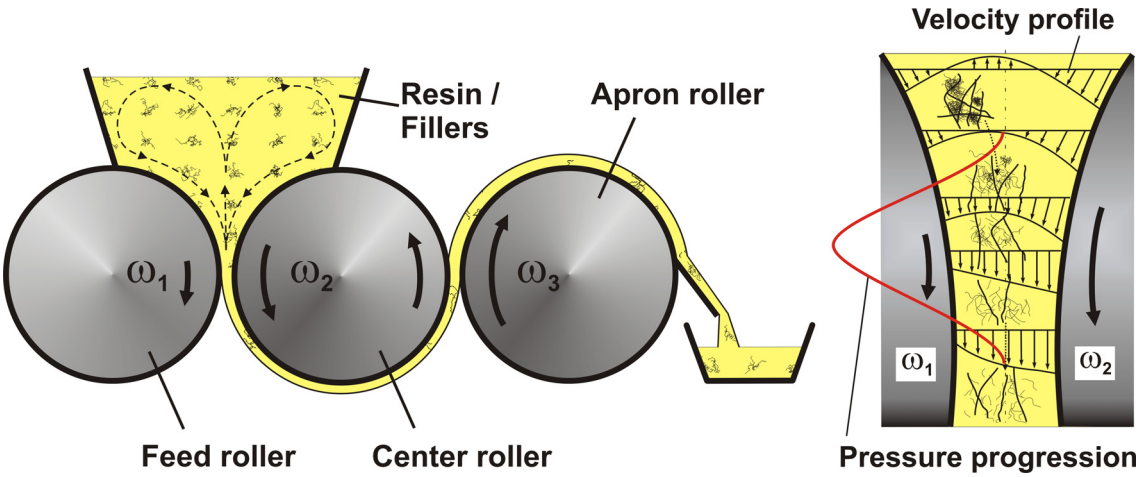

Figure 2.7: Three roll calender, schematic diagram and working principle; adapted from [107].

The three roll calender device (TRC) consists of three parallel rotating cylinders (Figure 2.7) with a polished ceramic surface and a defined distance gap between each other. The distance between the rolls can be adjusted up to a minimum of 5 μm. The mixture to be dispersed is placed between the feed and center rolls, each adjacent roll rotates at progressively higher speeds, the ratios between the rotation speeds being the following: $(\omega_1 : \omega_2 : \omega_3) = (1:3:9)$. Due to the difference in their rotation velocities, the rolling cylinders produce high shear forces within the mixture

as it flows between them [100-102] these forces achieve the dispersion of the agglomerates present in the mixture. Material is transferred from the center roll to the apron roll by adhesion. The milled material is then removed from the apron roll by a knife pressed against it.

The distance between the rolls, the pressure in the gap, the rotation speed and temperature of the rolls are process parameters than can be controlled. The pressure field in the gap between the rolls depends on the cylinder diameter and speed as well as on the viscosity of the medium that is being dispersed between the rolls [103,104]. The pressure maximum lies slightly before the narrower distance between the rolls [105,106]. The subsequent pressure drop promotes the wetting of the fillers in the fluid medium.

As mentioned in the introducting paragraphs of this section, dispersion of carbon nanotubes in a polymer matrix through calendering was first reported by Gojny et al. [98]. This technology achieved excellent dispersion results without reducing the aspect ratio of the nanotubes. Maintaining the characteristic high aspect ratio of the fillers is important to enable a good load transfer from the polymer matrix and to help achieve a low percolation threshold in the conductivity of the resulting composites [185]. One further advantage of the calendering method is the possibility of up-scaling the manufacturing process to meet technical demands.

3 Problem definition and objectives

The goal of this work was the investigation of the potential of carbon nanofibers and ceramic nanoparticles to, separately and collectively, improve the electrical and mechanical properties of an epoxy matrix. Therefore, the following objectives were addressed:

Carbon nanofiber composites:

Although calendering has been proved efficient in the dispersion of carbon nanotubes in epoxy [98], it remained to be seen whether its use could be extended to the achievement of a good dispersion and distribution of carbon nanofibers without affecting the nanofiber aspect ratio. A large aspect ratio is a crucial requirement in order to obtain a low percolation concentration and good electrical properties in the CNF–EP composites. A systematic study of the effect of the calendering process on the mechanical and electrical properties of the CNF composites was carried out in order to estimate the optimum dispersion parameters. Once an optimum dispersion was obtained the study focused on the dependence of the physical properties of the CNF composites with the volume loading of the carbonaceous fillers and the analysis of the structure-property relationships.

Ceramic nanoparticle composites:

As explained in the previous section, the dispersion of the quasi-spherical ceramic nanoparticles in the epoxy should be, theoretically, easier than the dispersion of CNFs. Previous research by Wetzel [107] has already proved the efficiency of high shear forces to disperse this kind of particles in epoxy. In our study, a torus bead mill was used to disperse 15 nm TiO_2 and 13 nm Al_2O_3 particles in epoxy in order to compare their effects on the mechanical and electrical properties of the resin.

Carbon nanofiber–ceramic nanoparticle composites:

The two kinds of fillers previously studied were independently dispersed and then conjointly added to the epoxy matrix to create CNF–ceramic nanoparticle–EP composites. The following topics were addressed:

- Examination of the effectiveness of the two masterbatch approach to create well dispersed ternary CNF–nanoparticle–EP composites.

- Analysis of the physical properties of the CNF–nanoparticle–EP composites. Study of the structure-property relationships:

  - Systematic analysis of the influence of CNF content on the mechanical and electrical properties of the TiO_2 and Al_2O_3 epoxy composites.

  - Systematic analysis of the effect of the inclusion of the TiO_2 and Al_2O_3 nanoparticles on the mechanical and electrical properties of the CNF composites

A significant issue in the design and manufacture of conductive polymer composites is the change in electrical conductivity with the content of conductive filler. As pointed out in the previous section, various theoretical models can be found in the literature attempting to explain the electrical behaviour of these composites based on numerous factors. A further objective of this study was to apply a theoretical model to the conductivity of the developed composites and compare the predicted values with the experimental measurements.

4 Experimental

4.1 Materials

4.1.1 Epoxy resin systems and hardener

Epoxy or polyepoxide is a thermosetting polymer that cures (i.e: polymerizes and cross-links) when mixed with a catalyzing agent known as hardener. Most common epoxy resins are produced from a reaction between epichlorohydrin and bisphenol-A. The first commercial attempts to prepare resins from epichlorohydrin occurred in 1927 in the United States. Credit for the first synthesis of bisphenol-A based epoxy resins is shared by Dr. Pierre Castan of Switzerland and Dr. S.O. Greenlee in the United States in 1936 [108].

In the frame of the present study, a series of nanoparticle and nanofiber filled epoxy resin composites were manufactured. The pure epoxy resin served as a reference material for the mechanical and electrical properties of the nanocomposites. The hot-curing epoxy resin system consisted of a low viscosity (η=1.0 - 1.4 Pa·s) epoxy resin (Araldite® LY 564 by Huntsman Advanced Materials GmbH, Switzerland). This resin is the liquid reaction product of epichlorohydrin and bisphenol-A (Figure 4.1) which additionally contains a 14 - 22 % concentration of a reactive diluent (1,4-Butandiol-diglycidylether), (Figure 4.2); the resin is characterized by an epoxy equivalent weight of 170 g /eq. [109].

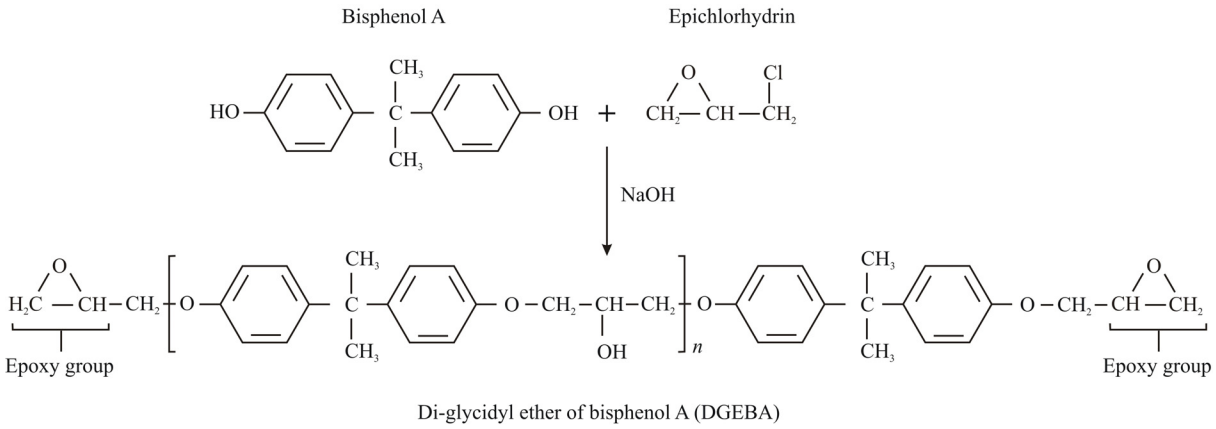

Figure 4.1: Chemical reaction leading to the synthesis of the DGEBA molecule.

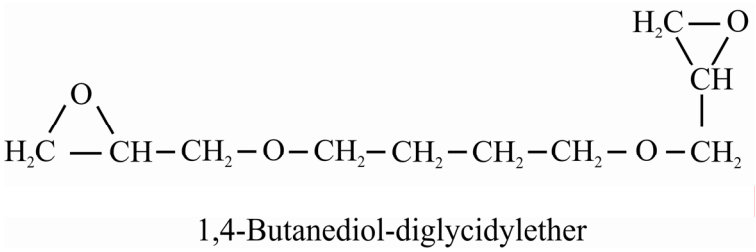

Figure 4.2: Molecular structure of the 1,4-Butanediol-diglycidylether reactive diluent from the Araldite® LY564 epoxy resin system.

In order to transform this liquid epoxy resin into a hard infusible thermoset network it is necessary to use a cross-linking agent also known as hardener or curing agent. The chosen hardener for this study was Aradur® HY 2954, a cycloaliphatic polyamine (2,2´-Dimethyl-4,4´methylenebis(cyclohexylamin)), (Figure 4.3); from the same manufacturers as the epoxy resin. All the composites in this research were prepared following the stoichiometric ratio recommended by the manufacturer which was 100 parts of resin to 35 parts of hardener by weight.

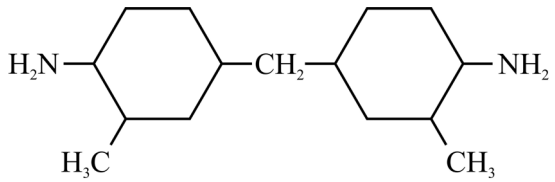

Figure 4.3: Molecular structure of the polyamine hardener Aradur® HY 2954 (Huntsman advanced materials).

4.1.2 Carbon nanofibers (CNFs)

Vapour-grown carbon nanofibers used in the present research (GANF 1) were manufactured by Grupo Antolín Ingeniería S.A. using the continuous floating catalyst method. Their diameters lied in the range of 30 to 300 nm with a typical mean value of 123 nm and they had lengths of up to 50 - 100 μm (Figure 4.4). These dimensions give the fibers a significantly high aspect ratio so an important increase in the mechanical properties of composites reinforced with these nanofibers is expected. Table 4.1 sums up some of the mechanical and physical properties of the carbon nanofibers used in the present research.

Property	Units		Ref.
Designation	-	Carbon nanofibers (CNF)	
Brand name	-	GANF 1	
Manufacturer	-	Grupo Antolín Ingeniería S.A.	
Elastic modulus (theoretical)	[GPa]	230	[48]
Tensile Strength (theoretical)	[GPa]	2.7	[48]
Electrical conductivity	[S/cm]	10^3	[48]
Average diameter (SEM)	[nm]	123 ± 33	[110]
Diameter distribution	[nm]	30-300	[110]
Length (SEM)	[μm]	50-100	[110]
Density	[g/cm^3]	1.97	[111]
Specific surface area BET (N_2)	[m^2/g]	178.4	[50]
Surface energy (stripped and debulked)	[mJ/m^2]	120	[48]
Metallic particles content	[%]	6-8	[50]

Table 4.1: Mechanical and physical properties of the carbon nanofibers.

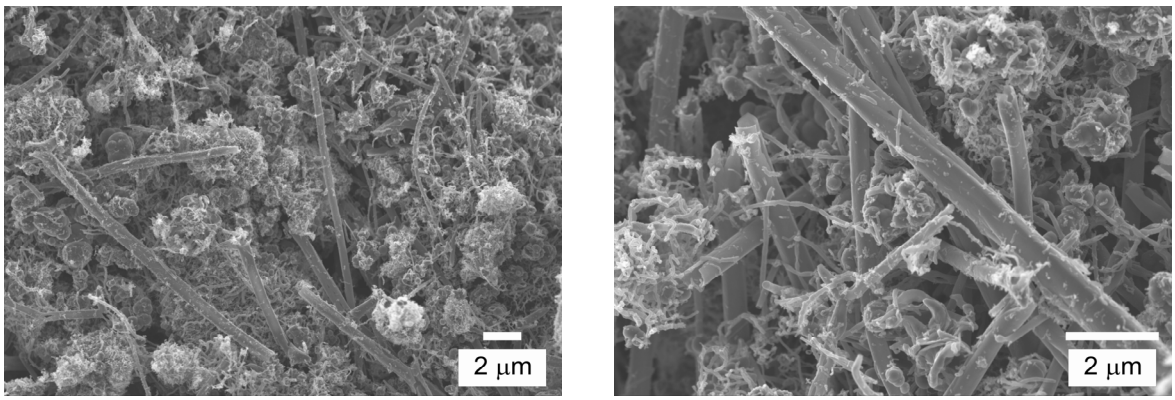

Figure 4.4: SEM pictures of carbon nanofibers (CNF GANF 1) as received. General view of the nanofiber agglomeration (left). Detail showing the distribution in nanofiber diameters (right).

The production of CNF by the floating catalyst method has the advantage of being extremely fast; nanofiber growth takes place in a matter of seconds, which allows higher production rates. However this production technique leads to structurally more imperfect fibers that show some contamination from residual catalyst nickel particles which are mostly incorporated into the fiber structure in oxidized form. Another disadvantage of this method is that the reaction process can not be precisely controlled. This leads to a more heterogeneous distribution in nanofibers lengths and

diameters (Figure 4.4, right). These products tend to be highly entangled as well; the agglomerations of entangled nanofibers have sizes of several micrometers up to hundreds of micrometers (Figure 4.4, left). Electronic, molecular and structural properties of carbon nanofibers are determined, mostly, by their practically one-dimensional structure. Carbon nanofibers are characterized by their excellent properties of electrical and thermal conductivity besides their high theoretical elastic modulus (230 GPa) and tensile strength (2.7 GPa).

4.1.3 Titanium dioxide (TiO_2) and aluminium oxide (Al_2O_3) nanoparticles

Two different kinds of ceramic nanoparticles, titanium dioxide (TiO_2) and aluminium oxide (Al_2O_3, alumina), were chosen as fillers for the epoxy polymer matrix. Table 4.2 summarizes some of the relevant properties of the particles used in this research.

Property	Units	Material		Ref.
Designation	-	Titanium dioxide (Anatase)	Aluminium oxide	
Chemical formula	-	TiO_2	Al_2O_3	
Commercial name	-	Hombitec® RM 300	Aeroxide® Alu C	
Manufacturer	-	Sachtleben Chemie	Evonik Degussa	
Elastic modulus	[GPa]	244	375	[112]
Poisson's ratio[1]	-	0.28	0.27	[113,114]
Fracture toughness	[MPa · $m^{1/2}$]	3.2	4.9 - 5.5	[115]
Mohs' Hardness	-	5.5 - 6	9 (Corundum)	[112]
Microhardness	[GPa]	6	unknown	[112]
Density	[g/cm^3]	4	2.9	[116,117]
Primary particle size (Schererr)	[nm]	15	13	[116,117]
Specific surface area (BET)	[m^2/g]	approx. 70	100 ± 15	[116,117]
Refraction index	-	2.55	1.66	[118,112]
Electrical conductivity @ 25 °C	[S/cm]	$1 \cdot 10^{-14}$	$1 \cdot 10^{-13}$	[119,120]
Dielectric strength	[kV/mm]	1.24 - 5.56	13.4	[121,119]
Crystal structure	-	Tetragonal	Hex.-rhomboedr.	[112]
Surface treatment	-	Polyalcohol (hydrophylic)	SiO_2,Fe_2O_3,TiO_2,HCl	[122,123]
[1]Full spectral method, Tabor-Winterton approximation [124]-				

Table 4.2: Mechanical and physical properties of the ceramic nanoparticles.

TiO_2 nanoparticles (Hombitec® RM 300) used in this research were provided by Sachtleben Chemie GmbH as a dry powder. Their primary particle size was in the range of 14 nm (Figure 4.5, right) and they had a specific surface area of approximately 70 m^2/g. They formed agglomerates in the range of micrometers (Figure 4.5, left) mainly due to electrostatic van der Waals' forces [125]

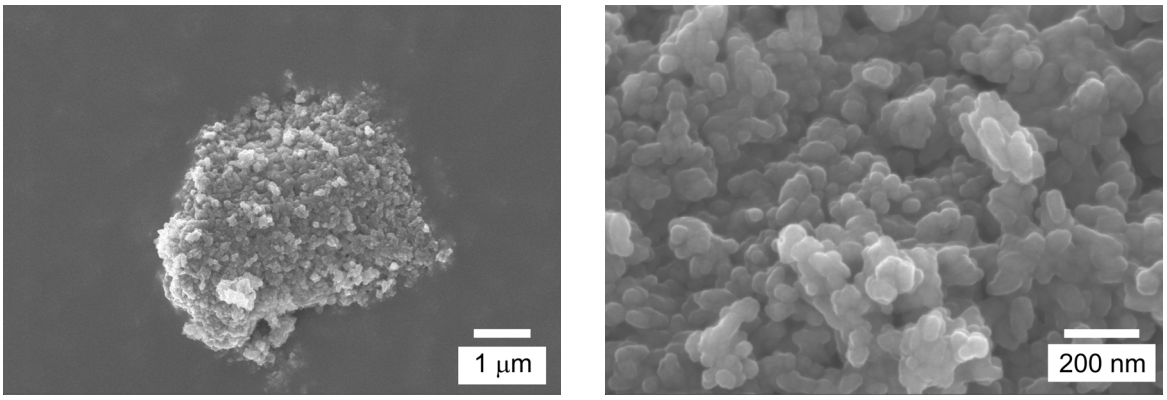

Figure 4.5: SEM pictures of titanium dioxide (TiO_2 Hombitec® RM 300) nanoparticles as provided by the manufacturer. Particle agglomerate of some micrometers in size (left). Detail showing the primary nanoparticles (right).

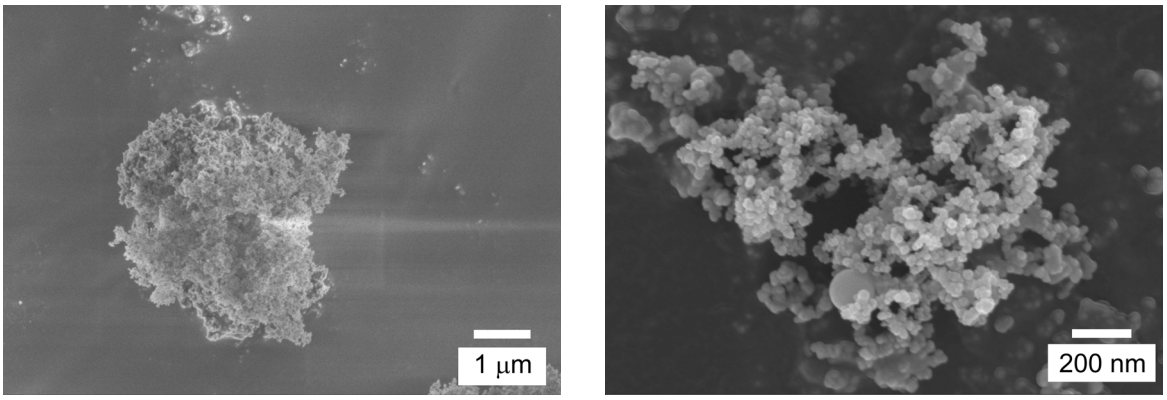

Figure 4.6: SEM pictures of aluminium oxide (Al_2O_3 Aeroxide® Alu C) nanoparticles as provided by the manufacturer. Particle agglomerate of some micrometers in size (left). Detail showing the primary nanoparticles (right).

Al_2O_3 nanoparticles (Aeroxide® Alu C) were manufactured by Evonik Degussa GmbH. The primary particles had a size range of about 13 nm (Figure 4.6, right).

Along with a spherical shape these nanoparticles are characterized by a very high specific surface area of 100 m^2/g. As in the titanium dioxide case the nanoparticle were provided as a white dry powder. This powder contains particle agglomerates in the micrometer range (Figure 4.6, left) which consists of primary nanoparticles strongly bonded together due to the afore mentioned adhesive inter-particle van der Waals' forces.

4.1.4 Production of the nanocomposites by different dispersion methods

The composites prepared and studied in this research were manufactured using a two masterbatch approach. The adequate dispersion device was used for the corresponding filler. The two ceramic nanoparticles (TiO_2 and Al_2O_3) epoxy masterbatches, containing a 14 vol. % loading of fillers, were dispersed using a laboratory torus mill (TML). A third carbon nanofiber–epoxy resin masterbatch, with a nanofiber content of 2.5 vol. %, was dispersed using a three roll calender (TRC). The three roll calender was chosen to disperse the nanofibers in the epoxy resin because a previous study carried out with carbon nanotubes had proved that this device was more effective to disperse fiber-like fillers in an epoxy matrix.

These masterbatches were thinned down with the addition of epoxy resin to obtain different series of nanocomposites containing increasing volume concentrations of one kind of nanofiller. Then, the nanocomposites were mechanically and electrically tested. Once the nanoparticle–epoxy composites and the nanofiber–epoxy composites were mechanically and electrically characterized and the optimum volume loading of nanocomposites was found, the original ceramic nanoparticle masterbatches and the nanofiber masterbatch were adequately mixed together using a vacuum dissolver to obtain the nanocomposites with different volume concentrations of CNF and nanoparticles.

4.1.4.1 Three roll calender processing

The masterbatch of carbon nanofibers was prepared by directly adding the nanofiber powder to the liquid epoxy resin at room temperature on a dissolver mixer (Kreis-Dissolver®, Wilhelm Niemann GmbH & Co., Germany). The solution, with a content of 2.5 vol. % of CNFs, was mechanically stirred under vacuum for about

45 minutes to remove most of the entrapped air introduced with the addition of the nanofibers and to form an homogeneous suspension. Thus, a dispersed masterbatch of the CNF–epoxy resin composites was obtained.

This masterbatch was dispersed with a three roll calender device (TRC) (Exakt 80 E, EXAKT Vertriebs GmbH & Co., Germany), (see section 2.4.2). The dispersion took place in 6 steps; on the first three, the distance between the calender rolls was set to 50 μm, 25 μm and 5 μm respectively, the last three times the gap measured 5 μm. The progressive reduction of the calender gap has the following explanation; if a small gap distance between the rolls is chosen at the beginning of the dispersion, the calender acts as a sieve for the larger nanofiber agglomerates. Therefore, instead of dispersing the nanofibers in the epoxy resin what we achieve is a filtering process with the corresponding, and undesired, reduction in filler volume loading. The rotation speeds of the cylinders were the following: $\omega_1 = 33.3\ r.p.m = 3.490\ rad/s$; $\omega_2 = 100\ r.p.m = 10.471\ rad/s$; $\omega_3 = 300\ r.p.m = 31.145\ rad/s$.

As mentioned in the introduction to this chapter, a preliminary research was carried out to compare the efficiency of the torus mill and the three roll calender when used to disperse carbon nanotubes in an epoxy resin matrix. The calender dispersed nanocomposites showed superior mechanical and electrical performance than the TML dispersed ones. That fact, combined with an easier processing explains the decision to use the calender as a dispersing tool in the manufacture of the carbon nanofiber epoxy nanocomposites.

4.1.4.2 Dissolver and torus mill processing

Nanoparticles were directly added into the liquid epoxy resin at room temperature on a vacuum dissolver mixer (Dispermat®, VMA-Getzmann GmbH, Germany). The solution was then dispersed for 120 min at 80 °C with a torus-mill laboratory mixing device (TML 5, VMA-Getzmann GmbH, Germany), (see section 2.4.1). The mill was operated at 2.500 rpm, 75 °C, under vacuum, during 120 min; a 60 vol. % of the milling chamber was filled up with ZrO_2 pearls with 1.2 - 1.7 mm of diameter.

After the adequate blending of the masterbatches, the hardener was added to the mixture and softly agitated for 15 minutes at 60 °C. Samples without filler addition

(neat epoxy resin / hardener samples) were also manufactured as reference. Finally, the composites and the reference suspension were casted into pre-heated ($210 \times 80 \times 10 mm^3$ and $36 \times 36 \times 4 mm^3$) aluminium moulds and cured in an oven at 80 °C for 1 h followed by 8 h at 140 °C. After curing, composites were left in the oven and allowed to cool gradually until they reached room temperature. Dog bone shaped samples for tensile tests were machined from the cured composite plates with a precision milling cutter. Compact tension (CT) specimens ($36 \times 36 \times 4 mm^3$) (Figure 4.7) were used for fracture toughness tests. Notched specimens ($80 \times 10 \times 4 mm^3$) for impact testing were manufactured with an especial ridged mould.

4.2 Material characterization

4.2.1 Material characterization of the uncured composites

4.2.1.1 Measurement of particle size distribution by dynamic light scattering (DLS)

The evolution of the particle size and the particle size distribution of the nanoparticles in the epoxy resin throughout the dispersion process were measured with a LB-550-dynamic light scattering nano-analyzer (HORIBA Instruments, Inc., USA). This instrument is able to detect the size of the particles in a liquid suspension in range of 1nm up to 6 μm by means of dynamic light scattering.

Dynamic light scattering (sometimes referred to as photon correlation spectroscopy or quasi-elastic light scattering) is a technique for measuring the size of particles typically in the sub micron region. DLS measures Brownian motion and relates this to the size of the particles. Brownian motion is the random movement of particles due to the bombardment by the solvent molecules that surround them. Normally DLS is concerned with measurement of particles suspended within a liquid. The larger the particle, the slower the Brownian motion will be.

The kinetic energy transferred from the solvent molecules to the particles is higher for smaller particles so these particles move more rapidly in the suspension. The velocity of the Brownian motion is defined by a property known as the translational diffusion coefficient (D). The size of a particle is calculated from the translational diffusion coefficient using the Stokes-Einstein equation (Eq. 4.1):

$$d_h = \frac{k_B T_S}{3\pi\eta D} \qquad \text{Eq. 4.1}$$

where d_h is the hydrodynamic diameter; D is the translational diffusion coefficient; k_B is the Boltzmann's constant; T_s is the absolute temperature of the suspension and η is the viscosity of the solvent.

It has to be noted that the diameter that is measured through DLS is a value that refers to how a particle diffuses within a fluid. Therefore, it is referred to as a hydrodynamic diameter. The diameter that is obtained by this technique is the diameter of a sphere that has the same translational diffusion coefficient as the particle or particle agglomerate. The translational diffusion coefficient will depend not only on the size of the particle "core", but also on any surface structure, as well as the concentration and type of ions in the medium.

In the present work, DLS was employed to study the effect that the TML dispersion had on the ceramic particle size distribution in the dispersed masterbatch. Samples of the dispersed epoxy–nanoparticle masterbatch were taken at different time intervals of the dispersion process. A drop of each sample was then dissolved with dichloromethane to create a suspension that was analyzed at room temperature via light scattering.

4.2.1.2 Plate-Plate rheometry

An important parameter to consider while manufacturing thermoset based nanocomposites is the viscosity of the pre cured mixture of polymer and nanofillers. The viscosity of the epoxy resin–nanofiller mixture plays an important role in the production of nanocomposites and the industrial processing of materials to fabricate mechanical components. A low viscosity of the stabilized nanofiller suspension and a low yield point are beneficial for the degassing, mixing and casting of the suspensions. On the other hand, to achieve a good dispersion of nanofillers in the resin, high shear forces need to be applied, a higher viscosity of the mixture is desirable for this purpose.

Rheological measurements were performed at 25 °C on a Rheometric Scientific ARES parallel plate rheometer with a torque transducer range of 0.004-100 g·cm using 45 mm diameter parallel plates separated 1 mm. An oscillatory strain ($\gamma(t)$) of the form:

$$\gamma(t) = \gamma_0 \sin(\omega t) \qquad \text{Eq. 4.2}$$

Where γ_0 is the amplitude and ω is the frequency, was applied on the sample. The resulting time-dependent linear shear stress ($\sigma(t)$) is interpreted as:

$$\sigma(t) = \gamma_0 (G' \sin(\omega t) + G'' \cos(\omega t)) \qquad \text{Eq. 4.3}$$

Where G' and G'' are the storage and loss moduli, respectively. All measurements in this study were assumed linear (i.e., G' and G'' are independent of γ_0) and interpreted using Eq. 4.3.

4.2.2 Material characterization after processing

4.2.2.1 Mechanical tests

4.2.2.1.1 Tensile tests

Tensile tests were conducted at room temperature on a universal testing machine (Zwick 1474, Zwick Roell AG, Ulm, Germany) in a tensile configuration according to Norm EN ISO 527-2. Dog-bone shape composite samples for mechanical tensile testing had a gauge length of 30 mm, width and thickness of 4 mm. The distance between the sample clampings was 40 mm and the testing speed was chosen to be 1 mm/min. From the resulting stress-strain diagrams the tensile modulus was determined from the slope of the curve between 0.05 and 0.25 % of the total strain. The tensile strength was determined from the material maximum sustained stress.

4.2.2.1.2 Fracture toughness tests

The plane strain fracture toughness (K_{IC}) of the composites was determined experimentally at room temperature by using compact tension (CT) samples under tensile loading conditions according to the Norm ASTM E 399. The samples were tested in a universal testing machine (Zwick 1474, Zwick Roell AG, Ulm, Germany).

To generate the required critical stress state in the material, a sharp crack of length a_0 ($0.45 \cdot W \leq a_0 \leq 0.55 \cdot W$, W being the distance between the applied load and the end of the sample) was created by the controlled impact of a razorblade. Figure 4.7 shows the shape and dimensions of the samples used for fracture testing.

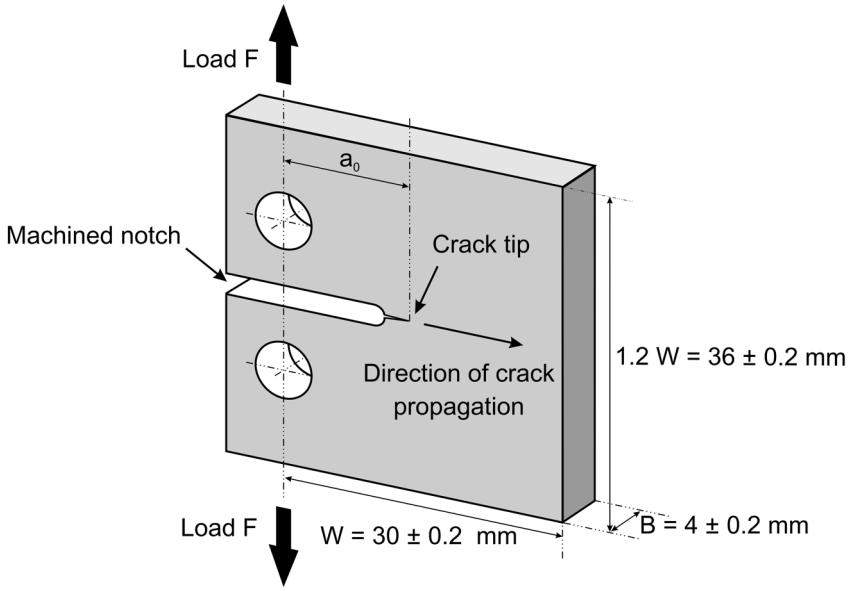

Figure 4.7: Dimensions of the compact tension samples used for fracture testing.

Previous research [126] demonstrated that this razorblade tapping was an adequate method of introducing an initial crack in rubber toughened and pure epoxy resin specimens. The linear elastic fracture mechanics approach assumes that the plastically deformed area in front of the crack tip is small compared with the overall crack length, if done carefully the tapping produces a straight crack front with the smallest pre crack tip radius and low residual stresses around the crack tip. Therefore the requirement to use the linear elastic approach is fulfilled and the experimental results give us reasonable values for the materials' fracture toughness.

Crack growth starts when the maximum sustained force $F_{Q,\max}$ is reached (see Figure 5.32, page 90). From this force the fracture toughness $K_{Q,\max}$ is calculated. In the case of critical plane strain conditions in front of the crack tip under mode I loading the stress intensity $K_{Q,\max}$ is identical to the critical stress intensity factor K_{IC}, which is associated with the fracture toughness of the material. The equation used to calculate the stress intensity in front of the crack tip is the following:

$$K_{IC} = K_{Q,\max} = \frac{F_{Q,\max}}{B\sqrt{W}} \cdot f(a_0/W) \qquad \text{Eq. 4.4}$$

Where $F_{Q,\max}$ is the maximum sustained force, B is the sample width, W the distance from the point where the force is applied to the end of the sample, a_0 is the distance from the applied force to the crack tip and $f(a_0/W)$ is a function of the dimensions of the sample that, in the case compact specimens as the ones used in this study, has the following form (Eq. 4.5) [127]:

$$f(a_0/W) = f(\alpha) = \frac{(2+\alpha)}{(1-\alpha)^{3/2}} \cdot (0.886 + 4.64\alpha - 13.32\alpha^2 + 14.72\alpha^3 - 5.60\alpha^4) \qquad \text{Eq. 4.5}$$

4.2.2.1.3 Impact fracture energy tests (Charpy)

Charpy impact tests are high speed fracture tests that measure the energy to break a specimen under bending conditions. The specimens are deformed within a short period of time and as a consequence they are exposed to high strain rates. Due to their highly cross-linked structure, non reinforced epoxy resins exhibit poor resistance to impact and crack propagation [128]. Therefore epoxies can be considered as brittle materials and as such they exhibit a high sensitivity to notches, micro-cracks and local inhomogeneities. The impact energies of notched specimens as the ones used in our research, for example, are generally much lower than that of unnotched specimens. The reason for this is that notches act as stress concentrators and much of the deformation of the sample on impact takes place in the vicinity of the notch tip where a higher apparent strain rate occurs in comparison with unnotched specimens [129].

Room temperature notched Charpy impact tests were performed using a pendulum testing machine (CEAST S.r.l., USA) according to the DIN-ISO179/1eU standard. Samples with rectangular dimensions of $80 \times 10 \times 4\,mm^3$ were fractured at room temperature by a swinging hammer with an impact energy of 4 J and an impact speed of 2.9 m/s. Distance between sample supports was set to 62 mm.

4.2.2.2 Electrical tests, volume conductivity measurement

Volume resistance (ρ_v) is a measure of how strongly a material opposes the flow of an electric current through its thickness. ρ_v, is defined in the literature [130-132] as the ratio of a DC voltage, U, to the current, I_s flowing between two electrodes of specified configuration that are in contact with opposing sides of the material under test The volume electrical conductivity (σ_v) can be directly calculated from the volume resistivity through the following equation (Eq. 4.6):

$$\sigma_v = \frac{1}{\rho_v} \qquad \text{Eq. 4.6}$$

To measure the volume resistivity of our materials samples with an area of $36 \times 30\, mm^2$ and thickness of $4\, mm$ were used. The surfaces of the samples were polished with 800 grit sand paper and cleaned with isopropanol in order to improve the quality of the contact surface between the sample and the electrodes. Electrical measurements (Norm ASTM D-257) were conducted at room temperature on an Hiresta UP MCP-HT450 ohmmeter system (Mitsubishi Chemicals, Japan) with a measurement range of 10^4 to 10^{14} Ω/cm. The electrode assembly fixture design is based on a concentric ring probe (UR-S Type, Mitsubishi Chemicals, Japan) and a measuring stage (Resitable UFL, Mitsubishi Chemicals, Japan) (Figure 4.8).

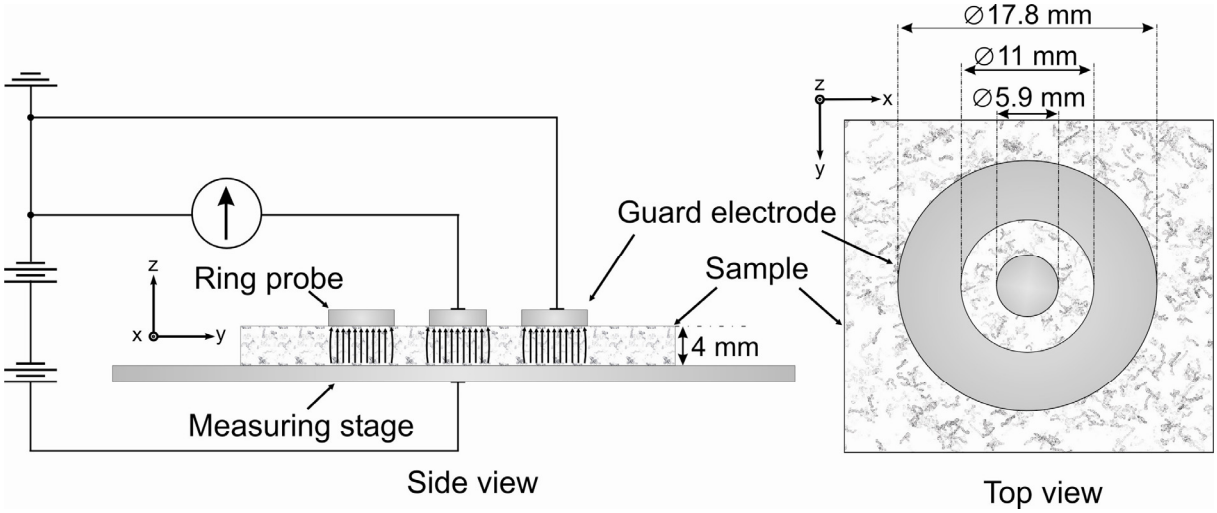

Figure 4.8: Configuration for the volume resistance measurements.

Samples were placed on the conductive metal surface of the measuring stage and the probe electrode was pressed upon them. The outer ring of the electrode probe acts as the guard electrode while electric current flows to the detecting inner electrode. A suitable voltage was applied through the thickness of the sample and the sample's resistivity was obtained. The volume resistivity was measured in two different samples of each material and the average value was obtained.

4.2.2.3 Analytical thermal characterization

The incorporation of fillers into an epoxy matrix changes the viscoelastic response of the polymer. The resulting effects are closely related to the compatibility of the components, the formation of phase and interphase and especially with the properties of the interface boundary surface between the particles and the polymer [133,134]. The mobility of the polymer chains changes with the presence of the fillers in the material. An indication of that change comes from the displacement of the glass transition temperature as well as the changes in elastic modulus and mechanical damping. Through dynamical mechanical thermal analysis (DMTA) of the composites, changes in the afore mentioned material properties as a function of temperature can be measured accurately.

DMTA analyses were carried out on an Eplexor™ 150 N (Gabo Qualimeter, Ahlden, Germany) testing machine in a tensile configuration. $50 \times 10 \times 4\, mm^3$ specimens were subjected to an oscillating dynamic loading consisting of a static preload of 20 N on which a sinusoidal dynamic force of constant 10 Hz frequency and 10 N amplitude was superimposed. The temperature during testing ranged from -140 °C to 230 °C with a heating rate of 2 °C/min. From these tests viscoelastic parameters such as the mechanical loss factor, $\tan\delta$, the loss E'' and storage E' modulus and the temperature for different relaxations (T_g, T_β) could be estimated.

4.2.2.4 Microstructure

4.2.2.4.1 Scanning electron microscopy (SEM)

The fractured surfaces of the polymer nanocomposites were studied in a field emission scanning electron microscope (SEM) (SUPRA™ 40 VP, Carl Zeiss NTS

GmbH, Oberkochen, Germany). A SEM is a type of microscope capable of producing high resolution pictures of a sample surface using electrons instead of light photons to form an image [135]. A beam of electrons is produced at the top of the microscope by an electron gun. The electron beam follows a vertical path through the microscope, which is held in vacuum. The electrons travel through electromagnetic fields which act as lenses focusing the beam down toward the sample. Once the beam hits the sample, electrons and X-rays are ejected from the sample. Detectors collect these X-rays, backscattered electrons, and secondary electrons and convert them into a signal that can interpreted as an image of the scattering surface. SEM images have a characteristic three dimensional appearance and are extremely useful to assess the surface structure of the samples.

Before being observed, the surfaces of the samples were first sputtered with an Au/Pd alloy for 90 s using a sputtering device (SCD-050, Balzers, Liechtenstein). This sputtering process creates a thin conductive coating over the polymer surface which is essential in order to obtain stable microscope images. Through this coating the electric charges placed on the sample surfaces by the microscope electron beam are able to flow away easily to earth. The use of the SEM technology delivered high resolution surface information which was effective to investigate micro and nanomechanisms (i.e., adhesion between filler and matrix, crack deflecting mechanisms at the nanofillers, location of failures) involved in the mechanical properties of the nanocomposites developed in this research.

4.2.2.4.2 Transmission electron microscopy (TEM)

The scanning electron microscope, though useful to analyze the surface and the structure near the surface of the composite samples does not to provide information of the whole composite structure and the state of dispersion of the nanofillers in the polymer matrix. In order to obtain that information the use of a transmission electron microscope (TEM Tecnai 12, Koninklijke Philips Electronics N.V. Netherlands) is necessary. The TEM also uses an electron beam focused by electromagnetic lenses. The difference with the scanning electron microscope is that in the TEM, electrons that transmitted through the sample are detected. Because the penetration depth of electrons is very low the samples for TEM analysis must be extremely thin.

In the present work the samples to be examined were cut at room temperature with a microtome (MT X2, RMC products by Boeckeler Instruments Inc., USA) to prepare slices with thickness between 50 and 90 nm thickness. By penetrating in the sample the electrons can be either deflected by elastic collisions or lose their energy through inelastic collisions [136]. The images achieved with this technique can provide information about the dispersion state of the nanofillers in the composites, the interparticulate distance and the possible presence of an interface between the fillers and the polymer matrix. This procedure could also detect the presence of sintered nanoparticle aggregates, in which the crystal structures of individual nanoparticles are bonded together. These aggregates can not be split up by the application of shear forces, sonication or any other dispersion method.

5 Results and discussion

5.1 Carbon nanofiber–epoxy matrix composites

Carbon nanofibers (CNFs) show lower mechanical, thermal and electrical properties compared with carbon nanotubes (see Table 4.1). However, CNFs represent a practical alternative for to the development of polymer composites with improved thermal, mechanical and electrical properties [137-141]. The characteristic nanoscopic dimensions of these fibers together with a relatively low cost, higher production levels and easier incorporation into polymers (especially when compared with carbon nanotubes) make CNFs firm candidates for the industrial production of high performance light materials.

5.1.1 Viscosity of the CNF–EP mixture as a function of dispersion

The commonly observed improvements in the mechanical and electrical properties of CNF–reinforced polymers are generally related to the formation of a nanofiber microstructure within the polymer. The formation of such microstructure can be easily investigated in the polymer liquid state with rheological experiments. Linear and non linear viscoelastic properties provide information on the dispersion of the filler in the matrix, the concentration and size distributions of the filler, the filler wettability and the resulting structure-property relationship. This information can also be used to improve the processability of the CNF–polymer nanocomposites.

The dynamic oscillatory analysis of the CNF suspensions were performed in a plate-plate rheometer as described in chapter 4.2.1.2. Samples were taken after each step of the TRC dispersion (see section 4.1.4.1) and tested at room temperature. From these tests, the storage (elastic) modulus G', loss (viscous) modulus G'', and complex viscosity $\left|\eta^*\right|$ were determined.

Figure 5.1 shows the storage (left) and loss (right) moduli, of the neat epoxy resin and of the 2.5 vol. % CNF suspension after the passes in the TRC. For the sake of clarity only a selection of passes are plotted. As it can bee seen and has been reported in the literature [142,143], the storage modulus was more sensible to the reinforcement resulting from the added nanofibers especially in the low frequency

range. Storage modulus dramatically increased with the incorporation of the nanofibers into the polymer matrix; this enhancement was significantly higher at lower frequencies. This comes as no surprise, since the CNF tend to form a percolated structure due to their high aspect ratio and surface area. The increase in modulus after the first pass in the three roll calender compared with the dissolver dispersed mixture can also be observed. This effect can be explained as a consequence of an increase in the interfacial area between the particles and the polymer resulting from the effective deagglomeration of the CNF agglomerates [144-146]. At low concentrations, the storage modulus enhancement is usually attributed to stiffness imparted by the solid particles that allow efficient stress transfer, which is mainly controlled by the matrix/fiber-matrix interface.

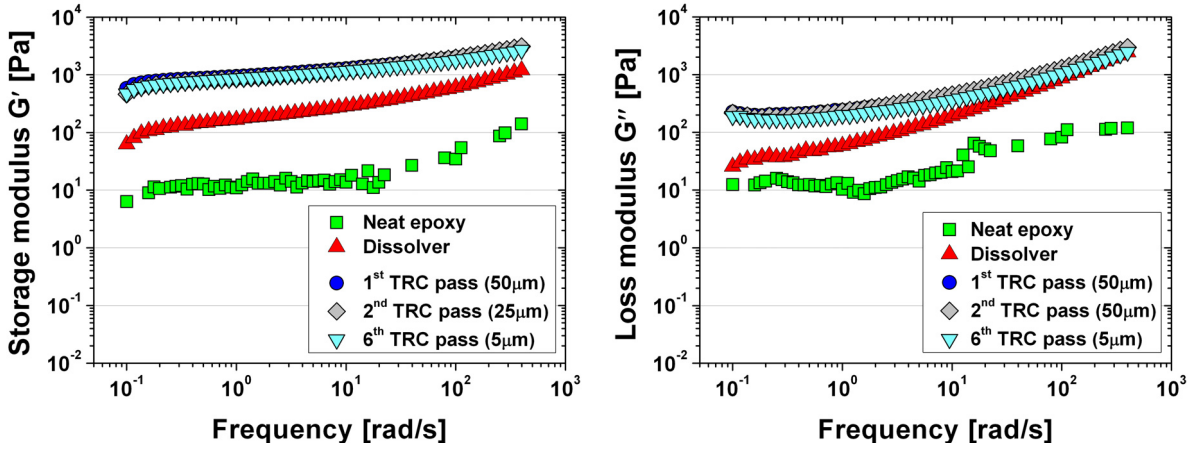

Figure 5.1: Storage (left) and loss (right) moduli versus frequency for the neat epoxy resin and the 2.5 vol. % CNF–EP suspension after the TRC processing steps.

It can also be observed that both the storage and loss moduli showed a frequency independent solid-like behaviour at low frequencies i.e., G' and G'' data showed the appearance of a plateau, an effect that increased with the improved dispersion of the CNFs in the resin, this suggests the formation of some interconnected nanofiber network within the matrix. It is well known from the literature that the interconnected structures of unsymmetrical fillers result in an apparent yield stress which corresponds, in dynamic measurements, to the plateau of G' or G'' at low frequencies [147-149]. This effect was more pronounced in G' than in G''. This is in accordance with theoretical expectations and experimental observations for

fiber-reinforced composites [150,152,153]. Indeed, as nanofiber dispersion improves, nanofiber-nanofiber interactions begin to dominate, eventually leading to percolation and to the formation of some interconnected structure.

The complex viscosity, $|\eta^*|$, is also an important parameter to characterize the rheological properties of a material. The real part of the complex viscosity is an energy dissipation term similar to the imaginary part of the complex modulus. The dependency of the melt state complex viscosity of the neat epoxy resin and the 2.5 vol. % CNF suspension on frequency and passes through the TRC is shown in Figure 5.2.

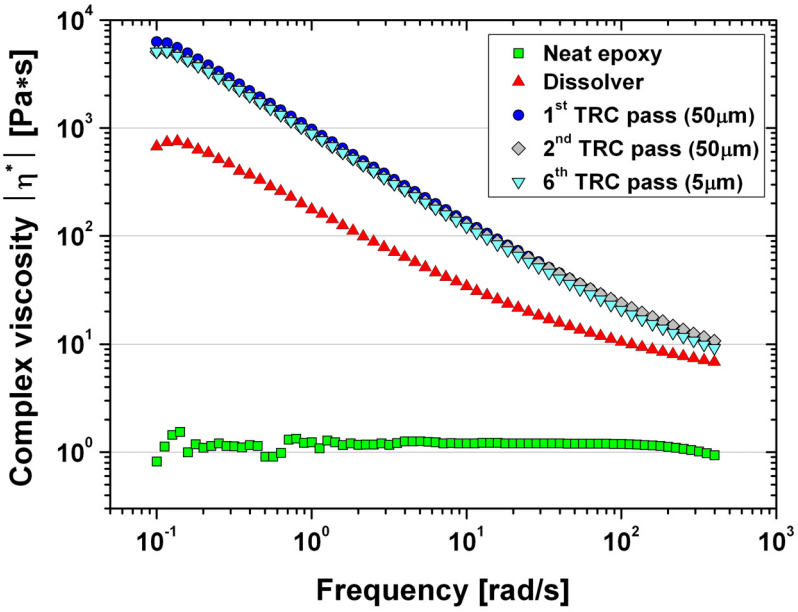

Figure 5.2: Complex viscosity versus frequency for the neat epoxy resin and the 2.5 vol. % CNF–EP suspension after the TRC processing steps.

The neat epoxy resin showed a typical Newtonian behaviour where the relatively low viscosity (1 Pa·s) of the resin was independent of the frequency of the applied stress. On the other hand, the CNF reinforced composites exhibited a typical pseudo-plastic shear thinning behaviour. As it can be seen in the graph, viscosity dramatically increased with the presence of nanofibers and with the first dispersion step through the calender and decreased with the increase in frequency. The subsequent passes through the TRC did not seem to have a significant effect on the viscosity of the mixture. In a filled polymer system the presence of fibers perturbs the normal flow of

the polymer and hinders the mobility of the polymer chain segments in flow; therefore the viscosity of the polymer system increases [151]. It can also be noted that the composites became more shear dependent in the low frequency range with the calender dispersion. This shear thinning behaviour can be attributed to an effective break up of the CNF agglomerates and a homogeneous CNF distribution in the polymer matrix which lead to a greater degree of polymer-fiber and fiber-fiber interaction. These interactions require high shear stresses and longer relaxation times for the polymer to flow, thus the observed increase in viscosity. The observed increase after the first calender dispersion could be attributed to a better dispersion of the nanofibers in the matrix which resulted in fiber wetting (polymer-fiber interaction) as well as fiber-fiber friction. The increase in viscosity at low frequencies through the presence of nanofibers was similar to other reported results in carbon nanofiber and carbon nanotube melts [152,153]. Therefore the significant decrease in viscosity at high frequencies shows that the difficulty of processing composites with nanofibers and nanotubes as fillers is not an issue if high shear rates are used.

5.1.2 Microstructure of the CNF–epoxy composites

Figure 5.3 shows three different TEM micrographs of a six times calender dispersed epoxy resin–CNF composite with a 0.5 vol. % content of CNF. The picture on the left shows that the nanofibers were properly dispersed in the resin. Only some small agglomerates of $d \leq 1.5$ μm could be observed (center picture). On the picture of the right an individual carbon nanofiber with a diameter of 60 nm showing a characteristic nanofiber stacked cup structure can be observed [154,155].

The pictures demonstrate that the calendering method is able to disperse fiber-like fillers in an epoxy matrix. Another possible advantage of this dispersion method is the homogeneous distribution of shear forces over the whole volume of the composite on the rolls, while the sonication process introduces the energy locally. For this reason calendering is not expected to significantly shorten and reduce the aspect ratio of the nanofibers.

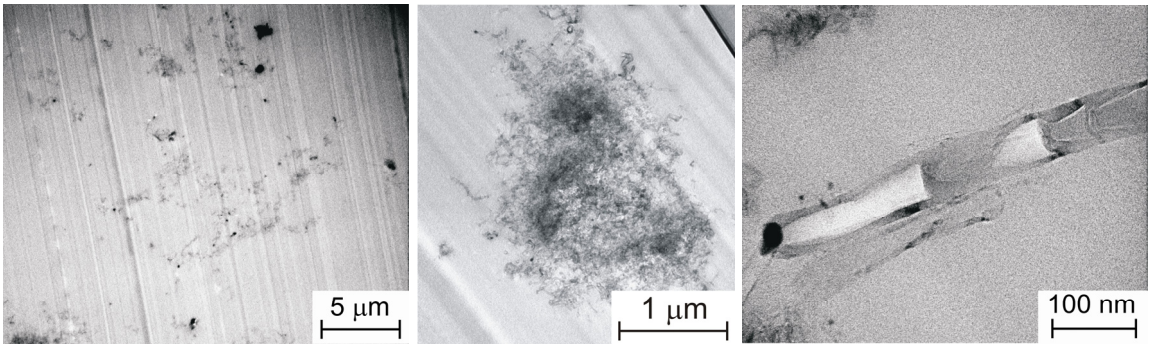

Figure 5.3: TEM images of a nanocomposite containing 0.5 vol. % CNF showing the achieved state of dispersion. General view showing the homogeneous dispersion of the nanofibers (left), detail of a nanofiber agglomerate (center), close up of an individual nanofiber (right).

5.1.3 Mechanical properties of the CNF–EP composites

5.1.3.1 Tensile properties of the CNF–EP composites

5.1.3.1.1 Influence of CNF dispersion on the tensile properties

The quality of the dispersion of the reinforcement filler has a strong influence on the physical properties nanoreinforced composites [156,185]. However, some properties are more sensible to the filler dispersion than others. The improvement of the elastic modulus, for example, depends on intrinsic properties of matrix and filler as well as interactions between them and is not so dependent in the state of dispersion. Ultimate properties, on the other hand, are more sensitive to defects [157]. To study how the dispersion state of the nanofibers within the epoxy resin affected the mechanical and electrical properties of the CNF–epoxy composites two different series of CNF–epoxy composites, with volume contents of 0.5 % and 2 % respectively, were prepared after each dispersion step in the calender. The average values of the tensile modulus and strength after the different dispersion steps through the TRC for the nanocomposites containing 0.5 and 2 vol. % of CNFs respectively can be seen in Figure 5.4. In both cases the modulus variation with the number of dispersion steps was almost negligible but a considerable improvement in strength (around +28 % in the case of the 0.5 vol. % CNF–EP composites and +600 % in the case of the composites with a 2 vol. % loading of CNFs) could be observed as the dispersion of the nanofibers was improved.

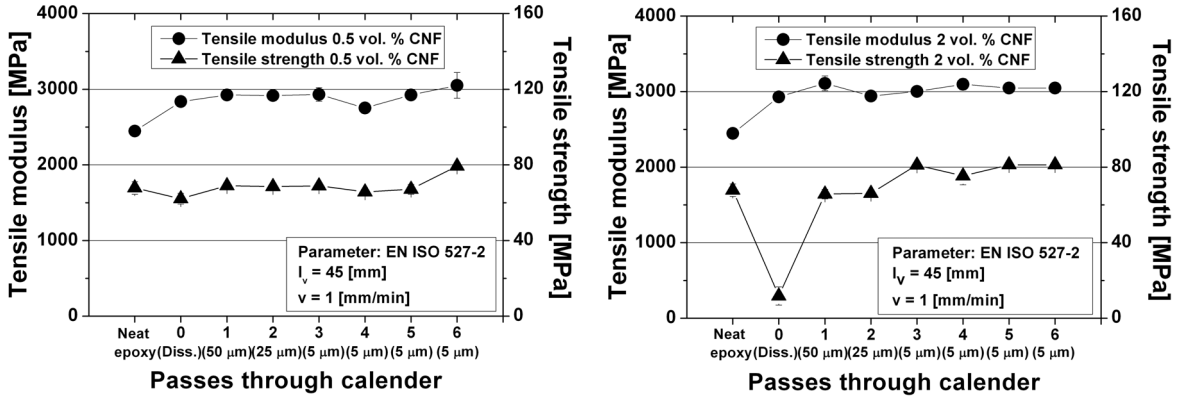

Figure 5.4: Tensile modulus and tensile strength of the 0.5 vol. % CNF (left) and the 2 vol. % CNF–EP composites (right) as a function of the dispersion steps in the three roll calender.

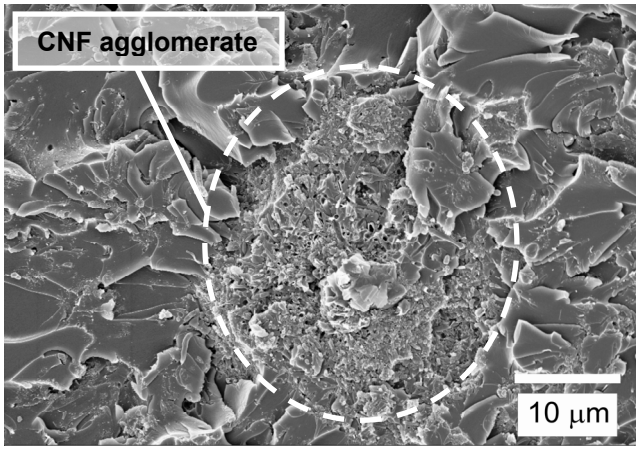

Figure 5.5: SEM micrograph of the tensile fracture surface of a 2 vol. % CNF–EP dissolver dispersed composite illustrating the size (>10μm) of the remaining CNF agglomerates.

The undispersed composites, in which the nanofibers were just incorporated and stirred at low rotation speed with a dissolver, showed a sharp decrease in strength in comparison with the neat epoxy resin. This decrease was more significant in the 2 vol. % case. The likely presence of nanofiber agglomerates (see Figure 5.5), which act as stress concentrators, in these poorly dispersed composites, lead to an early failure and the measured reduced strength of the dissolver mixed samples. Furthermore, the weak electrostatic bonding of the nanofibers in the nanofiber clusters, makes the propagation of the cracks through these agglomerates relatively simple; agglomeration also results in a reduction of the surface area for the

interaction between nanofillers and the polymer matrix [158]. Since the number of nanofiber agglomerates is larger with increasing volume of undispersed fillers, thus the sharper reduction in strength observed in the 2 vol. % case.

A similar behaviour could be observed for the tensile strain at the maximum sustained force (Figure 5.6). For both volume loadings (0.5 and 2 vol. %) the elongation at $F_{\max}$ increased with the dispersion steps. Once again, the 2 vol. % CNF–dissolver mixed composites showed a considerable decrease in their mechanical properties as expected.

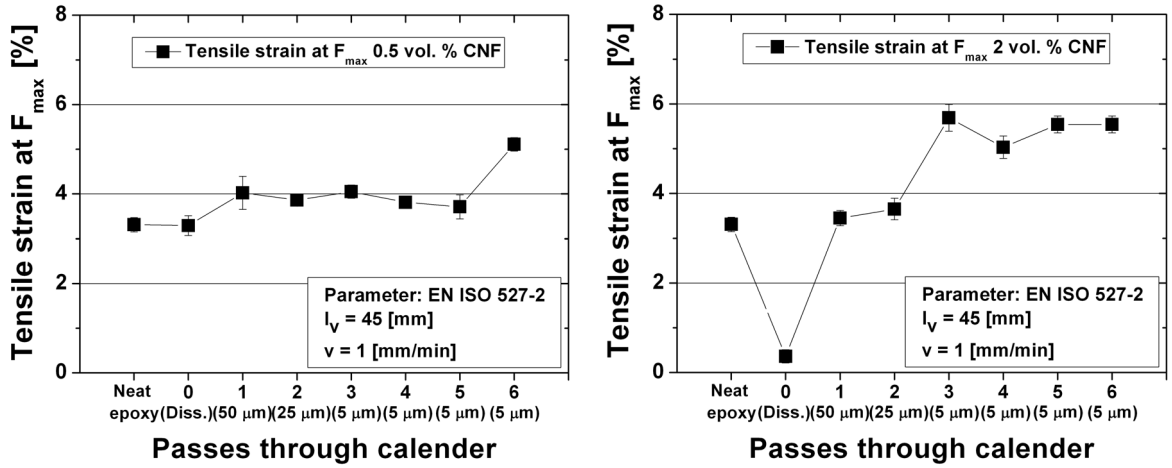

Figure 5.6: Tensile strain at maximum force for the 0.5 vol. % CNF (left) and the 2 vol. % CNF–EP composites (right) as a function of the dispersion steps in the three roll calender.

5.1.3.1.2 Influence of CNF content on the tensile properties

In the previous section (section 5.1.3.1.1) the effect that the successive dispersion steps on the three roll calender had on the mechanical properties of the CNF–epoxy composites was discussed. On this chapter the effect that the variation of the carbon nanofiber volume loading had on the mechanical and electrical properties of the epoxy resin is presented.

The effect that the volume content of CNFs had on the properties of the composites was determined preparing samples with different concentrations of nanofibers. Each of these series was obtained through an adequate dilution of the nanofiber–epoxy

mixture that had undergone the dispersion process 6 times with the addition of epoxy resin. Diluted mixtures were stirred under vacuum to remove entrapped air. The hardener was then added to the mixture and softly agitated for 15 minutes at 60 °C. Finally, the composites and the reference suspension were poured into aluminium moulds and cured in an oven at 80 °C for 1 h followed by 8 h at 140 °C.

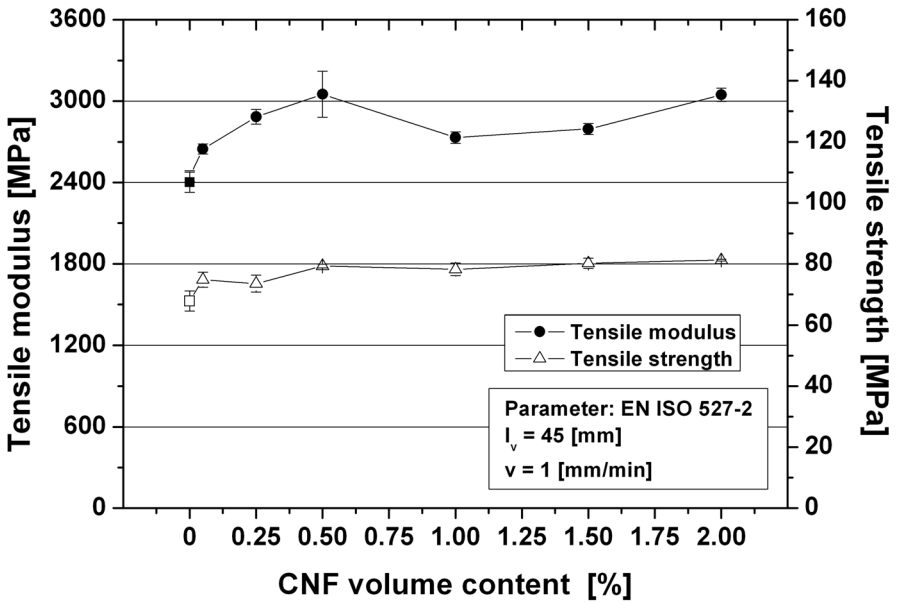

Figure 5.7: Tensile modulus and tensile strength of the CNF–EP composites as a function of CNF volume content.

The average values of the Young's modulus and the tensile strength of the composites containing different CNF volume concentrations, including the neat epoxy, are shown on Figure 5.7. A simultaneous improvement in modulus and strength was observed with the addition of carbon nanofibers to the epoxy resin. This increase was more noticeable in the modulus case with a gain of 25 % for a volume loading of nanofibers of 0.5 %. For nanofiber contents above 0.5 vol. % the tensile modulus showed a minor decrease, however the value measured for the nanocomposites containing 2 vol. % of CNFs approximately on the same level than the one obtained with the 0.5 vol. % content of CNFs. The tendency showed by the tensile strength was similar although the increase at lower concentrations of fillers was not as abrupt as in the modulus case and there was not an observed reduction of strength for volume contents above 0.5 vol. %. At higher filler volume concentrations nanofiber agglomerates are more likely to be found, due to poor

dispersion or reagglomeration, the weakening effects of the agglomerates can lead certain samples to an early failure and counteract the reinforcing effect that the well dispersed nanofibers have on the epoxy matrix.

The influence of rigid particulate fillers on the stress-strain behaviour of polymers is well known, at least for fillers in the size of micrometers and larger. Microfillers commonly increase the stiffness on the one hand, but on the other hand, they may have a detrimental effect on the strain at break [159]. The strength of microparticle filled composites is known to be reduced with rising filler content [159,160]. Some important characteristics of composites have to be considered in order to explain this phenomenon. The quality of the interface in composites, i.e. the static adhesion strength as well as the interfacial stiffness, usually plays a very important role in the materials' capability to transfer stresses and elastic deformation from the matrix to the fillers [161].

This is especially true for nanocomposites, because they impart a high portion of interface. If filler matrix interaction is poor, the particles are unable to carry any part of the external load. In that case, the strength of the composite cannot be higher than that of the neat polymer matrix. If the bonding between fillers and matrix is instead strong enough, the yield strength of a particulate composite can be higher than that of the matrix polymer [162]. In the same way a high interfacial stiffness corresponds to a high composite modulus. Hence, the gradual increase in stiffness and tensile strength, as observed for the nanocomposites, reveals that stresses are efficiently transferred via the interface.

As mentioned above, the strain at break usually declines with rising filler content. Low filler loadings can already cause a dramatic drop in the maximum sustained strain. One has to recall that the composite is part filler and part matrix. Due to the rigid nature of the fillers, most of the deformation comes from the polymer. The actual deformation experienced only by the polymer matrix is much larger than the measured deformation of the sample, with the result that the polymer reaches the failure strain limit at a lower total deformation. Hence, the total composite strain-to-break decreases. However, it is surprisingly observed for the nanocomposites in the present study that the strain-to-break behaves contrary to

conventionally filled composites. It tends to slightly higher values even for filler loadings as low as 0.05 vol. % (Figure 5.8). This increase suggests that the nanofibers are able to introduce additional mechanisms of failure and energy consumption without blocking matrix deformation. Nanofibers may induce matrix yielding under certain conditions and may furthermore act as stoppers to crack growth by pinning the cracks [73].

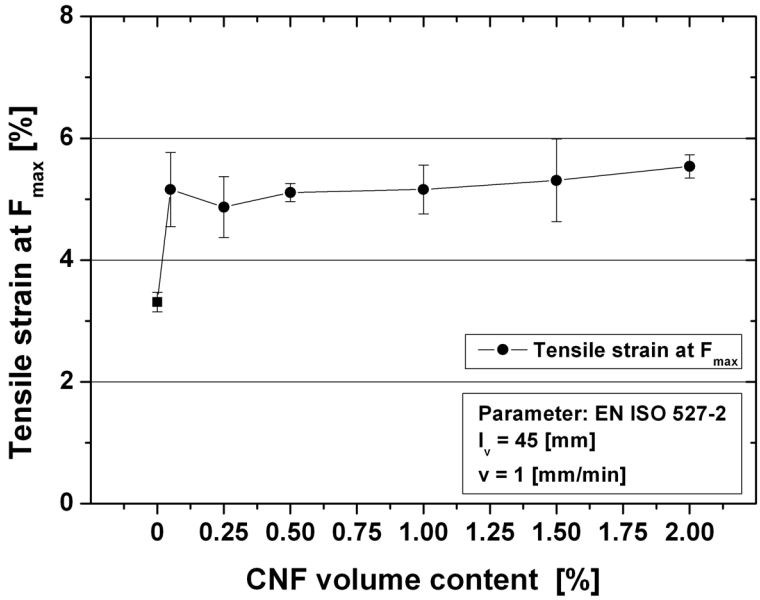

Figure 5.8: Tensile strain at maximum force of the CNF–EP composites as a function of CNF volume content.

The observed improvement on the mechanical properties of the CNF–EP composites showed a similar trend as the ones reported by Choi and co-workers [163] but were below other results reported in the literature, indicating that parameters such as the processing conditions [164] and the surface treatment of the fibers by oxidation [165] play and important role in the final performance of CNF composites.

5.1.3.2 Modelling the tensile modulus of the CNF–EP composites

Several theoretical models have been proposed to explain the mechanical properties of carbon nanotube and carbon nanofiber reinforced composites. Most of these models assume an homogeneous dispersion of the nanofillers in the matrix and perfect stress transfer from the matrix to the fillers. As a result, the predicted mechanical properties often exceed the experimental results since, in the real

composites; the fillers tend to form entangled agglomerates which are extremely difficult to break up. The presence of these fiber clusters tends to reduce the mechanical performance of the materials.

Table 5.1, below these lines, shows a comparison between the measured tensile modulus of the CNF–EP composites and the predictions of three different theoretical models: Voigt-Reuss', Halpin-Tsai's and Cox's. A brief explanation of each model can be found in section 7.1 of the appendix. The numbers between parentheses show the percentage of difference between predicted and experimental values. As it can be seen, none of the model offers an adequate fit to the experimental results. In general all models underestimate the reinforcing effect of the fillers at low volume concentrations while overestimating it for higher concentrations.

CNF volume fraction, ϕ_f [%]	$E_{c,\text{experimental}}$ [MPa]	$E_{c,Voigt-\text{Re}uss}$ [MPa]	$E_{c,\text{H}alpin-Tsai}$ [MPa]	$E_{c,\text{Cox}}$ [MPa]
0.05	2646.9 ± 37.2	2490.3 (-5.9 %)	2467.4 (-6.8 %)	2468.3 (-6.7 %)
0.25	2884.6 ± 53.5	2664.0 (-7.6 %)	2550.3 (-11.6 %)	2554.2 (-11.5 %)
0.5	3050.6 ± 168.9	2881.2 (-5.6 %)	2654.4 (-13.0 %)	2661.7 (-12.7 %)
1	2731.1 ± 42	3315.5 (+21.4 %)	2863.2 (+4.8 %)	2877.0 (+5.3 %)
1.5	2794.1 ± 40.9	3749.9 (+34.2 %)	3072.7 (+10 %)	3092.4 (+10.7 %)
2	3046.6 ± 49.9	4184.4 (+37.3 %)	3282.5 (+7.7 %)	3307.9 (+8.6 %)

Table 5.1: Tensile modulus of the CNF–EP composites as a function of CNF volume content. Comparison between experimental results and different theoretical predictions.

Recently, Guzmán de Villoria et al. [86] proposed a new micromechanical model (dilute suspension of clusters (DSC) model) which considers the influence of the state of dispersion of the fillers in the resulting composite stiffness. As can be seen in the TEM (Figure 5.3) and SEM micrographs (Figure 5.23) CNF–epoxy composites are not really short random fiber distributions of nanofibers in the resin; instead, agglomerates of fibers, few micrometers in size, can be seen in the material. Assuming these fiber clusters to be independent spherical particles, a random three dimensional orientation of fibers model can be used to calculate the effective mechanical properties of these agglomerations. Once the effective properties of the

clusters are determined, a dilute suspension of particles model can be used to predict the elastic properties of the whole composite material. On a first step, it is necessary to calculate the effective properties of the agglomerates as a function of the fiber phase properties, the matrix properties and the volumetric fraction of the filler. Due to the high aspect ratio of the nanofibers, finite length fiber effects are rejected. Furthermore, to simplify the calculations, no nanofiber-nanofiber interaction is considered either.

In the composite cylinder model [166], the fiber phase of the composite is assumed to be composed of infinite long circular cylinders embedded in a continuous matrix. A fiber is modeled as composite cylinder. In each composite cylinder a fiber of radius a is surrounded by a concentric cylinder of matrix of radius b. The ratio of radii a/b being constant for every composite cylinder. The study of an individual cylinder is sufficient to calculate the effective uniaxial (E_{11}), bulk plane strain (k_{23}), shear modulus in the fiber direction (μ_{12}) and Poisson's ratio (ν_{12}) of the aligned fiber material:

$$E_{11} = c_f E_f + (1-c_f)E_m + 4\,c_f(1-c_f)\left[\frac{(\nu_f-\nu_m)^2}{\frac{(1-c_f)\mu_m}{k_f+\frac{\mu_f}{3}}+\frac{c_f\mu_m}{k_m+\frac{\mu_m}{3}}+1}\right] \qquad \text{Eq. 5.1}$$

$$k_{23} = k_m + \frac{\mu_m}{3} + \frac{c_f}{\frac{1}{k_f - k_m\frac{\mu_f-\mu_m}{3}} + \frac{1-c_f}{k_m+4\frac{\mu_m}{3}}} \qquad \text{Eq. 5.2}$$

$$\mu_{12} = \frac{\mu_m[\mu_f(1+c_f)+\mu_m(1-c_f)]}{\mu_f(1-c_f)+\mu_m(1+c_f)} \qquad \text{Eq. 5.3}$$

$$\nu_{12} = \nu_{13} = c_f \nu_f + (1 - c_f)\nu_m + \frac{c_f (1 - c_f)(1 - c_f)\left(\frac{\mu_m}{k_m + \frac{\mu_m}{3}} - \frac{\mu_m}{k_f + \frac{\mu_f}{3}} \right)}{\left[\frac{(1 - c_f)\mu_m}{k_f + \frac{\mu_f}{3}} \right] + \frac{c_f \mu_m}{k_m + \frac{\mu_m}{3}} + 1} \quad \text{Eq. 5.4}$$

The transverse shear modulus (μ_{23}) is not easily determined with the composite cylinder model. In order to determine this parameter a three phase cylinder model has to be introduced where a single fiber, surrounded by a matrix cylinder is embedded in an equivalent homogeneous media.

$$\mu_{23} = \mu_m \left[1 + \frac{c_f}{\frac{\mu_m}{\mu_f - \mu_m} + \frac{\left(k_m + \frac{7\mu_m}{3} \right)(1 - c_f)}{2\left(k_m + \frac{4\mu_m}{3} \right)}} \right] \quad \text{Eq. 5.5}$$

Where $E_{m,f}$, $k_{m,f}$, $\mu_{m,f}$, $\nu_{m,f}$ are the elastic, bulk, shear modulus and Poisson's ratios of matrix and fillers respectively, and c_f is the volume fraction of fibers in agglomerated form. The bulk and shear modulus of the matrix and fibers are related to the elastic modulus and Poisson's ratios of the matrix and fibers by the following expressions:

$$k_{m,f} = \frac{E_{m,f}}{3(1 - 2\nu_{m,f})} \quad \text{Eq. 5.6}$$

$$\mu_{m,f} = \frac{E_{m,f}}{2(1 + \nu_{m,f})} \quad \text{Eq. 5.7}$$

The three dimensional problem is approached by taking a body of aligned fibers and imposing upon it a given strain condition. Then, a geometric average procedure is

performed which effectively corresponds to taking a random direction of imposed strain in the aligned fiber system [166]. With these considerations the Young's modulus and Poisson's ratio of a cluster of fibers take the following form.

$$E_{cluster} = \frac{[E_{11} + 4\,(1+\nu_{12})^2 k_{23}][E_{11} + (1-2\nu_{12})^2 k_{23} + 6\,(\mu_{12}+\mu_{23})]}{3\,[2E_{11} + (8\nu_{12}^2 + 12\nu_{12} + 7)k_{23} + 2\,(\mu_{12}+\mu_{23})]} \qquad \text{Eq. 5.8}$$

$$\nu_{cluster} = \frac{E_{11} + 2\,(2\nu_{12}^2 + 8\nu_{12} + 3)k_{23} - 4\,(\mu_{12}+\mu_{23})}{2\,[2E_{11} + (8\nu_{12}^2 + 12\nu_{12} + 7)k_{23} + 2\,(\mu_{12}+\mu_{23})]} \qquad \text{Eq. 5.9}$$

Once the effective elastic properties of the fiber agglomerates have been calculated, each cluster is assumed to behave as an homogenous particle. Since the concentration of agglomerates in the composite is low, it is assumed that the clusters are so small and so far apart that no significant interactions between clusters take place in the composite. Therefore, assuming the clusters to be spherical, a dilute suspension of particles model can be applied to the dispersion of CNF fibers in the polymer matrix. The effective bulk modulus and shear modulus of a dilute suspension of spherical particles in a continuous phase of an elastic material have the following form:

$$k_{dsc} = k_m + \frac{(k_{cluster} - k_m)\,c_c}{1 + \frac{(k_{cluster} - k_m)}{\left(k_m + \frac{4}{3}\mu_m\right)}} \qquad \text{Eq. 5.10}$$

$$\mu_{dsc} = \mu_m \left[1 - \frac{15\,(1-\nu_m)\left(1 - \frac{\mu_{cluster}}{\mu_m}\right)c_c}{7 - 5\nu_m + 2\,(4-5\nu_m)\frac{\mu_{cluster}}{\mu_m}} \right] \qquad \text{Eq. 5.11}$$

Where c_c is the volume fraction of clusters. The volume fraction of fibers in clusters c_f is calculated using the following relation:

$$\phi_f = c_c c_f \qquad \text{Eq. 5.12}$$

With ϕ_f the total filler volume fraction. Since the nanofiber clusters are considered an isotropic homogeneous media the bulk ($k_{cluster}$) and shear ($\mu_{cluster}$) modulus of the clusters can be calculated from the elastic modulus ($E_{cluster}$) and the Poisson's ratio ($\nu_{cluster}$) using Eq. 5.6 and Eq. 5.7 respectively. Analogously, the Young's modulus of the suspension of clusters (i.e: the whole composite) can be calculated with the following mathematical expression:

$$E_{dsc} = \frac{9k_{dsc}\mu_{dsc}}{3k_{dsc} + \mu_{dsc}} \qquad \text{Eq. 5.13}$$

In order to determine the modulus of the composite using this theoretical model, six independent variables need to be known. The Young's moduli and Poisson's ratios of the matrix and the fibers ($E_{m,f}$, $\nu_{m,f}$), the volume fraction of fibers in clusters c_f and the volume fraction of clusters in the composite c_c. Table 5.2 summarises the material properties used to estimate the modulus of the composite.

Material	$E_{m,f}$ [GPa]	$\nu_{m,f}$
Epoxy	2.45 (experimental result)	0.35 [107,[167]
CNF	230 [48]	0.25 [168]

Table 5.2: Mechanical properties of the matrix and fillers.

Different methods can be used to determine the volume fraction of nanofiber in agglomerated form. In our case, from conductivity considerations [185] (see chapter 5.1.5.1), we will initially consider a value of $c_c = \xi = 0.05$. (i.e: 5 % of the CNF present in the CNF–EP composites remained agglomerated). As it can be seen in Figure 5.8, this value of c_c, fits the data almost perfectly for nanofiber concentrations above 0.5 vol. %. However, a constant value of c_c fails to explain the big gain in modulus at low volume concentrations. It seems that the detrimental effect that nanofiber clusters have in the elasticity of the material increases with the volume concentration of nanofibers. To account for this effect, an exponential dependence of c_c with ϕ_f was included in the DSC model i.e: $c_c = Ae^{B\phi_f}$, with A and B free fitting parameters. As it can be seen in the graph, for values of $A = 4 \cdot 10^{-8}$ and $B = 400$, the improved

model is able to predict more accurately the experimental results at low concentrations of fillers and only diverges slightly for higher concentrations.

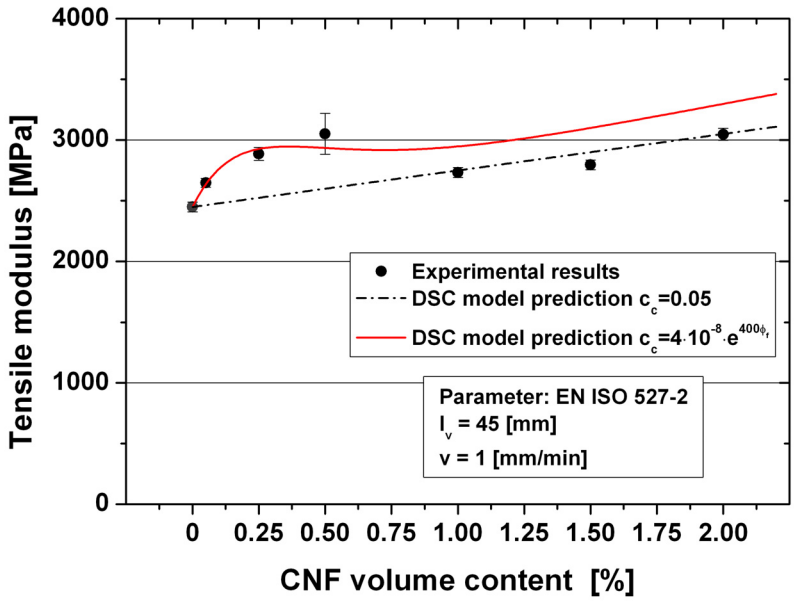

Figure 5.9: Tensile modulus of the CNF–EP composites. Experimental results and dilute suspension of clusters model predictions.

5.1.3.3 Fracture toughness of the CNF–EP composites

5.1.3.3.1 Influence of CNF dispersion on the fracture toughness

The static fracture toughness of the CNF–epoxy composites did not seem to be so sensitive to the state of dispersion of the fillers as the tensile properties of the composites. As can be observed in Figure 5.10 the undispersed composites (for both volume contents) showed a small increase (+5 % for the 0.5 vol. % and +13 % in the 2 vol. % case) in fracture toughness with respect to the epoxy resin (which already had a standard deviation of 2.4 %). Further dispersion did not improve significantly the fracture toughness for either volume content, the maximum measured gain covered roughly an increase of 8 % in the 0.5 vol. % case and of 16 % for the composites containing a volume loading of 2 % CNFs.

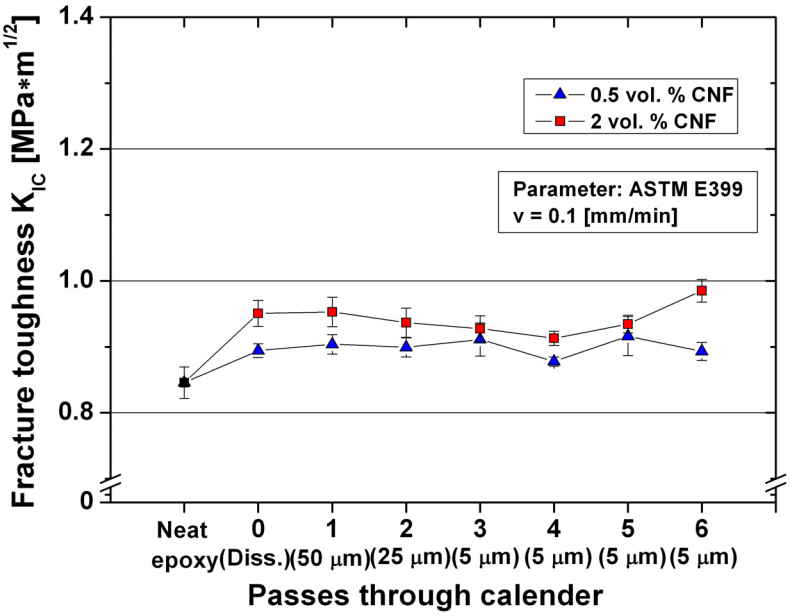

Figure 5.10: Static fracture toughness (K_{IC}) of the epoxy composites containing 0.5 and 2 vol. % content of CNFs as a function of the dispersion steps in the three roll calender.

5.1.3.3.2 Influence of CNF content on the fracture toughness

As could be observed in the previous section, the addition of nanofibers into the epoxy resin only contributed to a relatively small increase in the fracture toughness of the composites despite their state of dispersion. In this section we present the effect that the volume loading of nanofibers had on the fracture toughness. Figure 5.11 illustrates the evolution of the fracture toughness for composites containing different volume concentrations of carbon nanofiber all subjected to the complete (6 steps) dispersion process in the three roll calender. The experimental results showed a light improvement in fracture toughness over the whole range of filler loading tested. The reinforcing effect of the CNFs seemed to be effective already at low volume contents of only 0.25 %. At higher volume contents fracture toughness increased softly until reaching a maximum improvement of 16 % with respect to the fracture toughness of the pristine epoxy resin. As it will be discussed later, this reinforcement effect can be related to a raising dominance of crack deflection mechanisms.

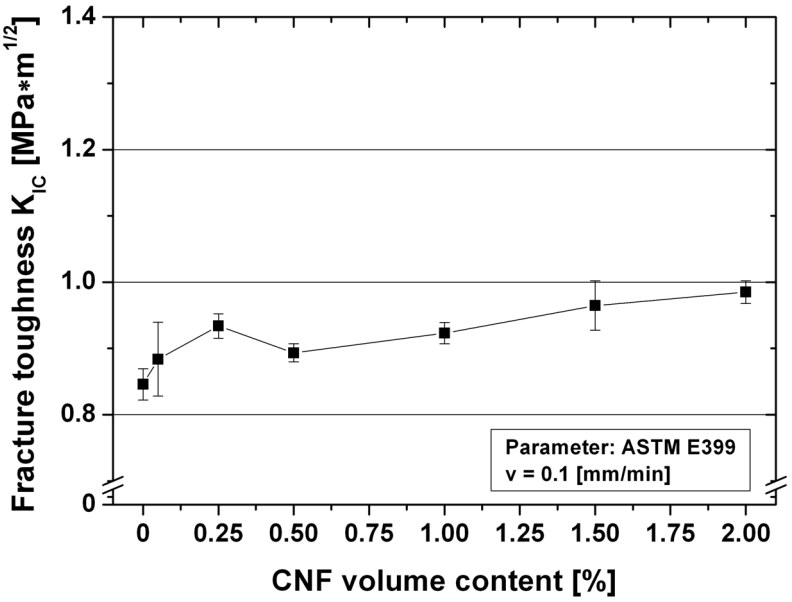

Figure 5.11: Static fracture toughness (K_{IC}) of the CNF–EP composites as a function of CNF volume content.

5.1.3.4 Impact energy of the CNF–EP composites

5.1.3.4.1 Influence of CNF dispersion on the impact energy

Figure 5.12 shows how the state of dispersion of the nanofibers in the epoxy resin affected the impact energy of the composites containing 0.5 vol. % of CNFs (left) and 2 vol. % of CNFs (right).

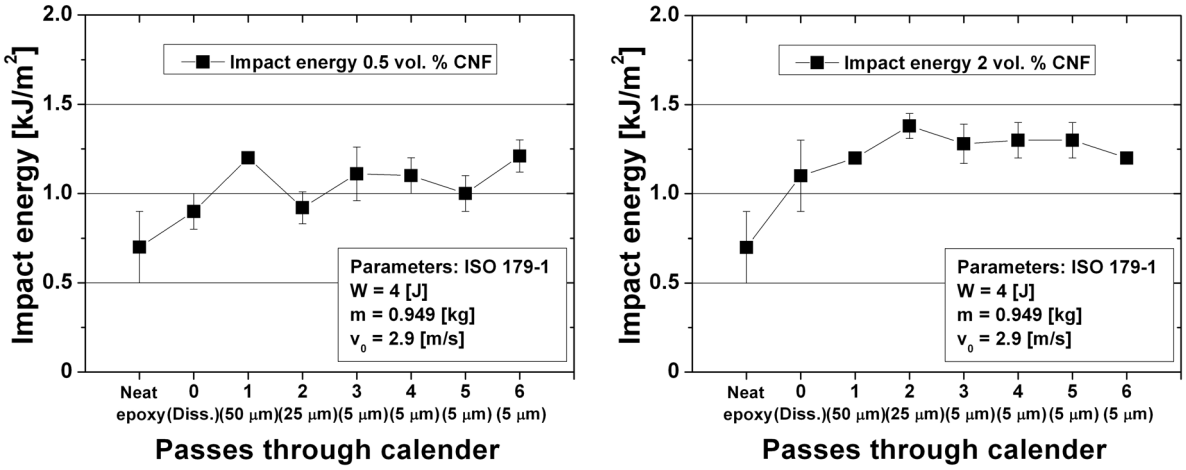

Figure 5.12: Impact energy (notched Charpy test) for the 0.5 vol. % CNF (left) and the 2 vol. % CNF–EP composites (right) as a function of the dispersion steps in the three roll calender.

Unlike the case of the tensile strength, there was no reduction in the impact energy of the dissolver treated composites. For both volume loadings, the impact resistance increased with the passes through the calender. That increase was more significant in the three first dispersion steps, after that the values of the impact energy remained almost constant. These results show that high speed fracture tests, such as the Charpy impact tests, are not as sensitive to the state of agglomeration of the fillers in the matrix as the tensile tests, where the speed of crack propagation is considerably lower [169,170].

5.1.3.4.2 Influence of CNF content on the impact energy

The experimental results of the notched impact Charpy tests measured for the epoxy nanocomposites are represented in Figure 5.13.The results offered an improving effect of the nanofibers on the impact behaviour for all volume loadings tested. This reinforcement seemed to be effective already at low filler contents of only 0.05 vol. % and reached the highest level observed for the present series at 0.25 vol. % CNF. Once that maximum value was reached increasing the volume content of nanofibers did not change the impact energy significantly, a behaviour similar to the one observed for both the modulus and strength of the CNF reinforced composites (see Figure 5.7).

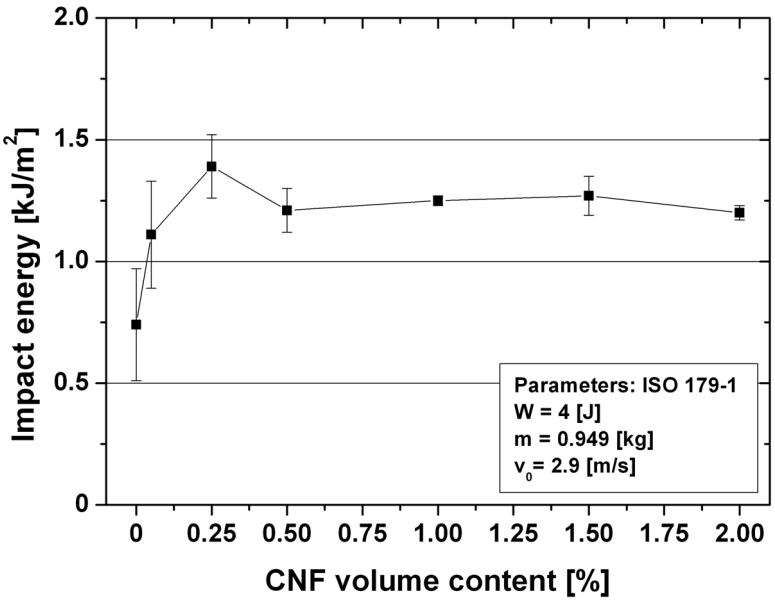

Figure 5.13: Impact energy (notched Charpy test) of the CNF–EP composites as a function of CNF volume content.

As mentioned in section 4.2.2.1.3, unreinforced epoxy resins can be considered as brittle materials and they exhibit a high sensitivity to notches, micro-cracks and local inhomogeneities. The reason for this is that notches act as stress concentrators and much of the deformation of the sample on impact takes place in the vicinity of the notch tip where a higher apparent strain rate occurs in comparison with unnotched specimens.

In our case the presence of nanofibers had a beneficial effect at low volume concentrations. However, the presence of more nanofibers in the resin did not further increase the resistance to impact fracture. A possible explanation is that nanofiber agglomerates, more numerous with higher volume loadings, act as stress concentrators and counteract the reinforcing effects of the individual nanofibers. Furthermore, the high aspect ratio of the nanofibers might induce additional stresses. These effects were confirmed by Riley [129], who found that the impact properties of polymers are mainly enhanced by small particles with low aspect ratio, since large particles can act as crack initiation sites and high aspect ratio particles are able to induce large stress concentrations near their edges.

5.1.4 Electrical properties of the CNF–EP composites

5.1.4.1 Influence of CNF dispersion on the volume conductivity

Figure 5.14 shows the evolution of the volume conductivity of the samples containing 0.5 vol. % CNFs (left) and 2 vol. % CNFs (right) with the dispersion runs in the three roll calender. As it can be appreciated, the state of dispersion did not affect significantly the conductivity of the composites in either case. Only a slight improvement could be observed after the first pass through the TRC for the 0.5 vol. % CNF composites. Since both CNF volume contents were above the percolation threshold estimated for this material (ϕ_c=0.14 vol. %, see Figure 5.15 in chapter 5.1.4.2) the improvement of the dispersion was not decisive in order to create conductive nanofiber pathways within the epoxy matrix.

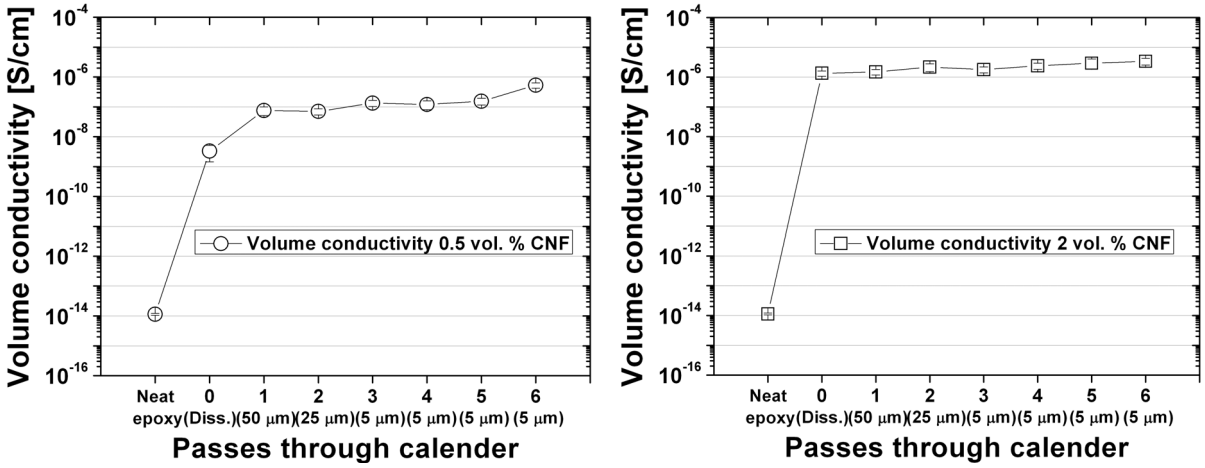

Figure 5.14: Volume electrical conductivity for the 0.5 vol. % CNF (left) and the 2 vol. % CNF–EP composites (right) as a function of the dispersion steps in the three roll calender.

5.1.4.2 Influence of CNF content in the volume conductivity

The volume conductivity of the CNF–epoxy composites as a function of nanofiber volume content can be seen in Figure 5.15. A steep conductivity increase was evident at a low volume concentration of fillers, around 0.15 vol. % (percolation threshold). At lower concentrations the fibers are separated and thus no conductive pathways can be created throughout the insulating epoxy matrix between adjoining fibers. The charge transport is inefficient and therefore the overall conductivity of the composites remains at low levels, similar to that of the non conductive epoxy.

Electrical conductivity rises abruptly when effective contacts are made among the nanofibers and a continuous conducting chain of macroscopic dimensions is created. Physical contact between the nanofibers is not strictly necessary in order to observe a conductivity increase, the distance between the fibers must be small enough (~10 nm) in order to allow to travel across the polymeric gap in between the conductive fibers and permitting current to flow, for example by electron hopping or tunnelling effects [171-173].

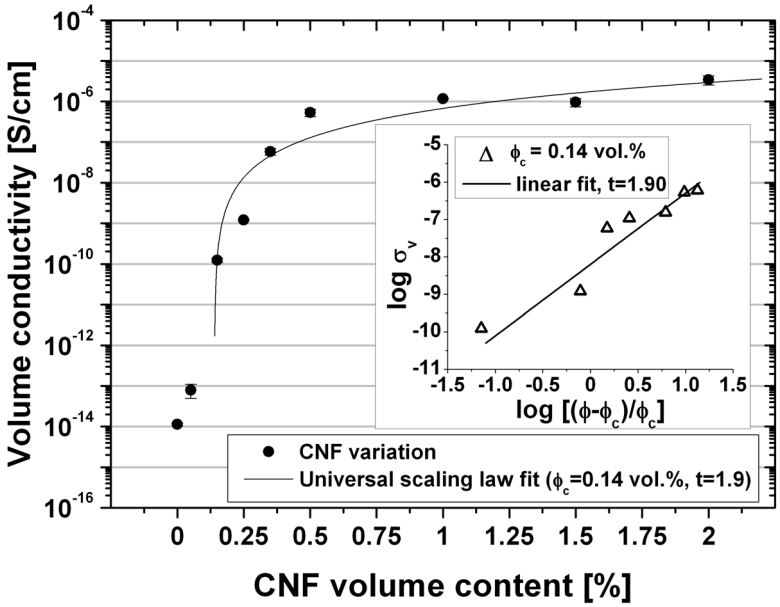

Figure 5.15: Volume conductivity of the CNF–EP composites vs. CNF volume content. Solid line is a fit to the universal scaling law (Inset: logarithm of volume conductivity as a function of logarithm of reduced volume fraction with linear fit).

The electrical conductivity increased 7 orders of magnitude with the addition of 0.9 wt. % (0.5 vol. %) of nanofibers into the epoxy resin. The final enhancement in conductivity, with the incorporation of 3.56 wt. % (2 vol. %) of CNFs, was 8 orders of magnitude. Once the percolation threshold is surpassed, percolation theory predicts power law scaling of conductivity. The data points in the vicinity of the transition, that is from 0.27 wt. % (0.15 vol. %) to 0.9 wt. % (0.5 vol. %) were fitted to the universal scaling law [60,61,174]:

$$\sigma_v \propto (\phi - \phi_c)^t \quad (for\ \phi > \phi_c) \qquad \text{Eq. 5.14}$$

Where σ_v is the volume electrical conductivity; ϕ, the volume fraction of CNFs; ϕ_c, the critical volume fraction of CNFs, and t the critical exponent related to the dimensionality of the system. For our calender dispersed CNF–EP system (see inset graph in Figure 5.15) it was found that the critical volume fraction was 0.14 vol. % (0.24 wt. %) and the critical exponent t=1.9 which is very close to the one corresponding to a three dimensional random system (t=1.94) [174]. This extreme was confirmed by independent measurements by Konter et al. [175] who found that

the percolation threshold for these CNF composites corresponded to a random statistical distribution of the carbon nanofibers in the epoxy resin. For volume concentrations above the percolation threshold the authors also postulated an improvement in the quality of the contacts between the carbon nanofibers which leads to the observed increase of the electrical conductivity of the CNF–EP composites. As mentioned before, the critical filler fraction corresponds to the formation of a tunnelling conductive network. This network is formed by aggregates and fibers that are close enough to each other (~10 nm) to allow tunnelling conduction between them [176].

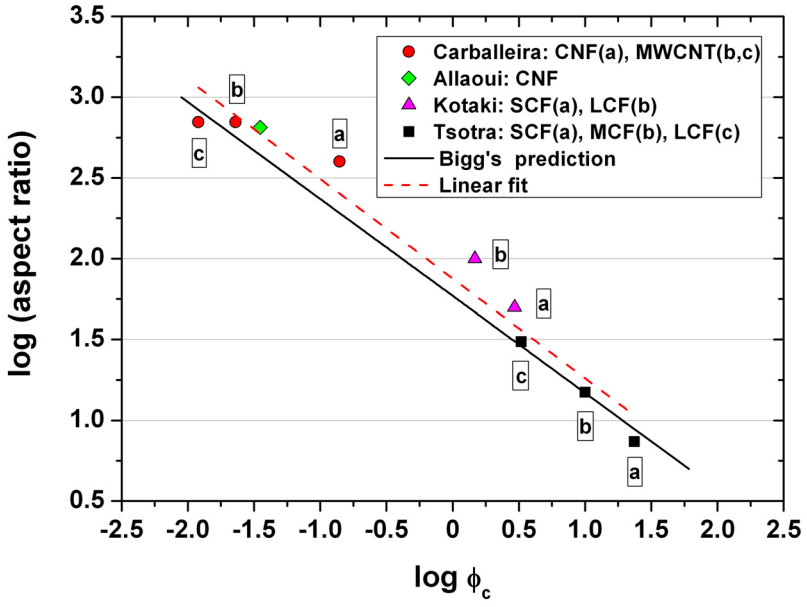

Figure 5.16: Filler aspect ratio versus percolation threshold. Experimental data [30,177,211], predicted values after Bigg [173] and linear fit.

The percolation threshold is highly dependent on the geometry of the fillers and their distribution in the matrix. Well dispersed fibers with high aspect ratio fibers have a high probability of making effective contact with adjacent fibers in order to form the required pathway for electrical conduction, and therefore the percolation threshold is shifted to lower values. The correlation between aspect ratio and percolation threshold has been previously confirmed in the literature [178,179]. Figure 5.16 shows the relationship between aspect ratio and percolation threshold for the CNF composites manufactured in the present research, for MWCNT–EP (torus mill dispersed (b) and calender dispersed (c)) composites produced in a previous study

and for other materials reported in the literature. As it can be seen there is a linear correlation on a log-log plot between aspect ratio and percolation threshold.

From empirical data, Bigg [173] established that the percolation threshold is inversely proportional to the 0.6 power of the aspect ratio for randomly dispersed fibers in a polymer matrix. This finding seems to be in agreement with the experimental data for well dispersed fibers with low aspect ratio and micrometer size [177], however as the filler aspect ratio increases and the size decreases [30,211], Bigg's prediction diverges from the experimental measurements.

In these composites not only the aspect ratio, but also the state of dispersion, play a significant role in the achievement of percolation. This is especially significant if we consider a permeable film (of thickness δ) around the fillers, which refers to an extended range in the polymer matrix that allows hopping of electrons from one conductive filler to another. The thickness of this film, which has been reported to range from a few nanometers to several hundreds of nanometers [180,181], can be influenced by many factors such as the processing of the composite material, the cross-linking of the polymer and the interaction between the polymer and filler.

For traditional conductive microfillers such as carbon fibers, with diameters far larger than δ, the geometrical effect of this thin penetrable shell is negligible. Therefore, the percolation threshold can still be accurately predicted by the classic percolation theory, even though the saturation conductivity of the composites can be much lower than the electrical conductivity of the individual fillers [177]. However, in conductive composites with nanofillers such as carbon nanotubes and nanofibers, which have diameters close to or even smaller than δ, the effect of δ becomes significant [182].

On the other hand, as it can be seen in Figure 5.17, the logarithm of the volume conductivity ($\log\sigma_v$) depends linearly with $p^{-1/3}$ (where p is the weight fraction of CNF), which indicates the possible preponderance of the tunnelling conducting mechanism over electron hopping in the CNF–EP composites [183].

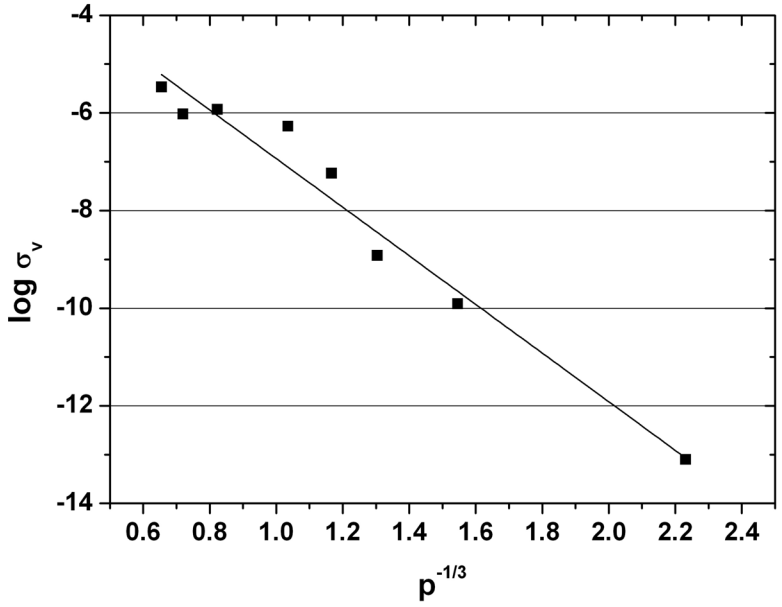

Figure 5.17: Logarithm of the volume conductivity as a function of the inverse of the cubic root of the weight fraction ($p^{-1/3}$) Solid line is a linear fit to the data points.

5.1.5 Conductivity modelling analysis

5.1.5.1 Indirect estimation of the state of dispersion of the CNF–EP composites

Based on the average interparticle distance (IPD) approach [184], Li and co-workers developed a theoretical model to correctly reflect the state of dispersion of carbon nanotubes in a polymer matrix and the effect that the distribution of the nanotubes and their aspect ratio had on the percolation threshold of the composites [185]. In order to do that they introduced two dispersion parameters to reflect two possible state of dispersion of the CNTs in the matrix; entangled agglomerates and well dispersed individual CNTs. Details of the developing of the model can be found on section 7.2.1 of the appendix. Their calculations led them to the following expression for the percolation threshold of these nanocomposites:

$$\phi_c = \frac{\xi\varepsilon\pi}{6} + \frac{(1-\xi)\,27\pi d^2}{4l^2} \qquad \text{Eq. 5.15}$$

Where, l and d are the filler length and diameter respectively; ε is the localized volume content of carbon nanofibers in an agglomerate, and ξ is the volume fraction

that the agglomerated nanofibers occupy in the composite. Mathematically:

$$\varepsilon = \frac{n\phi_{CNF}}{\pi D^3 / 6} \qquad \left(\frac{\phi_{filler}}{\phi_{total}} = \phi < \varepsilon < 1 \right) \qquad \text{Eq. 5.16}$$

$$\xi = \frac{\sum_{i=1}^{\phi_{total}/L^3} n_i \phi_{CNF}}{\phi_{filler}} \qquad (when\ n_i \geq 2)\,(0 < \xi < 1) \qquad \text{Eq. 5.17}$$

With ϕ_{total} the total volume of the composite, ϕ_{filler} the total volume of filler, ϕ_{CNF} the volume of an individual carbon nanofiber, n the number of nanofibers in an agglomerate (i.e., n=1 in the case of a perfect dispersion), D the diameter of the nanofiber agglomerates (assumed spherical) and L the length of a cubic element containing one conductive particle in the center (the total volume of the composite is divided in as many cubic elements as the number of conductive particles).

The higher the value of ε, the tighter the entanglement of the nanofibers in the nanofiber agglomerates. Consequently the volume filled by those agglomerates is smaller. The highest value of ε, (ε=1), corresponds to a state in which the nanofiber agglomerates are so packed together that the polymer matrix is unable to penetrate the localized area of the agglomerate. Conversely, a high value of ξ means that the portion of agglomerated nanofibers is higher indicating that few individually dispersed nanofibers can be found in the composite. The upper limit of ξ, (ξ=1) corresponds to a state of dispersion in which all the nanofibers of the composite are agglomerated. On the other hand, the minimum value of ξ, (ξ=0) corresponds to a state of perfect dispersion in which all the agglomerates have been untangled and the all the nanofibers are present as individual nanofibers in the composite.

To achieve a low percolation threshold the upper limits of the dispersion parameters, ε=1 and ξ=1, are undesirable, whereas the lower limits, ε=ϕ and ξ=0, which represent an ideal dispersion in which no nanofiber agglomerates remain in the composite, are favourable for achieving an ultralow percolation threshold for the nanocomposite conductivity. It should be noted that ε and ξ describe only the "degree of CNF entanglement", which is defined as the "nanoscopic dispersion" in

two different ways: i) ε describes how tight the entanglement in the CNF agglomerates is and ii) ξ represents how many individual nanofibers are entangled in a single agglomerate.

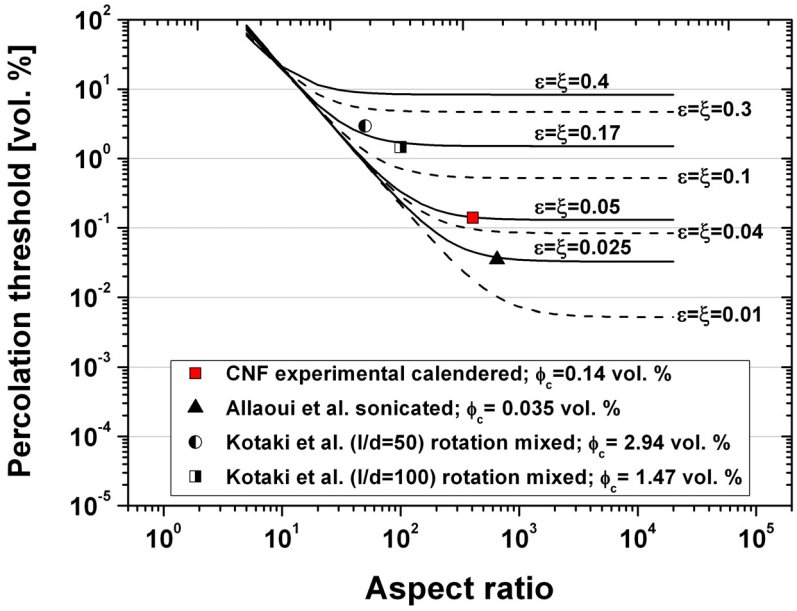

Figure 5.18: Effect of CNF aspect ratio on the percolation threshold of CNF–EP composites with different dispersion states. Experimental results of the present study (*l/d*=406.5) of Allaoui et al. [30] (*l/d*=650) and Kotaki et al. (*l/d*= 50 and 100) [211].

Figure 5.18 depicts the effect of aspect ratio (l/d) on the percolation threshold as predicted by Eq. 5.15 with varying dispersion parameters. Theoretical predictions were compared with the experimental results from our study as well as with data from the literature [30,211]. The dispersion parameters ε and ξ are assumed to be identical to simplify the calculations. As expected, higher values of the dispersion parameters (indicating poorer dispersions) lead to higher values of the percolation threshold. It can also be observed that for a given state of dispersion, the percolation threshold decreases linearly with the aspect ratio for fillers with low aspect ratios. As the aspect ratio of the filler is increased and surpasses a critical value (specific for each state of dispersion) the percolation threshold becomes almost constant and independent of the aspect ratio. The existence of these critical ranges of aspect ratios implies that there are two factors determining the percolation threshold; the

predominant factor changes from the aspect ratio of the fillers to the degree of dispersion with increasing aspect ratio of the CNFs.

This fact is clearly illustrated comparing the results of our study (calendered CNFs, l/d=406.5; ϕ_c=0.14 vol. %) with the ones from Allaoui et al. [30] (sonicated CNFs, l/d=600; ϕ_c=0.035 vol. %). The nanofibers used in both studies had aspect ratios of the same order of magnitude so, the observed difference in the measured percolation thresholds, can be attributed to the superior dispersion (without reduction of aspect ratio) achieved through sonication (ξ=0.025 i.e: 2.5 % of the nanofibers in the sonicated samples remained in agglomerated form compared to ξ=0.05 which indicates that 5 % of the nanofibers remained in clusters in the calendered samples). On the other hand, Kotaki et al. [211] used two different kinds of VGCNF, with aspect ratios of 50 and 100 respectively and dispersed them in epoxy using a planetary mixer. Assuming that the state of dispersion was similar for both mixtures, the difference in the observed percolation thresholds can clearly be attributed to the difference in aspect ratio of the fillers.

5.1.5.2 Tunnelling contact model

As it has been shown in Figure 5.17 (chapter 5.1.4.2), the logarithm of the volume conductivity of the CNF–epoxy samples showed a linear dependence with the inverse of the cubic root of the weight fraction of carbon nanofibers in the epoxy resin, an indication that tunnelling conduction might be responsible of the observed electrical properties of the composites. [183]. Allaoui et al. [30,186] proposed that in MWCNT and CNF epoxy composites a thin film of epoxy is present between the contacts of CNFs. When the thickness of that insulating film is sufficiently small (~1 nm), quantum mechanics laws state that there is a nonzero probability to find an electron on the other side of the film and that the electrons can cross this insulating barrier by ‘‘tunnel effect’’. In order to evaluate the thickness of the epoxy film the composite is modelled as a stacking of layers. The resistance of one layer is that of a network of parallel resistors. Each resistor has the same resistance, noted as $R_{contact}$, and represents the contact between the CNF with an epoxy film in their vicinity along with the segment of CNF between contacts. The thickness of one layer is assumed to

be equal to the distance between contacts, noted as λ. A composite sample of thickness e is a stacking of e/λ layers (the layers resistances are in series). The electrical resistance of the composite is:

$$R = \frac{e}{\lambda}\frac{R_{contact}}{N} \qquad \text{Eq. 5.18}$$

with N the number of contacts (in parallel) in one layer. Considering a composite sample of surface area S, the electrical conductivity is:

$$\sigma_v = \frac{1}{R}\frac{e}{S} = \frac{\lambda}{e}\frac{n\lambda S}{R_{contact}}\frac{e}{S} = \frac{n\lambda^2}{R_{contact}} \qquad \text{Eq. 5.19}$$

where n is the number of contacts per unit volume which in a three-dimensional random fiber network is given by [187]:

$$n = \frac{4\phi_f{}^2}{\pi d^3} \qquad \text{Eq. 5.20}$$

with ϕ_f the volume fraction of fibers and d their diameter. The distance between contacts in a three-dimensional random fiber network is given by [187]:

$$\lambda = \frac{\pi d}{8\phi_f} \qquad \text{Eq. 5.21}$$

Substituting the values of n and λ in Eq. 5.19, we can simply express the conductivity of the composite in the following form:

$$\sigma_v = \frac{\pi}{16d}\frac{1}{R_{contact}} \qquad \text{Eq. 5.22}$$

For this modelling at least two assumptions are made. In each layer, the network is perfectly three-dimensional random (as it was discussed in the previous section (section 5.1.4.2) the critical exponent of the universal scaling law was not far away from a theoretical random system) and all the contacts participate in the conduction (aggregation and dead-end branches are not taken into account; far from the transition, the latter may have a limited effect). All resistors have the same

resistance, that is, the distribution in diameter of the CNF or the variation of epoxy film thickness is not taken into account. The resistance of a contact is the sum of R_{EPfilm}, the resistance of an epoxy film with thickness s and surface area equal to that of a CNF-CNF contact, and of $R_{CNF-CNF}$, the resistance of the nanofiber segment between two contacts. Hence:

$$R_{contact} = R_{CNF-CNF} + R_{EPfilm} \qquad \text{Eq. 5.23}$$

A schematic illustration of the model is given in Figure 5.19: The complexity of the contact surface is not taken in to account and its size is approximated by a square of side equal to the diameter of a CNF.

$$S_{contact} = d^2 \qquad \text{Eq. 5.24}$$

This means that all nanofibers are assumed to cross each other perpendicularly and thickness variation along the nanofiber sections is neglected. As a result:

$$R_{EPfilm} = \rho_{tunnel} \frac{1}{d^2} \qquad \text{Eq. 5.25}$$

where is ρ_{tunnel} the tunnelling resistivity of the epoxy film (in $\Omega \cdot cm^2$). Even if the resistance between two contacts, that is, the resistance of a section of CNF, is negligible compared to that of a contact (the conductivity along a CNF is 10^3 S/cm compared to the bulk conductivity of a network of CNF at 10 vol. % which is three orders of magnitude smaller [30]), the term is not neglected in order to maintain the generality of the model. Thus the resistance of the CNF segment between two contacts is:

$$R_{CNF-CNF} = \frac{1}{\sigma_{CNF}} \frac{\lambda}{\pi d^2/4} = \frac{1}{\sigma_{CNF}} \frac{1}{2d\phi} \qquad \text{Eq. 5.26}$$

The combination of Eq. 5.22 - Eq. 5.26 gives the following mathematical expression for the electrical volume conductivity of the composite:

$$\sigma_v = \frac{\pi}{16d} \frac{1}{\rho_{tunnel} \frac{1}{d^2} + \frac{1}{2d\phi\sigma_{CNF}}} \quad \text{Eq. 5.27}$$

The volume fraction of CNF is given by Eq. 5.28:

$$\phi = 100 \cdot \left(1 + \frac{\rho_{CNF}}{\rho_{epoxy}} \frac{p_{CNF}}{p_{epoxy}} \right)^{-1} \quad \text{Eq. 5.28}$$

with ρ_{CNF} =2 g/cm^3 and ρ_{epoxy} =1.15 g/cm^3 the densities of CNF and epoxy, and p_{CNF} and p_{epoxy} the weight fractions of CNF and epoxy respectively.

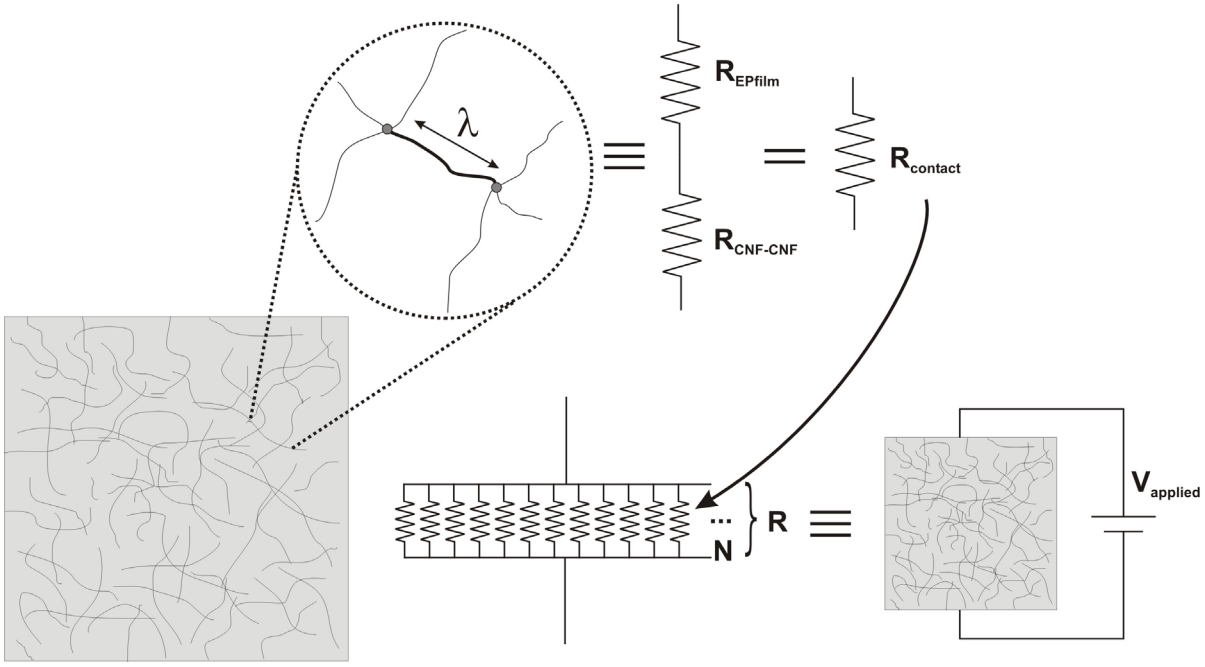

Figure 5.19: Schematic view of the network of parallel resistors, adapted from [186].

An important research effort [188-191] was dedicated to the calculation of the tunnelling resistivity of an insulator film between conducting electrodes based on quantum considerations. For low voltages, the Holm-Kirschstein [189,190] equation (Eq. 5.29) gives the tunnel resistivity in Ω·cm^2:

$$\rho_{tunnel} = \frac{10^{-22}}{2} \frac{A^2}{1 + AB} e^{AB} \quad \text{Eq. 5.29}$$

With $A = 7.32\times10^{5}\left(s-\frac{7.2}{\Phi}\right)$ and $B = 1.265\times10^{-6}\sqrt{\Phi-\frac{10}{s\varepsilon_r}}$. s being the film thickness in Å, Φ the work function of the metal in eV and ε_r the relative permittivity of the film material. Simmons [191] made refined calculations taking into account the true shape of the potential and not the approximate parabolic form assumed by Holm and Kirschstein [189]. He derived the following expression for the tunnelling current density, J, in A·cm:

$$J = \frac{6.2\times10^{10}}{s^2}\left\{\varphi\times\exp\left(-1.025s\varphi^{1/2}\right)-(\varphi+V)\times\exp\left(-1.025s(\varphi+V)^{1/2}\right)\right\} \qquad \text{Eq. 5.30}$$

Where $\varphi = \Phi-\left(\frac{V}{2s}\right)(s_1+s_2)-\left[\frac{5.75}{\varepsilon_r(s_2-s_1)}\right]\ln\left[\frac{s_2(s-s_1)}{s_1(s-s_2)}\right]$ and:

$$s_1 = \frac{6}{\varepsilon_r\Phi};\ s_2 = s\left(1-\frac{46}{3\Phi\varepsilon_r s+20-2V\varepsilon_r s}\right)+\frac{6}{\varepsilon_r\Phi}$$

Again s represents the film thickness in Å and Φ the work function of the metal in eV. The electroaffinity of the film material should be taken into account, but in the case of an insulator (as the epoxy resin), it is assumed that it may be negligible compared to the work function of the carbon nanofiber. The voltage, V, is given by considering one electron carrying the elementary charge $+e$ passing into the film of thickness s, surface area $S_{contact}$ and capacitance C:

$$V = \frac{e}{C} = \frac{e}{\varepsilon_r\varepsilon_0 S/s} \qquad \text{Eq. 5.31}$$

with ε_r and ε_0 =8.85·10^{-12} F/m, the permittivity of the film and vacuum respectively. The tunnelling resistivity is then obtained:

$$\rho_{tunnel} = \frac{V}{J} \qquad \text{Eq. 5.32}$$

The tunnel resistivity was calculated using the relative permittivity of the epoxy ε_r ~2.65 F/m [186], the work function of graphite [192] Φ =4.62 eV and an average

CNF diameter of d =123 nm. We assumed that the film thickness varies with the volume fraction of CNF following a power law dependence; $s = K\phi^{\beta}$. The experimental data were fitted to Eq. 5.27 with K and β as free parameters using the two different models, Holm-Kirschtein's and Simmons', for the tunnelling resistivity.

The experimental data together with the theoretical fits can be seen in Figure 5.20. As it can be appreciated the fitting lines for both models are practically identical and are superimposed. As mentioned before Simmons' model is a refined version of the Holm-Kirschtein's model, where the potential well used to simulate the film between the two conducting electrodes is the hyperbolic form of the image potential instead of the more crude approximation by a symmetric parabola.

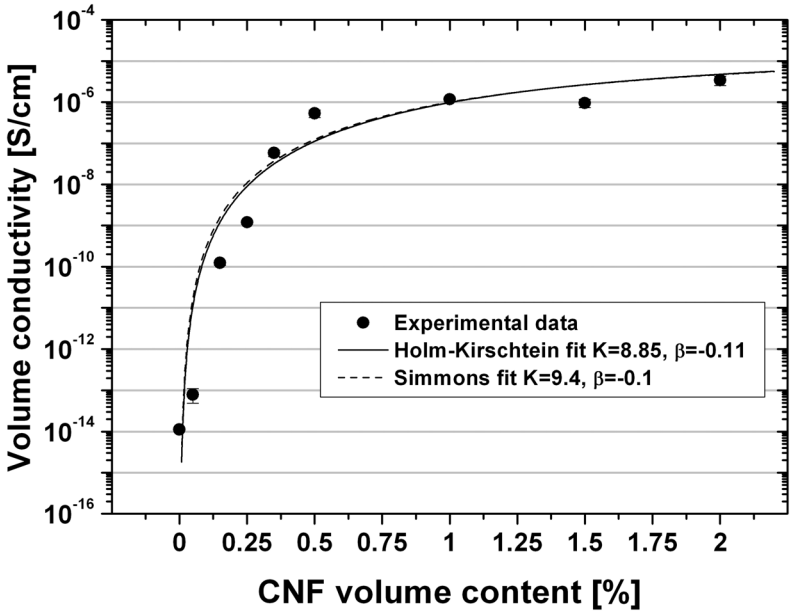

Figure 5.20: Volume electrical conductivity of the CNF–EP composites as a function of CNF volume content [%]. Solid lines are a fit to Eq. 5.27 using the Holm-Kirchstein's and Simmons' models respectively.

The estimation of the epoxy film thickness between the nanofibers using the values of the fitting parameters K and β and the assumed power law dependence of the film thickness with the volume fraction of fillers is plotted on Figure 5.21. The epoxy thickness is in the range of 13 - 24 Å and decreases with the increase of the CNF volume content. The thickness range corresponds to the size of a few epoxy

molecules [193]. As the graph shows, the difference in the estimated thickness varies less than 1.5 Å depending on the model used to calculate it with both models displaying a similar trend.

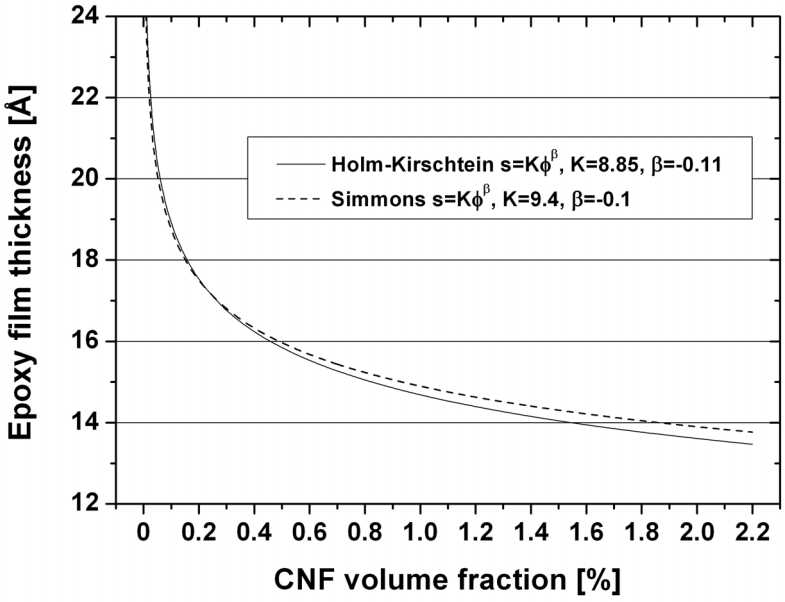

Figure 5.21: Thickness of the epoxy film between carbon nanofibers as a function of volume fraction of CNF.

5.1.6 Fracture surface analysis of the carbon nanofiber–epoxy composites

Visual analysis of the fracture surface of the tested specimens by means of electron microscope can give an insight on the cause and location of failure, the effect of the fillers in the micromechanical properties of the matrix as well as the dispersion state of the fillers in the composite. Figure 5.22 shows fracture surfaces of tensile tests corresponding to the neat epoxy resin (left) and CNF–EP composites with a volume content of nanofibers of 0.5 % and 2 % (center and right) respectively. The images where taken from similar areas of the failed specimens [208]. The general toughening effect of the fibers (see Figure 5.7) reflects itself in rougher structured fracture surfaces of the samples containing CNFs (Figure 5.22, center and right). Crack propagation in unreinforced epoxy resin (a brittle material) is relatively easy. As a result, fracture surfaces exhibit large smooth areas, hyperbolic markings and fracture steps in the direction of crack propagation (Figure 5.22, left). A comparison

of the epoxy surface with the CNF–EP composites underlines the effect of fibrous fillers in the mechanical properties.

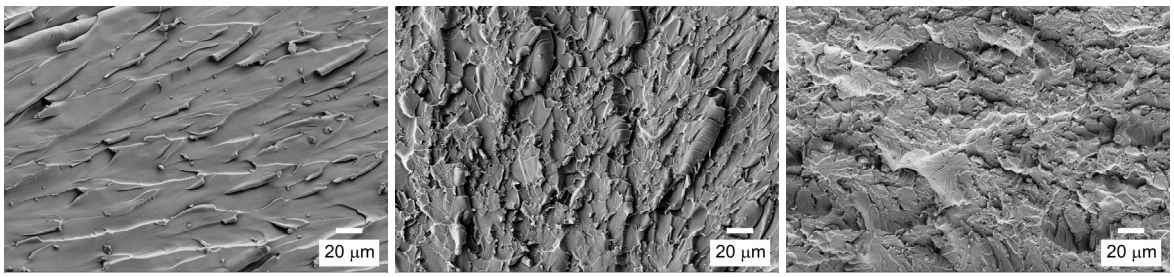

Figure 5.22: Micrographs of the fracture surface of the tensile tests. Neat epoxy resin (left), 0.5 vol. % CNF composite (center) and 2 vol. % CNF composite (right).

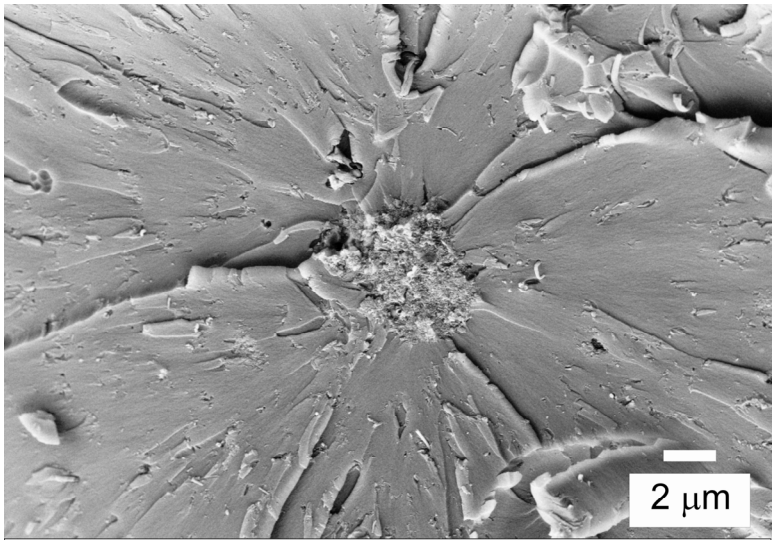

Figure 5.23: Detail of the fracture surface of a tensile specimen of a composite with a volume content of 2 % CNFs.

Toughening mechanisms such as localized inelastic matrix deformation and void nucleation, interfacial debonding and crack deflection at agglomerates are present in these composites since they are not dependent on particle shape [78,79]. These mechanisms could be identified in the SEM observation of the composites. Figure 5.23 shows a detail of the surface of a 2 vol. % CNF–EP specimen. A nanofiber agglomerate of a few micrometers is clearly visible in the middle of the picture. Shear bands can be seen originating from the agglomerate indicating void nucleation caused by plastic deformation of the matrix.

In the case of the CNF reinforced composites most of the toughening mechanisms such as crack deflection, crack pinning, crack blunting and the extension of the plastic deformation zone of the matrix take place at the microscale. Other toughening mechanisms observed, like inelastic matrix deformation with void nucleation and interfacial debonding, take place in the limit of the micro and nanoscale. Nano-reinforcement mechanisms such as fiber pull-out and crack bridging, observed in carbon nanotube reinforced epoxy [88], were not visible in the CNF–EP materials.

A similar microscopic analysis took place for the surfaces of the compact tension specimens. The fracture surface of the neat epoxy resin (Figure 5.24, left) revealed a brittle behaviour characterized by large straight primary cracks with large smooth areas in between. As in the case of the tensile tests surfaces, the nanofiber reinforced composites, exhibited rougher structured fracture surfaces as can be appreciated on Figure 5.24 (center) and Figure 5.24 (right).

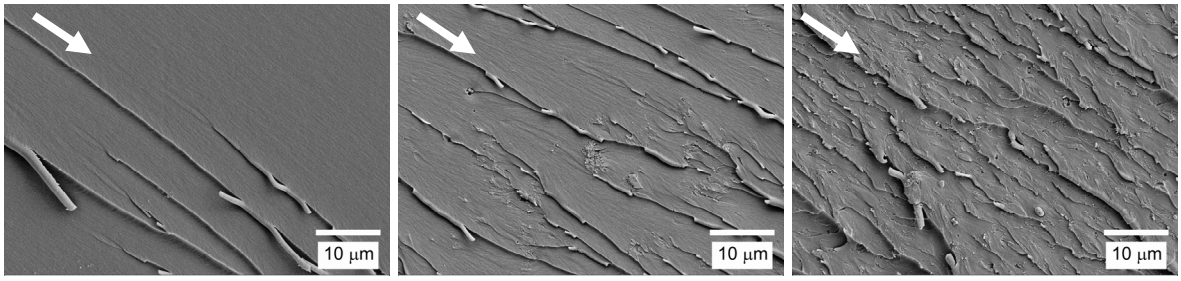

Figure 5.24: Neat epoxy fracture surface (left). Fracture surfaces of nanocomposites containing 0.5 and 2 vol. % CNF (center and right respectively). In all pictures white arrows indicate the direction of crack propagation.

A close up of the fracture surface from the CNF reinforced samples can be seen in Figure 5.25. In general a good dispersion of the fillers in the resin can be observed Nanofiber agglomerates of a few micrometers can be seen on both cases. An increase in fracture surface roughness with nanofiber content is clearly observed. This is an evidence of crack deflection which is associated with an increase in the crack length and the energy absorbed during crack propagation [107,200]. It can be concluded that interfacial debonding and crack deflection at agglomerates are mainly responsible for the observed linear increase of the fracture toughness of the CNF–EP composites with nanofiber content.

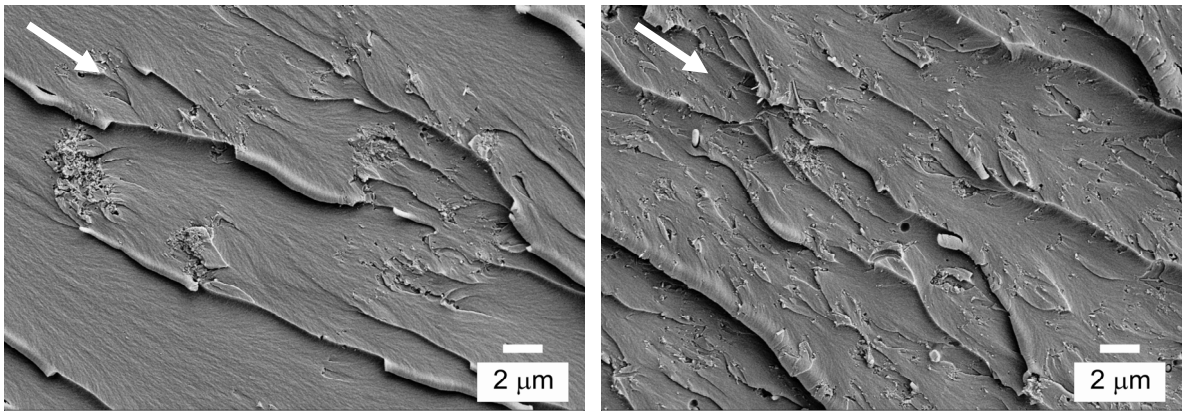

Figure 5.25: Compact tension test fracture surfaces of a 0.5 vol. % (left) and a 2 vol. % (right) CNF–EP composite. White arrows indicate the direction of crack propagation.

5.2 Ceramic nanoparticle–epoxy matrix composites

In the following section, the experimental results of the effect that the incorporation of mechanically dispersed titanium dioxide and aluminium oxide nanoparticles had on the mechanical properties of an epoxy matrix are presented. The nanoparticles were dispersed in the polymer matrix with the use of a laboratory torus mill as described in section 4.1.4.2.

5.2.1 Influence of the dispersion process on the particle size distribution of nanoparticle–EP masterbatches

5.2.1.1 Particle size distribution of the TiO_2–EP masterbatch

As mentioned previously a good dispersion of the nanoparticles in the epoxy resin is crucial to benefit from the nano-reinforcing effects they can provide to the polymer matrix. After incorporating the nanoparticles into the epoxy resin by means of a dissolver the epoxy–nanoparticle mixture was dispersed with a laboratory torus mill for 120 min (see section 4.1.4.2). Samples of the TiO_2–epoxy masterbatch were taken at different times of the TML dispersion process. Those samples were analyzed by means of dynamic light scattering (see chapter 4.2.1.1) to see how the dispersion affected the nanoparticle size distribution in the polymer suspension. Figure 5.26 (left), represents the statistical distribution of the mean measured particle size at three different moments of the dispersion.

The plot for 0 minutes corresponds to the measured particle distribution right after the nanoparticles had been incorporated to the matrix by the slow stirring of a dissolver; the other two plots correspond to particle distribution in the samples taken 10 min and 120 min into the dispersion time. The plot for the undispersed mixture shows that most of the nanoparticles can be found forming agglomerates in the range of 200 nm with some of the aggregates reaching values of up to 350 nm. After just 10 minutes of dispersion we can see a shift and a sharpening of the maximum of the curve to values of around 100 - 150 nm; the larger agglomerates have been broken down into primary particles or smaller agglomerates and their size distribution has become more homogeneous. Finally after 120 minutes of dispersion almost 90 % of the detected agglomerates have sizes between 50 and 100 nm. Figure 5.26 (right) shows the evolution of the mean particle diameter D_{50} with dispersion time. D_{50} indicates that 50 % of the measured particle diameters are under the given value. At the beginning of the process this value is approximately 170 nm decreasing sharply in the first minutes of dispersion and then showing a slower downward tendency until the end of the dispersion process where it reached the value of 80 nm.

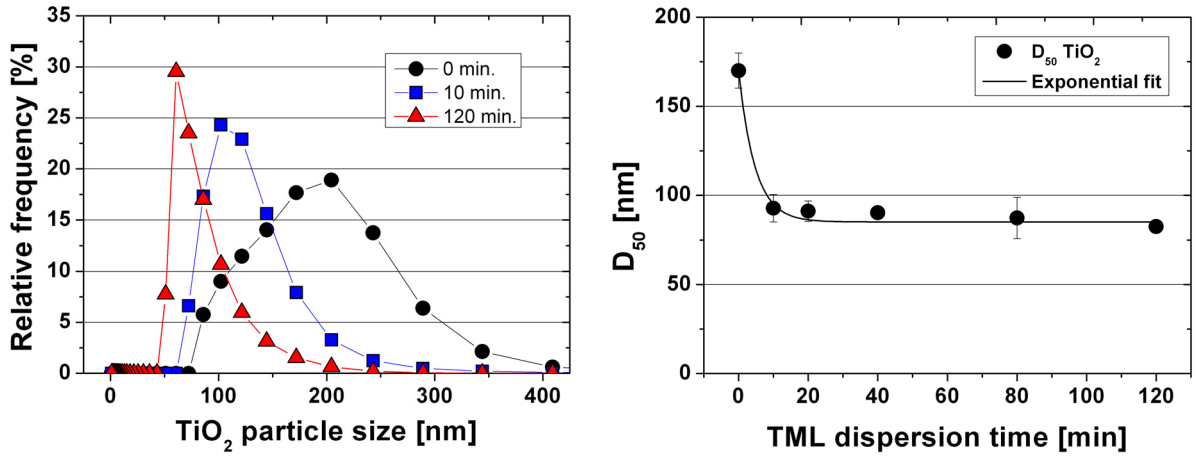

Figure 5.26: Dynamic light scattering measurements of the TiO_2 nanoparticle size distribution at different dispersion times in the torus mill. (Number distribution at three different dispersion times (left), mean particle diameter (D_{50}) evolution with dispersion time (right).

5.2.1.2 Particle size distribution of the Al_2O_3–EP masterbatch

A similar procedure to the one used to manufacture the TiO_2–epoxy nanocomposites analyzed in the previous section (5.1.4.1) was used to create Al_2O_3–epoxy nanocomposites. After adding the nanoparticles to the epoxy resin by means of a dissolver the epoxy–nanoparticle mixture was dispersed with a laboratory torus mill for 120 min. Samples of the Al_2O_3–epoxy masterbatch were taken at different times of the TML dispersion process. Those samples were analyzed by means of dynamic light scattering (see chapter 4.2.1.1) to see how the dispersion affected the nanoparticle size distribution in the polymer suspension. Figure 5.27 (left) represents the statistical distribution of the mean measured particle size at three different stages of the dispersion. The plot for 0 minutes corresponds to the measured particle distribution right after the nanoparticles were incorporated to the matrix by the slow stirring of the dissolver; the other two plots correspond to particle distribution in the samples taken 10 min and 120 min into the dispersion time. The plot for the undispersed mixture shows that most of the Al_2O_3 nanoparticles can be found forming agglomerates in the range of 100 to 150 nm with only a few aggregates exceeding the size of 200 nm. This result differs to the one observed in the TiO_2 masterbatch where the agglomerate sizes were considerably larger and the distribution broader (see Figure 5.26).

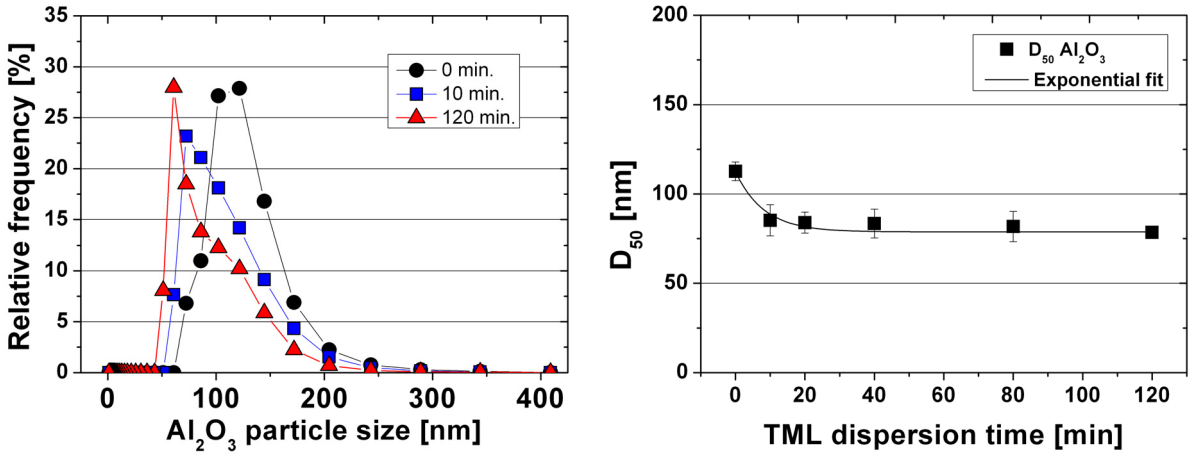

Figure 5.27: Dynamic light scattering measurements of the Al_2O_3 nanoparticle size distribution after different dispersion times in the torus mill. Number distribution at three different dispersion times (left), mean particle diameter (D_{50}) evolution with dispersion time (right).

As in the case of the TiO_2–epoxy masterbatch dispersion, after 10 minutes of dispersion we could see a shift and a sharpening of the maximum of the curve to values of around 70 - 100 nm; the larger agglomerates have been broken down into primary particles or smaller agglomerates and their size distribution has become more homogeneous. Finally after 120 minutes of dispersion almost 90 % of the detected agglomerates have sizes between 50 and 100 nm. Figure 5.27 (right) shows the evolution of the mean particle diameter D_{50} with dispersion time. At the beginning of the process this value was approximately 110 nm decreasing sharply in the first minutes of dispersion and then showing a slower downward tendency until the end of the dispersion process where it reached an approximate value of 80 nm.

It can be concluded that the torus mill was successful in achieving a homogeneous distribution of the ceramic nanoparticles in the epoxy resin. However, this technology alone is not capable of breaking up the smaller nanoparticle clusters present in the mixture. Slightly larger agglomerates are expected to be found in the TiO_2–EP composites (30 % of the measured clusters had sizes above 100 nm in the TiO_2 dispersion compared with 20 % in the Al_2O_3 case).

5.2.2 Microstructure of the nanoparticle–EP composites

The results of the dynamic light scattering measurements (see section 5.2.1) can be contrasted with observations of the cured samples by means of transmission electron microscopy. This technique allows us to directly visualize the dispersion state of the nanoparticles within the resin. TEM pictures of a nanocomposite containing a volume concentration of 4 % TiO_2 nanoparticles are displayed in Figure 5.28.

Nanoparticles can be seen distributed homogeneously but some particle agglomerates are also present. Some of the larger remaining agglomerates have sizes from 100 to 250 nm (Figure 5.28, left). Individual nanoparticles (slightly oblated) possess thicknesses in the range of the suppliers' information (around 14 nm) with lengths of nearly 50 nm. The particles can be seen forming small agglomerates of approximately 80 nm in diameter (Figure 5.28, right). The direct observation of the nanoparticle distribution in the resin corroborated the values obtained through the indirect dynamic light scattering measurements.

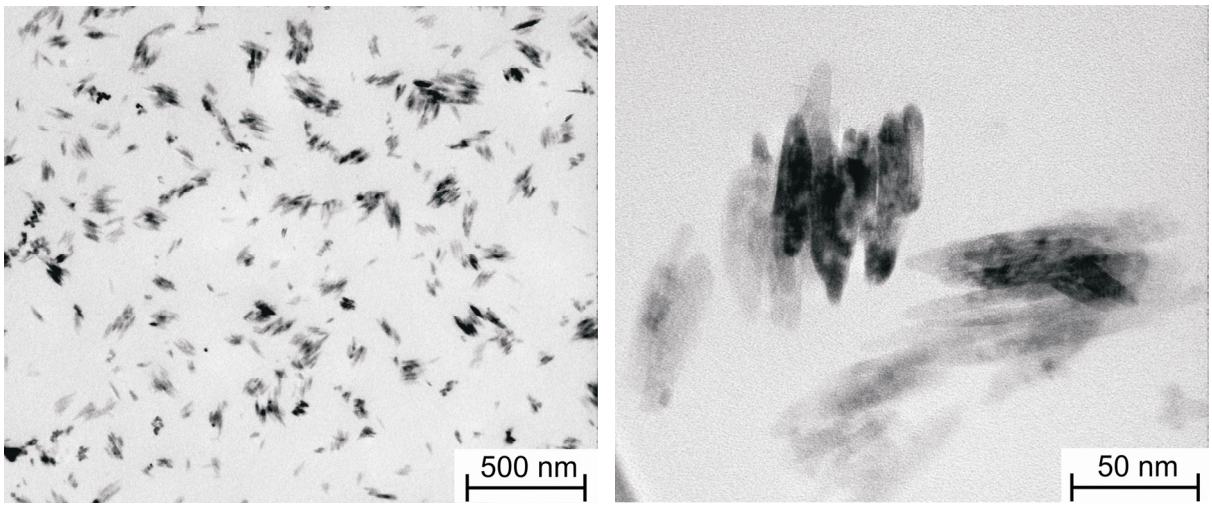

Figure 5.28: TEM micrographs of a nanocomposite containing 4 % volume of TiO_2 nanoparticles. Remaining agglomerates range from 100 to 250 nm (left). Detail showing small particle agglomerates formed by a reduced number of individual nanoparticles (right).

5.2.3 Mechanical properties of the nanoparticle–EP composites

5.2.3.1 Tensile properties of the nanoparticle–EP composites

As it has been discussed in chapter 5.1.3.1.2, the effect of rigid micro-scale fillers on the stress-strain behaviour of polymer matrices has been long known. These fillers commonly tend to increase the rigidity of the material but they may decrease its strength and strain at break. The average values of the Young's modulus, tensile strength and tensile strain at maximum force of the composites at different TiO_2 and Al_2O_3 volume concentrations are depicted in Figure 5.29 and Figure 5.30 respectively. In the modulus case (Figure 5.29, left), we could observe, as expected, a nearly linear increase with nanoparticle content, with an overall improvement of around 48 % and 41 % in modulus for nanocomposites containing 10 vol. % of TiO_2 and Al_2O_3 respectively.

Tensile strength (Figure 5.29, right) shows a slightly different behaviour. Composites with nanoparticle contents below 4 vol. % showed a steady increase in strength, independent of particle type. The total gain in strength, up to this volume concentration, was approximately 14 % in comparison with the neat epoxy. Further addition of fillers did not yield significant improvement in strength. There was even a

slight drop in the case of the TiO_2 fillers. Such a reduction implies that the large number of fillers now dominates and they reduce the matrix deformation by restraining it mechanically. However, this decrease in failure strain was not observed for high contents of Al_2O_3 particles.

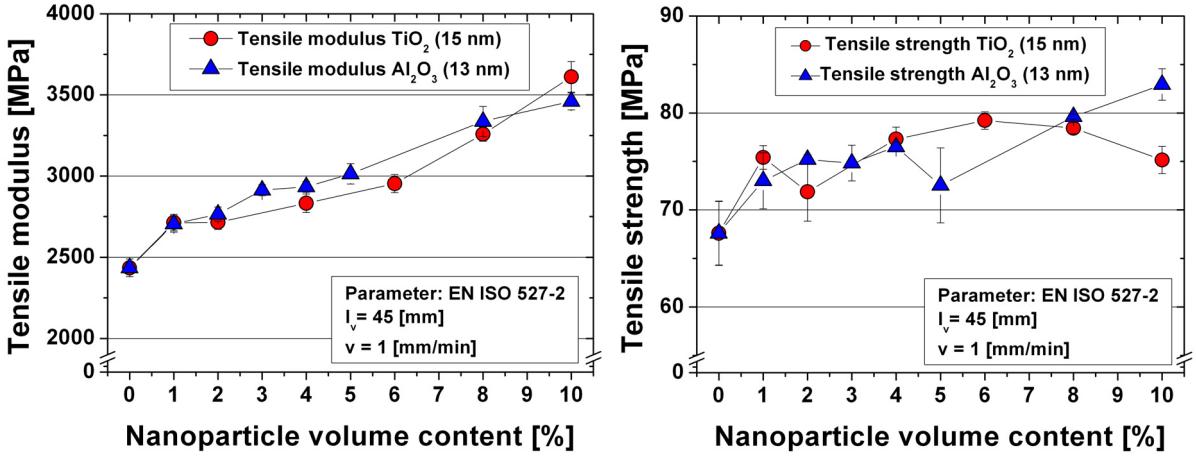

Figure 5.29: Tensile modulus (left) and strength (right) of the nanoparticle reinforced epoxy composites as a function of volume fraction of filler content.

This divergence in behaviour could be related to another important aspect that might play a significant role; the state of dispersion of the nanoparticles. In the case that relatively large agglomerates remain in the matrix, a crack propagating through the composite could encounter local areas of stress concentration and easily induce the initiation of the final failure. This embrittling effect of particle clusters is more likely to occur at high filler contents where the probability of finding agglomerates in the composite is higher. Therefore, the difference between the observed strain at failure of the TiO_2 and Al_2O_3 composites with high loading of fillers might be explained by a slightly better dispersion in the Al_2O_3 case. In both cases the absolute improvements with respect to the epoxy resin are quite similar for both kind of particles (TiO_2, +48 % in modulus, +16 % in strength; Al_2O_3, +41 % gain in modulus and +23 % in strength).

Surprisingly, the failure strain of the composites (Figure 5.30) grew almost linearly with increasing particle content only to decrease slightly when that content reached 10 vol. %. As mentioned previously, this behaviour contradicts the one normally observed when micro-sized fillers are used as reinforcements where the presence of the filler leads to a decrease in strain at break. As Figure 5.30 shows, there was no

significant decrease in the strain at failure in these nanocomposites. In fact, the strain showed a slight linear increase with the nanofiller content.

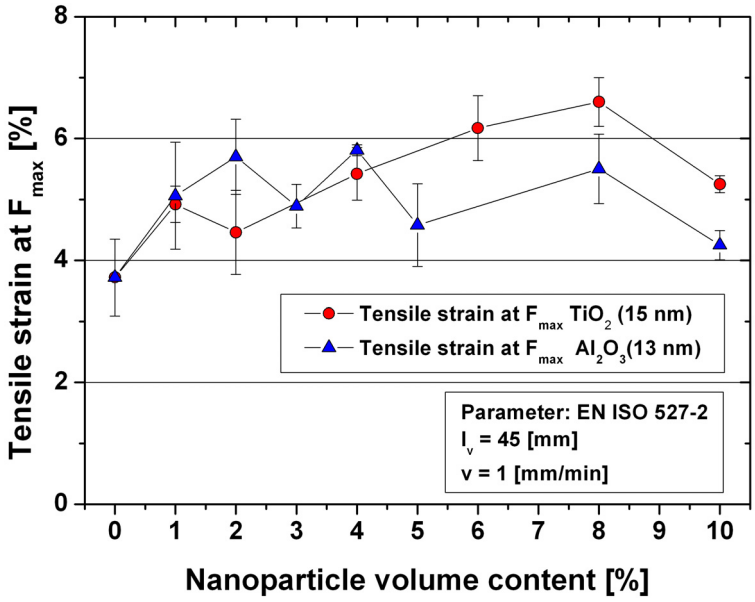

Figure 5.30: Maximum sustained strain by the ceramic nanoparticle reinforced epoxy composites as a function of volume fraction of filler content.

To explain this behaviour, we have to consider some important characteristics of particle reinforced composites. The quality of the interface between matrix and fillers i.e. the static adhesion strength and interfacial stiffness plays a crucial role in the materials' capability of transferring stresses and elastic deformations from the matrix to the fillers [161]. This interaction between filler surface and matrix is especially relevant in the nanocomposite case because well dispersed nanoparticles in a polymer matrix impart a high portion of interface due to their high specific surface.

If the nanoparticle-matrix interaction is weak the particles are unable to carry part of the external load applied to the composite, in fact the mode of yielding for glassy, amorphous polymers changes from cavitational to shear, which leads to a brittle-to-ductile transition [194]. Thus, the material strength cannot be higher than that of the matrix polymer. On the other hand a strong bonding between nanoparticle and matrix that allows a good stress transfer, increases the yield strength of the composites [162]. The increase in the failure strain suggests that the nanoparticles introduce additional mechanisms of energy consumption without hindering the polymer matrix deformation.

Counto [195] proposed a simple model to estimate the elastic modulus of a two phase system with perfect binding between the particles and the matrix. The author originally proposed this model to estimate the elastic properties of concrete. However, considering the brittle nature of concrete, the structure development through a chemical hardening reaction and the internal structure with near spherical fillers (sand, gravel) in a matrix, there are important similarities between concrete and a system of particle reinforced epoxy resin. Counto's model consists of a combination of the lineal (parallel, Voigt) and inverse (series, Reuss) rules of mixtures. The elasticity modulus of the composite according to Counto can be estimated with the following expression:

$$E_c = \left(\frac{1-\sqrt{\phi_f}}{E_m} + \frac{1}{\frac{1-\sqrt{\phi_f}}{\sqrt{\phi_f}} E_m + E_f} \right)^{-1} \qquad \text{Eq. 5.33}$$

Where ϕ_f is the volume fraction of fillers and E_m, E_f are the elasticity modulus of the matrix and the fillers respectively. As it can be seen in Figure 5.31, despite its relative simplicity, Counto's model offers an excellent approximation to the experimental results, especially in the case of the Al_2O_3 reinforced composites, Figure 5.31 (right).

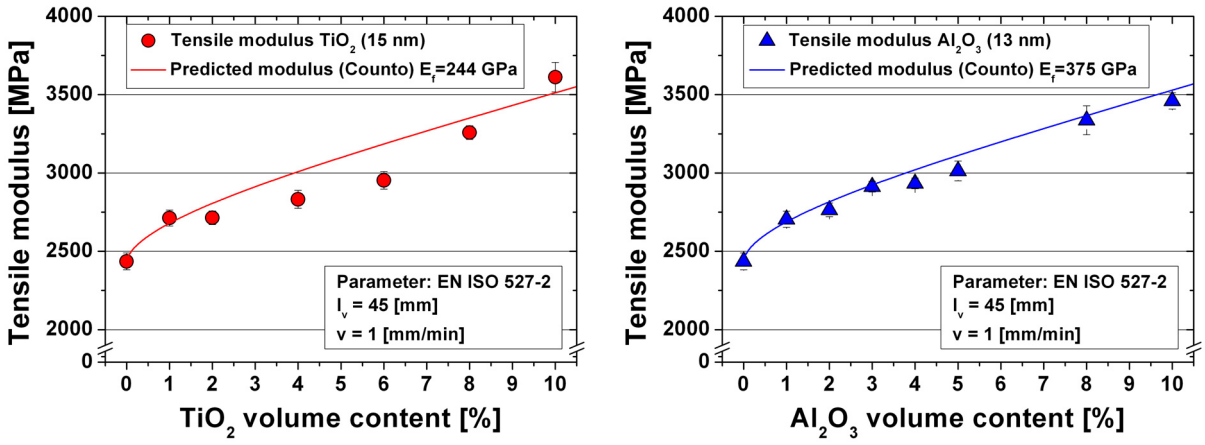

Figure 5.31: Experimental results for the tensile modulus as a function of nanoparticle content for the TiO_2–EP composites (left) and Al_2O_3 composites (right) compared with Counto's model prediction.

5.2.3.2 Fracture toughness of the nanoparticle–EP composites

As mentioned in the introduction of this chapter one of the particularities of nanocomposites is the possibility to simultaneously improve the fracture toughness as well as the stiffness and strength of the neat polymer. The plane strain fracture toughness (K_{IC}) was determined experimentally by using compact tension (CT) samples under tensile loading conditions.

Figure 5.32 shows the load displacement curves for the neat epoxy resin and for materials containing 4 and 10 vol. % TiO_2 nanoparticles respectively. The graph illustrates clearly the increase in applied work necessary to propagate the crack through the material with increasing nanoparticle content. In all cases the samples exhibited the stick-slip behaviour characteristic of unstable brittle crack propagation. Crack instability in these materials may happen for a number of reasons.

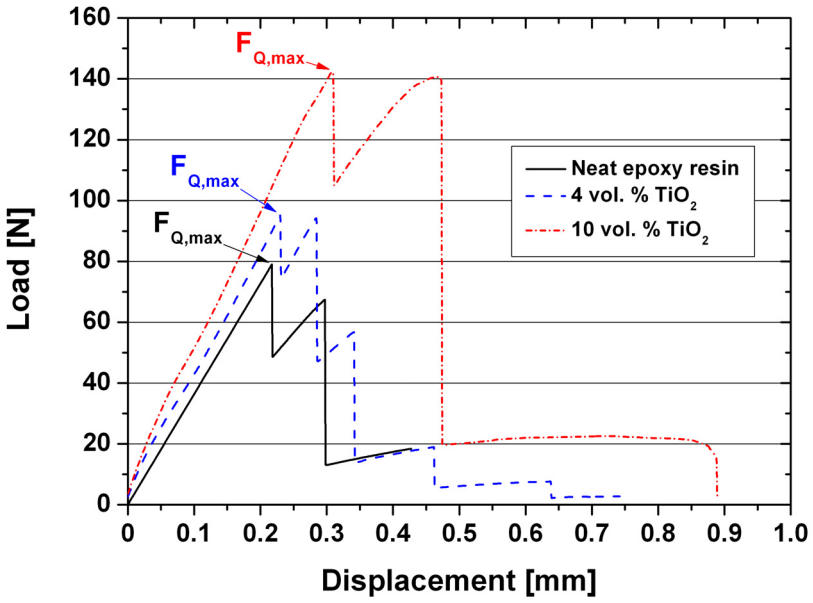

Figure 5.32: Load displacement graphs obtained during testing of CT samples for the neat epoxy resin and samples containing 4 and 10 vol. % of TiO_2 nanoparticles.

Many authors [196-198] have identified the fundamental role of plastic flow and local plastic deformation with the subsequent crack tip blunting. With low load rates, as the one used in our tests (0.1 mm/min), failure tends to occur in the stick-slip manner. In these cases, the yield stress of the material is lower and larger plastic deformation

can take place around the crack tip. This deformation causes the crack to blunt out and take a rounded up appearance [199]. When the crack finally resharpens the release of energy is significantly greater than that required to create a fracture surface and the crack accelerates sometimes up to several hundred of meters per second [200]. Nanoparticles introduce additional energy absorbing mechanisms which act as obstacles for the crack re-sharpening and propagation thus the higher work necessary to fracture the nanocomposites.

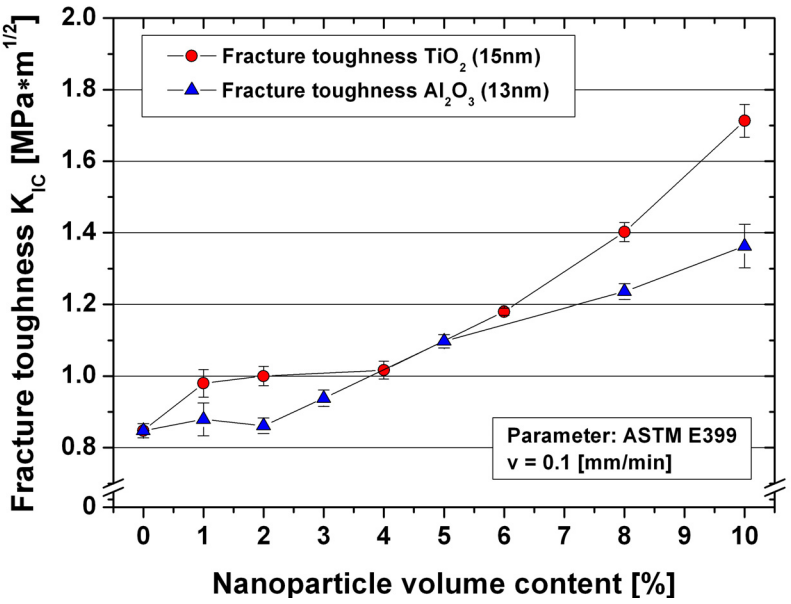

Figure 5.33: Static fracture toughness (K_{IC}) of the ceramic nanoparticle–epoxy composites as a function of filler content.

Figure 5.33 shows that the fracture toughness of epoxy resin nanocomposites increased with rising nanoparticle content. Low filler contents of nanoparticles were already beneficial to the resistance to crack propagation. Up to a concentration of 4 vol. % the results obtained for the TiO_2 and the Al_2O_3 nanoparticles were very similar. For higher filler loadings, the performance of the TiO_2–EP composites was significantly better. Altogether; the gain in toughness of the EP–TiO_2 nanocomposites with 10 vol. % of nanoparticles, covered roughly an increase of 102 %. When alumina nanoparticles were incorporated to the epoxy, the maximum improvement in fracture toughness corresponded to the 10 vol. % Al_2O_3 composites with an increase in toughness of approximately 65 % with respect to the neat epoxy resin.

It has already been established that, with increasing intrinsic toughness of the unfilled polymer matrix, the toughness of the composites increased as well. So, improvements in the energy absorption and resistance to crack growth of the matrix are translated in the response of the composites. Therefore, the normalized toughness ($K_{IC,composite} / K_{IC,matrix}$) diminishes with increasing $K_{IC,matrix}$; this is a well known rule of thumb for all composites [201]. This fact accounts for the differences observed between our results (see Figure 5.34) with $K_{IC,matrix} = 0.84\ MPa \cdot \sqrt{m}$, and the ones reported by Wetzel [107] ($K_{IC,matrix} = 0.63\ MPa \cdot \sqrt{m}$) despite using similar nanoparticles and achieving comparable states of nanoparticle dispersion.

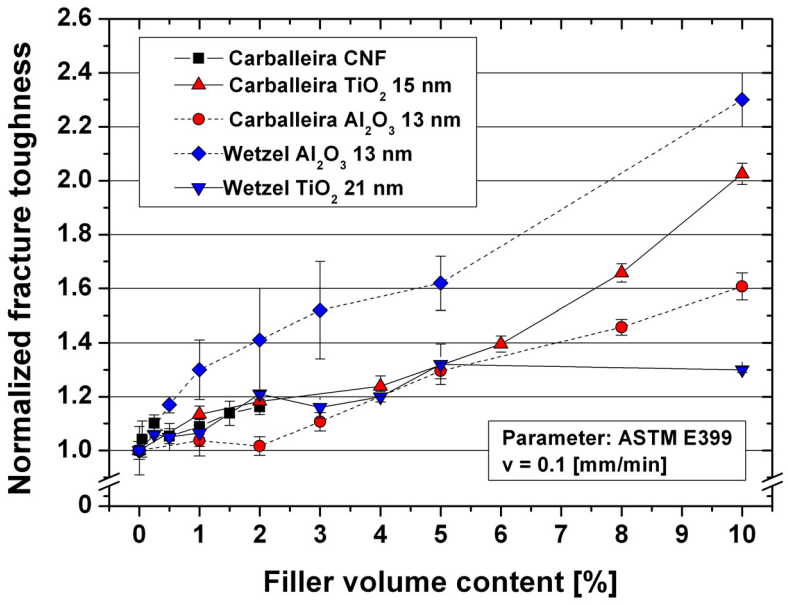

Figure 5.34: Normalized fracture toughness ($K_{IC,composite}$ / $K_{IC,matrix}$) as a function of filler content [vol. %]. Comparative results of the composites containing CNF, TiO_2 and Al_2O_3 with reported results by Wetzel [107] using similar ceramic nanoparticles as fillers in a less tough epoxy matrix.

Equally important is the fact that the strong interfacial interaction between the nanofillers and the polymer during processing may alter the matrix structure which, particularly in the case of semycristalline polymers, can significantly affect the mechanical behaviour of the nanocomposites, independently of the load-bearing capacity of the fillers [202]. The surface functionality of the nanoparticles may also participate in the epoxy curing process which might result in different epoxy network

structures. This could contribute to the different toughening effects that have been described previously. In fact, the possible changes in epoxy network structure are indicated by the increase in glass transition temperatures in both TiO_2–EP and Al_2O_3–EP systems (Figure 5.35, left).

Dynamic mechanical thermal analysis (DMTA) results revealed a shift of the peak in mechanical damping ($\tan\delta$) towards higher temperatures, e.g. from 145 °C (epoxy) to 170 °C in the case of Al_2O_3–EP (10 vol. %). Besides, the storage modulus (E') in the rubbery plateau (T_g +50 °C) rose from 19.8 MPa (epoxy) to 56.6 MPa (10 vol. % Al_2O_3) and indicated that alumina nanoparticles act as physical cross-linkers by increasing the apparent cross-link density [203]. Wetzel et al. [85] reported similar differences in the effect that nano-Al_2O_3 (13 nm) and nano-TiO_2 (300 nm) particles had on the thermal stability of an epoxy matrix. Vassileva [204] also reported similar trends in the alpha relaxation temperature (T_g) of an epoxy/nano-alumina system. This effect was verified by both DMTA and differential scanning calorimetry.

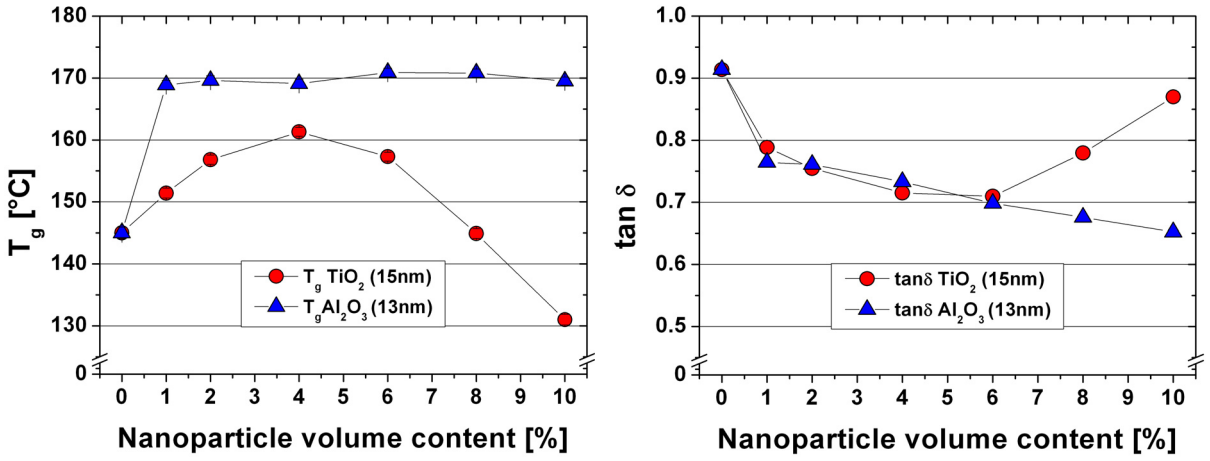

Figure 5.35: Glass transition temperature (T_g) (left) and mechanical damping at T_g (right) as a function of nanoparticle content.

Higher T_g values were also observed in the case of TiO_2 nanocomposites, but here, T_g rose from 145 °C to 160 °C with the incorporation of 4 vol. % of particles and descended to 130 °C for the composites with 10 vol. % of titania particles, the rubbery plateau modulus reached a maximum 41.4 MPa for the TiO_2–EP (4 vol. %) and then descended to a value of 33.9 MPa when the TiO_2 loading was 10 vol. %

(a value higher than the one measured for the neat EP (19.8 MPa). The rise in T_g was stronger in the case of Al_2O_3–EP composites. Because the specific surface of the alumina is larger and the state of dispersion better than that of TiO_2; the shift in T_g may possibly be ascribed to the formation of a larger portion of immobilized polymer chains at the interface between Al_2O_3 and epoxy. The shift is expected to be proportional to the surface area of the filler, so the effect should increase with concentration and with decreasing particle size. Surprisingly, the decrease observed in the glass transition temperature for the TiO_2 composites with volume loadings above 4 %, (which might correspond to the influence of TiO_2 clusters) corresponded with higher toughness improvement of the composites (see Figure 5.33).

Conversely, the mechanical damping of the composites at the glass transition temperature (Figure 5.35, right) decreased with nanofiller content. For volume loadings below 4 % both systems behaved similarly, however higher volume loadings of titania resulted in an increase of $\tan\delta$ at T_g an indication that the different state of dispersion and surface treatment of the TiO_2 nanoparticles might have affected the EP microstructure differently. For now it is not exactly known, how the alumina or titanium dioxide nanoparticles affect the microstructure of the epoxy matrix itself. Further research work on this topic will provide more information, especially about relationships between the local microstructure and the toughness of epoxy nanocomposites.

5.2.3.3 Impact energy of the nanoparticle–EP composites

The experimental results for the notched Charpy impact test of the ceramic nanoparticle epoxy nanocomposites are depicted on Figure 5.36. The nanocomposites showed a strong improvement in the impact behaviour over the whole range of filler loading tested. Like in the fracture toughness case the increase in the impact energy of the TiO_2–EP composites, showed a linear dependence with the filler content. The maximum gain in the impact energy (around a 160 % increase with respect to the neat epoxy) corresponded to the TiO_2–EP nanocomposites with 10 vol. % of nanoparticles. The Al_2O_3 nanocomposites also showed a strong improvement in their impact energy with increasing nanoparticle content. This

reinforcement seemed to be effective already at low filler contents of only 1 vol. % and reached the highest level (+95 % improvement with respect to the neat epoxy) with the incorporation of 2 vol. % Al_2O_3 nanoparticles to the epoxy resin. At higher volume contents, the impact energy stayed almost constant, remaining above the value measured for the neat polymer and without any observed sudden drop.

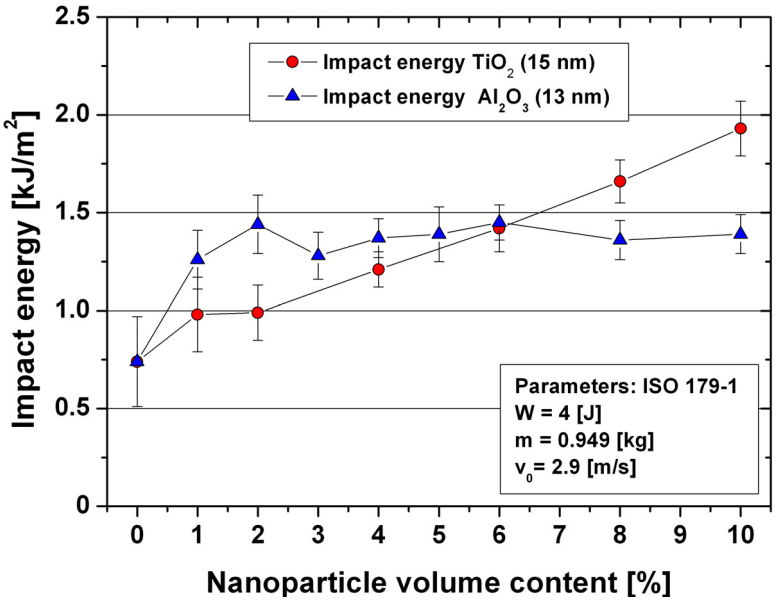

Figure 5.36: Impact energy of the TiO_2–epoxy nanocomposites as a function of filler content.

A similar behaviour has already been reported in the literature [4]. It is possible to interpret the results in terms of stress concentration effects. The intensity of the stress concentration around the well dispersed nanoparticles should be small since there is no weakening of the impact performance by the presence of nanoparticles in the polymer matrix. This means that no embrittling effect is observed under high strain rate and that the fillers (even if some agglomerates still remain in the composite) introduce reinforcing mechanisms that effectively counteract the possible failure initiations created by the presence of those agglomerates.

Besides, considering the effectiveness of the mechanical dispersion process (see section 5.2.1) the size of the unbroken particle clusters which remain in the matrix should be small enough not to induce a brittle and detrimental failure in the way that micro-sized particles would do [205]. Considering again the strong increase in impact energy, it is obvious that the nanoparticles must induce several energy

absorbing mechanisms in the matrix such as crack deflection [78,79,206,207], crack pinning [4,167] and plastic deformation of the matrix [4].

The impact fracture results of the ceramic nanoparticle–EP composites showed a similar trend as the one observed for the fracture toughness (Figure 5.33). Up to volume contests of 4 % alumina and titanium dioxide nanoparticles showed a similar behaviour; with rising filler content the TiO_2 filled epoxy displayed a higher improvement in toughness. These results are quite surprising since the evidence from the dynamic light scattering particle size estimation (chapter 5.2.1) and the microscopic analysis (chapter 5.2.5) suggested that the state of dispersion of the alumina nanoparticles in the epoxy resin was better than for the TiO_2 nanoparticles. As it was also seen in the carbon nanofiber case (chapters 5.1.3.3.1 and 5.1.3.4.1), it seems that the state of filler agglomeration is not a critical factor for the outcome of the high-speed crack propagation K_{IC} and Charpy tests. Another possible explanation for the difference in the mechanical behaviour observed between the TiO_2 and the alumina fillers could be that the polyalcohol surface treatment of the TiO_2 particles results in a better interaction and stress transfer between the nanoparticles and the polymer matrix.

5.2.4 Electrical properties of the nanoparticle–EP composites

As in the case of the CNF–EP composites (see chapter 5.1.4.2), the dependence of the electrical conductivity of the ceramic nanoparticle–EP composites with the volume content of nanofillers was also studied. The obtained results are displayed in Table 5.3.

TiO_2 vol. content [%]	0 (Neat epoxy resin)	1	2	4	6	8	10
Volume conductivity [S/cm]	$1.13 \cdot 10^{-14} \pm 8.55 \cdot 10^{-16}$	$6.16 \cdot 10^{-14} \pm 1.85 \cdot 10^{-15}$	$< 10^{-14}$ S/cm				

Al_2O_3 vol. content [%]	0 (Neat epoxy resin)	1	2	3	5	8	10
Volume conductivity [S/cm]	$1.13 \cdot 10^{-14} \pm 8.55 \cdot 10^{-16}$	$3.32 \cdot 10^{-14} \pm 7.43 \cdot 10^{-15}$	$< 10^{-14}$ S/cm				

Table 5.3: Electrical conductivities of the ceramic nanoparticle–EP composites as a function of nanoparticle content (TiO_2, top; Al_2O_3, bottom) compared with the untreated epoxy resin.

The initial addition of a small quantity of nanoparticles (1 vol. %) resulted in a minute increase of the conductivity of the samples (although it remained in the same order of magnitude as the epoxy resin for both kinds of ceramic nanoparticles). Further incorporation of the non-conductive ceramic particles reduced the conductivity of the composites leaving it out of the detection range of our measuring device (i.e: the samples had conductivities lower than 10^{-14} S/cm which is, approximately, the value of the conductivity of the neat epoxy resin). Therefore, unlike the case of the nanofiber composites, the inclusion of ceramic nanoparticles into the epoxy resin resulted in a reduction of the volume conductivity of the resulting polymer composite.

5.2.5 Fracture surface analysis of the nanoparticle–EP composites

Figure 5.37 shows the fracture surfaces of tensile tests corresponding to the neat epoxy resin (left) and ceramic nanoparticle–EP composites with a volume content of 4 % TiO_2 and Al_2O_3 nanoparticles (center and right) respectively. The images where taken from similar areas of the failed specimens. As in the case of the reinforcing of the epoxy with carbon nanofibers, the toughening effect of the ceramic fillers (see Figure 5.29) reflects itself in rougher structured fracture surfaces (Figure 5.37, center and right).

Crack propagation through the brittle epoxy resin is relatively easy. As a result, fracture surfaces exhibit large smooth areas, hyperbolic markings and fracture steps in the direction of crack propagation (Figure 5.37, left). Ceramic nanoparticle–EP composites showed a rougher surface (Figure 5.37, center and right). The presence of agglomerates was more obvious in the TiO_2 composites, and again these agglomerates were the cause of crack deflection and matrix plastic deformation.

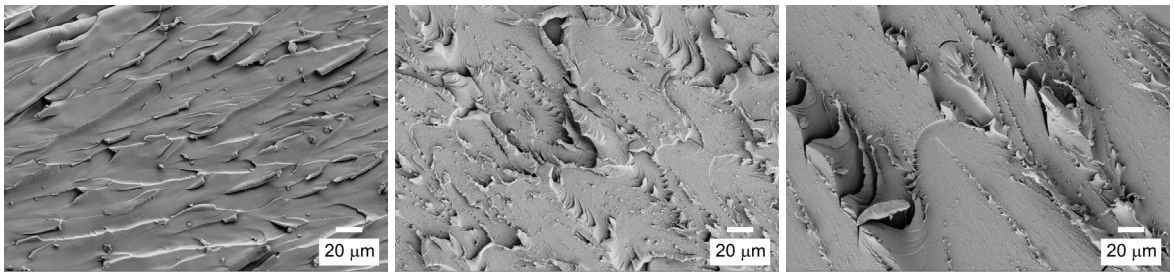

Figure 5.37: Tensile test fracture surfaces. Neat epoxy (left), 4 vol. % TiO_2 composite (center), 4 vol. % Al_2O_3 composite (right).

Observing with more detail the fracture surface of the TiO_2 and Al_2O_3 composites (Figure 5.38) we can see that in the first, the remaining agglomerates are easily recognizable (Figure 5.38, left) whether nanoparticle clusters are not distinct in the latter (Figure 5.38, right). No significant debonding or particle pull-out was observed in either of the composites, an indication of good particle-matrix adhesion. At higher magnifications (not shown here) the fracture surfaces for both kinds of fillers became almost undistinguishable.

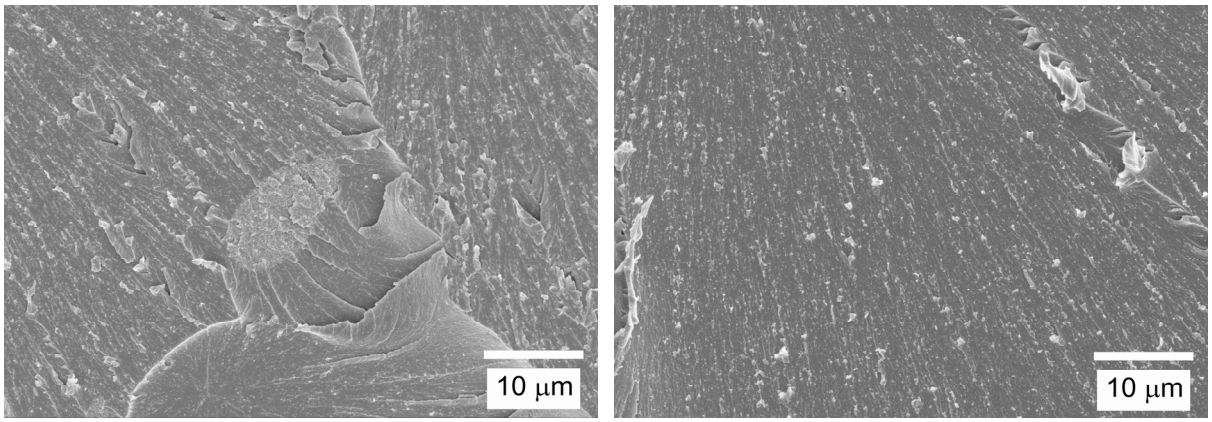

Figure 5.38: Tensile test fracture surfaces details; 4 vol. % TiO_2 composite (left), 4 vol. % Al_2O_3 composite (right).

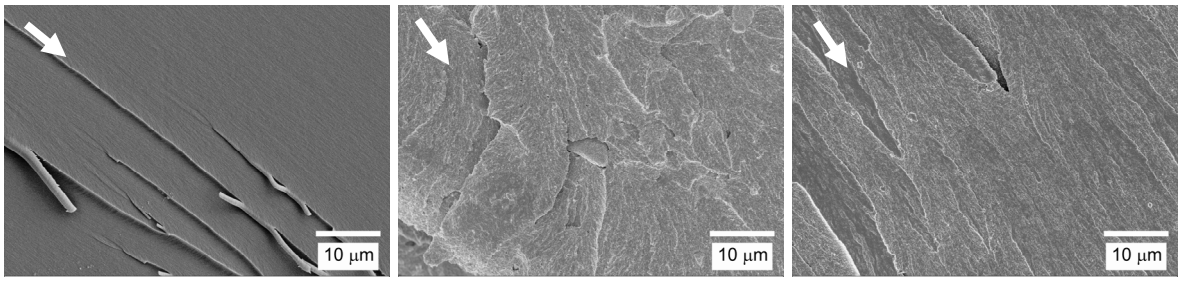

Figure 5.39: Fracture surfaces from fracture toughness CT tests. Neat epoxy resin (left), 10 vol. % TiO_2–EP composite (center) and 10vol. % Al_2O_3–EP composite (right). Arrows on the top left corner indicate the direction of crack propagation.

The fracture surface of the neat epoxy resin resulting from the fracture toughness test (Figure 5.39, left) reveals a brittle behaviour characterized by large smooth areas, big branched marks and straight primary cracks in the direction of crack propagation. The nanoparticle reinforced composites, on the other hand, exhibit rougher structured fracture surfaces as can be appreciated on the center and right

images in Figure 5.39. Nanoparticle agglomerates of a few micrometers can be seen on both cases, especially in the TiO_2 composite (center of the picture), along with individual nanoparticles, visible as small white dots. A certain degree of plastic deformation and debonding was observed around individual nanoparticles and nanoparticle agglomerates in the highly filled ceramic nanoparticle–EP composites.

Some toughening mechanisms like localized inelastic shear matrix deformation and void nucleation have been reported in the literature [73,74]. Interfacial debonding and crack deflection at agglomerates [78,79] are present in these nanocomposites as they do not depend of the filler particle shape. The increase in fracture surface roughness can be used as evidence of crack deflection by the nanoparticles which is associated with an increase in the total crack length and the energy absorbed during the crack propagation [208,209].

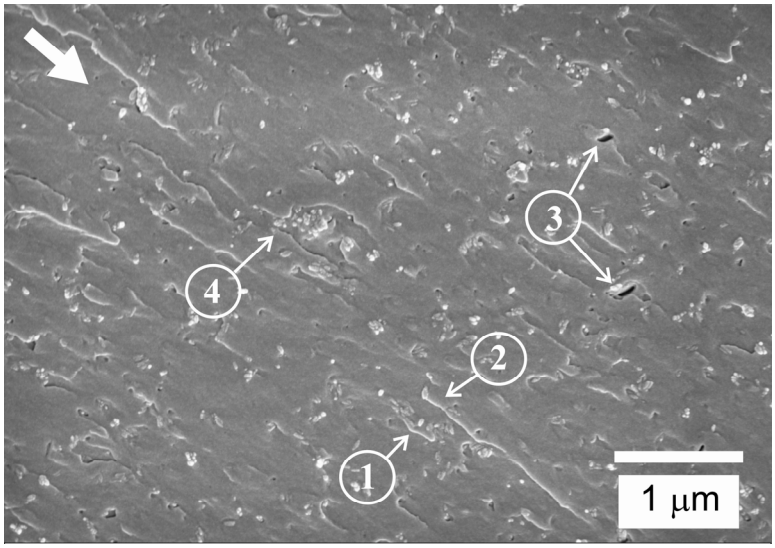

Figure 5.40: 4 vol. % TiO_2–epoxy nanocomposite. Fracture surface from CT test showing a homogeneous dispersion of particles with the presence of some small agglomerates. White arrow on the top left corner shows the direction of crack propagation.

Figure 5.40 shows a close up of the crack surface in a nanocomposite containing 4 volume % of titanium dioxide nanoparticles, some nano and micro reinforcing mechanisms can be observed with more detail. Some of these mechanisms include interparticle crack propagation (item 1), particle crack pinning [75,80,84] (indicated by the small tails behind the particles, these ridges are caused by the reunification of the crack front after passing the obstacle created by the particle filler, the ridge is caused

due to the fact that the crack front moving around each side of the particle never ends in the same plane item 2) and particle pull-out (item 3). The micro reinforcing mechanisms correspond to the presence of the remaining particle agglomerates in the polymer matrix. Item 4 points out the crack deflection at these agglomerates [78,79]. Particle pull-out and plastic void growth around individual nanoparticles are not expected to be major reinforcing mechanisms due to the good quality of the particle-matrix bonding in these composites.

5.3 Ceramic nanoparticle–CNF–epoxy matrix composites

In previous sections, the mechanical and electrical properties of binary composites which consisted of an epoxy matrix reinforced with different kinds of fillers (CNFs, TiO_2 and Al_2O_3 nanoparticles) were discussed. Table 5.4 summarizes the experimental results obtained for the nanocomposites that showed a higher enhancement on their mechanical behaviour compared with the neat epoxy resin. The percentage of improvement with respect to the reference value of the unmodified polymer matrix is displayed in parentheses below the measured value for each property.

	Materials			
	EP	EP–CNFs	EP–TiO_2	EP–Al_2O_3
Filler volume content [%]	0	2	10	10
Tensile modulus [MPa]	2446.9 ± 40.0	3046.6 ± 49.9 **(+25 %)**	3612.3 ± 94.3 **(+47 %)**	3460.8 ± 52.0 **(+41 %)**
Tensile strength [MPa]	67.8 ± 3.3	81.2 ± 0.3 **(+19.8 %)**	79.2 ± 0.9 (1) **(+16 %)**	83.8 ± 0.9 **(+23 %)**
Tensile strain at F_{max} [%]	3.31 ± 0.16	5.54 ± 0.2 **(+67.4 %)**	6.60 ± 0.4 (1) **(+99 %)**	6.21 ± 0.4 **(+87 %)**
Static fracture toughness K_{IC} [MPa·$\sqrt{m}$]	0.85 ± 0.02	0.98 ± 0.02 **(+15.3 %)**	1.71 ± 0.05 **(+103 %)**	1.36 ± 0.06 **(+65 %)**
Impact energy (notched) [kJ·m^2]	0.74 ± 0.23	1.20 ± 0.03 **(+62.2 %)**	1.93 ± 0.14 **(+160 %)**	1.39 ± 0.10 **(+87 %)**
Electrical volume conductivity [S/cm]	$1.13\cdot10^{-14} \pm 8.55\cdot10^{-16}$	$3.41\cdot10^{-6} \pm 8.60\cdot10^{-6}$	---	---
(1) Corresponds to a 6 vol. % loading of TiO_2 nanoparticles				

Table 5.4: Experimental results for the mechanical and electrical properties of composites reinforced with different nanofillers compared with the untreated epoxy resin.

It is easy to see that all the nanofillers increased the modulus and strength without reducing the maximum sustained strength of the polymer matrix. The maximum gain in modulus (+25 %) for the fiber-like fillers (CNFs) was not as high as in the nanoparticle case (+47 % and +41 % for the TiO_2 and Al_2O_3 nanoparticles respectively). Nevertheless, we have to keep in mind that the achieved volume concentration for the fiber-like fillers is considerably lower than for the nanoparticle-filled epoxy resin. In contrast, the increase in tensile strength achieved with the addition of just 2 vol. % CNFs is comparable to the ones obtained with the addition 10 vol. % of nanoparti-cles, despite the presence of CNF agglomerates in the samples. This result confirms the efficiency of nanofibers as reinforcing fillers in polymer matrices thanks to their outstanding tensile strength (230 GPa), large aspect ratio (~400) and specific surface area (~180 m^2/g).

However, the main difference in the mechanical behaviour was measured in the fracture and impact resistance of the composites. The increase in these properties observed with the addition of the ceramic nanoparticles strongly surpassed the one obtained with the addition of nanofibers. This confirmed previous research [129] where it was found that, in general, the impact properties of polymers are more enhanced by small particles with low aspect ratios, while large particles can act as flaws, and high aspect ratio particles are able to induce large stress concentrations near their edges. On the other hand, the carbon nanofillers, thanks to their good conductive properties, were able to increase the conductivity of the insulating polymer matrix by several orders of magnitude. The purpose of the following study was to systematically create ternary nanocomposites by combining different volume concentrations of ceramic nanoparticles and carbon nanofiber as fillers in the epoxy resin (CNF–TiO_2–EP and CNF–Al_2O_3–EP composites). The idea behind this mixture was to combine the good electrical properties that the nanofibers impart to the polymer matrix with the reinforcing effects of the nanoparticles in the fracture toughness and impact resistance of the composites.

The purpose of the following study was to systematically create ternary nanocomposites by combining different volume concentrations of ceramic nanoparticles and carbon nanofiber as fillers in the epoxy resin (CNF–TiO_2–EP and CNF–Al_2O_3–EP composites). The idea behind this mixture was to combine the good

electrical properties that the nanofibers impart to the polymer matrix with the reinforcing effects of the nanoparticles in the fracture toughness and impact resistance of the composites.

In order to optimize the dispersion of the nanofillers the ternary composites were developed by mixing together the TRC dispersed masterbatch used to prepare the CNF–EP composites and the TML-dispersed masterbatches used to manufacture the TiO_2–EP and Al_2O_3–EP composites previously studied. Each of the composite series was obtained through mixing in a dissolver the adequate quantities of the original masterbatches with the addition of epoxy resin. Diluted mixtures were stirred under vacuum to remove entrapped air. Since the maximum filler concentration in the masterbatches corresponded to a 14 vol. % for the ceramic nanoparticles and around 2.5 vol. % for the carbon nanofibers there is a limit in the concentration of each filler that can be reached by combining those masterbatches to create the ternary composites analyzed in the following chapter.

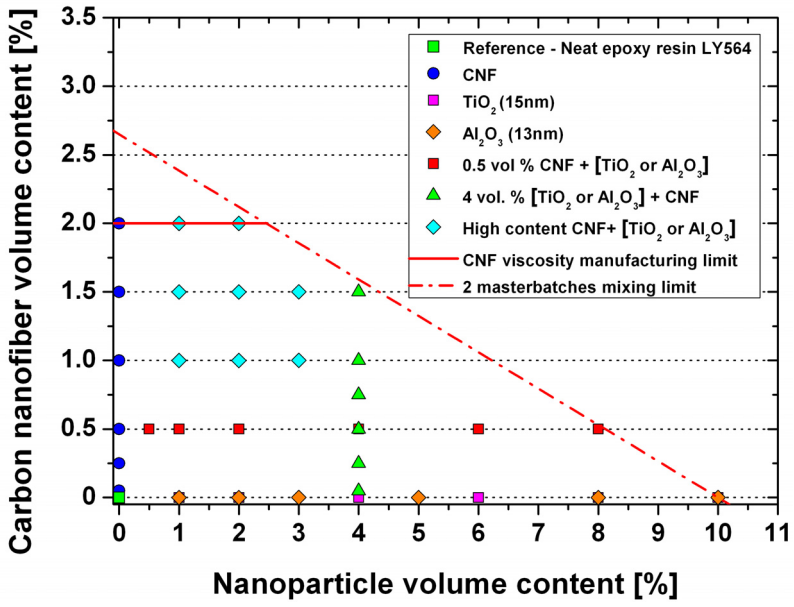

Figure 5.41: Graph showing the volume content of nanofillers (carbon nanofibers and ceramic nanoparticles) present in the different composites manufactured and tested in the present work.

On a first approach, composites containing a volume concentration of 4 % ceramic nanoparticles were modified with the incorporation of an increasing volume

concentration of carbon nanofibers. Similarly different volume concentrations of ceramic nanoparticles were added to composites with a volume concentration of 0.5 vol. % CNFs. This concentration was chosen because it had been proved to be sufficient to significantly improve the mechanical properties of the neat epoxy resin without increasing the viscosity of the masterbatch to levels which difficulted the degassing of the mixture. Finally, a series of composites with high concentrations of nanofibers (1, 1.5 and 2 vol. %) combined with ceramic nanoparticles were manufactured and studied. The following diagram (Figure 5.41) illustrates the nanofiller volume content for all the binary and ternary composites manufactured and studied during the course of this work.

5.3.1 Microstructure of the nanoparticle–CNF–EP composites

The following TEM micrographs (Figure 5.42) belong to a composite containing 4 vol. % TiO_2 and 0.5 vol. % of CNF. On the left and center picture the homogeneous dispersion of the nanoparticles in the resin can be observed. There is no visible reagglomeration of the nanoparticles and the aggregates have similar sizes as the ones observed in the composites containing 4 % volume loading of TiO_2 nanoparticles (see Figure 5.28 on page 86). Unlike the case of the TEM micrographs of the composite containing just the presence of 0.5 vol. % nanofibers (Figure 5.3, page 50), the presence of nanofibers is not visible at first sight in the pictures of the ternary composites.

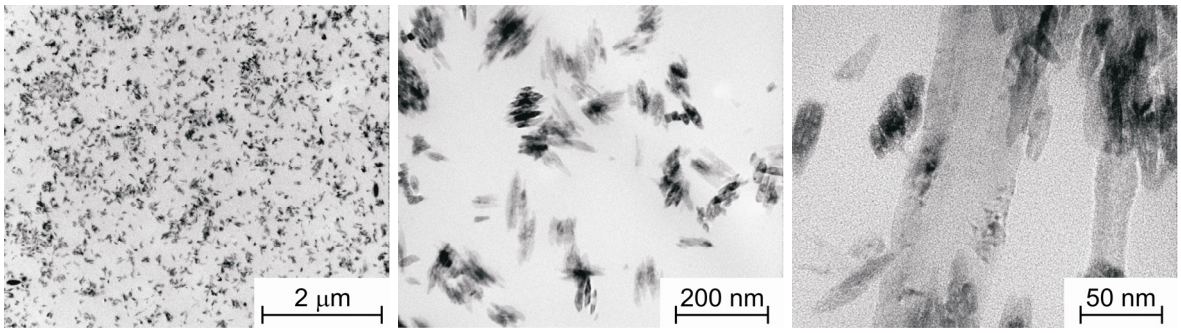

Figure 5.42: TEM micrographs of a 4 vol. % TiO_2 + 0.5 vol. % CNF nanocomposite.

The TEM samples thickness of 50 to 90 nm, combined with the size, high aspect ratio and random orientation of the nanofibers make them difficult to be detected in combination with the TiO_2 nanoparticles. However, in the high magnification picture

on the left of Figure 5.42, an individual nanofiber with a diameter of approximately 70 nm can be seen together with a nanoparticle agglomerate (top right) and single primary nanoparticles. This picture is a good evidence of how the nanoparticles, due to their size and good dispersion in the polymer matrix, might be able to interpenetrate the CNF network and reduce the number of contact points between the fibers which result in the observed electrical properties of the ceramic nanoparticle–CNF–EP composites described in chapter 5.3.3.

5.3.2 Mechanical properties of the nanoparticle–CNF–EP composites

5.3.2.1 Tensile properties of the nanoparticle–CNF–EP composites

The results for the measured tensile modulus and strength of composites containing a constant content of 4 vol. % ceramic nanoparticles, to which different volume loadings of CNFs were added, are plotted as a function of the CNF volume content on Figure 5.43. A minor increase in modulus could be observed with the addition of a low volume loading (0.05 %) of nanofibers to the TiO_2–EP composite. Higher volume contents of nanofibers tended to gradually decrease the modulus of the composites although the combined CNF–TiO_2 composite modulus remained slightly above the one measured for the 4 vol. % TiO_2–EP nanocomposite. Conversely, a slight drop in modulus could be observed with the addition of a low volume loading (0.05 %) of nanofibers to the Al_2O_3–EP composite. Higher volume contents of nanofibers gradually increased the modulus of the composites until it reached a similar level as the one observed for the unaltered Al_2O_3 composite.

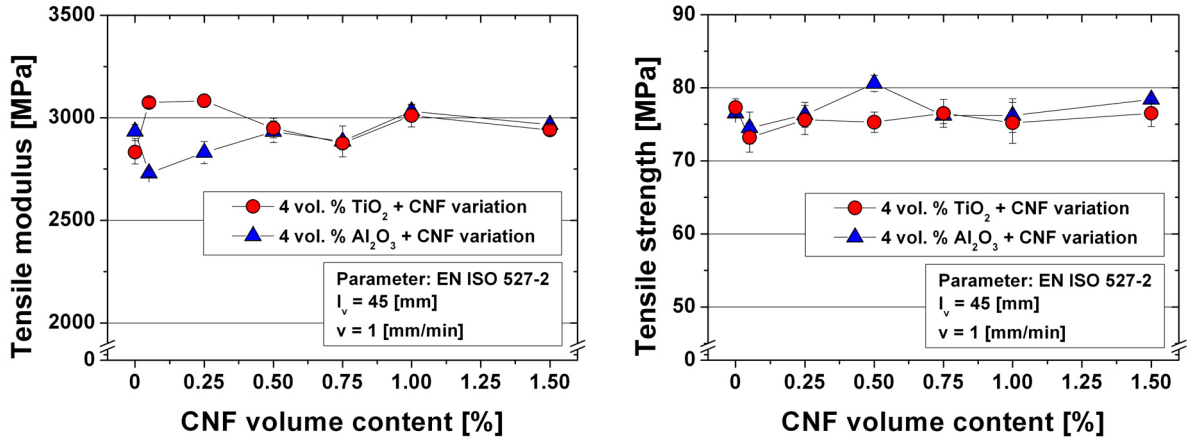

Figure 5.43: Tensile modulus (left) and strength (right) of nanocomposites containing 4 vol. % of ceramic nanoparticles with an increasing volume of CNFs.

Tensile strength of the TiO_2–EP composite declined minimally with the incorporation of a low volume content of nanofibers. Further addition of nanofibers slightly improved the tensile strength of the composite. In any case, the overall gain is almost negligible (less than 5 %). We have to keep in mind that all this improvement discussion takes as reference the composite containing a volume loading of 4 vol. % TiO_2 nanoparticles, the improvements are much higher if we consider the neat epoxy resin as our reference (see chapter 5.1.3.1). As in the case of the addition of CNFs to the TiO_2–EP composites there was no significant variation of the tensile strength of the Al_2O_3–EP composite.

If we consider that the values of the tensile modulus and strength for the composites containing 4 vol. % of ceramic nanoparticles are comparable to the maximum values obtained for the CNF–EP composites (~3000 MPa and 80 MPa for modulus and strength respectively with the addition of 0.5 vol. % CNF) it can be concluded that those values are an upper limit for the reinforcement of the polymer matrix with the addition of nanofibers with the dispersion technology employed in our research.

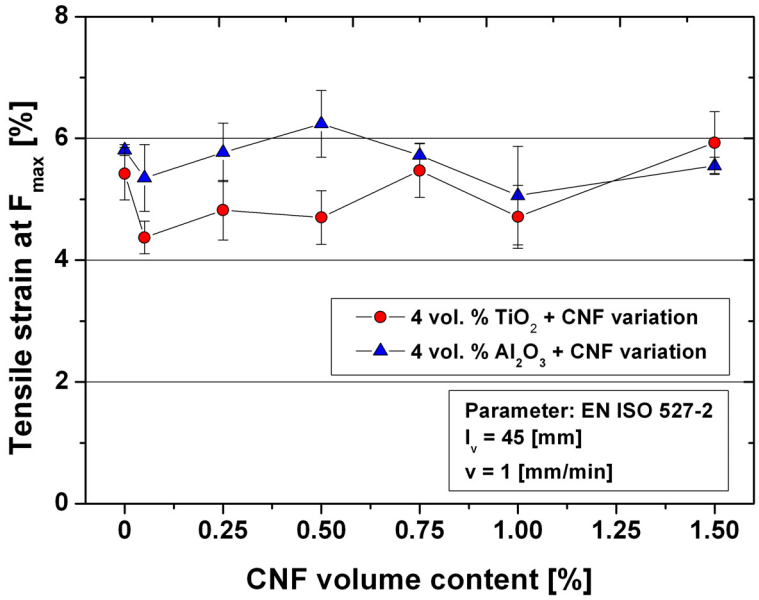

Figure 5.44: Maximum sustained strain by the nanocomposites containing 4 vol. % of ceramic nanoparticles with an increasing volume of CNFs.

The effect that the introduction of the high modulus nanofibers had on the maximum sustained strain of the ceramic nanoparticle epoxy composites can be seen in Figure 5.44. After an initial drop the strain showed an upward tendency with

nanofiber content. However, considering that the standard deviations in the experimental values laid around 10 % it can be concluded that the inclusion of the nanofibers did not affect the strain at break of the ceramic nanoparticle–EP composites.

Figure 5.45 shows the measured tensile modulus and strength of the composites containing a constant volume content of 0.5 vol. % CNF to which different volume fractions of TiO_2 and Al_2O_3 nanoparticles were incorporated. In the case of the CNF–TiO_2–EP composites for volume loadings of nanoparticles below 4 % there was no significant alteration in the tensile modulus. Higher volume loadings of nanoparticles increased the modulus dramatically. On the other hand, both tensile strength and strain at maximum sustained force (Figure 5.45 (right) and Figure 5.46) did not change significantly with the nanoparticle content.

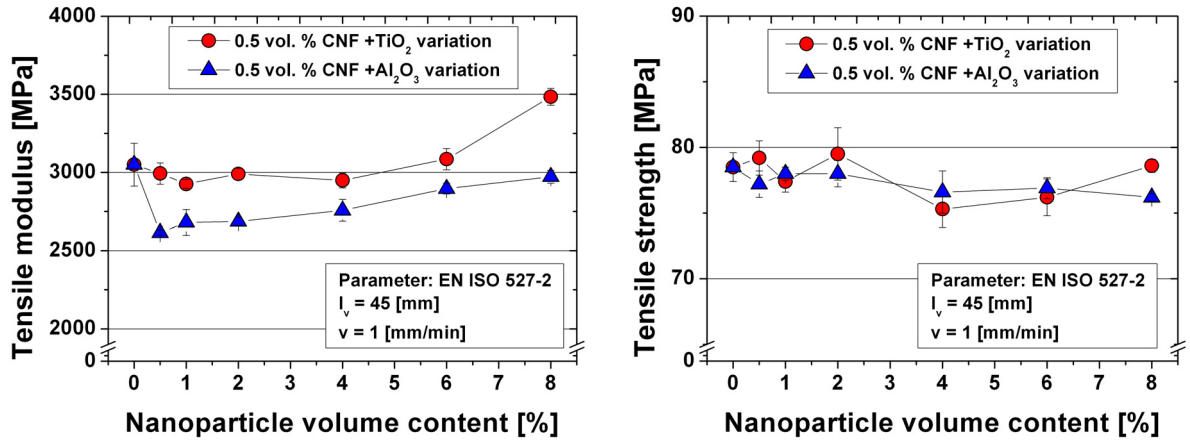

Figure 5.45: Tensile modulus (left) and strength (right) of the nanocomposites containing 0.5 vol. % of CNF with an increasing volume of ceramic nanoparticles.

Alternatively the alumina nanoparticles seemed to affect differently the CNF composite. A volume loading of 0.5 % Al_2O_3 particles decreased the modulus of the 0.5 vol. % CNF composite by 15 %. Further addition of nanoparticle increased the modulus of the composites, however for the maximum value (8 vol. %) of nanoparticles introduced in the CNF composite, the value of the tensile modulus still remained slightly below the one measured for the CNF–EP composite. It can also be seen in the graph (Figure 5.45, right) how the addition of the alumina diminished the tensile strength of the CNF composite, however the reduction is almost negligible,

around 3 % for the 0.5 vol. % CNF + 8 vol. % Al_2O_3 nanocomposite, which is comparable with the measured standard deviations. The strain at the maximum sustained force (Figure 5.46) increased steadily with the alumina nanoparticle content reaching a gain of 30 % ± 5 % with the addition of 8 vol. % of nanoparticles.

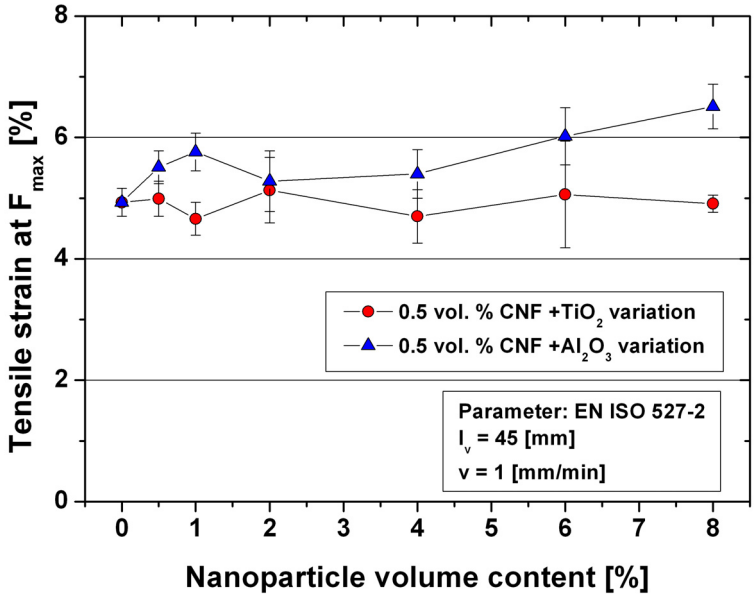

Figure 5.46: Tensile strain at maximum force of the nanocomposites containing 0.5 vol. % of CNF with an increasing volume of ceramic nanoparticles.

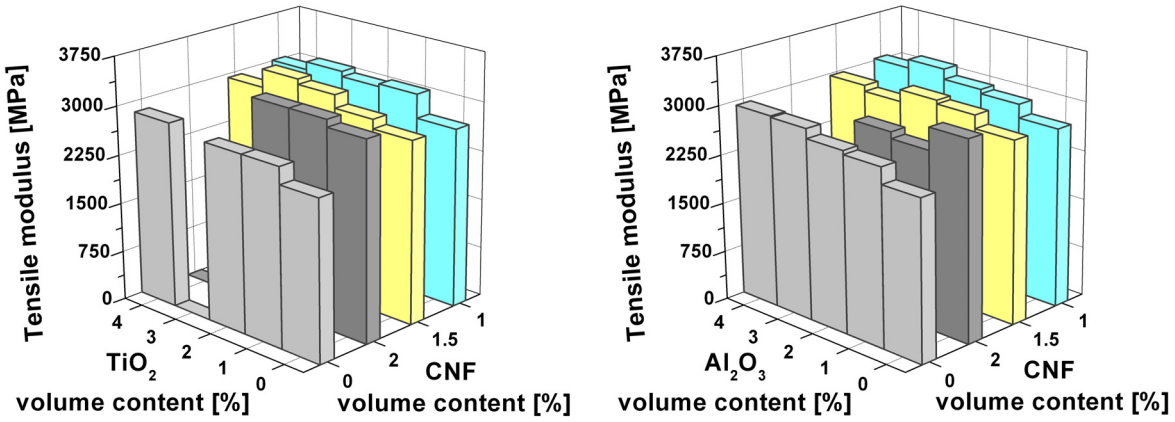

Figure 5.47: Tensile modulus of the nanocomposites containing a high loading of CNFs (1, 1.5 and 2 vol. %) with an increasing volume of ceramic nanoparticles (TiO_2 (left), Al_2O_3 (right)) compared with the nanocomposites containing just ceramic nanoparticles.

Figure 5.47 is a three dimensional plot of the tensile modulus of composites containing a high content of carbon nanofibers (1, 1.5 and 2 vol. %) with the addition of TiO_2 (left) and Al_2O_3 nanoparticles (right). The x and y axes display the nanoparticle and nanofiber volume content respectively. The values of the modulus belonging to the ceramic nanoparticle–EP composites can be seen on the foreground as a reference. The standard deviations of the results (which are not displayed in the diagram) had a mean value of 2.15 % for the modulus and of 2.53 % for the strength and did not exceed 5 % for any material. It can be seen that the inclusion of the nanoparticles in the CNF–EP mixture increased the modulus of the composites; the increment was more pronounced the lower the volume content of CNFs in the initial composite was.

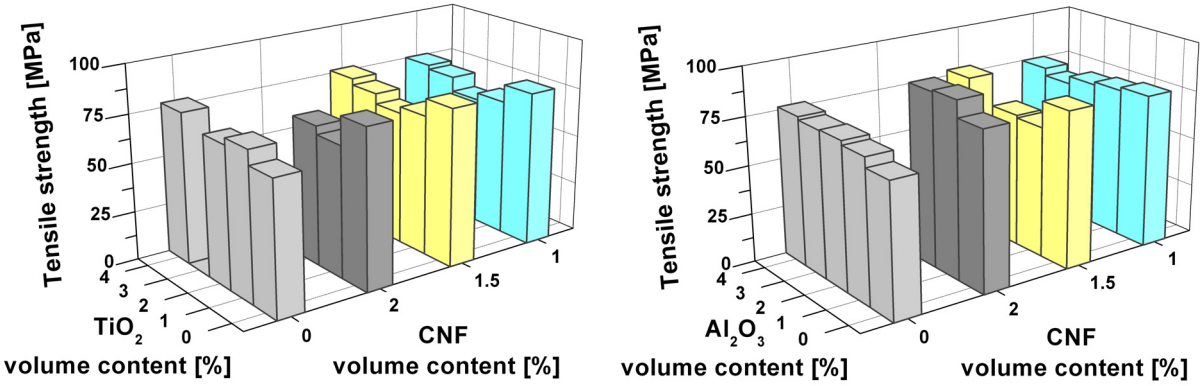

Figure 5.48: Tensile strength of the nanocomposites containing a high loading of CNFs (1, 1.5 and 2 vol. %) with an increasing volume of ceramic nanoparticles (TiO_2 (left), Al_2O_3 (right)) compared with the nanocomposites containing just ceramic nanoparticles.

A similar diagram, illustrating the tensile strength of the ceramic nanoparticle–CNF–EP composites as a function of their CNF and ceramic nanoparticle volume contents, can be seen in Figure 5.48; the mean value of the standard deviations of the experiments was 2.5 %, with none surpassing 5 %. Contrary to the observed results for the modulus, the addition of the ceramic nanoparticles had a negative effect on tensile strength of the composites. The addition of a low volume content of TiO_2 nanoparticles decreased the strength of the CNF composites by 16 % in the 1 vol. % case, by 10 % in the 1.5 vol. % case and by 20 % in the composites with 2 vol. % loading of nanofibers. Further addition of titania nanoparticles proved beneficial to the

strength and the 1 vol. % and 1.5 vol. % strength of the CNF composites with 4 vol. % of additional nanoparticles yielded strength values similar to the ones obtained for the CNF composites without the ceramic nanoparticle modification.

The Al_2O_3–CNF–EP composites behave similarly, with an initial decrease in strength (-2 % and -16 % in the 1 and 1.5 vol. % CNF composites respectively) with the addition of a low quantity of ceramic nanoparticles and a further increase in strength with increasing presence of nanoparticles. A notable exception were the composites containing 2 vol. % of carbon nanofibers where the inclusion of the alumina nanoparticles resulted in a direct increase of 11 % in their strength.

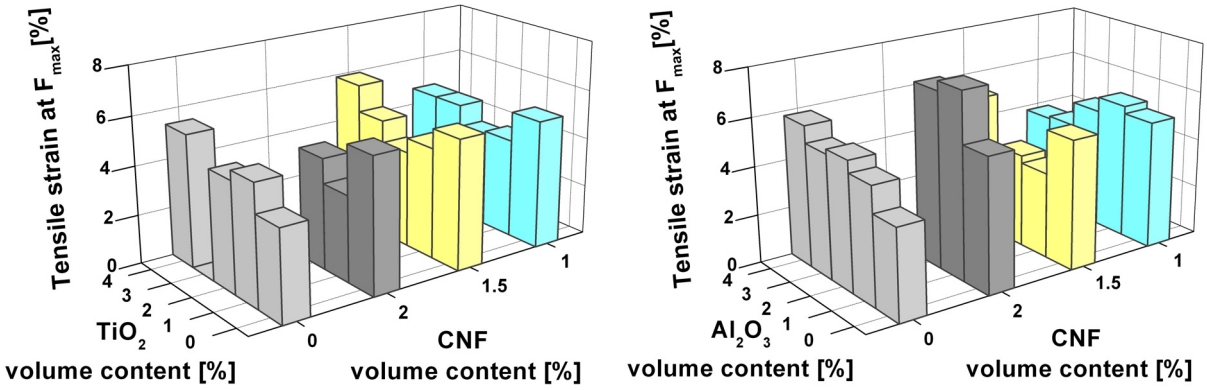

Figure 5.49: Tensile strain at maximum force of the nanocomposites containing a high loading of CNFs (1, 1.5 and 2 vol. %) with an increasing volume of TiO_2 nanoparticles compared with the nanocomposites containing just TiO_2 nanoparticles.

The combination of the TiO_2 nanoparticles with the CNF composites had a similar effect on the tensile strain at the maximum sustained force as they did on the tensile strength as can be seen on Figure 5.49; the mean value of the standard deviations of the results was 8.7 %, slightly larger than in the modulus and strength case. The addition of a low quantity of nanoparticles reduced sharply the maximum sustained strain of the composites, the drop was especially acute (-40 ± 20 % considering the standard deviation) for the nanocomposites containing a volume concentration of 2 % carbon nanofibers.

As in the case of the tensile strength when the quantity of nanoparticles in the composites increased so did the strain at break, for the nanoparticles where the

volume loading of 4 % nanoparticles could be reached the measured values of maximum supported strain where at the same level than for the CNF–EP composites. Once more, there were no major differences observed when alumina instead of titania nanoparticles were built-in the CNF–EP blends. Only the 2 vol. % CNF composites showed a different behaviour and saw their maximum sustained strain improved (+38 %) by the presence of the alumina nanoparticles.

5.3.2.2 Fracture toughness of the nanoparticle–CNF–EP composites

Figure 5.50 shows the fracture toughness of the CNF–EP composites compared with the results from the 4 vol. % ceramic nanoparticle + CNF variation composites. The toughness of the ceramic nanoparticle–epoxy resin nanocomposites experienced a minor increase with the addition of the carbon nanofibers. The total increases were 5 and 10 % for the TiO_2 and Al_2O_3 composites respectively. However, the results obtained by combining the two types of nanofillers are higher than the ones obtained with the carbon nanofiber modified epoxy resin.

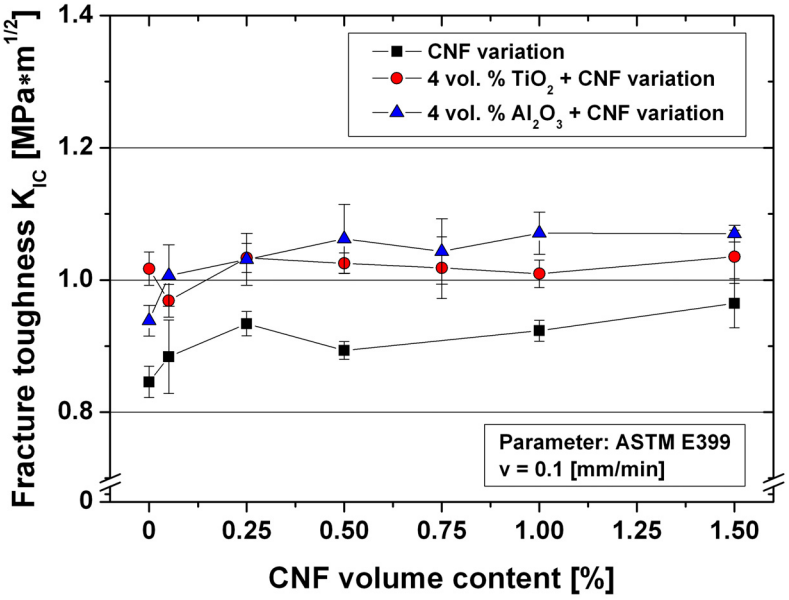

Figure 5.50: Static fracture toughness (K_{IC}) of the nanocomposites containing 4 vol. % ceramic nanoparticles with an increasing volume of CNFs compared with the nanocomposites containing just CNFs.

As can be appreciated in the graph, the toughness of the nanocomposites followed a similar trend, with the CNF–epoxy resin material showing a slightly better

improvement. However, as mentioned in chapter 5.1.3.3.2, the gain in toughness with the addition of carbon nanofibers to the polymer matrix only reached a maximum of 16 % for the 2 vol. % CNF epoxy composites (the standard deviation for the tests had an average value of ±3 %).

It has been shown that the inclusion of carbon nanofibers in a composite containing a certain volume loading of ceramic nanoparticles nanoparticles did not yield any significant increase in the fracture toughness of the resulting ternary composite. Figure 5.51, on the other hand, shows the experimental results of the effect that the addition of TiO_2 and Al_2O_3 nanoparticles had on the fracture toughness of a composite containing 0.5 vol. % of carbon nanofibers. As can be seen on the graph, the only noticeable difference between the behaviour of both series occurred at a low volume content loading of TiO_2 nanoparticles where a small synergistic effect on the fracture toughness seemed to take place. For volume loadings over 2 % the toughness increased linearly with no significant difference in the fracture toughness of the TiO_2–CNF–EP composites and the Al_2O_3–CNF–EP composites. Altogether, the 0.5 vol. % CNF + 8 vol. % nanoparticles composites showed an increment in toughness of 50 % with respect to the 0.5 vol. % CNF composite

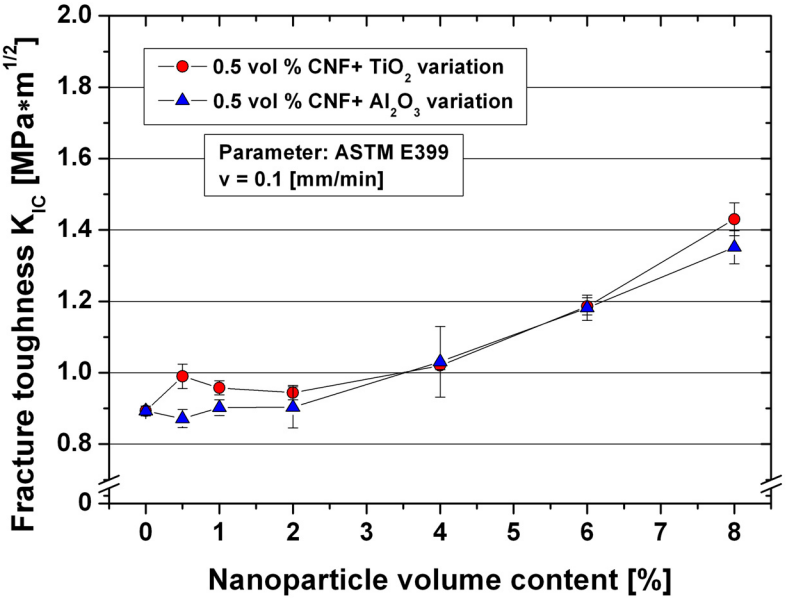

Figure 5.51: Static fracture toughness (K_{IC}) of the epoxy nanocomposites containing 0.5 vol. % of CNF with an increasing volume of ceramic nanoparticles.

If we compare the results with the ones measured for the ceramic nanoparticle–EP composites (Figure 5.33), it can be seen that the values and the trends observed are almost identical, with only a small divergence of less than 10 % at the end. These results are not surprising, since the volume loading of nanoparticles is far larger than the volume loading of nanofibers it is logical to assume that the reinforcing mechanisms in the polymer could be attributed mostly to the higher presence of nanoparticles in the composite and that the nanofibers have only a secondary role in the improvement of the fracture toughness of these composites.

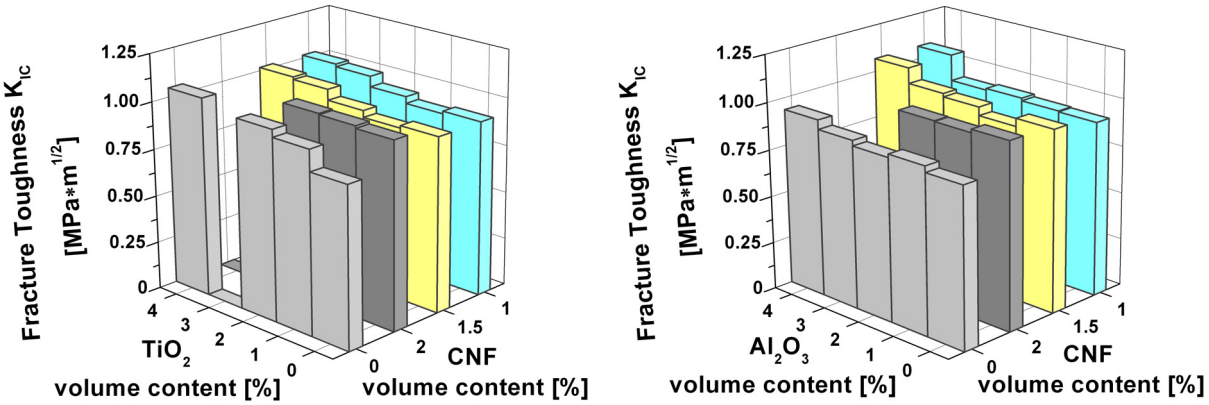

Figure 5.52: Static fracture toughness (K_{IC}) of the nanocomposites containing a high loading of CNFs (1, 1.5 and 2 vol. %) with an increasing volume of ceramic nanoparticles (TiO_2 (left), Al_2O_3 (right)) compared with the nanocomposites containing just ceramic nanoparticles.

The reinforcing effect of the nanoparticles on the fracture toughness of the CNF–composites was also evident at higher volume concentrations (1, 1.5 and 2 %) of nanofibers in the resin (Figure 5.52).The average value of the experimental results' standard deviations was just 2.1 % and did not exceed 5 % in any case . Due to the two masterbatch approach chosen to manufacture the composites, the addition of higher quantities of nanoparticles was possible only in the case of the composites containing 1 and 1.5 vol. % CNF and a higher enhancement of the toughness could be achieved. For the composites containing 2 vol. % CNF the maximum possible addition of nanoparticles was 2 vol. % and, as it can be seen in the graphs, that volume concentration proved not to be sufficient to significantly affect the toughness the CNF–EP composite These results confirm that the nanoparticles are able to

introduce additional energy dissipating mechanisms that contribute to the observed increase in toughness in the CNF composites.

5.3.2.3 Impact energy of the nanoparticle–CNF–EP composites

The following graph (Figure 5.53) shows the impact energy measured through notched Charpy fracture tests. On the diagram, the average values of the impact energy of composites containing CNFs and 4 vol. % ceramic nanoparticles (both TiO_2 and Al_2O_3) together with CNFs are plotted against the nanofiber volume content variation. Both series of nanocomposites followed a similar trend; initially there was a small increase in toughness with the addition of a low volume of nanofibers. After that, further addition of nanofibers left the toughness unchanged; a similar behaviour as the one observed for the fracture toughness results (Figure 5.50). In general, the nanocomposites with the combination of nanoparticles and nanofibers showed a higher resistance to impact (with an approximate increase of 20 %) than the plain CNF–EP composites.

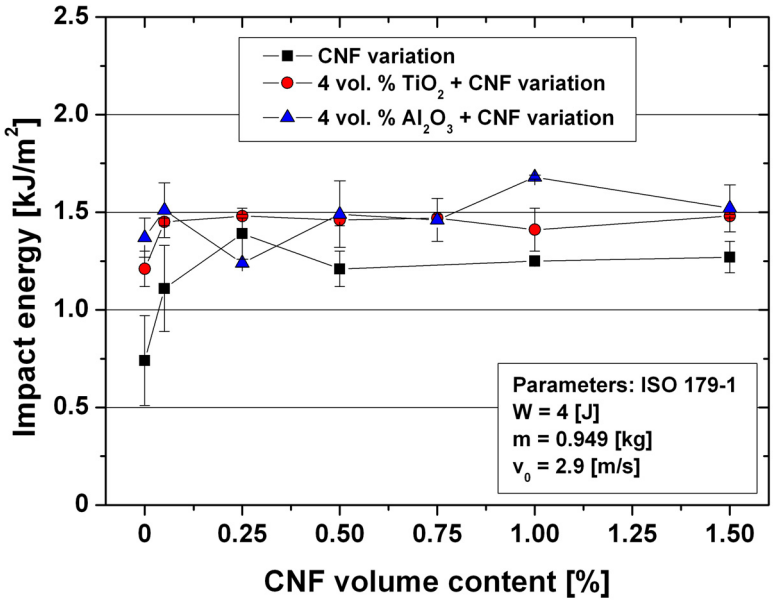

Figure 5.53: Impact energy of the nanocomposites containing 4 vol. % of ceramic nanoparticles with an increasing volume of CNFs compared with the nanocomposites containing just CNFs.

In contrast, adding nanoparticles to the 0.5 vol. % CNF composite increased noticeably the resistance against impact of the CNF composite, as can be seen in

Figure 5.54. As in the case of the static fracture toughness (Figure 5.51, page 111) low volume contents of nanoparticles already proved beneficial. Comparing these results with the ones obtained for the ceramic nanoparticle–EP composites (Figure 5.36 on page 95) it can be seen that differences between the impact resistance of the ceramic nanoparticle composites and the 0.5 vol. % CNF + ceramic nanoparticles was more noticeable at low volume concentrations of nanoparticles when the difference between nanoparticle and nanofiber concentration is not very high. When the volume of nanoparticles increases in the 0.5 vol. % CNF + ceramic nanoparticles composites the differences between the two series of composites diminished. As mentioned before, as the presence of nanoparticles increases in the composite, most of the reinforcing can be attributed to the nanoparticles.

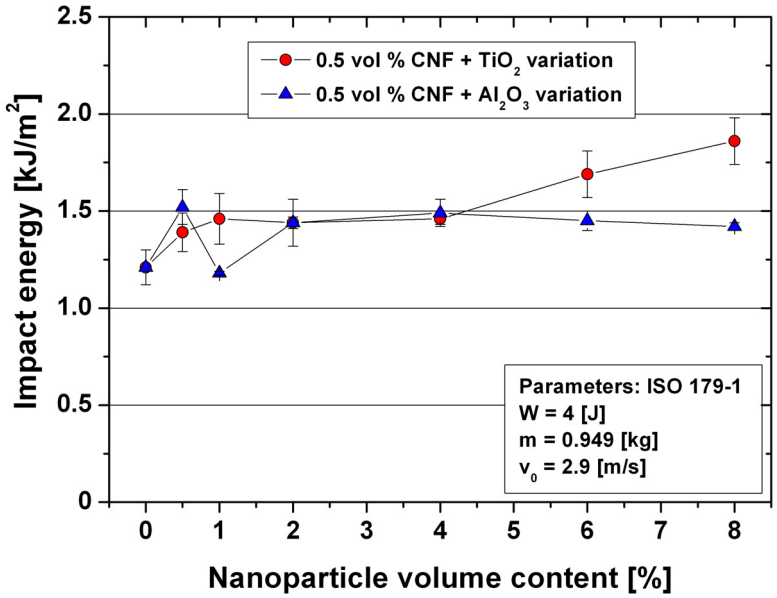

Figure 5.54: Impact energy of the nanocomposites containing 0.5 vol. % of CNF with an increasing volume of ceramic nanoparticles.

Once more, an increase in the impact energy with the addition of nanoparticles to the composites with higher content of carbon nanofibers could be observed (Figure 5.55). In this occasion the mean value of the standard deviations of the measurements was 5.1 % and 6.9 % for the TiO_2–CNF and Al_2O_3–CNF composites respectively. The absolute gain in resistance against impact with respect to the CNF composites was below 20 % in every case. In general, the combination of the fibers and the nanoparticles yielded composites with higher impact energy than the ones where only one of the solid phases was dispersed in the resin. However, there was

no evidence of synergistic effects associated to the combination of both kinds of fillers.

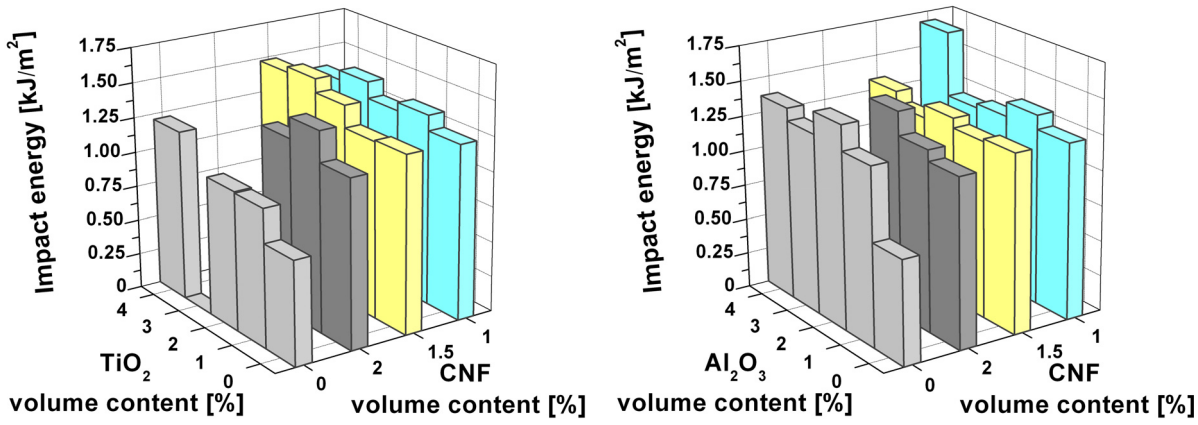

Figure 5.55: Impact energy of the nanocomposites containing a high loading of CNFs (1, 1.5 and 2 vol. %) with an increasing volume of ceramic nanoparticles (TiO_2 (left), Al_2O_3 (right)) compared with nanocomposites containing just ceramic nanoparticles.

Similar improvements in the mechanical properties of micro-reinforced epoxy resin with the addition of nanoparticles have been reported by Wetzel et al. [4,107]. The authors found that adding 13 nm Al_2O_3 particles to an epoxy resin reinforced with $CaSiO_3$ microparticles and glass microspheres respectively, resulted in an improvement of the flexural modulus, strength, fracture toughness and impact energy of the $CaSiO_3$–EP and glass spheres–EP composites. However, the authors also reported a decrease in the maximum sustained strain of those composites; the presence of nanoparticles did not overcome the detrimental effect of the micro-sized fillers but induced a further decrease in the ductility of the matrix.

5.3.3 Electrical properties of the nanoparticle–CNF–EP composites

As mentioned in the introduction and observed experimentally (chapter 5.1.4), one of the features of carbon nanofibers was that, when added to the non-conductive epoxy matrix, they significantly increased the electrical conductivity of the resulting composite. This behaviour is particularly useful in order to avoid electrostatic charging of the insulating matrix which could lead to electrostatic discharges that would make the composite unsuitable to be used as a part of electronic devices.

Figure 5.56 shows the electrical volume conductivity at room temperature of nanocomposites containing 1 and 2 vol. % TiO_2 (Figure 5.56, left) and Al_2O_3 (Figure 5.56, right) nanoparticles with the incorporation of carbon nanofibers, compared with the conductivity of the CNF composites. As it was discussed previously, a steep conductivity increase, indicative of a percolation transition; was evident in the carbon nanofiber series with a very low volume addition of fillers. Percolation theory predicts that there is a critical concentration of conductive fillers at which a conductive path is formed in the composite causing the material to change from capacitor to conductor. As it was discussed extensively in section 5.1.4, the critical concentration or percolation threshold was determined to be 0.14 vol. % for these composites.

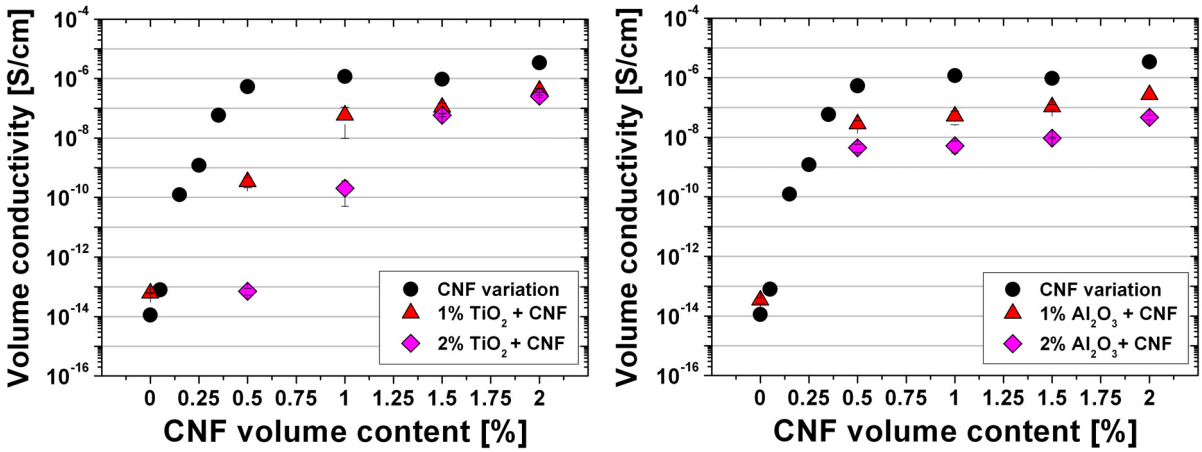

Figure 5.56: Volume conductivity of the CNF–EP composites and composites containing CNFs with the addition of 1 and 2 vol. % TiO_2 (left) and Al_2O_3 (right) as a function of the volume content of carbon nanofibers.

The presence of ceramic nanoparticles in combination with carbon nanofibers seemed to have a shielding effect in the transmission of the electrical current through the composites. The nanocomposites with a combination of TiO_2 and carbon nanofibers (Figure 5.56, left) did not show a significant increase in volume conductivity for low volume concentrations of nanofibers. Nanoparticles resulted in a shift to higher values in the percolation threshold and a decrease of the overall conductivity of the composites. The increase in the volume of nanofibers necessary to achieve percolation was more accused in the TiO_2–CNF composites compared with the Al_2O_3–CNF composites (Figure 5.56, right). The final decrease in conductivity, once percolation was accomplished, was slightly higher in the Al_2O_3–CNF composites. The somewhat higher dielectric strength and resistivity

of the insulating alumina (13.4 $kV \cdot mm^{-1}$, $1 \cdot 10^{14}$ $\Omega \cdot cm$) compared with the TiO_2 (1.24 - 5.56 $kV \cdot mm^{-1}$, $1 \cdot 10^{13}$ $\Omega \cdot cm$) might have played a role in that result, by reducing the intensity of observed electric field within the material and increasing the resistance to charge propagation [210].

The shift in the percolation content of nanofibers could also be measured in the composites which contained a 3 and 4 vol. % loading of nanoparticles (Figure 5.57).Yet again, the increase in the percolation threshold caused by the addition of the alumina nanoparticles to the CNF–EP composite was lower than the one observed with the inclusion of TiO_2 nanoparticles in the CNF nanocomposites. In this occasion, the final decrease in conductivity caused by the addition of 4 vol. % alumina nanoparticles to the 1.5 vol. % CNF composite was a couple of orders of magnitude lower than the TiO_2 case. However, the TiO_2–CNF composites seemed to be close to the percolation transition for that volume concentration of nanofibers which could account for the difference in conductivity observed.

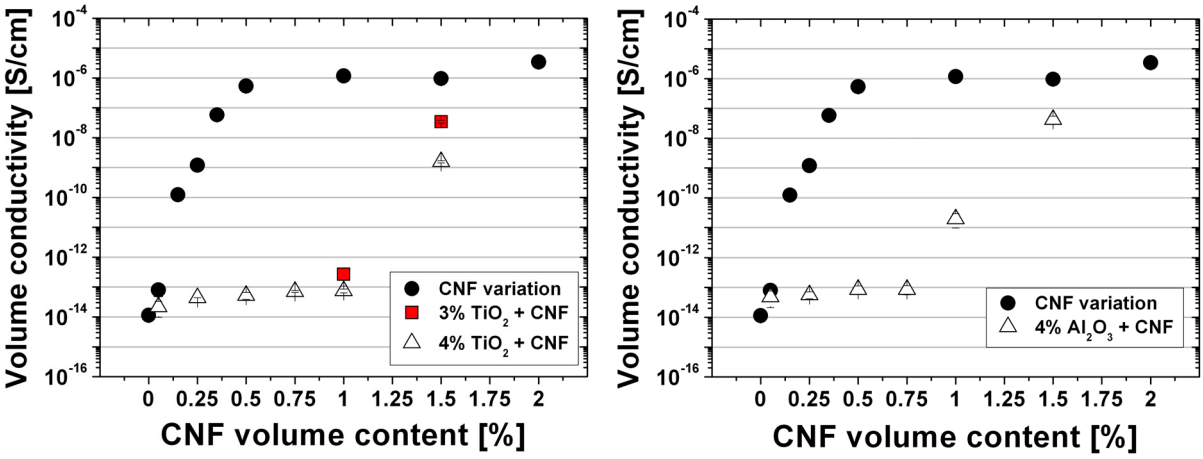

Figure 5.57: Volume conductivity of the CNF–EP composites, composites containing CNFs with the addition of 3 and 4 vol. % TiO_2 (left) and 4 vol. % Al_2O_3 (right) as a function nanofiber volume content.

The shielding effect that the ceramic nanoparticles had on the electrical transmission through the polymer matrix is clearly illustrated in the following diagrams (Figure 5.58). In them, the volume conductivities of the composites containing a constant volume concentration of 0.5, 1, 1.5 and 2 vol. % of CNF with an increasing volume content of TiO_2 (Figure 5.58, left) and Al_2O_3 (Figure 5.58, right) nanoparticles, are plotted against the volume variation of nanoparticles.

It can be seen that as the content of nanofiber increases the drop in conductivity with the addition of nanoparticles decreases. Thanks to their small size and their state of dispersion, nanoparticles seem to be able to interpenetrate the carbon nanofiber network, disrupting it and decreasing the number of effective contacts between the nanofibers. This, in turn, leads to the observed reduction in conductivity and increase in critical percolation volume observed.

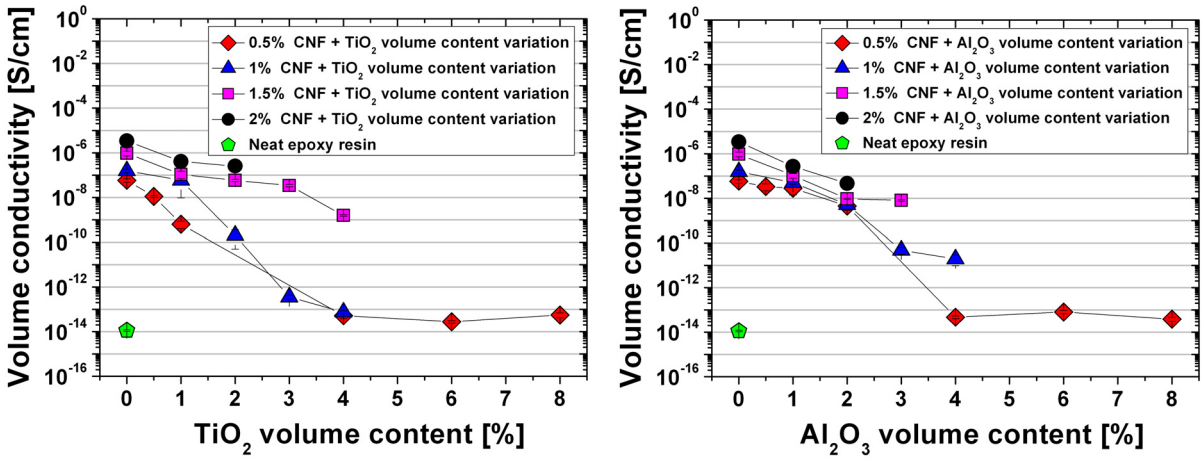

Figure 5.58: Volume conductivity as a function of the volume content of TiO_2 (left) and Al_2O_3 nanoparticles (right) for the composites containing 0.5, 1, 1.5 and 2 vol. % CNF with a volume variation of TiO_2 and Al_2O_3 nanoparticles.

A schematic illustration of the effect that the ceramic nanoparticles have on the conductivity of the carbon nanofibers composites can be seen in Figure 5.59. On the left hand side we have a CNF–EP composite in which contacting fibers have created a conductive path (indicated by the darker colour of the fibers). For the sake of simplicity, only individual fibers and not nanofiber clusters are represented in the picture. As discussed in section 5.1.5.1, nanofiber agglomerates represent only a small volume fraction (5 %) of the total amount of nanofibers and consequently they are not expected to contribute significantly to the total electrical conduction. The contact points between the fibers in the conductive path are highlighted with circles. The picture on the right shows the effect that the presence of well dispersed nanoparticles has on the CNF–EP composite. Individual nanoparticles and small nanoparticle agglomerates are able to occupy the space surrounding the conductive nanofibers (see right TEM picture of Figure 5.42), effectively preventing them

from making adequate contacts thus increasing the percolation threshold and decreasing the overall electrical conductivity as has been observed in the ceramic nanoparticle–CNF–EP composites.

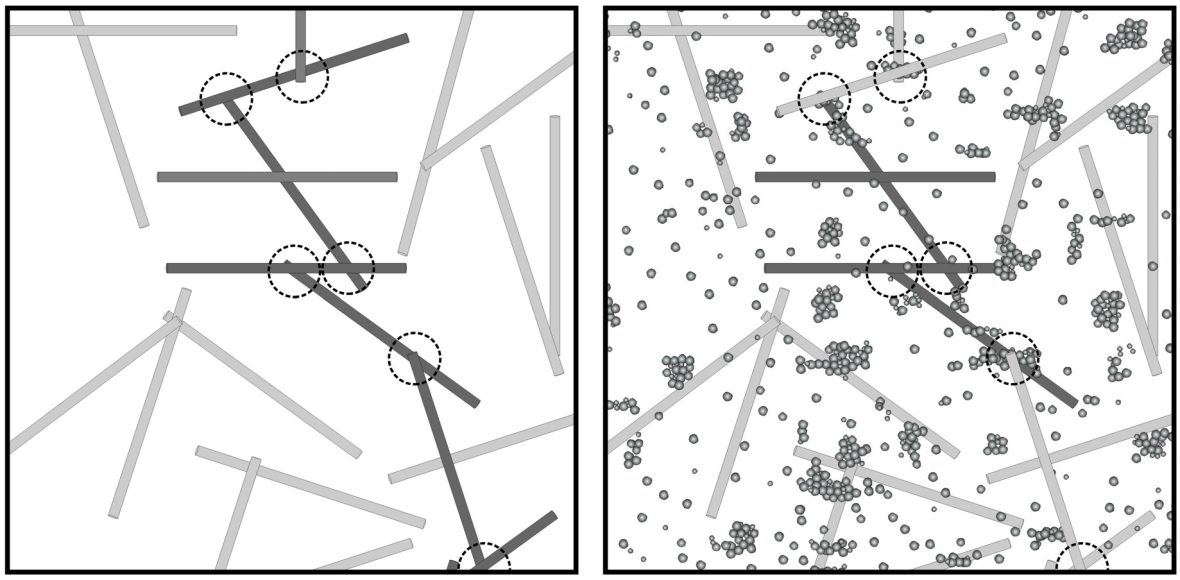

Figure 5.59: Schematic illustration of a CNF–EP composite (left) and a ceramic nanoparticle–CNF–EP composite (right).

The results from the present research seem to contradict the ones reported by Kotaki et al. [211] where they observed a decrease in the percolation threshold (from 2.5 wt. % to 1 wt. %) of VGCNF–epoxy composites with the incorporation of highly exfoliated clay to the mixture. The authors attributed the reduction of percolation to a more effective distribution of VGCNF. The nanofibers where excluded from the volume occupied by the exfoliated clay, as confirmed from their TEM observations. To evaluate the volume excluded by 2.5 wt. % clay, the authors added polyvinylidene fluoride (PVDF) spherical particles of 100 μm in diameter to 1 wt. % VGCNF reinforced PVDF/epoxy composite. It was found that 30 - 40 wt. % of PVDF was required to produce a composite having electrical conductivity similar to that of 1 wt. % VGCNF–epoxy containing 2.5 wt. % clay. This observation revealed that the volume exclusion effect of 2.5 wt. % clay in epoxy is about 30 - 40 vol. %.

Narkis and co-workers [212] reported that adding glass fibers (GFs) to a PP/PA/CB composite dramatically decreased the percolation threshold of the system. The reduction was ascribed to the encapsulation of the GFs by the PA phase and the

selective localization of CB at the PA/PP continuous interface. On the other hand, Chatterjee and co-workers [213], found out that adding 5 wt. % GFs to 5 wt. % VGCNF/PP composites decreased the composite electrical resistivity (i.e: there was an increase in conductivity) from 6184 to 325 Ω·cm. No explanation was given by the authors for this increase in conductivity and the influence of GF addition on the percolation threshold was not discussed.

Finally, Su and Kuramoto [214] synthesized a polyaniline (PANI)/TiO_2 nanocomposite by “in-situ” polymerization of the PANI in the presence of titanium dioxide (anatase) nanoparticles, they found out that the presence of the nanoparticles resulted in a decrease in conductivity and concluded that the reduction in conductivity might be due to particle blockage of conduction path by the TiO_2 nanoparticles embedded in the PANI matrix.

Considering the contradicting reports of the literature and the results presented in this work, it can be concluded that the size of the fillers used in combination with the conductive filler phase plays a fundamental role in the resulting electrical properties of the ternary composites. Micro-sized fillers cause a reduction of the matrix volume available for the nanofibers and consequently the virtual increase in the loading of nanofibers result in the observed reduction of the percolation threshold. Alternatively, well dispersed nano-sized fillers seem to occupy the space between the fibers in the conductive network, obstruct contact formation and reduce the total number of contacts between the fibers, increasing the percolation volume and decreasing the conductivity.

5.3.4 Conductivity modelling analysis

As it was shown in chapter 5.1.4.2, the logarithm of the conductivity of the CNF–EP composites showed a linear dependence with the inverse of the cubic root of the weight fraction of carbon nanofiber which indicated that tunnelling conduction played an important role in the conductivity of those materials. Based on that fact, a couple of models were used to explain the tunnelling conductivity of the CNF–EP composites. The predicted values fitted extraordinarily well the experimental values (see Figure 5.20, page 78).

On the other hand, as the previous chapter (5.3.3) illustrates, the combination of CNF and ceramic nanoparticles as fillers in the epoxy matrix, although beneficial for the mechanical properties, increased the percolation threshold while decreasing the electrical conductivity of the composites. A different model was applied in the case of the ceramic nanoparticle–CNF–EP composites. In these composites, due to the presence of the nanoparticles, the logarithm of the conductivity depends linearly with the cubic root of the nanofiber content only for contents above the percolation threshold, indicating that tunnelling conduction is only relevant for CNF contents above those values. The conductivity of these composites was compared with the predictions of a modified Weber and Kamal fiber contact model (FCM) [59]. According to this model the volume conductivity of a polymer matrix filled with conductive fibers can be calculated with the following expression:

$$\sigma_c = \sigma_m + \frac{4}{\pi}\left(\frac{d_c}{d}\cdot\frac{l}{d}\cdot\cos^2\theta\right)\left(\phi_p\sigma_f\right)\cdot X \qquad \text{Eq. 5.34}$$

Where σ_c, σ_m and σ_f are the conductivities of the composite, the matrix and the fibers respectively; d_c is the diameter of the contact surface between the fibers (assumed circular); d the diameter of the fibers; l the average fiber length and θ the fiber orientation angle. ϕ_p represents the volume fraction of fibers which participate in the conductive network, ϕ_p can be written as:

$$\phi_p = \beta\cdot\phi_f \qquad \text{Eq. 5.35}$$

where β is equal to 0 below the percolation threshold, ($\phi_f < \phi_c$), (i.e: none of the fibers form a complete conductive path), and to 1 at high volume concentrations of fillers ($\phi_f \geq \phi_t$), when the composite is saturated (i.e: all of the fibers take part in the conductive network). For concentrations in the range $\phi_c < \phi_f < \phi_t$, β can be estimated by:

$$\beta = \frac{\phi_f - \phi_c}{\phi_t - \phi_c} \qquad \phi_c < \phi_f < \phi_t \qquad \text{Eq. 5.36}$$

A value of ϕ_t at which β will be equal to 1 is assumed (in our case, a value 10 % above the maximum volume loading of nanofibers achieved experimentally), and the percolation volume fraction ϕ_c is estimated from the experimental data. β is then calculated with Eq. 5.36, and ϕ_p is determined with Eq. 5.35.

The parameter X in Eq. 5.34 depends on the number of contacts between the fibers m, according to Weber and Kamal X and m are related by the following expression:

$$X = 0.59 + 0.15 \cdot m \qquad \text{Eq. 5.37}$$

Where:

$$m = m_{\max}\left(\frac{\phi_p}{\phi_t}\right) \qquad \text{Eq. 5.38}$$

Weber and Kamal assumed that the number of contacts m, varied from 2 to a maximum of 15 [59]. This means that for fiber loadings near the percolation threshold each fiber has a minimum of two contact points with other fibers, while at the saturated filler fraction the number of contacts reaches a maximum of 15. In our case we assumed that the maximum number of contacts is given by the following expression [187]:

$$m_{\max} = \frac{4\phi_f{}^2}{\pi d^3} \qquad \text{Eq. 5.39}$$

Which is the number contact of fibers in a three dimensional random fiber network. A more detailed review of the fiber contact model can be found in the appendix.

Therefore, in order to calculate the conductivity of composite with Eq. 5.34, several parameters must be known $\cos^2\theta$, d_c/d, ϕ_p, and X. Assuming a three dimensional random distribution of the fibers in the resin we have that $\cos^2\theta = 1/3$ [215]. Since the diameter of the contact between the nanofibers d_c, is very small it is not possible to measure its value accurately. Therefore the ratio between the contact diameter and the fiber diameter (d_c/d) was left as a free parameter which was determined by

fitting the calculated theoretical curves with the experimental results. ϕ_p was determined with Eq. 5.35 where the value of β is given by Eq. 5.36, the percolation threshold ϕ_c was estimated from the experimental measurements. Once ϕ_p was known at each fiber loading, m could be determined with Eq. 5.38 and the parameter X was given by Eq. 5.37.

Materials						
		CNF	CNF + TiO_2			
Parameter	Units	CNF	1% TiO_2	2% TiO_2	3%TiO_2	4% TiO_2
d_c / d	[1]	$2 \cdot 10^{-11}$	$2 \cdot 10^{-12}$	$1.23 \cdot 10^{-12}$	$1.23 \cdot 10^{-12}$	$1.23 \cdot 10^{-12}$
ϕ_c	[%]	0.14	0.5	1	1.25	1.5
ϕ_t	[%]	2.2				
d	[nm]	123				
l	[μm]	50				
$\cos^2 \theta$	[1]	0.33				
σ_f	[S/cm]	1000				

Table 5.5: Parameter values used in the FCM model for the CNF–EP composites and the CNF–TiO_2 nanoparticle–EP composites.

Materials					
		CNF	CNF + Al_2O_3		
Parameter	Units	CNF	1% Al_2O_3	2% Al_2O_3	4% Al_2O_3
d_c / d	[1]	$2 \cdot 10^{-11}$	$1 \cdot 10^{-12}$	$3 \cdot 10^{-13}$	$4 \cdot 10^{-13}$
ϕ_c	[%]	0.14	0.2	0.3	1
ϕ_t	[%]	2.2			
d	[nm]	123			
l	[μm]	50			
$\cos^2 \theta$	[1]	0.33			
σ_f	[S/cm]	1000			

Table 5.6: Parameter values used in the FCM model for the CNF–EP composites and the CNF–Al_2O_3 nanoparticle–EP composites.

Table 5.5 and Table 5.6 summarize the microstructural parameters used to model the measured conductivity of the CNF–EP and the CNF–ceramic nanoparticle–EP

composites. As mentioned in the previous paragraph the value of d_c/d was determined fitting the predicted curves with the experimental data. The percolation value for each material ϕ_c was estimated from the conductivity values (Figure 5.56, Figure 5.57). It has to be noted that the values for the percolation thresholds of the ceramic nanoparticle–CNF–EP composites could not be pinpointed exactly, as it was done in the case of the CNF–EP composites (see chapter 5.1.4.2), since not enough conductivity values under, and above the percolation threshold could be measured.

As it can be appreciated in the tables, the reduction in conductivity that the presence of nanoparticles bring to the CNF–EP composites is introduced in the model by decreasing the contact diameters between the nanofibers, and hence decreasing the d_c/d ratio. As the tables show, the decrease was higher when the well dispersed insulating Al_2O_3 nanoparticles were incorporated to the CNF–EP composites. Another fact clearly visible in the tables, is the shift in the percolation threshold to higher values with the addition of nanoparticles to the CNF–EP composites, an effect more accused in the case of the CNF–TiO_2 nanoparticle–EP composites

The results of the modelling of the CNF–EP and the ceramic nanoparticle–CNF–EP composites are illustrated in the following graphs (Figure 5.60 to Figure 5.63). For comparison purposes the conductivity of the CNF–EP is shown modelled with the Simmons' model for tunnelling conductivity and Weber and Kamal's FCM model. Both models show a fairly good correlation between the predicted values and the experimental data. In the case of the CNF–EP composites, the FCM offers a good agreement with the measured values for high loadings of nanofibers. However, the experimental percolation curve shows a smooth increase in conductivity above the percolation threshold while the FCM model predicts a sharper change of conductivity. Simmons' model, on the other hand, predicts more accurately the behaviour of the conductivity of the CNF–EP composites for the whole range of CNF loadings.

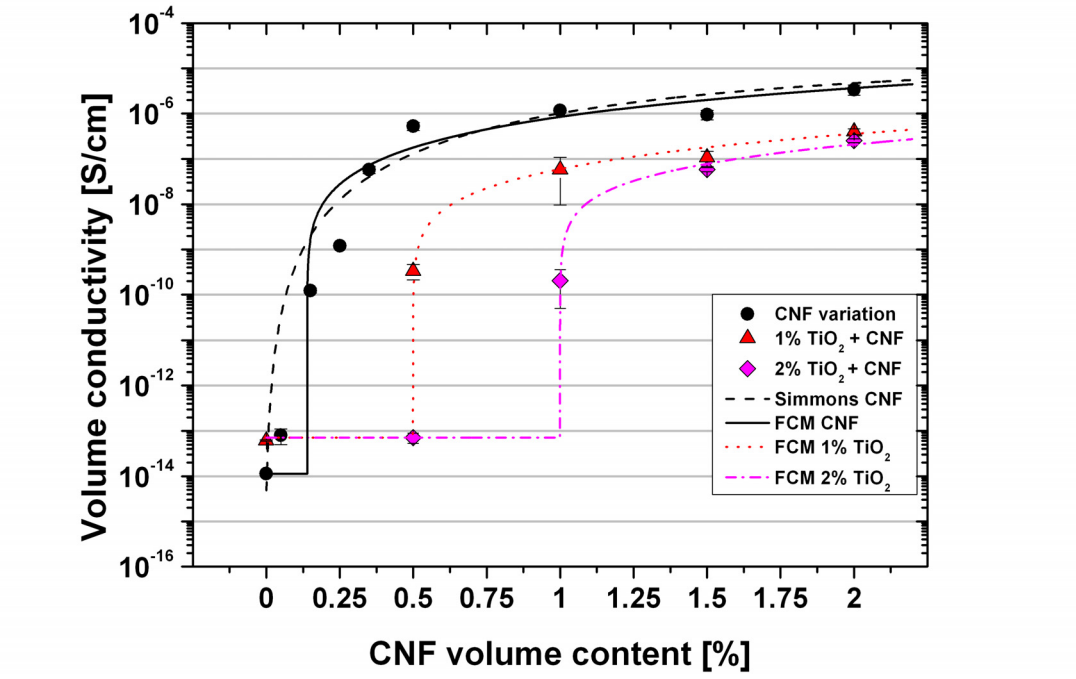

Figure 5.60: Comparison between experimental and predicted values for the volume conductivity of the CNF–TiO_2 nanoparticle–EP composites.

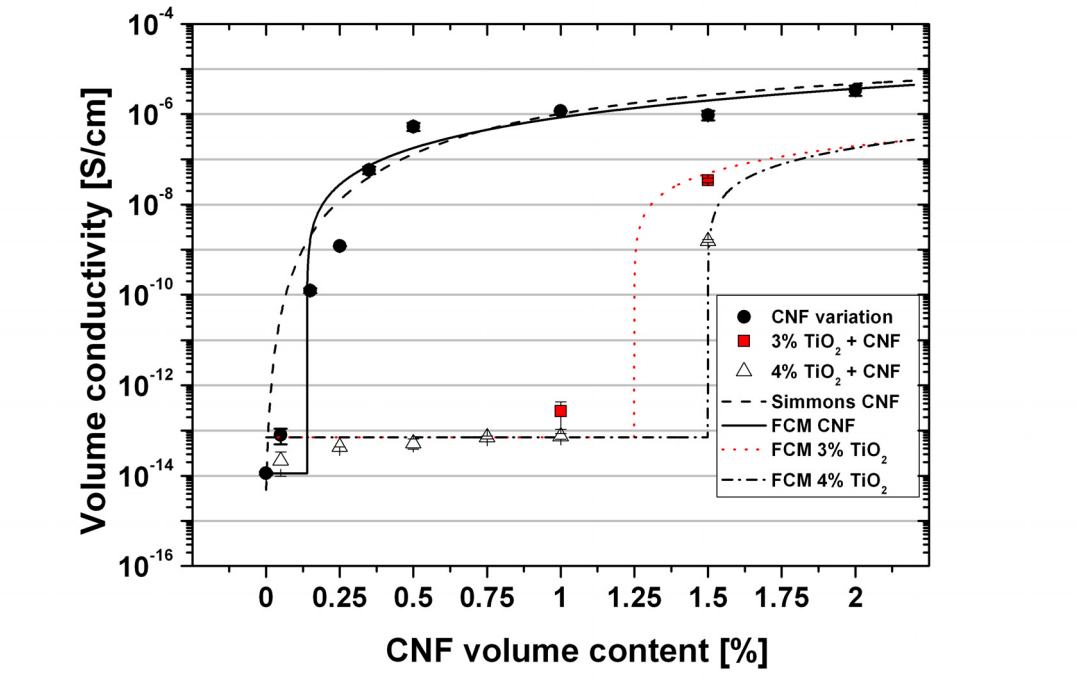

Figure 5.61: Comparison between experimental and predicted values for the volume conductivity of the CNF–TiO_2 nanoparticle–EP composites.

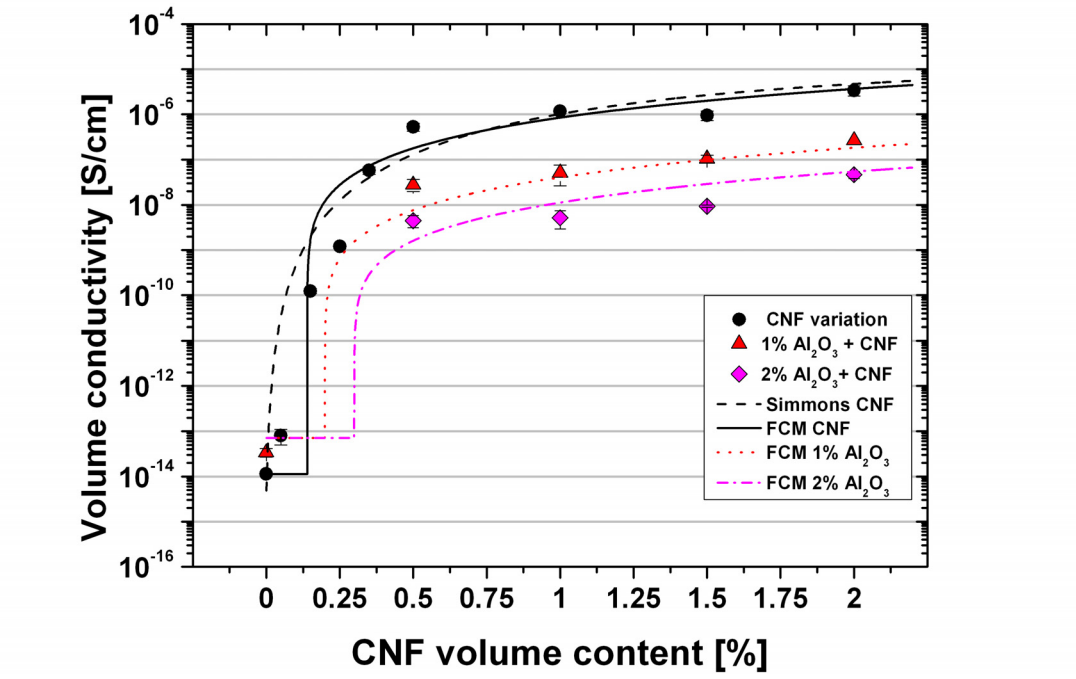

Figure 5.62: Comparison between experimental and predicted values for the volume conductivity of the CNF–Al_2O_3 nanoparticle–EP composites.

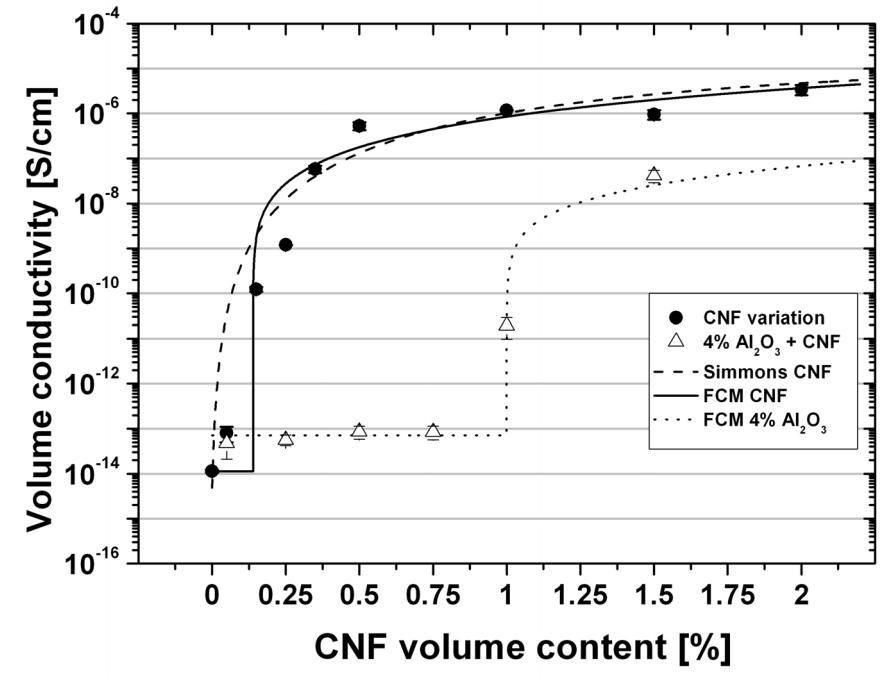

Figure 5.63: Comparison between experimental and predicted values for the volume conductivity of the CNF–Al_2O_3 nanoparticle–EP composites.

5.3.5 Fracture surface analysis of the nanoparticle–CNF–EP composites

As it was discussed in the previous chapters, introducing ceramic nanoparticles in the CNF–EP composites resulted in an increase of the tensile properties of the CNF composites. The comparison of the fracture surfaces of the CNF–EP and the ceramic nanoparticle–CNF–EP composites (Figure 5.64) shows an increase in the surface roughness when nanoparticles are present in the mixtures, an indication that the nanoparticles are able to bring in additional reinforcements mechanisms such as crack deflection and crack pinning [75,80,81,83,200], to the CNF–EP composites.

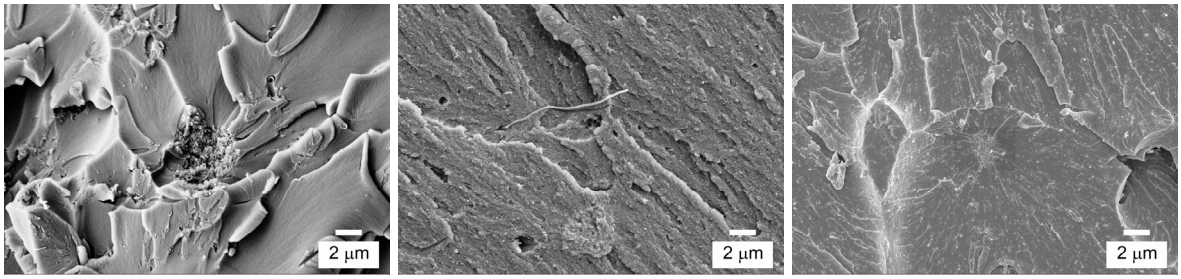

Figure 5.64: Tensile test fracture surfaces. 0.5 vol. % CNF (left), 0.5 vol. % CNF + 4 vol. % TiO_2 (center), 0.5 vol. % CNF + 4 vol. % Al_2O_3 (right).

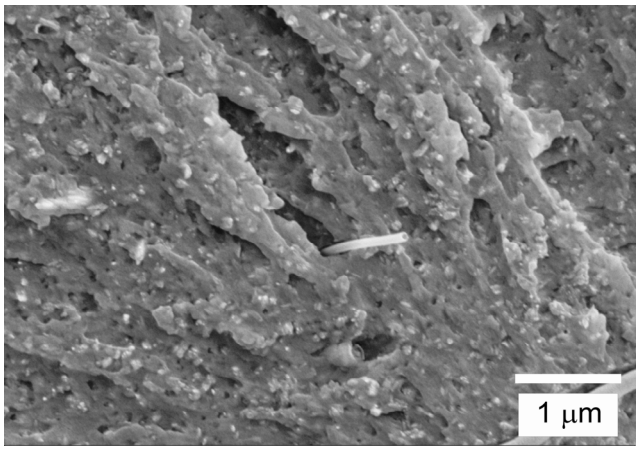

Figure 5.65: Detail of the tensile test fracture surface of a 0.5 vol. % CNF + 4 vol. % TiO_2 composite.

Examining with more detail the fracture surface of the CNF–TiO_2–EP composite (Figure 5.65) additional reinforcing mechanisms can be observed such as particle pull-out (which leaves hemispherical holes on the fracture surface) and plastic deformation of the matrix. Since the matrix-particle bonding in the ceramic nanoparticle-epoxy composites is quite strong, particle pull-out and plastic void

growth around the nanoparticles is only expected to play a minimal role in the total reinforcing effect of the nanoparticles [167].

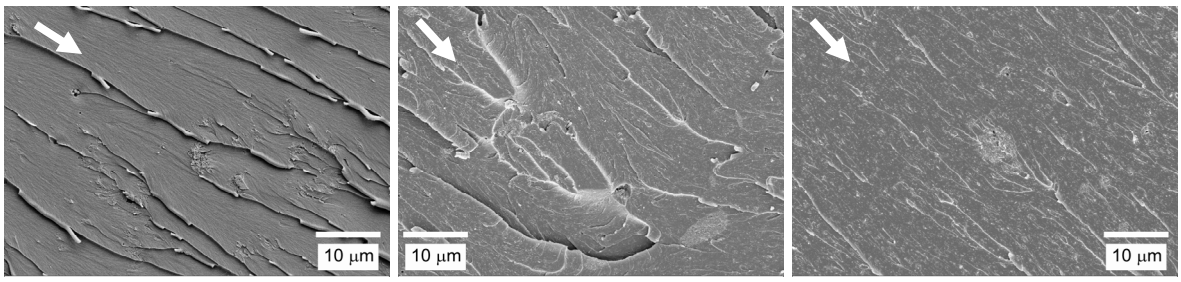

Figure 5.66: Compact tension fracture surfaces. 0.5 vol. % CNF (left), 0.5 vol. % CNF + 4 vol. % TiO_2 (center), 0.5 vol. % CNF + 4 vol. % Al_2O_3 (right).

The K_{IC} fracture surfaces of the CNF–EP composite (K_{IC}~0.89 $MPa \cdot \sqrt{m}$, Figure 5.66, left) and of the CNF–TiO_2–EP and CNF–Al_2O_3–EP composites (K_{IC}~1.02 $MPa \cdot \sqrt{m}$, K_{IC}~1.03 $MPa \cdot \sqrt{m}$, Figure 5.66, center and right, respectively) show different morphologies. Compared with the CNF filled epoxy resin composite the ceramic nanoparticle–CNF–EP composites show a rougher structure as it was seen in the surfaces of the tensile tests. As it occurred during tensile deformation, the nanoparticles increase the toughness of the composites by deflecting the propagating crack. Some remaining micrometer-sized nanoparticle clusters were present in the composites containing TiO_2 nanoparticles while the presence of agglomerates was not marked in the Al_2O_3 composites. This slight qualitative difference in the dispersion state of the two different nanoparticles used during this research did not result in big differences of mechanical behaviour; either in the binary ceramic nanoparticle–EP composites or in the combination of the nanoparticles with the CNF–EP composites. The only divergence was observed in the electrical performance of the ceramic nanoparticle–CNF–EP composites (see chapter 5.3.3) where the slightly larger TiO_2 clusters might have played a role in the observed properties.

A closer inspection of the fracture surfaces of the CNF and the nanoparticle–CNF composites (Figure 5.67) highlights the disparity of morphologies. The good matrix-TiO_2 nanoparticle adhesion results in a minimal presence of debonding and plastic void growth in the plastic zone ahead of the crack tip in the high-speed crack propagation K_{IC} tests. Due to the weak electrostatic adhesion

between the nanoparticles in the nanoparticle clusters, trans-agglomerate crack propagation is favored as can be appreciated in Figure 5.67, (right).

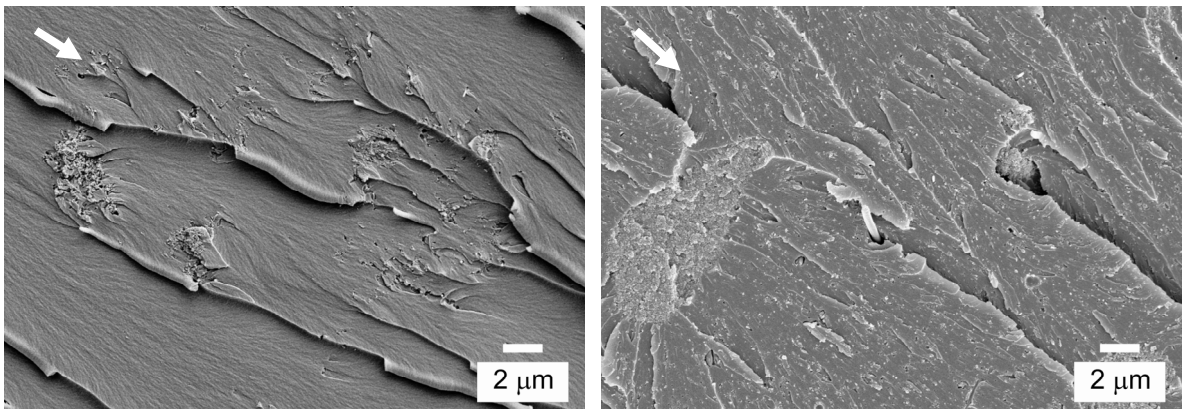

Figure 5.67: Compact tension fracture surfaces. 0.5 vol. % CNF (left), 0.5 vol. % CNF + 4 vol. % TiO_2 (right).

Plastic deformation of the matrix around the nanoparticles, which was observed in the tensile tests (Figure 5.65), was only evident around the larger nanoparticle agglomerates (indicated by the presence of shear bands originating from the agglomerates). This fact might account for the slightly enhanced results observed in the Charpy and fracture toughness tests when the somewhat more agglomerated TiO_2 particles were used instead of the well dispersed Al_2O_3 particles. Nevertheless, the SEM pictures make clear that nanoparticles introduce additional reinforcing mechanisms in the CNF–EP composites which result in the improved mechanical performance illustrated in previous chapters.

6 Summary and outlook

The present research focused in the development and study of composites having ceramic nanoparticles and carbon nanofibers as fillers in a polymer matrix. In a first step of the work, in order to understand which effect each filler had when added to the polymer matrix, CNF–EP and ceramic nanoparticle–EP composites were manufactured and tested. Each kind of fillers were dispersed in the epoxy polymer matrix using two different dispersion technologies, a torus mill for the ceramic nanoparticles and a three roll calender for the carbon nanofibers.

Figure 6.1 gives a quick overview of the different improvements, with respect to the unmodified epoxy matrix, in the mechanical and electrical properties of the composites created in this work. For the sake of comparison, the increase in one order of magnitude in the electrical conductivity of the composites is arbitrarily represented in the graph as a 20 % improvement.

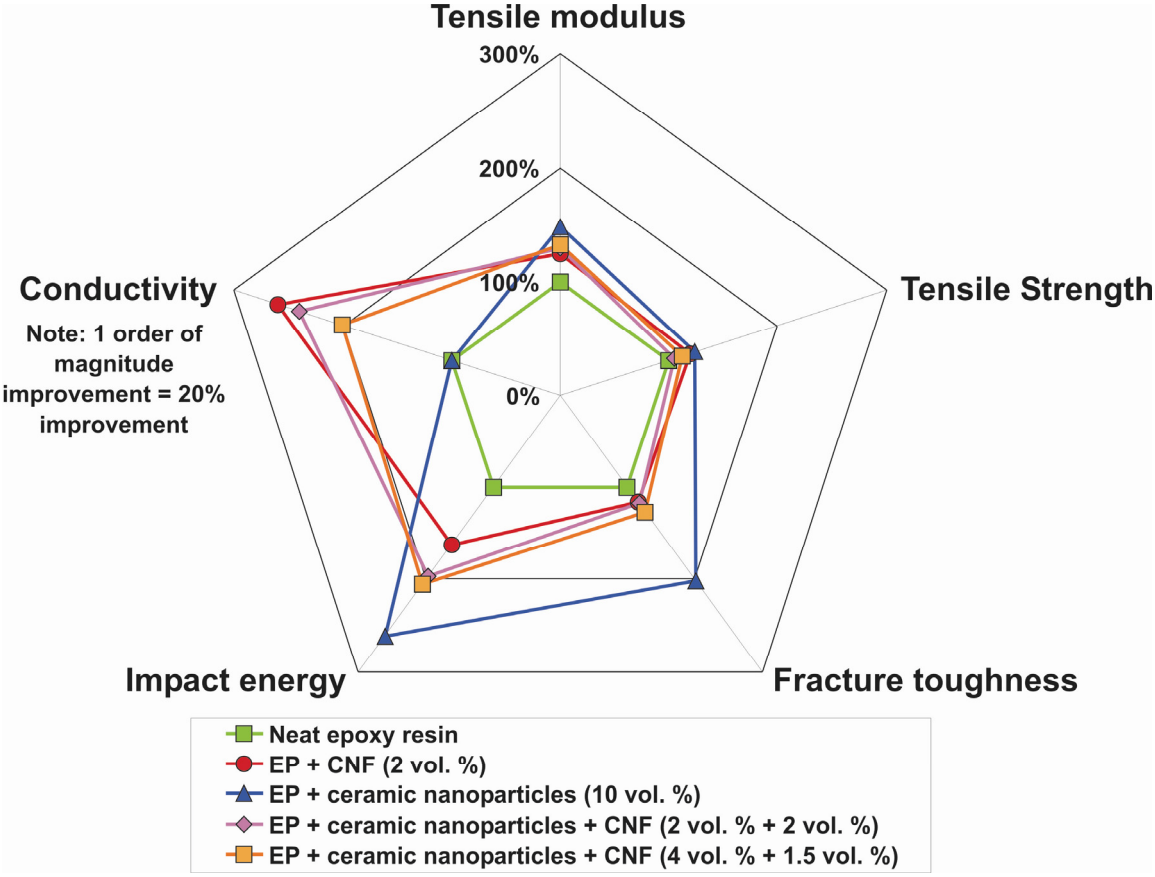

Figure 6.1: Comparison of the improvements achieved with respect to the neat epoxy resin for the different materials studied in this work.

It can be clearly seen that the ceramic nanoparticle–EP composites showed excellent mechanical improvements especially in fracture toughness and impact energy, with moderate improvements in the tensile behaviour and no change in the electrical conductivity. CNF–EP composites, on the other hand, dramatically improved the conductivity of the polymer matrix (by 8 orders of magnitude) while providing fair enhancements to the rest of the mechanical properties. The combination of nanoparticles and CNFs resulted in an increase in the mechanical properties compared with just the addition of CNFs. In these composites, however, the electrical conductivity was slightly reduced when compared with the CNF–EP composites. A more thorough comment of the experimental results of this study is given in the following sections.

CNF–EP composites

The three roll calender proved to be a fairly efficient method to deagglomerate and disperse the untreated CNFs in the polymer matrix. The study of the physical properties of undispersed CNF composites showed that certain material properties, such as the tensile strength and the maximum sustained strain, are much more sensitive to the state of dispersion of the fillers in the matrix than others like the elastic modulus, fracture toughness, impact energy and conductivity (for filler loadings well above the percolation threshold of the system). It could also be determined that composites dispersed 3 times in the calender bench already showed the maximum improvement achievable with the dispersion parameters used. Additional dispersion steps did not yield any further improvement in the performance of the CNF composites.

Rheological investigation of the uncured dispersed mixture indicated the formation of an interconnected nanofiber network within the matrix after the initial steps of calendering. Microscopical analysis of the dispersed composites showed a good distribution of the fibers in the epoxy with remaining nanofiber entanglements on the micro scale. Despite that, CNF–EP composites showed a better mechanical performance than the unmodified polymer matrix. Tensile modulus and strength accused the presence of remaining nanofiber clusters and did not reach theoretically predicted values. The polymer matrix fracture toughness and resistance against

impact also improved with the incorporation of the carbon nanofibers. The main reinforcing mechanisms, such as crack deflection and inelastic matrix deformation, took place on the micro scale. Several theoretical models were used to explain the observed evolution of the Young's modulus of the composites with nanofiber increasing nanofiber content. A slight modification of the fiber cluster model (FCM) developed by Guzmán de Villoria and co-workers [86], which accounts for the effect of filler agglomeration in the modulus of the composite, offered the best fit to the experimental data.

The high aspect ratio of the conductive fibers was not significantly altered during dispersion and the resulting CNF composites saw a percolative increase in the electrical conductivity by several orders of magnitude. The percolation threshold for the achieved level of CNF dispersion was found to be 0.14 vol. %. It was also determined that, for these composites, the main mechanism of electrical transmission was the electron tunnelling mechanism. To estimate the state of dispersion of the nanofibers in the CNF epoxy, the conductivity measurements were fitted to a theoretical model which Li et al. [185] proposed to explain the influence of the filler dispersion on the percolation threshold of nanotube filled matrices. Comparing the results of our study with other reported works [30,211] it could be concluded that percolation is strongly related with the aspect ratio of the fillers and also with the quality of the dispersion of the fillers in the polymer. Assuming that the calender dispersion did not alter the aspect ratio of the nanofibers it was estimated that 5 % of the carbon nanofibers remained in agglomerated form in the manufactured CNF–EP composites. The effect that CNF content had on the conductivity of the epoxy resin was modeled using the Holm-Kirchstein estimation [189,190] for tunnelling conductivity as proposed by Allaoui and co-workers [30]. The predicted values were in rather good agreement with the experimental measurements.

Ceramic nanoparticle–EP composites

Two kind of ceramic nanoparticles (TiO_2 and Al_2O_3) were used as fillers in an epoxy resin to create ceramic nanoparticle–EP composites. The physical properties of the fillers were all in the same range with the exception of the hardness and the dielectric strength. Geometrically, the particles were also analogous, the primary particle size

was similar for both types of fillers; their main differences lied in the slightly higher surface area of the alumina particles and the polyalcohol surface treatment of the titania particles. It has to be noted that the surface area of the particles was significantly lower than the CNF surface area. This, combined with the lower aspect ratio of the particles, made possible higher volume loadings of nanoparticles in the polymer compared with the maximum loading attained with the nanofibers. Consequently, nanoparticle reinforced composites exhibited higher mechanical performance than the CNF–EP composites.

Mechanical dispersion of the nanoparticles in the fluid epoxy resin by means of a torus mill dissolver led to homogeneous distributions of particles in the polymer matrix. Remaining particle agglomerates had a mean value of 80 nm. The dispersion state achieved by the alumina particles was more homogeneous than in the TiO_2 case. Micrometer sized agglomerates of the latter particles could clearly be observed in the microscopical analysis of the composites.

The inclusion of the ceramic nanoparticles in the epoxy resin resulted in a general improvement of the modulus, strength, maximum sustained strain, fracture toughness and impact energy of the polymer matrix. Nanoparticles were able to overcome the stiffness/toughness problem. Thermosetting matrixes reinforced with nanoparticles have shown simultaneous improvements in fracture toughness, stiffness and strength. For volume concentrations of fillers below 4 %, no significant differences were observed between the mechanical behaviour of the TiO_2–EP and the Al_2O_3–EP composites. Despite the observed particle agglomerates, composites with higher volume loadings of TiO_2 nanoparticles showed a better improvement of fracture toughness (+103 %) and impact energy (+160 %) than the alumina filled epoxy samples (+65 and +87 % for fracture toughness and strength respectively). Several energy dissipating mechanisms were responsible for the observed improvement of the mechanical properties of the nanoparticle reinforced matrix. These mechanisms included, crack pinning, plastic shear deformation of the matrix, crack deflection at the agglomerates and, to a lesser extent due to the good particle matrix bonding, particle pull out and plastic void growth. Unlike the CNF–EP composites, the presence of a nanosized secondary phase made possible that some of the reinforcing of the particle filled resin took place in the nanoscale.

Counto's theoretical model was used to describe the elastic behaviour (Young's modulus) of the nanoreinforced thermosetting matrix. Despite its simplicity, the model fitted quite precisely the experimental results; the correlation between predicted values and empirical results was exceptionally good in the case of the Al_2O_3–EP composites.

Unlike the case of the nanofiber composites, the addition of the non-conductive ceramic nanoparticles resulted in a reduction of the electrical conductivity of the resulting blends. Ceramic nanoparticle–EP composites had conductivities lower than that of the neat epoxy resin which was 10^{-14} S/cm approximately.

CNF–ceramic nanoparticle–EP composites

Based on the previous results, we proceeded to combine carbon nanofibers and ceramic nanoparticle as fillers to create a nanocomposite that could benefit from the electrical properties provided by the conductive nanofibers and at the same time have improved mechanical performance thanks to the presence of the well dispersed ceramic nanoparticles.

To manufacture these ternary nanocomposites a 2 masterbatch approach was followed; the ceramic nanoparticles and the nanofibers were mixed and dispersed separately to create two batches which were then blended together in a dissolver mixer. TEM analysis showed no visible CNF or nanoparticle reagglomeration in the ternary composites. This method proved effective to create well dispersed nanofiber–nanoparticle–epoxy composites which showed improved electrical and mechanical properties compared with the neat polymer matrix.

Composites with a constant 4 % volume loading of nanoparticles and an increasing volume of carbon nanofibers showed no significant increase in the mechanical properties compared with the nanoparticle filled EP composites. The conflict between the strengthening effect that the individual dispersed nanofibers might have on the mechanical behaviour and the weakening effect introduced by the remaining nanofiber clusters might be responsible for the observed results.

On the other hand, composites with a constant volume content of 0.5 % nanofibers with an increasing volume of ceramic nanoparticles saw an increase in tensile

modulus, maximum sustained strain, fracture toughness and impact energy and a slight decrease in tensile strength with the incorporation of the ceramic nanofillers. The well dispersed nanosized fillers were able to introduce additional energy dissipating mechanisms in the CNF–EP composites that resulted in a general improvement of the mechanical performance. In general, there were minimal differences between the measured results for the TiO_2–CNF–EP and the Al_2O_3–CNF–EP composites; at high volume loadings of nanoparticles most of the reinforcement came from the presence of nanoparticles in the polymer matrix so the observed trends were, in essence, similar to the ones observed in the TiO_2–EP and the Al_2O_3–EP composites. Addition of nanoparticles also had beneficial effects on the mechanical properties of CNF–EP with high loadings of nanofibers (1, 1.5 and 2 vol. %).

The enhancement in the mechanical performance of the CNF composites with the inclusion of ceramic nanoparticles came at the price of an increase in the percolation threshold and a reduction of the electrical conductivity of the CNF–EP materials. The presence of the nanoparticles in the matrix hindered the formation of a CNF conductive network, increasing the percolation threshold, and reduced the number of fiber contacts, decreasing the conductivity. The raise in percolation threshold was more distinct in the case of the TiO_2–CNF–EP mixtures whereas the reduction in electrical conductivity was slightly higher in the Al_2O_3–CNF–EP composites. The state of agglomeration of the TiO_2 nanoparticles might be an explanation for the first, while the better dispersion (with an associated decrease in fiber-fiber contacts) and higher dielectric strength of the alumina nanoparticles could explain the latter.

A slightly modified Weber and Kamal's fiber contact model (FCM) [59] was used to explain the electrical behaviour of the CNF–ceramic nanoparticle–EP composites. The model was not proposed to predict when the percolation of a fiber filled system would occur but to describe the evolution of conductivity once percolation was achieved. In that aspect, the model was not helpful to predict the observed shifts in percolation in the CNF composites with the incorporation of nanoparticles but, in the other hand was able to fit rather accurately the resulting conductivity of the composites.

The reduction in conductivity observed in the CNF–ceramic nanoparticle–EP does not necessarily have to be considered a drawback. The sharp increase in conductivity of the CNF–EP composites occurring within the range of 10^{-9} - 10^{-6} S/cm might render these materials unsuitable when considered for ESD applications. On the other hand, adding nanoparticles to the CNF composites not only improves the mechanical response of the composite but also offers a way of controlling the resulting composite conductivity and percolation threshold which could be useful when ESD applications are considered.

The fine microstructure and good particle adhesion created by the addition of nanofillers in the epoxy matrix also make these materials appropriate for sensitive applications where no removal of particles from the material surface should take place (e.g. in contrast with carbon black composites). CNF–ceramic nanoparticle–EP composites can hence be used for packaging or coatings applications in order to protect sensitive electronics from the damaging effects of electrostatic discharge.

Outlook

The combination of CNFs and nanoparticles offers new possibilities of creating functional materials with tailored electrical and mechanical properties. The present work opens the door to further possibilities of research. A few of them are outlined below:

- Improvement of the dispersion of the CNFs in the epoxy resin by means of surface functionalization. Other surface treatments (such as oxidation) of the nanofibers could improve matrix filler interface and increase the mechanical performance of the CNF–EP composites.

- Use other fillers as the conductive phase. For example the high aspect ratio, mechanical properties and electrical conductivity of MWCNTs would make them an optimum candidate for the development of MWCNT–ceramic nanoparticle–EP composites with novel electrical and mechanical performances.

- Optimization of the material development: First, create a torus mill dispersed ceramic nanoparticle–epoxy masterbatch, once a homogeneous dispersion of the nanoparticles in the resin is achieved, add carbon nanofibers into the mixture.

Finally disperse the nanoparticle–nanofiber mixture with the three roll calender. From the TEM observations of the state of dispersion of the nanoparticles in the epoxy resin it is not likely that the remaining particle agglomerates could interfere negatively in the dispersion of the nanofibers by the high shear forces created in the calender bench. In this manner we can achieve composites with a high (1.5 - 2.5 vol. %) loading of nanofibers and also a higher loading of nanoparticles (4 - 8 vol. %) than the one we could achieve by the two-masterbatch method. It is reasonable to believe that these composites may show a combination of good electrical properties and increased toughness due to the higher concentration of ceramic nanoparticles

- Study of the effect that different nanoparticle properties (composition, size, surface treatment, electric and magnetic properties…) have in the mechanical, electrical and magnetical properties of the CNF–epoxy composites.

7 Appendix

7.1 Analytical micromechanical models to estimate the Young's modulus of short fiber reinforced composites

7.1.1 Voigt-Reuss model

The Voigt-Reuss model estimates the elastic modulus of a lamina of short random fibers by combining the Voigt-Reuss equations for the longitudinal $E_{\parallel}$, and transverse $E_{\perp}$ modulus:

$$E_{\parallel} = \phi_f E_f + (1-\phi_f) E_m \qquad \text{Eq. 7.1}$$

$$E_{\perp} = \frac{E_f E_m}{E_f (1-\phi_f) + E_m \phi_f} \qquad \text{Eq. 7.2}$$

using Akasaka's simplified equation:

$$E_c = \frac{3}{8} E_{\parallel} + \frac{5}{8} E_{\perp} \qquad \text{Eq. 7.3}$$

with the following result:

$$E_{c,Voigt-\mathrm{Re}uss} = \frac{3}{8}(\phi_f E_f + (1-\phi_f) E_m) + \frac{5}{8}\left(\frac{E_f E_m}{E_f (1-\phi_f) + E_m \phi_f} \right) \qquad \text{Eq. 7.4}$$

7.1.2 Thostenson and Chou modified Halpin Tsai model

Thostenson and Chou [216] modified the Halpin Tsai theory [217] for unidirectional orientation of reinforcements towards its applicability to nanotube reinforced composites. Applying their approach to the Halpin Tsai's equation for random orientation of short fibers [218], the maximum obtainable Young's modulus for a composite with a perfect distribution and impregnation of the fibers within the polymer is: given by:

$$E_{c,Halpin-Tsai} = \frac{3}{8}\left(1 + 2\left(\frac{l}{d}\right) A\phi_f\right) \times \left(1 - A\phi_f\right)^{-1} E_m + \frac{5}{8}\left(1 + 2A\phi_f\right) \times \left(1 - A\phi_f\right)^{-1} E_m \qquad \text{Eq. 7.5}$$

where:

$$A = \left(\frac{\left(E_f / E_m \right) - \left(d / 4t \right)}{\left(E_f / E_m \right) + \left(l / 2t \right)} \right) \qquad \text{Eq. 7.6}$$

with $E_{m,f}$ the Young's modulus of the matrix and the fillers (2446.9 MPa and 230 GPa respectively), l, d length and diameter of the fillers (50 mm and 123 nm respectively and t=0.34 nm the thickness of the graphite layer [98].

7.1.3 Modified Cox model

Tibbets et al. [219] proposed a modified Cox model [220] to calculate the Young's modulus of the CNF–EP nanocomposites. The model estimates the stress transfer to nanofibers of length l, diameter d, axial tensile modulus E_f and volume fraction ϕ_f in a matrix of modulus E_m with the following expression:

$$\beta = \sqrt{\frac{2\pi E_m}{(1+\nu_m) E_f \cdot \ln\left(1 / \phi_f \right)}} \qquad \text{Eq. 7.7}$$

Where ν_m is the matrix Poisson's ratio. Combining the above expression with the rule of mixtures, the modified Cox model gives the following equation to calculate the modulus of the reinforced composite E_c:

$$E_{c,Cox} = (1-\phi_f) E_m + \eta_0 \left(1 - \frac{\tanh \beta s}{\beta s} \right) \phi_f E_f \qquad \text{Eq. 7.8}$$

Where η_0 is the orientation factor of the reinforcement and $s = 2l/d$. Assuming a random orientation of the nanofibers in the resin η_0=1/3. Poisson ratio for epoxy ν=0.35 [221].

7.2 Conductivity models

7.2.1 Improved interparticle distance (IPD) model with two descriptive dispersion parameters

Based on the average IPD approach [184] the composite is divided into cubic elements with length L, each containing one conductive particle in the center, and the total number of cubic elements is equal to the total number of particles. Here, the conductive particles could be either a single carbon nanofiber or an agglomerate of carbon nanofibers, depending on the dispersion state of the nanofibers in the composite.

$$\frac{\phi_{total}}{L^3} = \frac{\phi_{filler}}{n\phi_{CNF}} \qquad \text{Eq. 7.9}$$

where ϕ_{total} is the total volume of composites, ϕ_{filler} is the total volume of filler, ϕ_{CNF} is the volume of the individual carbon nanofiber, and n is the number of nanofibers in an agglomerate (i.e., n=1 in the case of a perfect dispersion). The conducting fillers are assumed to be homogeneously distributed within the matrix and perfectly bonded to the polymer. Two extreme cases were considered for the dispersion of CNFs within the polymer matrix: i) all of cylindrical CNFs are perfectly dispersed in the matrix and ii) all of the CNFs are present in the form of agglomerates. Let's assume that the individual nanofibers are cylindrical with length l and diameter d, and that the CNF agglomerates are spherical in shape with a diameter D and a higher concentration of CNFs than the average filler content. For a perfect dispersion where all CNFs are present in the form of individual cylinders, the filler volume fraction, ϕ, is given by [184]:

$$\phi = \frac{\phi_{filler}}{\phi_{total}} = \frac{\phi_{CNF}}{L^3} = \frac{\pi d^2 l / 4}{[< \cos^2\theta > \cdot (l + IPD)]^3} \qquad \text{Eq. 7.10}$$

Where θ represents the angle between the CNFs and the direction of preferred orientation, and the angular brackets $\langle\ \rangle$ represent the orientation average. For a three dimensional random distribution this average is given by [215]:

$$< \cos^2 \theta > = \frac{1}{3} \qquad \text{Eq. 7.11}$$

When the interparticle distance between the nanofibers is equal to or less than 10 nm, electron hopping occurs resulting in an abrupt increase of the electrical conductivity of the composite, according to the tunnelling mechanism [188-191]. And the filler content, ϕ, becomes the percolation threshold ϕ_c. Therefore, IPD=10 nm was taken as the criterion for the calculation of percolation thresholds, as the nanofiber average length, l, is much longer than 10 nm , l>>IPD. Thus, combining Eq. 7.10 and Eq. 7.11we arrive to the following expression:

$$\phi_c \approx \frac{\pi d^2 l / 4}{l^3 / 3} = \frac{27 \pi d^2}{4 l^2} \qquad \text{Eq. 7.12}$$

On the other hand, if all the nanofibers in the composite remain agglomerated, ϕ_c is given by:

$$\phi_c = \frac{\phi_{filler}}{\phi_{total}} = \frac{n \phi_{CNF}}{L^3} \qquad \text{Eq. 7.13}$$

In order to understand haw the dispersion state and the aspect ratio of the CNFs affect the percolation threshold of the nanocomposites , two descriptive dispersion parameters can be introduced. ε is the localized volume content of carbon nanofibers in an agglomerate, and ξ is the volume fraction that the agglomerated nanofibers occupy in the composite. Mathematically:

$$\varepsilon = \frac{n \phi_{CNF}}{\pi D^3 / 6} \qquad \left(\frac{\phi_{filler}}{\phi_{total}} = \phi < \varepsilon < 1 \right) \qquad \text{Eq. 7.14}$$

$$\xi = \frac{\sum_{i=1}^{\phi_{total} / L^3} n_i \phi_{CNF}}{\phi_{filler}} \qquad (when\ n_i \geq 2)\,(0 < \xi < 1) \qquad \text{Eq. 7.15}$$

A non uniform distribution was not specifically considered in this model because the overall distribution was assumed to be homogeneous. Incorporating Eq. 7.14 into Eq. 7.13 and considering D >>IPD at the percolation threshold, we obtained a simplified equation that depicts the percolation thresholds of nanocomposites with all nanofibers in the agglomerated form:

$$\phi_c = \frac{n\phi_{CNF}}{L^3} = \frac{\varepsilon\pi D^3 / 6}{(D + IPD)^3} \approx \frac{\varepsilon\pi}{6} \qquad \text{Eq. 7.16}$$

In real nanocomposites, however, both individual, perfectly dispersed CNFs and CNF agglomerates coexist simultaneously. The percolation threshold of these nanocomposites can be estimated with the following expression:

$$\phi_c = \frac{\xi\varepsilon\pi}{6} + \frac{(1-\xi)\ 27\pi d^2}{4l^2} \qquad \text{Eq. 7.17}$$

7.2.2 Modified fiber contact model (FCM) (Weber-Kamal)

Most of the existing conductivity models do not accurately predict the volume conductivity of a composite because they do not account for particle-to-particle contacts. It is usually assumed in these models, as well as in the model described in the previous section, that the conductivity of the connected string is equal to the conductivity of the fiber. However, this is an idealized case and only gives a lower bound for the conductivity. The contacts between fibers are rarely perfectly end-to-end; they are usually end-to-body or, most likely, body-to-body. The area of contact for these situations is much smaller than in perfect end-to-end alignment, and thus will have an effect on composite conductivity [222,223]. Therefore, a model which accounts for realistic contacts is needed.

Batchelor and O'Brien [224] derived a model for the thermal or electrical conduction through a granular material consisting of conducting particles in a matrix. The conductivity of the particles is very high, and the ratio of particle to matrix conductivity is much greater than one. The particle surfaces were assumed to be rounded with curvatures of the same order of magnitude, and all inclusions were assumed to be in

conductive “strings.” Three different cases of particle-to-particle contact were considered:

1. Particles are separated by a thin layer

2. Particles are in contact at a single point

3. Particles have a flat circle of contact

The first case is analogous to quantum mechanical tunnelling, where heat or electricity may be conducted in particles that are nearly touching. Cases 2 and 3 are likely to be found in a typical composite. Batchelor and O’Brien studied the effect of particle-to-particle contact for a composite consisting of a random array of close-packed spheres with σ_f / σ_m>10^3. The predicted results compared well with experimental data. The following treatment applies the Batchelor and O’Brien model, which was developed for thermal conductivity, to electrical conductivity and extends its application to fiber-filled composites. Details regarding the mathematical derivation of the equations may be found elsewhere [225].

For composites, where the conductivity of the inclusion is large compared with that of the matrix, essentially all of the current flows through the inclusions. The potential gradient within a particle is very small, except near points of contact with other particles. In the vicinity of these points, the magnitude of the current density and the gradient of potential are large compared to values far from a contact point. Therefore, the conditions near the contact points determine the total current through the particle. For particles which are locally spherical with radius a, the current density near the contact point is:

$$\left\langle \vec{J} \right\rangle = n \left\langle \sum_i \vec{r}_i I_i \right\rangle \qquad \text{Eq. 7.18}$$

Where $\vec{J}$ is the current density, n the number density of particles , i the location of contact point i, $\vec{r}_i$ the position of contact point i and I_i the current flowing through contact point i. The symbol $\langle\ \rangle$ denotes a volume average over a region containing a large number of particles. Using the general Eq. 7.18, the specific case of fibers with a flat circle of contact can be modelled.

Let's consider a fiber with multiple contacts, as shown in Figure 7.1. Five fibers are shown: a reference fiber, fiber 0, which is contacted by four other fibers, numbered from 1 to 4. All five fibers have the same length l and diameter d. Each fiber has an angle of orientation $\pm\theta$ such that $\cos^2\theta$ is equivalent for all fibers. The number of contact points is an even number m, four in this case, and the contacts are equally spaced along the length of fiber 0.

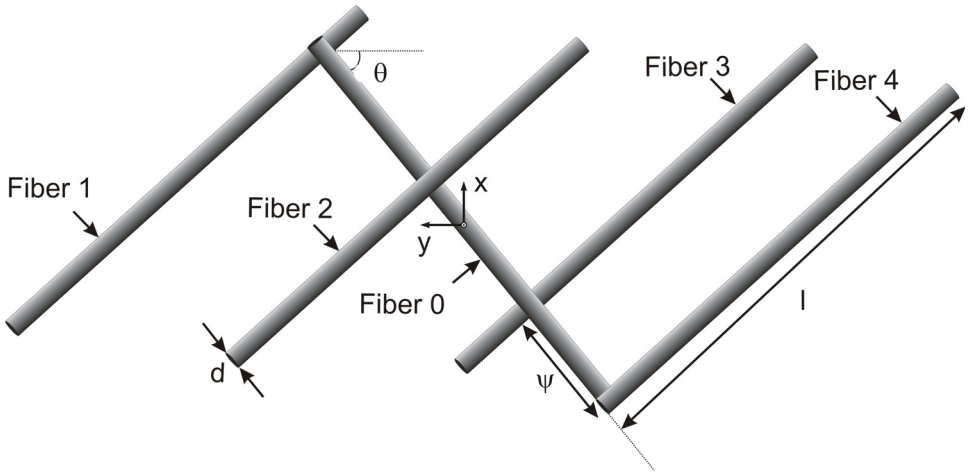

Figure 7.1: Arrangement of fibers with multiple contacts for the fiber contact model, adapted from [59].

The origin of the coordinate system is at the center of the central fiber. In order to simplify the mathematics, the distance from the center of fiber 0 to the contact point with one of the fibers is equal to the distance from the contact point to the center of that fiber.

For particles with a flat area of contact, the current may be written:

$$I = \sigma_f d_c \Delta U \qquad \text{Eq. 7.19}$$

Where σ_f is the conductivity of the fibers, d_c the diameter of the contact circle (see Figure 7.2) and ΔU the potential difference between the centers of two fibers. The potential difference ΔU can be replaced by:

$$\Delta U = -2\vec{r}_i \langle \Delta U \rangle \qquad \text{Eq. 7.20}$$

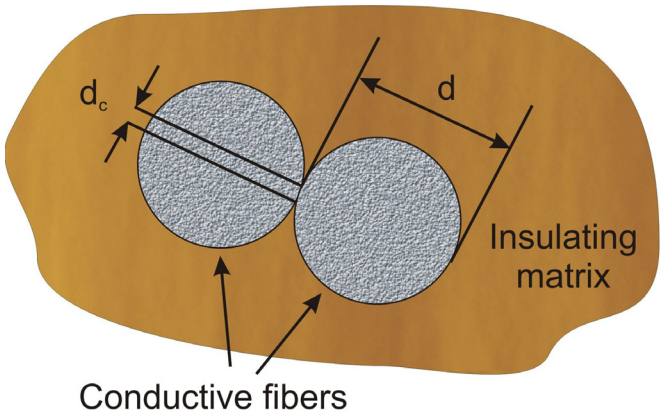

Figure 7.2: Cross section of a contact between two conducting fibers.

Substituting Eq. 7.20 and Eq. 7.19 into Eq. 7.18 and relating the number density of fibers to the fiber volume fraction, ϕ_f gives:

$$\left\langle \vec{J} \right\rangle = -8\frac{\phi_f}{\pi d l} d_c \sigma_f \left\langle \Delta U \right\rangle \sum_{I=1}^{m} \vec{r}_i^{\,2} \qquad \text{Eq. 7.21}$$

The longitudinal position of contact i can be expressed as:

$$\vec{r}_i = x_i \cos\theta \qquad \text{Eq. 7.22}$$

For the current density in the longitudinal direction, i the relation between current density and potential is defined by Ohm's Law:

$$\left\langle \vec{J} \right\rangle = -\sigma_c \left\langle \Delta U \right\rangle \qquad \text{Eq. 7.23}$$

Where σ_c is the conductivity of the composite. Using Eq. 7.22 and Eq. 7.23, Eq. 7.21 can be rewritten as:

$$\sigma_c = \frac{8\phi_f d_c \sigma_f \cos^2\theta \sum_{i=1}^{m} x_i^2}{\pi d^2 l} \qquad \text{Eq. 7.24}$$

Since fibers 1 and 3 are equidistant from the center of fiber 0, as are fibers 2 and 4, the summation term can be rewritten as:

$$\sum_{i=1}^{m} x_i^2 = 2\sum_{i=1}^{m/2} x_i^2 \qquad \text{Eq. 7.25}$$

Defining the distance between two contact points as:

$$\psi = \frac{l}{m-1} \qquad \text{Eq. 7.26}$$

The x_i component in Eq. 7.24 can be rewritten as:

$$x_i = \left(\frac{l}{m-1}\right) \cdot \left(i - \frac{1}{2}\right) \qquad \text{Eq. 7.27}$$

So the sum term in Eq. 7.24 takes the following form:

$$\sum_{i=1}^{m/2} x_i^2 = \frac{l^2}{4(m-1)^2} \sum_{i=1}^{m/2} (2i-1) \qquad \text{Eq. 7.28}$$

Substituting Eq. 7.28 into Eq. 7.24 gives the following expression for the conductivity of the polymer composite:

$$\sigma_c = \frac{4\phi_f d_c \sigma_f \cos^2\theta}{\pi d^2} \cdot X \qquad \text{Eq. 7.29}$$

Where:

$$X = \frac{\sum_{i=1}^{m/2} (2i-1)^2}{(m-1)^2} \qquad \text{Eq. 7.30}$$

A similar derivation can be made for the case of an odd number of contacts, m. The only difference is that the X term is defined as follows:

$$X = \frac{4\sum_{i=1}^{m-1/2} i^2}{(m-1)^2} \qquad \text{Eq. 7.31}$$

Using Eq. 7.30 and Eq. 7.1, the following mathematical expression can be obtained for the relation between X and m:

$$X = 0.59 + 0.15 \cdot m \qquad \text{Eq. 7.32}$$

The proportion of fibers that takes part in a conductive string is now considered. The volume fraction of fibers participating in these conductive paths, ϕ_p can be written as:

$$\phi_p = \beta \cdot \phi_f \qquad \text{Eq. 7.33}$$

It is assumed that above a certain saturated volume fraction, all fibers participate in conductive paths. Therefore, at volume fractions greater than ϕ_t, β is 1. At volume fractions below the percolation threshold, ϕ_c, β, is zero. For concentrations in the range $\phi_c < \phi_f < \phi_t$, β can be estimated by:

$$\beta = \frac{\phi_f - \phi_c}{\phi_t - \phi_c} \qquad \phi_c < \phi_f < \phi_t \qquad \text{Eq. 7.34}$$

A value of ϕ_t at which β will be equal to 1 is assumed (in our case, a value 10 % higher than the maximum volume loading of nanofibers achieved experimentally), and the percolation volume fraction ϕ_c is estimated from the experimental data. β is then found, and ϕ_p is calculated with Eq. 7.33.

Rearranging Eq. 7.29 and taking into account the conductivity of the matrix the electrical conductivity of a composite can be estimated with the following expression:

$$\sigma_c = \sigma_m + \frac{4}{\pi}\left(\frac{d_c}{d} \cdot \frac{l}{d} \cdot \cos^2\theta\right)\left(\phi_p \sigma_f\right) \cdot X \qquad \text{Eq. 7.35}$$

In order to calculate the conductivity with Eq. 7.35, several parameters must be known $\cos^2\theta$, d_c/d, ϕ_p, and X. Assuming a three dimensional random distribution of the fibers in the resin we have that $\cos^2\theta = 1/3$ [215]. The ratio between the contact diameter and the fiber diameter d_c/d is determined by fitting the calculated theoretical curves with the experimental results. ϕ_p is determined with Eq. 7.33

where the value of β is given by Eq. 7.34 and ϕ_c is estimated from the experimental results. Once ϕ_p is known at each fiber loading, m can be found:

$$m = m_{\max}\left(\frac{\phi_p}{\phi_t}\right) \qquad \text{Eq. 7.36}$$

where $m_{\max}$ is given by [187]:

$$m_{\max} = \frac{4\phi_f{}^2}{\pi d^3} \qquad \text{Eq. 7.37}$$

Which is the number fiber contacts of in a three dimensional random fiber network.

8 Literature

[1] Vaia RA, Giannelis EP. Polymer nanocomposites: Status and opportunities. Materials Research Society Bulletin (2001); 26(5): 394-401.

[2] Kinloch AJ, Mohammed RD, Taylor AC, Eger C, Sprenger S, Egan D. The effect of silica nano particles and rubber particles on the toughness of multiphase thermosetting epoxy polymers. Journal of Materials Science (2005); 40(18): 5083-5086.

[3] Li D, Zhang X, Sui G, Wu D, Liang J. Toughness improvement of epoxy by incorporating carbon nanotubes into the resin. Journal of Materials Science Letters (2003); 22(11): 791-793.

[4] Wetzel B, Haupert F, Zhang MQ. Epoxy nanocomposites with high mechanical and tribological performance. Composites Science and Technology (2003); 63(14): 2055-2067.

[5] Shi G, Zhang MQ, Rong MZ, Wetzel B, Friedrich K. Sliding wear behavior of epoxy containing nano-Al_2O_3 particles with different pretreatments. Wear (2004); 256(11-12): 1072-1081.

[6] Sandler J, Shaffer MSP, Prasse T, Bauhofer W, Schulte K, Windle AH. Development of a dispersion process for carbon nanotubes in an epoxy matrix and the resulting electrical properties. Polymer (1999); 40(21): 5967-5971.

[7] Brown JM, Anderson DP, Justice RS, Lafdi K, Belfor M, Strong KL, Schaefer DW. Hierarchical morphology of carbon single-walled nanotubes during sonication in an aliphatic diamine. Polymer (2005); 46(24): 10854-10865.

[8] Sandler JKW, Kirk JE, Kinloch IA, Sha MSP, Windle AH. Ultra-low electrical percolation threshold in carbon-nanotube-epoxy composites. Polymer (2003); 44(19): 5893-5899.

[9] English LK. The ABC's of electromagnetic interference/radio frequency interference/electrostatic discharge shielding. Material Engineering (1989): 37-40.

[10] Blythe T, David Bloor D. Static charges. In: “Electrical Properties of polymers”, 2nd Edition Cambridge University Press (2005): 217-250.

[11] Dahman SJ. Conducting polymer composites. Chapter 10 in Handbook of polymer blends and composites, Volume 2. Vasile C, Kulshreshtha AK. (Eds.) iSmithers Rapra Publishing, (2002): 335-370.

[12] Al-Saleh MH, Sundararaj U. A review of vapor grown carbon nanofiber/polymer conductive composites. Carbon (2009); 47(1): 2-22.

[13] Sproston JL. Electrostatic damage in the electronic industry: Proceedings of a one-day meeting of the Static Electrification Group of the Institute of Physics. Issue 8 of IOP short meetings series, Taylor & Francis Group (1988).

[14] Amarasekera J. Conductive plastics for electrical and electronic applications. Reinforced Plastics (2005); 49(8): 38-41.

[15] Murthy M. Permanent EMI shielding of plastics using copper fibers. In: Annual technical conference – ANTEC. San Francisco, CA, USA: Society of Plastics Engineers; (1994): 1396-1397.

[16] Huang JC. Carbon black filled conducting polymers and polymer blends. Advances in Polymer Technology (2002); 21(4): 299-313.

[17] Feng J, Chan CH. Electrical properties of carbon black-filled polypropylene/ultra-high molecular weight polyethylene composites. In: Conductive polymers and plastics in industrial applications. Rupprecht L. (Ed.) William Andrew Publishing. Plastics Design Library (1999).

[18] Baughman RH, Zakhidov AA, de Heer WA. Carbon nanotubes – the route toward applications. Science (2002); 297(5582): 787-792.

[19] Breuer O, Sundararaj U. Big returns from small fibers: A review of polymer/carbon nanotube composites. Polymer Composites (2004); 25(6): 630-645.

[20] Winey KI, Vaia RA. Polymer nanocomposites. Materials Research Society Bulletin (2007); 32(4): 314-319.

[21] Maruyama B, Alam H. Carbon nanotubes and nanofibers in composite materials. SAMPE Journal (2002); 38(3): 59-70.

[22] Smith JG, Delozier DM, Connell JW, Watson KA. Carbon nanotube-conductive additive-space durable polymer nanocomposite films for electrostatic charge dissipation. Polymer (2004); 45(18): 6133-6142.

[23] Schulte K, Gojny FH, Fiedler B, Broza G, Sandler J. Carbon nano tube reinforced polymers. A state of the art-review. In: Polymer-composites – from nano to macro scale. Friedrich K, Fakirov S, Zhang Z. (Eds.). Dordrecht: Kluwer Publishers (2005): 3-23.

[24] Rutkofsky M, Banash M, Rajagopal R, Chen J. Using a carbon nanotube additive to make electrically conductive commercial polymer composites. SAMPE Journal (2005); 41(2): 54-55.

[25] Das NC, Maiti S. Electromagnetic interference shielding of carbon nanotube/ethylene vinyl acetate composites. Journal of Materials Science (2008); 43(6): 1920-1925.

[26] Lee BO, Woo WJ, Kim MS. EMI shielding effectiveness of carbon nanofiber filled poly(vinyl alcohol) coating materials. Macromolecular Materials and Engineering (2001); 286(2): 114-118.

[27] Cortes P, Lozano K, Barrera EV, Bonilla-Rios J. Effects of nanofiber treatments on the properties of vapor-grown carbon fiber reinforced polymer composites. Journal of Applied Polymer Science (2003); 89(9): 2527-2534.

[28] Tibbetts GG, Lake ML, Strong KL, Rice BP. A review of the fabrication and properties of vapor-grown carbon nanofiber/polymer composites. Composites Science and Technology (2007); 67(7-8): 1709-1718.

[29] Yang YL, Gupta MC, Dudley KL, Lawrence RW. A comparative study of EMI shielding properties of carbon nanofiber and multi-walled carbon nanotube filled polymer composites. Journal of Nanoscience and Nanotechnology (2005); 5(6): 927-931.

[30] Allaoui A, Hoa SV, Pugh MD. The electronic transport properties and microstructure of carbon nanofiber/epoxy composites. Composites Science and Technology (2008); 68 (2): 410-441.

[31] Gelves GA, Lin B, Sundararaj U, Haber JA. Low electrical percolation threshold of silver and copper nanowires in polystyrene composites. Advanced Functional Materials (2006); 16(18): 2423-2430.

[32] White S, Vemulkar T; Fischer J, Winey K. Electrical conductivity in polymer composites containing metal nanowires: Simulation and experiment. American Physical Society Meeting, March 16-20, 2009, abstract #P19.008.

[33] Iijima S. Helical microtubules of graphitic carbon. Nature (1991); 354: 56-58.

[34] Andrews R, Weisenberger MC. Carbon nanotube polymer composites. Current Opinion in Solid State and Materials Science (2004); 8(1): 31-37.

[35] Lau AK-T, Hui D. The revolutionary creation of new advanced materials—carbon nanotube composites. Composites Part B (2002); 33(4): 263-277.

[36] Shaffer MSP, Sandler JKW. Carbon Nanotube/Nanofibre Polymer Composites. In: Processing and properties of nanocomposites. Advani SG. (Ed.) World Scientific Publishing Co. Pte. Ltd (2006): 1-61.

[37] Thostenson ET, Li CY, Chou TW. Nanocomposites in context. Composite Science and Technology (2005); 65(3-4): 491-516.

[38] Moniruzzaman M, Winey KI. Polymer nanocomposites containing carbon nanotubes. Macromolecules (2006); 39(16): 5194-5205.

[39] Coleman JN, Khan U, Gun'ko YK. Mechanical reinforcement of polymers using carbon nanotubes. Advanced Materials (2006); 18(6): 689-706.

[40] Coleman JN, Khan U, Blau WJ, Gun'ko YK. Small but strong: A review of the mechanical properties of carbon nanotube–polymer composites. Carbon (2006); 44(9): 1624-1652.

[41] Miyagawa H, Misra M, Mohanty AK. Mechanical properties of carbon nanotubes and their polymer nanocomposites. Journal of Nanoscience and Nanotechnology (2005); 5(10): 1593-1615.

[42] Xie XL, Mai YW, Zhou XP. Dispersion and alignment of carbon nanotubes in polymer matrix: A review. Materials Science & Engineering R: Reports (2005); 49(4): 89-112.

[43] Mordkovich VZ. Carbon nanofibers: a new ultrahigh strength material for chemical technology. Theoretical Foundations of Chemical Engineering (2003); 37(5): 429-438.

[44] Cooper CA, Ravich D, Lips D, Mayer JJ, Wagner HD. Distribution and alignment of carbon nanotubes and nanofibrils in a polymer matrix. Composites Science and Technology (2002); 62(7-8): 1105-1112.

[45] Sherman LM. Carbon nanotubes lots of potential—if the price is right. Plastics Technology (2007); 53(7): 68-73.

[46] [cited on September 2009]; Available from: < http://www.cheaptubesinc.com/>

[47] Lozano K. Vapor-grown carbon-fiber composites: Processing and electrostatic dissipative applications. JOM Journal of the Minerals, Metals and Materials Society (2000); 52(11): 34-36.

[48] GANF 1 technical data sheet. Grupo Antolín Ingeniería S.A <http://www.grupoantolin.com>

[49] Peigney A, Laurent C, Flahaut E, Bacsa RR, Rousset A. Specific surface area of carbon nanotubes and bundles of carbon nanotubes. Carbon (2001); 39(4): 507-514.

[50] Martín-Gullón I, Vera J, Conesa JA, González JL, Merino C. Differences between carbon nanofibers produced using Fe and Ni catalysts in a floating catalyst reactor. Carbon (2006); 44(8): 1572-1580.

[51] Zhang B, Fu RW, Zhang MQ, Dong XM, Wang LC, Pittman CU. Gas sensitive vapor grown carbon nanofiber/polystyrene sensors. Materials Research Society Bulletin (2006); 41(3): 553-562.

[52] Pelsoci TM. Composites manufacturing technologies: Applications in automotive, petroleum and civil infrastructure industries. (2004) <http://www.atp.nist.gov/eao/grc04-863/gcr04-863.pdf>

[53] Endo M, Kim YA, Hayashi T, Nishimura K, Matusita T, Miyashita K, Dresselhaus MS. Vapor-grown carbon fibers (VGCFs) – basic properties and their battery applications. Carbon (2001); 39(9): 1287-1297.

[54] Subramanian V, Zhu HW, Wei BQ. High rate reversibility anode materials of lithium batteries from vapor-grown carbon nanofibers. Journal of Physical Chemistry B (2006); 110(14): 7178-7183.

[55] Shim BS, Starkovich J, Kotov N. Multilayer composites from vapor-grown carbon nano-fibers. Composites Science and Technology (2006); 66(9): 1174-1181.

[56] Mu M, Walker AM, Torkelson JM, Winey KI. Cellular structures of carbon nanotubes in a polymer matrix improve properties relative to composites with dispersed nanotubes. Polymer (2008); 49(5): 1332-1337.

[57] Lux F. Review. Models proposed to explain the electrical conductivity of mixtures made of conductive and insulating materials. Journal of Materials Science (1993); 28(2): 285-301.

[58] Clingerman ML, King JA, Schulz KH, Meyers JD. Evaluation of electrical models for conductive polymer composites. Journal of Applied Polymer Science (2002); 83(6): 1341-1356.

[59] Weber M, Kamal RM. Estimation of the volume resistivity of electrically conductive composites. Polymer Composites (1997); 18(6): 711-725.

[60] Kirkpatrick S. Percolation and conduction. Reviews of Modern Physics (1973); 45(4): 574-588.

[61] Zallen R. The percolation model. Chapter 4 in “The physics of amorphous solids” New York John Wiley & Sons Inc. (1983).

[62] Trionfi A, Wang DH, Jacobs JD, Tan L-S, Vaia RA, Hsu JWP. Direct measurement of the percolation probability in carbon nanofiber-polyimide nanocomposites. Physical review letters (2009); 102(11): 116601.1-116601.4.

[63] Sumita M, Sakata K, Hayakawa Y, Asai S, Miyasaka K, Tanemura M. Double percolation effect on the electrical conductivity of conductive particles filled polymer blends. Colloid & Polymer Science (1992); 270(2): 134-139.

[64] Wessling B. Dispersion hypothesis and non-equilibrium thermodynamics: Key elements for a materials science of conductive polymers. A key of

understanding polymer blends or other multiphase polymer systems. Synthetic metals (1991); 45(2): 119-149.

[65] Mamunya EP, Davidenko VV, Lebedev EV. Effect of polymer-filler interface interactions on percolation conductivity of thermoplastics filled with carbon black. Composite Interfaces (1997); 4(4): 169-176.

[66] Malliaris A, Turner DT. Influence of particle size on the electrical resistivity of compacted mixtures of polymeric and metallic Powders. Journal of Applied Physics (1971); 42(2): 614-618.

[67] Bhattacharya SK, Chaklader ACD. Review on metal-filled plastics. Part1. Electrical conductivity. Polymer-Plastics Technology and Engineering (1982); 19(1): 21-51.

[68] Singh RP, Zhang M, Chan D. Toughening of a brittle thermosetting polymer: Effects of reinforcement particle size and volume fraction. Journal of Material Science (2002); 37: 781-788.

[69] Wetzel B, Haupert F, Friedrich K, Zhang MQ, Rong MZ. Mechanical and tribological properties of particulate and nanoparticulate reinforced polymer composites. Proceedings of the 13th ECCM Brugge, Belgium (2001).

[70] Laine RM, Choi JW, Lee I. Organic-inorganic nanocomposites with completely defined interfacial interactions. Advanced Materials (2001); 13 (11): 800-803.

[71] Manchado MAL, Valentini L, Biagotti J, Kenny JM. Thermal and mechanical properties of single-walled nanotubes-polypropylene composites prepared by melt processing. Carbon (2005); 43 (7): 1499-1505.

[72] Komarneni S. Nanocomposites. Journal of Materials Chemistry (1992); 2(12): 1219-1230.

[73] Roulin-Moloney AC. Fractography and failure mechanisms of polymers and composites. Elsevier Applied Science London and New York (1989).

[74] Heutling F, Franz HE, Friedrich K. Mikrofraktographische Analyse des Delaminationswachstums in zyklisch belasteten Kohlenstofffaser /

Duroplastharz-Verbundwerkstoffen. Materialwissenschaften und Werkstofftechnik (1998); 29(5): 239-253.

[75] Kinloch AJ, Young RJ. Fracture Behaviour of Polymers. Elsevier Applied Science, New York (1983).

[76] Friedrich K. Scherbändern und Bruch in amorphen un teilkristallinen Polymeren. Progress in Colloid & Polymer Science (1981); 259(2): 190-201.

[77] Sue H-J, Puckett PM, Bertram JL, Walker LL. The network structure of epoxy systems and its relationship to toughness and toughenability. In: Toughening of plastics: Advances in modelling and experiments. Pearson, Sue, Yee (eds): ACS symposium series 759 (2000).

[78] Faber KT, Evans AG. Crack deflection processes – I. Theory. Acta Metallurgica (1983); 31(4): 565-576.

[79] Faber KT, Evans AG. Crack deflection processes – II. Experiment. Acta Metallurgica (1983); 31(4): 577-584.

[80] Lange FF. The interaction of a crack front with a second-phase dispersion. Philosophical Magazine (1970); 22(179): 983-992.

[81] Evans AG. The strength of a brittle material containing second phase dispersions. Philosophical Magazine (1972); 26(6): 1327-1344.

[82] Green DJ, Nicholson PS, Embury JD. Fracture of a brittle particulate composite. Part 1 Experimental aspects. Journal of Materials Science (1979); 14(6): 1413-1420.

[83] Green DJ, Nicholson PS, Embury JD. Fracture of a brittle particulate composite. Part 2 Theoretical aspects. Journal of Materials Science (1979); 14(7): 1657-1661.

[84] Kinloch AJ, Maxwell D, Young RJ. Micromechanisms of crack propagation in hybrid-particulate composites. Journal of Materials Science Letters (1985); 4(10): 1276-1279.

[85] Wetzel B, Rosso P, Haupert F, Friedrich K. Epoxy nanocomposites – fracture and toughening mechanisms Engineering Fracture Mechanics (2006); 73(16): 2375-2398.

[86] Guzmán de Villoria R, Miravete A. Mechanical model to evaluate the effect of the dispersion in nanocomposites. Acta Materialia (2007); 55(9): 3025-3031.

[87] Azimi HR, Pearson RA, Hertzberg RW. Fatigue of hybrid epoxy composites: Epoxies containing rubber and hollow glass spheres. Polymer Engineering & Science (1996); 36(18): 2352-2365.

[88] Gojny FH, Wichman MHG, Fiedler B, Schulte K. Influence of different carbon nanotubes on the mechanical properties of epoxy matrix composites – A comparative study. Composites Science and Technology (2005); 65(15-16): 2300-2313.

[89] Avella M, Errico ME, Martelli S, Martuscelli E. Preparation methodologies of polymer matrix nanocomposites. Applied Organometallic Chemistry (2001); 15(5): 435-439.

[90] Dennis HR, Hunter DL, Chang D, Kim S, White JL, Cho JW. Nanocomposites: The importance of processing. Plastics Engineering (2001); 57(1): 56-57.

[91] Wang Q, Xia H, Zhang C. Preparation of polymeric/inorganic nanoparticles composites through ultrasonic radiation. Journal of Applied Polymer Science (2001); 80: 1478-1488.

[92] Adebahr T, Roscher C, Adam J. Reinforcing nanoparticles in reactive resins. European Coatings Journal (2001); 4: 144-149.

[93] Kang S, Hong SI, Choe CR, Park M, Rim S, Kim J. Preparation and characterization of epoxy composites filled with functionalized nanosilica particles obtained via sol–gel process. Polymer (2001); 42(3): 879-887.

[94] Becker C, Krug H, Schmidt H. Tailoring of thermomechanical properties of thermoplastic nanocomposites by surface modification of nanoscale silica particles. Materials Research Society Symposium Proceedings (1996); 435: 237-242.

[95] Rong MZ, Zhang MQ, Zheng YX, Zeng HM, Walter R, Friedrich K. Irradiation graft polymerization on nano-inorganic particles: An effective means to design

polymer based nanocomposites. Journal of Materials Science Letters (2000); 19(13): 1159-1161.

[96] Lu KL, Lago M, Chen YK, Green MLH, Harris PJF, Tsang SC. Mechanical damage of carbon nanotubes by ultrasound. Carbon (1996); 34(6): 814-816.

[97] Buffa F, Abraham GA, Grady BP, Resasco D. Effect of nanotube functionalization on the properties of single-walled carbon nanotube/polyurethane composites Journal of Polymer Science Part B: Polymer Physics (2007); 45(4): 490-501.

[98] Gojny FH, Wichmann MHG, Köpke U, Fiedler B, Schulte K. Carbon nanotube-reinforced epoxy-composites – enhanced stiffness and fracture toughness at low nanotube contents. Composites Science and Technology (2004); 64(15): 2363-2371.

[99] Tadmor Z, Costas GG. Principles of polymer processing 2nd edition. John Wiley & Sons (2006) Chapter 15: 865.

[100] Goldschmidt A, Streitberger HJ. BASF Handbuch Lackiertechnik Hannover Vincentz Verlag; Auf. 12 (2002).

[101] Morton-Jones DH. Polymer Processing. Chapman & Hall (1993).

[102] Schwarz O, Ebeling FW, Furth B, Kunststoffverarbeitung. Vogel Buchverlag (2002).

[103] Agassant JF, Espy M. Theoretical and experimental study of the molten polymer flow in the calender bank. Polymer Engineering and Science (1985); 25 (2): 118-121.

[104] Takserman-Krozer R, Schenkel G, Ehrmann G. Fluid flow between rotating cylinders. Rheologica Acta (1975); 14(12): 1066-1076.

[105] Luther S, Mewes D. Three-dimensional polymer flow in the calender bank Polymer Engineering and Science (2004); 44(9): 1642-1647.

[106] Unkrüer W, Beitrag zur Ermittlung des Druckverlaufes und der Fließvorgänge im Walzspalt bei der Kalanderverarbeitung von PVC hart zu Folien, Phd Thesis IKV Technischen Hochschule Aachen, Germany (1970).

[107] Wetzel B. Mechanische Eigenschaften von Nanoverbundwerkstoffen aus Epoxydharz und keramischen Nanopartikeln. PhD Technische Universität Kaiserslautern, IVW Schriftenreihe Band 69 (2006). ISBN: 3-934930-65-4.

[108] Ellis B. Chemistry and technology of epoxy resins. Blackie Academic & Professional, an imprint of Chapman & Hall. Glasgow (1993).

[109] Huntsman Advanced materials GmbH: Product specifications for the Araldite® LY 564 / Aradur® 2954 hot curing epoxy matrix system 07.03.2007 and Sichereitsdattenblatt Araldite® LY 564 17.01.2006.

[110] Merino C. Producción industrial y aplicaciones de nanofibras de carbono. Grupo Antolín Ingeniería. Conferencias Instituto Nacional del Carbón. Memoria de Actividades (2004).

[111] GANF 1 safety data sheet 12.2006, Grupo Antolín Ingeniería S.A <http://www.grupoantolin.com>

[112] Diebold U: The surface science of titanium dioxide Surface Science Reports (2003); 48(5-8): 53-229.

[113] Salmang H, Scholze H. Keramik 7, vollständig neubearbeitete und erweiterte Auflage, Berlin Springer (2007).

[114] Shackelford JF, Alexander W. Materials Science and Engineering Handbook 3rd Edition. CRC Press, Boca Raton, FL (2001): 538.

[115] Breviary Technical Ceramics (Taschenbuch) von Verband d. Keramischen Industrie e.V. (Herausgeber) Hans Fahner Verlag; Auflage: 4., veränd. Aufl. (Dezember 2004).

[116] Evonik Degussa GmbH: Produktspezifikation (1387/1) and Datenblatt Aeroxide® Alu C (03/112/EG).

[117] Sachtleben Chemie GmbH: Sicherheitsdatenblatt Hombitec® RM , (91/155EWG).

[118] Winkler J. Titandioxid. Vincentz Network GmbH & Co KG Hannover (2003).

[119] CRC Handbook of Chemistry and Physics, Lide DR. (Ed.) 80th Edition, CRC Press, Boca Raton, FL, (1999).

[120] Wefers K, Misra C. Oxides and hydroxides of aluminum, Alcoa Technical Paper No. 19, Revised, Alcoa Laboratories, (1987).

[121] Lundstrom JM, Rinehart LF, Pate RC, Smith TL, Krogh ML, Huebner W. Measurement of the dielectric strength of titanium dioxide ceramics.12th IEEE International Pulsed Power Conference, Digest of Technical Papers (1999); 2: 1489-1491.

[122] Stappert S. <SStapper@sachtleben.de> Sachtleben Chemie GmbH Duisburg "Oberflächen von Hombitec" Personal e-mail communication from the manufacturer (21st April 2006).

[123] Technical Bulletin Fine Particles No.11: Basic characteristics of AEROSIL® fumed silica. Company publication, Evonik Degussa AG, Frankfurt (2003): 68.

[124] French RH. Origins and applications of London dispersion forces and Hamaker constants in ceramics. Journal of the American Ceramic Society (2000); 83(9): 2117-2146.

[125] Hamaker, HC: The London-Van der Waals attraction between spherical particles. Physica (1937); 4(10): 1058-1072.

[126] Xiao K, Ye L, Kwok YS. Effects of pre-cracking methods on fracture behaviour of an Araldite-F epoxy and its rubber-modified systems. Journal of Material Science (1998); 33(11): 2831-2836.

[127] Tada H, Paris PC, Irwin GR. The stress analysis of cracks handbook. American Society of Mechanical Engineers, New York (2000).

[128] Yee AF, Du J, Thouless MD. Toughening of epoxies. Chapter 26 in “Polymer blends. Volume 2: Performance” Paul DR, Bucknall CB (eds). John Wiley & Sons Inc. New York (2000): 225-226.

[129] Riley AM, Paynter CD, McGenity PM, Addams JM. Factors affecting the impact properties of mineral filled polypropylene. Plastic and Rubber Processing and Applications (1990); 14(2): 85-93.

[130] ASTM Standard D 257-99. Standard test methods for D-C resistance or conductance of insulating materials, (1999).

[131] Heaney MB. The measurement, instrumentation and sensors handbook. chapter Electrical conductivity and resistivity. CRC Press, (1999).

[132] EC 61340-5-1 Standard. Electrostatics – part 5-1: Protection of electronic devices from electrostatic phenomena - general requirements, (1998).

[133] Karger-Kocsis J, Friedrich K. Microstructure-related fracture toughness and fatigue crack growth behavior in toughened, anhydride-cured epoxy resins. Composites Science and Technology (1993); 48 (1-4): 263-272.

[134] Menard KP. Dynamic mechanical analysis: A practical introduction. CRC Press LLC, Boca Raton, (1999).

[135] Goldstein J, Newbury D, Joy D, Lyman C, Echlin P, Lifshin E, Sawyer L, Michael J. Scanning electron microscopy and X-ray microanalysis. Kluwer Academic, Plenum Publishers, 3rd Edition, New York (2003).

[136] Reimer L, Kohl H. Transmission electron microscopy: Physics of image formation. Springer, Berlin (2008).

[137] Yang S, Taha-Tijerina J, Serrato-Diaz V, Hernandez K, Lozano K Dynamic mechanical and thermal analysis of aligned vapor grown carbon nanofiber reinforced polyethylene. Composites Part B (2007); 38(2): 228-235.

[138] Kelarakis A, Yoon K, Somani R, Sics I, Chen XM, Hsiao BS, Chu B Relationship between structure and dynamic mechanical properties of a carbon nanofiber reinforced elastomeric nanocomposite. Polymer (2006); 47(19): 6797-6807.

[139] Gao Y, He P, Lian J, Wang LM, Qian D, Zhao J, Wang W, Schulz MJ, Zhang J, Zhou XP, Shi DL. Improving the mechanical properties of polycarbonate nanocomposites with plasma-modified carbon nanofibers. Journal of Macromolecular Science: Physics (2006); 45(4): 671-679.

[140] Choi YK, Sugimoto KI, Song SM, Endo M. Mechanical and thermal properties of vapor-grown carbon nanofiber and polycarbonate composite sheets. Material Letters (2005); 59(27): 3514-3520.

[141] Xu J, Donohoe JP, Pittman CU. Preparation, electrical and mechanical properties of vapor grown carbon fiber (VGCF)/vinylester composites. Composites Part A (2004); 35(6): 693-701.

[142] Ceccia S, Ferri D, Tabuani D, Maffettone PL. Rheology of carbon nanofiber-reinforced polypropylene. Rheologica Acta (2008); 47(4): 425-433.

[143] Krishnamoorti R, Giannelis EP. Rheology of end-tethered polymer layered silicate nanocomposites. Macromolecules (1997); 30(14): 4097-4102.

[144] Kim JA, Seong DG, Kang TJ, Youn JR. Effects of surface modification on rheological and mechanical properties of CNT/epoxy composites. Carbon (2006); 44(10): 1898-1905.

[145] Song YS, Youn JR. Influence of dispersion states of carbon nanotubes on physical properties of epoxy nanocomposites. Carbon (2005); 43(7): 1378-1385.

[146] Mitchell CA, Bahr JL, Arepalli S, Tour JM. Dispersion of functionalized carbon nanotubes in polystyrene. Macromolecules (2002); 35(23): 8825-8830.

[147] Shenoy AV. Rheology of filled polymer systems. Kluwer Academic Publishers, Dordrecht (1999).

[148] Utracki LA. Flow and flow orientation of composites containing anisometric particles. Polymer Composites (1986); 7(5): 274-282.

[149] Dealy M, Wissbrun KF. Melt rheology and its role in plastic processing theory and application. Kluwer Academic Publishers, Dordrecht (1999).

[150] Shaffer MSP, Fan X, Windle AH. Dispersion and packing of carbon nanotubes. Carbon (1998); 36(11): 1603-1612.

[151] Jin Z, Pramoda KP. Dynamic mechanical behavior of melt-processed multi-walled carbon nanotube/poly(methyl methacrylate) composites. Chemical Physics Letters (2001); 337(1-3): 43-47.

[152] Lozano K, Yang S, Zeng Q. Rheological analysis of vapor-grown carbon nanofiber-reinforced polyethylene composites. Journal of Applied Polymer Science (2004); 93(1): 155-162.

[153] Pötschke P, Fornes,TD, Paul DR. Rheological behavior of multiwalled carbon nanotube/polycarbonate composites. Polymer (2002); 43(11): 3247-3255.

[154] Endo M, Kim YA, Hayashi T, Fukai Y, Oshida K, Terrones M, Yanagisawa T, Higaki S. Structural characterization of cup-stacked-type nanofibers with an entirely hollow core. Applied Physics Letters (2002); 80(7): 1267-1269.

[155] Vera-Agulló J, Varela-Rizo H, Conesa JA, Almansa C, Merino C, Martín-Gullón I. Evidence for growth mechanism and helix-spiral cone structure of stacked-cup carbon nanofibers. Carbon (2007); 45(14): 2751-2758.

[156] Marur PR, Batra RC, García G, Loos AC. Static and dynamic fracture toughness of epoxy/alumina composite with submicron inclusions. Journal of Materials Science (2004); 39(4): 1437-1440.

[157] Schaefer DW, Justice RS. How nano are nanocomposites? Review. Macromolecules (2007); 40(24): 8501-8517.

[158] Berlin AA, Volfson SA, Enikolopian NS, Negmatov SS. Principles of polymer composites. Springer-Verlag, Berlin (1986).

[159] Nielsen L, Landel R. Mechanical properties of polymers and composites. New York (USA): Marcel Decker; (1994).

[160] Nicolais L, Narkis M. Stress-strain behaviour of styrene-acrylonitrile/glass bead composites in the glassy region. Polymer Engineering and Science (1971); 11(3): 194-199.

[161] Zhang M, Zeng H, Zhang L, Lin G, Li RKY. Fracture characteristics of discontinuous carbon fibre-reinforced PPS and PESC composites. Polymers and Polymer Composites (UK) (1993); 1(5): 357-365.

[162] Wu CL, Zhang MQ, Rong MZ, Friedrich K. Tensile performance improvement of low nanoparticles filled polypropylene composites. Composites Science and Technology (2002); 62: 1327-1340.

[163] Choi YK, Sugimoto KI, Song SM, Gotoh Y, Ohkoshi Y, Endo M. Mechanical and physical properties of epoxy composites reinforced by vapor grown carbon nanofibers. Carbon (2005) 43(10): 2199-2208.

[164] Patton RD, Pittman CU, Wang L, Hill JR. Vapor grown carbon fiber composites with epoxy and poly(phenylene sulfide) matrices. Composites Part A: Applied Science and Manufacturing (1999); 30(9): 1081-1091.

[165] Lafdi K and Matzek M. Carbon nanofibers as a nano-reinforcement for polymeric nanocomposites. In: 48th International SAMPE symposium proceedings, Long Beach, USA; (2003).

[166] Christensen RM. Mechanics of Composite Materials. Malabar, FL: Krieger Publishing Company (1991).

[167] Johnsen BB, Kinloch AJ, Mohammed RD, Taylor AC, Sprenger S. Toughening mechanisms of nanoparticle-modified epoxy polymers, Polymer (2007); 48(12): 530-541.

[168] Wei C, Srivastava D. Nanomechanics of carbon nanofibers: Structural and elastic properties, Applied Physics Letters (2004); 85(12): 2208-2210.

[169] Zhao S, Schadler LS, Hillborg H, Auletta T. Improvements and mechanisms of fracture and fatigue properties of well-dispersed alumina/epoxy nanocomposites. Composites Science and Technology (2008); 68(14): 2976-2982.

[170] Zhao S, Schadler LS, Hillborg H, Auletta T. Mechanisms leading to improved mechanical performance in nanoscale alumina filled epoxy. Composites Science and Technology. (2008); 68(14): 2965-2975.

[171] Kalyon DM, Birinci E, Yazici R, Karuz B. Electrical properties of composites as affected by the degree of mixedness of the conductive filler in the polymer matrix. Polymer Engineering and Science (2002); 42(7): 1609-1618.

[172] Jana PB, Mallick AK, De SK. Electrical conductive rubber and plastic composites with carbon particles or conductive fibres. In “Short Fibre-polymer Composites” De SK, White JR. (Eds.) Cambridge: Woodhead (1996) Chap. 7: 170-172.

[173] Bigg, D.M. Electrical Properties of Metal-filled Polymer Composites, Metal Filled Polymers (Properties and Application), Marcel Dekker, Inc., New York. (1986): 165-222.

[174] Stauffer D. Introduction to percolation theory. London: Taylor and Francis; (1985).

[175] Konter M, Carballeira P, Haupert F, Wetzel B, Pelster R. On the quality of electrical contacts between carbon nano-fibers in composite-materials. 73. Jahrestagung der DPG (Deutsche Physikalische Gesellschaft) und DPG Frühjahrstagung des Arbeitskreises Festkörperphysik Dresden, 22-27. März 2009.

[176] Fiuschau GR, Yoshikawa S, Newnham RE. Resistivities of conductive composites, Journal of Applied Physics (1992); 72(3): 953-959.

[177] Tsotra P. Electrically conductive epoxy matrix composites. PhD Technische Universität Kaiserslautern, IVW Schriftenreihe Band 50 (2004). ISBN: 3-934930-46-8.

[178] Taipalus R, Harmia T, Zhang MQ, Friedrich K. The electrical conductivity of carbon-fibre-reinforced polypropylene/polyaniline complex-blends: Experimental characterisation and modelling. Composites Science and Technology (2001); 61: 801-809.

[179] Carmona F, Barreau F, Delhaes P, Canet R. An experimental model for studying the effect of anisotropy on percolative conduction. Journal de Physique Lettres (1980) 41(22): 531-533.

[180] Du F, Scogna RC, Zhou W, Brand S, Fischer JE, Winey KI. Nanotube networks in polymer nanocomposites: Rheology and electrical conductivity. Macromolecules (2004); 37(24): 9048-9055.

[181] Aggarwal M, Khan S, Husain M, Ming TC, Tsai MY, Perng TP, Khan ZH. Variable-range hopping in $Fe_{70}Pt_{30}$ catalyzed multi-walled carbon nanotubes film. The European Physical Journal B (2007); 60(3): 319-324.

[182] Chang L, Friedrich K, Ye L, Toro P. Evaluation and visualization of the percolating networks in multi-wall carbon nanotube/epoxy composites. Journal of Materials Science (2009); 44(15): 4003-4012.

[183] Connor MT, Roy S, Ezquerra TA, Baltá Calleja FJ. Broadband AC conductivity of conductor–polymer composites. Physical Review B (1998); 57(4): 2286-2294.

[184] Li J, Kim JK. Percolation threshold of conducting polymer composites containing 3D randomly distributed graphite nanoplatelets Composites Science and Technology (2007); 67(10): 2114-2120.

[185] Li J, Ma PC, Chow WS, To CK, Tang BZ, Kim J-K. Correlations between percolation threshold, dispersion state, and aspect ratio of carbon nanotubes. Advanced Functional Materials (2007); 17(16): 3207-3215.

[186] Allaoui A. Comportement mécanique et électrique des enchevêtrements de nanotubes de carbone. École Centrale, Paris. Thèse de Doctorat; (2005).

[187] Alkhagen MI. Nonlinear elasticity of fiber masses. Chalmers University, Göteborg, Sweden. PhD thesis; (2002).

[188] Sommerfeld A, Bethe H. Elektronentheorie der metalle. In:Handbüch der Physik, vol. 24/2. Geiger H, Scheel K. (Eds.) Berlin: Springer- Verlag; (1933).

[189] Holm R, Kirschstein B. Über den Widerstand dünnster fremdschichten in metallkontakten. Zeitung Technische Physik (1935); 16: 488.

[190] Holm R. Electric contacts: Theory and application. New York: Springer-Verlag; (1967): 123.

[191] Simmons JG. Generalized formula for the electric tunnel effect between similar electrodes separated by a thin insulating film. Journal of Applied Physics (1963); 34(6): 1793-1803.

[192] Ubbelohde AR, Lewis FA. Graphite and its crystal compounds. London: Oxford University Press (1960).

[193] Liang Z, Gou JJ, Zhang C, Wang B, Kramer L. Investigation of molecular interactions between (10, 10) single-walled nanotube and Epon 862 resin/DETDA curing agent molecules. Materials Science and Engineering A (2004); 365(1-2): 228-234.

[194] Ash BJ, Siegel RW, Schadler LS. Mechanical behaviour of alumina/poly (methyl methacrylate) nanocomposites. Macromolecules (2004); 37(4): 1358-1369.

[195] Counto UJ. The effect of the elastic modulus of the aggregate on the elastic modulus, creep and creep recovery of concrete. Magazine of Concrete Research (1964); 16(48): 129-138.

[196] Young RJ. Beaumont PWR Crack propagation and arrest in epoxy resins. Journal Material Science Letters (1976); 11(4): 778-779.

[197] Yamini S, Young RJ. Stability of crack propagation in epoxy resins. Polymer (1977); 18(10): 1075-1080.

[198] Phillips DC, Scott JM, Jones M. Crack propagation in an amine-cured epoxide resin. Journal of Materials Science (1978); 13(2): 311-322.

[199] Scott JM, Wells GM, Phillips DC. Low temperature crack propagation in an epoxide resin. Journal of Materials Science (1980); 15(6): 1436-1448.

[200] Cantwell WJ, Roulin-Moloney AC, Kausch HH. Dynamic crack propagation in the double-torsion test geometry. Journal of Materials Science Letters (1988); 7(9): 976-980.

[201] Karger-Kocsis J. On the toughness of “nanomodified“ polymers and traditional polymer composites thereof. Chapter 12 in Nano- and Micromechanics of Polymer Blends and Composites. Karger-Kocsis J, Fakirov S. (Eds.) Hanser Fachbuchverlag, Munich (2009).

[202] Galeski A. Strength and toughness of crystalline polymer systems. Progress in Polymer Science (2003); 28(12): 1643-1699.

[203] Gam KT, Miyamoto M, Nishimura R, Sue H-J. Fracture behaviour of core-shell rubber-modified clay-epoxy nanocomposites. Polymer Engineering and Science (2003); 43(10):1635-1645.

[204] Vassileva E, Friedrich K. Epoxy/alumina nanoparticle composites. I. Dynamic mechanical behavior. Journal of Applied Polymer Science (2003); 89(14): 3774-3785.

[205] Walter R, Friedrich K, Privalko V, Savadori A. On modulus and fracture toughness of rigid particulate filled high density polyethylene. The Journal of Adhesion (1997); 64(1-4): 87-109.

[206] Spanoudakis J, Young RJ. Crack propagation in a glass particle-filled epoxy resin Part 1. Effect of particle volume fraction and size. Journal of Materials Science (1984); 19(2): 473-486.

[207] Spanoudakis J, Young RJ. Crack propagation in a glass particle-filled epoxy resin Part 2. Effect of particle-matrix adhesion. Journal of Materials Science (1984); 19(2): 487-496.

[208] Hull D. Fractography: Observing, measuring and interpreting fracture surface topography. Cambridge University Press (1999).

[209] Hull, D. Influence of stress intensity and crack speed on fracture surface topography: mirror to mist to macroscopic bifurcation. Journal of Material Science (1996); 31: 4483-4492.

[210] Tuncer E, Sauers I, James DR, Ellis A, Paranthaman MP, Goyal A, More KL. Enhancement of dielectric strength in nanocomposites. Nanotechnology (2007); 18(32): 325704-325705.

[211] Kotaki M, Wang K, Toh ML, Chen L, Wong SY, He CB. Electrically conductive epoxy/clay/vapor grown carbon fiber hybrids. Macromolecules (2006); 39(3): 908-911.

[212] Narkis M, Lidor G, Vaxman A, Zuri L. Innovative ESD thermoplastic composites structured through melt flow processing. IEEE Transactions on Electronics Packaging Manufacturing (2000); 23(4): 239-245.

[213] Chatterjee A, Alam K, Klein P. Electrically conductive carbon nanofiber composites with high-density polyethylene and glass fibers. Materials and Manufacturing Processes (2007); 22(1): 62-65.

[214] Su S-J, Kuramoto N. Processable polyaniline–titanium dioxide nanocomposites: Effect of titanium dioxide on the conductivity. Synthetic Metals (2000); 114(2): 147-153.

[215] Chandrasekhar S, Liquid crystals. Cambridge University Press, New York (1992).

[216] Thostenson ET, Chou TW. On the elastic properties of carbon nanotube-based composites: Modeling and characterization. Journal of Physics D: Applied Physics (2003); 36(5): 573-582.

[217] Halpin JC, Kardos JL. The Halpin-Tsai Equations: A Review. Polymer Engineering and Science (1976); 16(5): 344-352.

[218] Halpin JC, Tsai SW. Environmental factors in composite material design. US Air Force Materials Laboratory Report (1969); AFMLTR 67-423.

[219] Tibbetts GG, McHugh JJ. Mechanical properties of vapor-grown carbon fiber composites with thermoplastic matrices. Journal of Materials Research (1999); 14(7): 2871-2880.

[220] Cox HL. The elasticity and strength of paper and other fibrous materials. British Journal of Applied Physics (1952); 3: 72-79.

[221] Lourie O, Cox DM, Wagner HD. Buckling and collapse of embedded carbon nanotubes. Physical review letters (1998); 81(8): 1638-1641.

[222] Rajagopal C, Satyam M. Studies on electrical conductivity of insulator-conductor composites. Journal of Applied Physics (1978); 49: 5536-5542.

[223] Bridge B. Simulation of the percolation threshold in metal fibre loaded conductive polymer composites. Journal of Materials Science Letters (1988); 7(6): 663-665.

[224] Batchelor GK, O'Brien RW. Thermal or Electrical Conduction through a granular material. Proceedings of the Royal Society A: Mathematical, Physical and Engineering Sciences (1977); 355(1682): 313-333.

[225] Weber M. PhD thesis, McGill University. Montreal, Quebec, Canada (1995).

9 List of publications

1. Carballeira P, Haupert F. Toughening effects of titanium dioxide nanoparticles on TiO_2/ epoxy resin nanocomposites. (accepted for publication in Polymer Composites, Published Online: Aug 17 2009; DOI: 10.1002/pc.20911).

2. Carballeira P, Haupert F, Toro P, Schlarb AK. Mechanical and electrical properties of MWCNTs / epoxy resin nanocomposites - Influence of the dispersion process. Submitted to Composites Science and Technology (Currently under review).

3. Carballeira P, Haupert F, Schlarb AK. Mechanical properties of carbon nanofiber-polymer nanocomposites. International Conference "Advanced Processing of Novel Functional Materials – Dresden 2008".

4. Carballeira P, Haupert F, Schlarb AK. Upgrading thermosets by nanofibers. 9th Trends in Nanotechnology International Conference (TNT2008) 1-5 September 2008 Oviedo (Spain).

5. Carballeira P, Haupert F, Schlarb AK. Mechanical properties of multi-walled carbon nanotubes reinforced epoxy nano-composites. IVW-Kolloquium 2006, IVW Schriftenreihe Band 68, Prof. Dr.-Ing. Alois K. Schlarb (Hrsg.), Kaiserslautern, 14-15. November 2006, S. 162-163.

6. Konter M, Carballeira P, Wetzel B, Schlarb AK, Pelster R. Charge transport in composite-materials containing carbon nano-tubes and carbon nano-fibers. 72. Jahrestagung der DPG (Deutsche Physikalische Gesellschaft) und DPG Frühjahrstagung des Arbeitskreises Festkörperphysik Berlin 25-29. February 2008.

7. Toro P, Carballeira P, Haupert F, Schlarb AK. Application of some dispersion processes for multi-walled carbon nanotubes in an epoxy matrix and the resulting mechanical properties. 6th International Nanotechnology Symposium New Ideas for Industry; Nanofair 2008; 11-12 March 2008 Dresden.

8. Carballeira P, Haupert F, Schlarb AK. Developing new carbon nanofiber reinforced epoxy resin composites through a calendering process. IVW-Kolloquium 2008, IVW Schriftenreihe Band 80, Prof. Dr.-Ing. Alois K. Schlarb (Hrsg.), Kaiserslautern, 16-17. September 2008, S. 195-196.

9. Carballeira P, Haupert F. Wear behaviour of carbon nanofiber-epoxy composites. Admitted for poster presentation at the 10th Trends in Nanotechnology International Conference (TNT 2009) 07-11 September 2009 Barcelona (Spain).

10. Konter M, Carballeira P, Haupert F, Wetzel B, Pelster R. On the quality of electrical contacts between carbon nano- fibers in composite-materials. 73. Jahrestagung der DPG (Deutsche Physikalische Gesellschaft) und DPG Frühjahrstagung des Arbeitskreises Festkörperphysik Dresden, 22-27. März 2009.

10 List of student support works

Mateu Piulats J. Tribological behaviour of carbon nanofibers-ceramic nanoparticles epoxy composites, Institut für Verbundwerkstoffe GmbH, Diplomarbeit, 2007.

Curriculum Vitae

Personal Data:

Family name:	Carballeira
First name:	Pablo
Date and place of birth:	12th December 1975; Oviedo, Spain
Nationality:	Spanish
Family status:	Single
Correspondence address:	Kurt Schumacher Strasse 14, App. 1.3 67663, Kaiserslautern, Germany

Education:

1997 – 2004	University of Salamanca (Spain). MSc. Degree in Physics.
2001 – 2002	Bristol University (UK). Stay abroad as a part of the EU Program Socrates / Erasmus.
2004 – 2005	Institut für Verbundwerkstoffe GmbH. (Germany). Practical training in the materials science department as a part of the EU Program Argo / Leonardo da Vinci.

Working experience:

2005 – 2009	Research associate at the Institut für Verbundwerkstoffe GmbH. PhD student in the “Nano research group“ of the materials science department.
2008	DADD financed student interchange program. Stay abroad in the research group of Prof. T. Tanimoto. Shonan Institute of Technology, Fujisawa, Japan.

Languages: Spanish (mother tongue), English, German, French.